STUDIES ON RADIATION SYNTHESIZED CONDUCTING POLYMERIC NANO COMPOSITES FOR CHEMIRESISTIVE SENSORS

By

Raj Kumar Mondal

CHEM01201404018

Bhabha Atomic Research Centre, Mumbai, INDIA

A thesis submitted to the

Board of Studies in Chemical Science

In partial fulfilment of requirements

for the Degree of

DOCTOR OF PHILOSOPHY

of

HOMI BHABHA NATIONAL INSTITUTE

October 2018

Homi Bhabha National Institute

Recommendations of the Viva Voce Committee

As members of the Viva Voce Committee, we certify that we have read the dissertation prepared by **Mr. Raj Kumar Mondal** entitled **"Studies on Radiation Synthesized Conducting Polymeric nano Composites for Chemiresistive Sensors."** and recommend that it may be accepted as fulfilling the thesis requirement for the award of Degree of Doctor of Philosophy.

Chairman – Prof. R.C. Bindal	**Date:** 09/09/2019
Guide / Convener – Prof. Lalit Varshney Lalit Varshney	**Date:** 09/09/2019
Examiner – Prof. Tokeer Ahmad	**Date:** 9/9/19
Member 1- Prof. Manmohan Kumar Manmohan Kumar	**Date:** 9/9/2019
Member 2- Prof. Y. K. Bhardwaj YK Bhardwaj	**Date:** 09/09/2019
Member 3- Prof. Virendra. Kumar	**Date:** 09/09/2019

Final approval and acceptance of this thesis is contingent upon the candidate's submission of the final copies of the thesis to HBNI.

I/We hereby certify that I/we have read this thesis prepared under my/our direction and recommend that it may be accepted as fulfilling the thesis requirement.

Date: 09/09/2019

Place: Mumbai

Lalit Varshney

(Signature)

Guide

Prof. LALIT VARSHNEY

STATEMENT BY AUTHOR

This dissertation entitled **“Studies on Radiation Synthesized Conducting Polymeric Nano Composites for Chemiresistive Sensors”** has been submitted in partial fulfillment of requirements for an advanced degree at Homi Bhabha National Institute (HBNI) and is deposited in the Library to be made available to borrowers under rules of the HBNI.

Brief quotations from this dissertation are allowable without special permission, provided that accurate acknowledgement of source is made. Requests for permission for extended quotation from or reproduction of this manuscript in whole or in part may be granted by the Competent Authority of HBNI when in his or her judgment the proposed use of the material is in the interests of scholarship. In all other instances, however, permission must be obtained from the author.

Raj Kumar Mondal
11/09/19

(Raj Kumar Mondal)

DECLARATION

I, hereby declare that the investigation presented in the thesis entitled **"Studies on Radiation Synthesized Conducting Polymeric Nano Composites for Chemiresistive Sensors"** has been carried out by me. The work is original and has not been submitted earlier as a whole or in part for a degree / diploma at this or any other Institution / University.

Raj Kumar Mondal
11/09/19

(Raj Kumar Mondal)

LIST OF PUBLICATIONS

Journals

1. Novel hybrid nanocarbons/poly(dimethylsiloxane) nanocomposite based chemiresistors for real time detection of hazardous aromatic hydrocarbons. **R. K. Mondal**, K. A. Dubey, Y. K. Bhardwaj, L. Varshney, Carbon 100(2016) 42-51.
2. Network density tailored standalone-flexible fluorocarbon elastomer/nanocarbon black chemiresistors for 2-propanone field detection. **R. K. Mondal**, Jitendra Kumar, K. A. Dubey, Y. K. Bhardwaj, J.S. Melo, L. Varshney, Sensors and Actuators B: Chemical 265 (2018) 193–203.
3. Carbon Nanotube Functionalization and Radiation Induced Enhancements in the Sensitivity of Standalone Chemiresistors for Sensing Volatile Organic Compounds. **R. K. Mondal**, K. A. Dubey, Jitendra Kumar, Jagannath, Y. K. Bhardwaj, J.S. Melo, L. Varshney. ACS Applied Nano Materials 1(10) (2018) 5470-5482.
4. Development of a novel strain sensor based on fluorocarbon–elastomeric nanocomposites: Effect of network density on the electromechanical properties. K. A. Dubey, **R. K. Mondal**, V. Grover, Y. K. Bhardwaj, A.K. Tyagi. Sensors and Actuators A: Physical 221 (2015) 33–40.

Conferences/Symposia

1. Radiation effects on fluorocarbon-elastomeric nanocomposites. **R. K. Mondal**, K. A. Dubey, Y. K. Bhardwaj, L. Varshney, NICSTAR-2015, March 4-6, 2015.
2. Development of radiation crosslinked strain sensor based on fluorocarbon-elastomeric nanocomposites. K. A. Dubey, **R. K. Mondal**, V. Grover, Y. K. Bhardwaj, A. K. Tyagi , L. Varshney, ISMC-2014, December 9-12, 2014.

3. Development of radiation processed graphene/polymer composite based chemiresistors for real-time detection of toxic organic volatiles. **R. K. Mondal**, K. A. Dubey, Y. K. Bhardwaj, L. Varshney. 6th Interdisciplinary Symposium on Material Chemistry held during 6-10 December 2016 (ISMC-2016).
4. Dielectric loss in irradiated high-dielectric fluorocarbon elastomer/ nano carbon black nanocomposites. **R. K. Mondal**, K. A. Dubey, Y. K. Bhardwaj, L. Varshney, NICSTAR-2018, March 5-7, 2018.
5. CNT induced coagulated NRL/CNT nanocomposites based chemiresistors for sensitive detection of Isoprene vapour. **R. K. Mondal**, C. V. Chaudhary, K. A. Dubey, Y. K. Bhardwaj, L. Varshney. 7th Interdisciplinary Symposium on Material Chemistry (ISMC-2018).

Raj Kumar Mondal
11/09/19

(Raj Kumar Mondal)

Dedicated

To

My Parents

ACKNOWLEDGEMENTS

During the course of my thesis work there were many people who were instrumental and influential in helping me. I would like to thank all those people who made this thesis possible and enjoyable.

My foremost thanks go to my research advisor Prof. Lalit Varshney for his guidance, patience, encouragement and for allowing me freedom to pursue my interests. Under his guidance I not only learned how to conduct research, but also how to communicate my ideas. I would also express my deepest sense of gratitude towards my doctoral committee Chairman Dr. R. C. Bindal, and members of my doctoral committee Dr. Manmohan Kumar, Dr. Y.K. Bhardwaj and Dr. Virendra Kumar for their insightful comments and constant encouragement throughout the tenure of my doctoral work and during my review meetings. Equally significant is the contribution of my research partner Dr. K. A. Dubey in giving shape and direction to my work. I owe my utmost gratitude to him for all the invaluable time he spent in guiding me and helping to design and execute my work. My sincere thanks go to Mr. C. V. Chaudhary and Mr. S. P. Shejwal for always offering a helping hand in experimental work during the course of study. I express my gratitude to all colleagues in the Radiation Research and Application Development Section for their unconditional support, encouragement and co-operation. Special thanks to Dr. Jitendra Kumar and Dr. Jagganath for extending their support at various stages of my work.

Also I express my sincere note of thanks to everybody who has extended their helping hands towards the successful accomplishment of this thesis work, as well as expressing my apology not been able to mention all those individual names.

Nothing can be accomplished without support from family and friends. I would like to extend my special gratitude to my family. I am forever indebted to my parents, from whom I learned a great deal of life. Their infallible love and support has always been my strength. Their patience and sacrifice will remain my inspiration throughout my life. I would also like to thank my friends for their constant support and encouragement.

Finally, my greatest regards to the Almighty for bestowing upon me the courage to face the complexities of life and complete this project successfully.

Raj Kumar Mondal
11/09/19

(Raj Kumar Mondal)

CONTENTS

SYNOPSIS

Since the discovery of X-ray in 1895, Radiation Technology has been contributing in advancement of science and technology. It is also responsible for development of new materials for various applications in industry, health care and agriculture. Ever increasing environmental pollution has been a serious concern for human health. Volatile organic compounds (VOCs) are one of the main reasons behind it. Monitoring and identification of VOCs is a primary challenge before any solution is perceived. Thus, in order to maintain their concentration within permissible limit and avoid exposure associated health hazards, rapid detection and identification of VOCs is desired [1, 2]. Volatile organic compounds (VOCs) are a diverse group of carbon-based chemicals that are volatile at ambient temperature. There are various sources of VOCs exposure which include petroleum products, synthetic rubber industries, plastics industries, leather industry, insecticides and paints etc. Some VOCs are also generated from incomplete combustion of wood and fossil fuels [3, 4] . Chronic exposure of VOCs are associated with serious health concerns such as skin and sensory irritation, carcinogenesis, mutagenesis, central nervous system depression and respiratory system damage etc [3, 5]. This kind of exposure along with severity of health affects demand for the development of fast low cost and sensitive VOCs detection systems. In the present study we have studied and tried to develop fast, sensitive and low cost sensors for detection and identification of VOCs. Particularly, radiation technology has been utilized due to its inherent advantages and ability to form desired level of cross-linking in the polymer matrix without any chemical additives.

Our exhale breath contains minuscule amount of over 200 different types of VOCs besides CO_2, N_2 and oxygen. Alteration of these VOCs concentration in exhale breath is an indication of metabolic and physiological disorder. Thus the exhaled breath analysis is a promising noninvasive method for early diagnosis of many lives threatening diseases. The detection and identification of VOCs in exhaled breath may lead to the development of novel, noninvasive diagnostic methods for a wide range of diseases, such as different types of cancer [6], liver failure [7], kidney failure, diabetics [8] etc. This kind of breath analysis is now considered to be futuristic, low cost sensitive technique for early detection of diseases.

In general VOCs are analyzed using gas chromatography mass spectroscopy (GC-MS) [9], FT-IR spectroscopy and HPLC, but such techniques suffer from complexity, non-portability and are of high cost and time consuming [10, 11]. There are many different approaches that can be used to synthesize portable sensors for VOC field detection, viz surface plasmon resonance, chemiresistivity, surface acoustic wave and quartz crystal microbalance [12]. Among them Chemiresistive sensors have many advantages over others in terms of cost, response time, ease of production, real-time monitoring and the possibility of an easy integration into a chemiresistive array [13, 14]. Chemiresistive materials include metal oxide semiconductor and conducting polymers. Zhang et al reported that maize straw-templated hierarchical porous ZnO:Ni have high sensitivity for acetone vapour but the response was humidity dependent and the operating temperature was 340 ◦C [15]. SnO_2 hollow spheres activated by Ni templates have enhanced response and recovery time for ethanol vapour but also operating at 400 ^{o}C [16]. Ultrafine Fe_2O_3 nanoparticles showed sensitivity for acetone vapour in a broad range but at temp of 340 ◦C and have very poor cross-sensitivity for ethanol [17]. All these examples established the fact that metal oxide semiconductor based sensors generally operate at high temperature, consumes more power, sensitive to humidity and are complex devices [18-20]. Conducting polymer based sensors are simple, sensitive, cost effective and operate at room temperature [14, 21]. In this study we have investigated and developed conducting polymeric composite based sensors.

Electrical conductivity and a responsive polymer phase are two essential requirements for developing chemiresistive sensors. In the present study different thermoplastic and elastomeric polymer matrices have been explored for the chemiresistive application. Nanocarbon based materials have attracted significant attention from the scientific community for various application due to their unique electrical, electronic, optical, thermal, mechanical, and chemical properties. Most of the atoms in case of nano-dimensional carbon materials when exposed to the environment offer high specific surface area, which is ideal for adsorption of vapour molecules leading to high sensitivity. As a result, there is an increased interest in development of nanocarbon based sensors with fast response time, high sensitivity, selectivity, portability and process ease. Conducting nanocarbon black (NCB) [22], Carbon nanotube(CNT) [10] and graphene [23] are among the most promising nano carbon materials for developing nanocarbon based chemiresistor, owing to their low cost and high conductivity.

Melt and shear compounding are most effective approaches to synthesize Conducting polymer composites (CPC) chemiresistoirs as they do not involve any solvent or added chemicals and can be easily up scaled. However, in compounding techniques the percolation threshold (minimum concentration of conducting filler required to get electrical conductivity) of conducting filler is much higher than in-situ polymerization or in sonication assisted solvent/emulsion dispersion. To over-come this difficulties innovative strategies such as hybrid fillers, functionalization of filler or selective percolation can be used to achieve desired electrical conductivity at lower loading of filler as well as to improve desired functionality. This study describes use of hybrid and functionalized filler using melt and shear compounding techniques.

High energy radiation can produce cross-linked networks in a polymer matrix. It forms linkages in the polymer and polymer-filler interface [24]. High energy irradiation forms free radicals on filler surfaces; interface of polymer and filler and in the bulk which initiate reactions to bring changes in the polymer composites. Cross-linked networks are expected to improve dimensional stability under chemiresistive pressure and thus providing an important contribution to the development of a standalone chemiresisitor. The thesis work has been structured into six chapters.

Chapter 1: Introduction

First chapter of the thesis gives brief description of different VOCs present in environment, their sources and impact on human body. Detection and identification of hazardous VOCs are some time useful for diagnosis of diseases as these have been observed to be released in certain disease condition in exhaled breath. An over view of different biomarker present in exhaled breath is also presented in this context. The advantages of biomarker analysis by chemiresistive VOC sensors over the other conventional methods of breath analysis are also mentioned. A detailed description of literature on the different polymer and nanocarbon materials based VOCs sensors is also provided. Finally, the focus is given to radiation processed carbon nanomaterials based conducting polymer nanocomposite chemiresistors which can be used as a basic component for VOC sensors.

Chapter 2: Experimental methods and Characterization techniques

This chapter deals with the preparation of CPC by adopting different strategies and techniques (e.g melt compounding/shear compounding and solution casting). CPC prepared by melt compounding/shear compounding discussed here. The process describes making of CPC by taking different amount of conducting fillers and prerequisite amount of polymer as per their bulk density and are mixed homogenously in Brabender plasticordar at elevated temperature. The cooled homogeneous mixture so obtained is cut into small pieces. Then these small pieces are compression molded at elevated temperature into different thicknesses sheets. The compression molded CPCs were then exposed to graded doses of high energy Co-60 gamma radiation in a gamma chamber (GC-5000) to get suitable cross linked CPCs for further studies. Prior to irradiation the dose rate of the gamma chamber is ascertained by Fricke dosimetry. The details of all the instruments used for characterizing the synthesized CPCs are discussed in this chapter. Fabrications of sensing elements and vapour sensing setup both static as well as dynamic have been discussed in details.

Results and discussion of all the experiments are divided into the following three chapters (chapter 3, chapter 4 and chapter 5). In order to develop the sensors selective towards different targeted VOC, different methodologies have been developed. Each of the undertaken methods aiming to develop radiation processed conductive nanocomposites based chemiresistive sensors are separately focused in these chapters along with their selective, sensitive and room temperature vapour sensing performance. The VOC's selected for the studies included Benzene, Toluene, Xylene, Ethyl benzene, 2-propanone, Isoprene and Ethanol.

Chapter 3: Nanocarbon black and carbon nanotube based conducting polymeric composites as chemiresistive sensors.

This chapter describes various results and discussions on chemiresistive behavior of radiation crosslinked and chemical crosslinked Nano carbon black (NCB) and carbon nanotube (CNT) based CPCs.

First section of the chapter describes development of a novel stand-alone radiation crosslinked highly sensitive and selective chemiresistive sensor for 2- propanone. Fluorocarbon elastomer (FCE)/nanocarbon black (NCB) conducting composites based chemiresistors were synthesized via shear compounding. High energy Co-60 radiation was used to impart different crosslinked network densities in FCE/NCB chemiresistors.

Physicomechanical and electrical properties of these crosslinked CPCs were thoroughly studied by four probe technique. Conducting composites in different parts of the percolation profile were chosen to establish the dependence of 2-propanone sensing response on the conducting network and the radiation cross-linked network. The chemiresistor showed a highly selective response for 2-propanone whereas a considerably lower response was noted for benzene, toluene, xylene, ethanol, methanol and water.

In the second section of this chapter preparation of a CNT induced coagulated natural rubber latex (NRL) nanocomposites is described. These NRL/ CNT based chemiresistors were irradiated with high energy gamma radiation and chemiresistive behavior have been evaluated. Surface charge neutralization of the NRL particles by CNT leads to coagulation of NRL. The mechanism of charge neutralization has been discussed here and this was confirmed by zeta potential measurement. This crosslinked NRL/CNT based nanocomposite showed good selective response towards Isoprene vapor and negligible response was obtained for water, methanol and ethanol vapor. Alcohol being an interesting VOC for detection a chemically crosslinked polyvinyl butyral/CNT based chemiresistor for ethanol sensor has been discussed in the last part of this chapter. Crosslinking of the polymer nanocomposites improve the sensing response of the chemiresistors.

Chapter 4: Hybrid Nanocarbon black and Multi walled carbon nanotube based conducting polymeric composites for detection of aromatic hydrocarbon.

This chapter is devoted to development of conductive nanohybrid composites which are essentially multicomponent systems where two nanomaterials are incorporated. Efforts were made to understand how two geometrically different nanocarbons can affect the response of a chemiresistive sensor. The study described results of development of poly(dimethylsiloxane) (PDMS)/carbon nanotube (CNT) and nanocarbon black based novel hybrid chemiresistive sensors. These PDMS based sensors demonstrated high sensitivity and reversible response for benzene, toluene, ethyl benzene and xylene (BTEX) under dynamic flow as well as under static vapour conditions. PDMS-BTEX interaction parameter (χ_{12}) has a strong correlation on sensing response. Addition of CNT improves temperature stability of composites and its electrical conductivity upto 120 ^{o}C. While sensitivity did not change significantly on addition of CNT into composites, detection limit for VOCs increased. Using an array of CPCs having different concentration of CNT enables detection of benzene in a mixture of BTEX. This study indicates the observed behavior is due to varying diffusion characteristics of the BTEX into composites.

Chapter 5: Enhancement of chemiresistivity of CPCs by using functionalized CNT-polymer composites.

This chapter is mainly focused on development of radiation crosslinked chemiresistive sensors containing Functionalized Carbon Nanotube. The results elucidate the effect of the CNT-functionality on chemiresistive behavior of the chemiresistor. Polymer-filler interactions were modified by gamma irradiation that in turn affected chemiresistivity of the matrix. PDMS/CNT conducting composites with un-functionalized (CNT-UF), hydroxyl functionalized (CNT-OH), amine functionalized (CNT-NH2) and carboxylic functionalized (CNT-COOH) were prepared and were irradiated. At the same volume fraction, amine functionalized chemiresistor exhibited least response while carboxylic functionalized shows highest response against toluene vapors. Hydroxyl functionalized chemiresistors manifested poor nanotube dispersion and low electrical conductivity. Rheological study shows PDMS/CNT-COOH chemiresistors has the high critical strain for CNT-CNT structure breakdown under shear strain. Complex viscosity of the composites increased with CNT-COOH concentration. This is due to interfacial grafting and immobilization of PDMS segments on to CNT-COOH surface. The PDMS/CNT-COOH composites displayed highly sensitive, reversible and reproducible sensing behavior for toluene vapor. The gel content of the composites increased with radiation dose. Gel content for PDMS/CNT-NH_2 was observed to be low compare to PDMS/CNT-UF and PDMS/CNT-COOH composites because CNT-NH_2 inhibits interfacial radical combinations. Chemiresistivity of the composites increased with radiation dose for both PDMS/CNT-COOH and PDMS/CNT-UF composites. But the magnitude of increase in chemiresistivity is higher in case of PDMS/CNT-COOH composites than PDMS/CNT-UF composites. This observation indicates that the enhancement of chemiresistivity is due to radiation induced modification of CNT-COOH PDMS interface.

Chapter 6: Summary and Scope of future study

This chapter summarizes the results of the studies carried out as a part of this thesis. The important outcomes of the study are following:

(i) Fluorocarbon elastomer and NCB based radiation crosslinked chemiresistor can be useful for rapid, sensitive and room temperature detection of acetone vapour. Irradiation using high energy radiation was found to improve sensing characteristics due to crosslink and alteration in filler-polymer interactions.

(ii) It was found that use of NCB and CNT nanohybrid and PDMS based CPCs chemiresistors are useful for detection of BTEX vapor. Use of CNTs not only increase electrical conductivity but also lowers the temperature dependence of resistivity. Detection range of VOCs was found to increase with increase of CNT loading. A distinct pattern of analyte can be resolved by using an array of four chemiresistors with different CNT content with the help of principle component analysis.

(iii) CNT functionality has a distinct effect on the chemiresistivity of PDMS/CNT composites. With the increase in radiation dose, the chemiresistivity increased, suggesting the possibility of interfacial grafts and immobilization of PDMS segments on to CNT-COOH surface. The better interfacial interactions between the COOH functionalized CNT and PDMS translated in radiation induced modifications of PDMS/CNT-COOH interface, which eventually lead to a marked enhancement in the sensitivity of the chemiresistor.

The future study involves improvement in detection limit of the chemiresistive sensors and field trials. In order to enhance sensitivity of CPC based chemiresistors large surface area porous polymer matrix can be used, which will increase the diffusion and contact area of analyte molecules inside chemiresistor efficiently. The present study shows that radiation crosslinked polymer-nanocarbon/ CNT based conductive polymer nanocomposites sensors can find applications in field detection of VOCs for industrial and medical applications.

References

[1] C.-T. Chang, B.-Y. Chen, Toxicity assessment of volatile organic compounds and polycyclic aromatic hydrocarbons in motorcycle exhaust, Journal of hazardous materials 153(3) (2008) 1262-1269.
[2] Z. He, G. Li, J. Chen, Y. Huang, T. An, C. Zhang, Pollution characteristics and health risk assessment of volatile organic compounds emitted from different plastic solid waste recycling workshops, Environment international 77 (2015) 85-94.
[3] M. Belloc-Santaliestra, R. van der Haar, E. Molinero-Ruiz, Occupational Exposure Assessment of Highway Toll Station Workers to Vehicle Engine Exhaust, Journal of occupational and environmental hygiene 12(1) (2015) 51-61.
[4] M. Girschikofsky, M. Rosenberger, S. Belle, M. Brutschy, S.R. Waldvogel, R. Hellmann, Optical planar Bragg grating sensor for real-time detection of benzene, toluene and xylene in solvent vapour, Sensors and Actuators B: Chemical 171 (2012) 338-342.
[5] E. Durmusoglu, F. Taspinar, A. Karademir, Health risk assessment of BTEX emissions in the landfill environment, Journal of hazardous materials 176(1-3) (2010) 870-877.
[6] Z. Xu, Y.Y. Broza, R. Ionsecu, U. Tisch, L. Ding, H. Liu, Q. Song, Y. Pan, F. Xiong, K. Gu, A nanomaterial-based breath test for distinguishing gastric cancer from benign gastric conditions, British journal of cancer 108(4) (2013) 941.
[7] K. Wlodzimirow, A. Abu-Hanna, M. Schultz, M. Maas, L. Bos, P. Sterk, H. Knobel, R. Soers, R.A. Chamuleau, Exhaled breath analysis with electronic nose technology for detection of acute liver failure in rats, Biosensors and Bioelectronics 53 (2014) 129-134.
[8] T.D.C. Minh, D.R. Blake, P.R. Galassetti, The clinical potential of exhaled breath analysis for diabetes mellitus, Diabetes Research and Clinical Practice 97(2) (2012) 195-205.

[9] B. Agnieszka, T. Ettje, S. Agnieszka, W.D. Jan, J.C.M. Edwin, A.M.D. Jackie, W. Cisca, Z. Alexandra, J.v.S. Frederik, Profile of volatile organic compounds in exhaled breath changes as a result of gluten-free diet, Journal of Breath Research 7(3) (2013) 037104.

[10] A. Allouch, S. Le Calvé, C.A. Serra, Portable, miniature, fast and high sensitive real-time analyzers: BTEX detection, Sensors and Actuators B: Chemical 182 (2013) 446-452.

[11] I. Ueta, Y. Saito, M. Hosoe, M. Okamoto, H. Ohkita, S. Shirai, H. Tamura, K. Jinno, Breath acetone analysis with miniaturized sample preparation device: In-needle preconcentration and subsequent determination by gas chromatography–mass spectroscopy, Journal of Chromatography B 877(24) (2009) 2551-2556.

[12] M. Myers, J. Cooper, B. Pejcic, M. Baker, B. Raguse, L. Wieczorek, Functionalized graphene as an aqueous phase chemiresistor sensing material, Sensors and Actuators B: Chemical 155(1) (2011) 154-158.

[13] T. Zhang, S. Mubeen, N.V. Myung, M.A. Deshusses, Recent progress in carbon nanotube-based gas sensors, Nanotechnology 19(33) (2008) 332001.

[14] S.-W. Chiu, K.-T. Tang, Towards a chemiresistive sensor-integrated electronic nose: A review, Sensors 13(10) (2013) 14214-14247.

[15] X. Zhang, Z. Dong, S. Liu, Y. Shi, Y. Dong, W. Feng, Maize straw-templated hierarchical porous ZnO:Ni with enhanced acetone gas sensing properties, Sensors and Actuators B: Chemical 243 (2017) 1224-1230.

[16] H.-R. Kim, K.-I. Choi, K.-M. Kim, I.-D. Kim, G. Cao, J.-H. Lee, Ultra-fast responding and recovering C2H5OH sensors using SnO2 hollow spheres prepared and activated by Ni templates, Chemical Communications 46(28) (2010) 5061-5063.

[17] S. Liang, J. Li, F. Wang, J. Qin, X. Lai, X. Jiang, Highly sensitive acetone gas sensor based on ultrafine α-Fe2O3 nanoparticles, Sensors and Actuators B: Chemical 238 (2017) 923-927.

[18] F. Liu, X. Yang, B. Wang, Y. Guan, X. Liang, P. Sun, G. Lu, High performance mixed potential type acetone sensor based on stabilized zirconia and NiNb2O6 sensing electrode, Sensors and Actuators B: Chemical 229 (2016) 200-208.

[19] A. Güntner, N.A. Sievi, S.J. Theodore, T. Gulich, M. Kohler, S.E. Pratsinis, Noninvasive body fat burn monitoring from exhaled acetone with Si-doped WO3-sensing nanoparticles, Analytical Chemistry 89(19) (2017) 10578-10584.

[20] F. Liu, C. Ma, X. Hao, C. Yang, H. Zhu, X. Liang, P. Sun, F. Liu, X. Chuai, G. Lu, Highly sensitive gas sensor based on stabilized zirconia and CdMoO4 sensing electrode for detection of acetone, Sensors and Actuators B: Chemical 248 (2017) 9-18.

[21] M. Castro, J. Lu, S. Bruzaud, B. Kumar, J.-F. Feller, Carbon nanotubes/poly(ε-caprolactone) composite vapour sensors, Carbon 47(8) (2009) 1930-1942.

[22] H. Deng, L. Lin, M. Ji, S. Zhang, M. Yang, Q. Fu, Progress on the morphological control of conductive network in conductive polymer composites and the use as electroactive multifunctional materials, Progress in Polymer Science 39(4) (2014) 627-655.

[23] F. Yavari, N. Koratkar, Graphene-based chemical sensors, The journal of physical chemistry letters 3(13) (2012) 1746-1753.

[24] K. Dubey, Y. Bhardwaj, C. Chaudhari, V. Kumar, N. Goel, S. Sabharwal, Radiation processed ethylene vinyl acetate-multiple walled carbon nanotube nano-composites: effect of MWNT addition on the gel content and crosslinking density, Lett 3 (2009) 492-500.

LIST OF SYMBOLS

Symbol	**Definition of symbol with unit**
ΔA_D	Change in absorbance
A_r	Relative resistance change or sensing response($A_r = \Delta R/R_0$)
Ar,p	Base line corrected sensing response
σ_{AC}	AC conductivity (S/cm)
σ_{DC}	DC conductivity (S/cm)
$\tan\delta$	Loss factor
D	Dissipation factor
ϕ	Volume fraction
ϕ_c	Percolation concentration of fillers
χ_{12}	Flory-Huggins interaction parameter
δ_p	Energy from polar bonds between molecules ($MPa^{1/2}$)
δ_d	Energy from dispersion bonds between molecules ($MPa^{1/2}$)
δ_H	Energy from hydrogen bonds between molecules ($MPa^{1/2}$)
δ_T	Total energy from bonds between molecules ($MPa^{1/2}$)
γ-ray	Gamma radiation
γ	Shear strain (%)
γ_c	Critical strain (%)
ω	Angular frequency (rad/s)
ω_c	Critical angular frequency (rad/s)
G'	Storage modulus (Pa)
G''	Loss modulus (Pa)
G'_0	Shear storage modulus at low strain
G'_∞	Shear storage modulus at very high strain
ε'	Dielectric permittivity
ε''	Loss permittivity
ε_0	Permittivity of vacuum ($8.854 \times 10^{-12}\ J^{-1}\ C^2\ m^{-1}$)
ε_r	Relative permittivity
δ	Phase shift

ρ	Resistivity (Ohm/cm)
γ_l^d	Dispersive component (mN/m)
γ_l^d	Polar component (mN/m)
γ_{lv}	Surface tension (mN/m)
$\sigma(t)$	Shear stress, time dependent
η	Coefficient of viscosity (Pa.s)
η^*	Complex viscosity (Pa.s)
ε	Molar extinction coefficient (M^{-1} cm^{-1})
$G(p)$	Radiation chemical yield (number of molecules per 100 eV)
M_c	Molecular weight between crosslinks
β	Lattice constant
R	Universal gas constant (8.314 Joule/mol. K)
k_H	Henry's diffusion parameter
b_L	Langmuir's affinity parameter
M_t	Absorbed mass of analytes at time t
M_∞	Absorbed mass of analytes at saturation
M_e	Molecular weight between entanglement
Z	Electrical impedance (Ohm)
Z'	Real part of impedance
Z''	Imaginary part of impedance
ν_e	Entanglement density
λ	Elongation ratio
Ω	Resistance (Ohm)
τ	Relaxation time (sec)
ζ	Zeta potential

LIST OF ABBRIVIATIONS

Abbreviation	**Full form**
AC	Alternating current
AML	Acute myelogenous leukemia
BTEX	Benzene, Toluene, Ethyl benzene and Xylene
CNS	Central nervous system
CNT	Carbon nanotube
CNT-COOH	Carboxylic functionalized carbon nanotube
CNT-NH_2	Amine functionalized carbon nanotube
CNT-OH	Hydroxyl functionalized carbon nanotube
CNT-UF	Unfunctionalized carbon nanotube
CPC	Conducting polymeric composites
DC	Direct current
DMTA	Dynamic mechanical thermal analysis
EPA	Environmental Protection Agency
FCE	Fluorocarbon elastomer
FTIR	Furrier transformed infrared spectroscopy
GC	Gas Chromatography
HPLC	High Performance Liquid Chromatography
ID	Inner diameter

ICP	Intrinsically conducting polymer
IDHL	Immediately dangerous to life or health
LOD	Lower limit of detection
MWCNT	Multi walled carbon nanotube
NCB	Nano carbon black
NRL	Natural rubber latex
OD	Outer diameter
OSHA	Occupational Safety and Health Administration
PANI	Polyaniline
PCA	Principle Component analysis
PDMS	Polydimethyl siloxane
PEL	Permissible emission limit
PMMA	Polymethyl methacrylate
PTC	Positive temperature coefficient
PVB	Polyvinyl Butyral
PVC	Positive vapour coefficient
S/N	Signal to noise ratio
SAW	Surface acoustic wave
SD	Standard deviation
SEM	Scanning Electron microscope
SRF	Standard rectangular fixture

SSA	Specific surface area
SWCNT	Single walled carbon nanotube
TVL	Threshold limit value
VOC	Volatile Organic compounds
VTMS	Vinyl trimethoxy silane
XPS	X-ray photo electron spectroscopy

LIST OF FIGURES

Change in A_r after exposure to successive air-toluene cycles, three cycles of a fixed concentration were used followed by increased concentrations. (D) Reproducibility of PDMS/CNT-COOH chemiresistors against toluene vapour.

LIST OF TABLES

CHAPTER 1

Introduction

1.1. Background

Rapid increase in environmental pollution has been a serious concern for human health [1, 2]. Volatile organic compounds (VOCs) are one of the main reasons behind it. These compounds are a diverse group of carbon-based compounds which are volatile at ambient temperature. The VOC family is composed of saturated and unsaturated hydrocarbons, aromatic compounds, alcohols, aldehydes, ketones and nitriles etc. There are varied sources of VOCs exposure which include petroleum products, consumer products, synthetic rubber, plastics, leather industry, insecticides and paints. They are also reported in exhaust gases of motor vehicles, incomplete combustion of wood and fossil fuels [3, 4]. Inhalation is the major route of exposure of VOCs and get readily absorb in lungs gastrointestinal track and skin. The effects ranging from Central nervous system (CNS) toxicity to carcinogenicity of VOCs have been reported on animals and humans. Chronic exposure of VOCs such as benzene, toluene, ethyl benzene, xylene, formaldehyde have negative effects on human health including skin and sensory irritation, carcinogenesis, mutagenesis, CNS depression and respiratory system damage [3, 5-8]. In this context, regulatory agencies like the US Environmental Protection Agency (EPA), The Agency for Toxic Substances and Disease Registry, and the Occupational Safety and Health Administration (OSHA), have determined health advisory levels for VOCs exposure. The highest exposures of VOCs occur at working places of various chemical industries, oil refineries, petrol pump etc. In order to protect against the acute effects of high-level and short-term exposure to VOCs at the workplace the US EPA and OSHA established threshold limit values for an 8-h workday and 40-h workweek. As for examples, permissible exposure limit (PEL) for benzene [9], toluene and acetone [10] as per OSHA is 5 ppm, 200 ppm and 1000 ppm respectively at a time weighted average concentration for eight hours shift. Thus detection, identification and quantification of VOCs are primary challenge in order to maintain their concentration within permissible limit and avoid exposure associated health hazards[11, 12].

Another motivation is that, VOCs exhaled from human body can provide information about health condition of an individual. Therefore, quantitative and qualitative analysis of VOCs excreted from human body can be used for monitoring body chemistry. Various diseases induce alteration of metabolism, which results in a different microenvironment and generation of several biomarkers [13-15]. After the first instrumental analysis in 1971 by Linus Pauling, diagnosis of biomarkers in exhaled breath has attracted increasing interest and is a rapidly growing research area [16]. Breath analysis has been used since ancient times, as a diagnostic tool for diseases such as a sweet breath odour related to diabetics, a fishy breath related to liver disease [17]. Detection of volatile organic compounds (VOCs) is a new frontier in rapid, sensitive, selective and non-invasive analysis and medical diagnosis of human diseases [18]. Such a wide extent of exposure along with severity of health consequences put a pressing need for development of fast responsive VOCs detection systems. The demand for low-cost, low-power, and portable volatile organic compound (VOC) detection is increasing dramatically due to the need for environment monitoring as well as for medical applications [19]. Conducting polymeric nanocomposites (CPC) based chemiresistive sensors for VOCs detection have drawn signification attention due to their low cost, light weight, room temperature operation and portability [20-22]. Particularly, radiation technology has been utilized due to its inherent advantages and ability to form desired level of cross-linking in the polymer matrix without any chemical additives.

1.2. Some typical VOCs and their toxic effects

VOCs are numerous, varied, and ubiquitous. There are several VOCs which are hazardous to human health. There are substantive evidences that exposure to VOCs can produce eye, nose, and throat irritation; headaches, loss of coordination, nausea; and damage to the liver, kidney, and central nervous system. Some of the VOCs are known carcinogenic and some of them are potential carcinogenic to human and other animals. Chemicals included in this section are aromatic hydrocarbons, such as benzene, toluene, xylene, ethylbenzene together they are called (BTEX), haloalkanes and haloalkenes, aldehydes, glycols and glycol ethers, and nitroamines. Table 1.1 summaries some typical VOCs and their major emitters along with concentration limit.

Table 1.1: Some typical VOCs emitted from industries.

Industries	Major emitted VOCs	Concentration (mg/m^3)	Emission characteristics
Automobile	Toluene Ethyl benzene p-Xylene	13.34 2.95 4.13	Large volume emission during spraying and baking
Printing	o-Xylene Isopropyl alcohol Ethyl acetate 1-Methoxy 2-propanol	10.16 1.73 2.64 2.16	Steady emission with middle level concentration
Pharmacy	Ethanol	1.67	Intermittent emission with low
Furniture manufacturing	Toluene Acetic acid Ethyl benzene Cyclohexane p-Xylene	23.5 26.5 10.9 6.56 10.16	Unsteady emission with moderate concentration

1.2.1. Benzene

Benzene is primarily produced from commercial petroleum. It has been used as a solvent for general purpose and also in the synthesis of other chemicals. In general, 1 to 2 % by volume benzene present in gasoline. Due to the antiknock properties of benzene it plays an important role in unleaded gasoline (UG). Cigarette smoking is the main source of benzene in indoor area [23]. In compare to non-smokers, smokers generally have 6 to 10 times higher benzene body burdens. The most adverse effect of benzene is hematopoietic toxicity, which leads to leukaemia. The bone marrow damage, which may be noticeable initially as anemia can lead to, leukopenia, thrombocytopenia, or a combination of these by chronic and high benzene exposure There is strong support of evidence from epidemiological studies that high-level benzene exposures will result in an increased risk of acute myelogenous leukemia (AML) in humans [24]. Benzene is considered to be a known human carcinogen by regulatory agencies around the world.

1.2.2. Toluene

Toluene may be found in many household products like paints, lacquers, thinners, cleaning agents, glues etc. It is also used in the production of other chemicals. 5 to 7 % toluene is present in gasoline. It is the largest source of atmospheric emissions and exposure of the general populace. Primary route of exposure for toluene is inhalation, although skin contact of toluene occurs frequently. Toluene can rapidly accumulate in brain due to the high rate of blood perfusion hence can damage brain tissue. Another factor is the relatively high lipid content can also affect brain cell. The CNS is the primary targeted organ of toluene and other alkylbenzenes [25]. Cardiac, renal, and hepatic toxicities as well as fetal alcohol-like syndrome have occasionally been reported.

1.2.3. Xylene and Ethyl benzene

Large numbers of people are exposed to xylenes and ethylbenzene occupationally and environmentally. Like other aromatic hydrocarbons, Xylenes and Ethylbenzene are major components of gasoline and fuel oil. They are primarily used in industries as solvents and synthetic intermediates in very large amounts. Most of these aromatics that are released into the environment evaporate into the atmosphere. Xylenes and the others are well absorbed from the lungs and GI tract, distributed to well-perfused and lipophilic tissues such as liver, fat, brain, and skin. Generally, Xylenes and ethylbenzene don’t have significant adverse affects on the organs other than the CNS. Upon high exposure of xylene a transient liver and kidney toxicity have occasionally been reported in humans. The current permissible emission limit (PEL) for xylenes and ethylbenzene is 100 ppm.

1.2.4. Acetone

Acetone is a common reagent used widely in industries and laboratories. The compound is extensively used to dissolve plastics, purify paraffin and dehydrate tissues, and also is used in pharmaceutics. Acetone is harmful to health and its inhalation can cause irritation of the eyes, nose, and throat. A short exposure for 5 min to 300–500 ppm can be slightly irritating to humans. In high concentrations, it can produce dryness in the mouth, fatigue, headache, nausea, dizziness, muscle weakness, loss of coordinated speech, and drowsiness. Ingestion can cause headache, dizziness, and dermatitis. The inhalation of acetone causes headache, fatigue and even narcosis and harmfulness to nerve system. Therefore, it is necessary to monitor the acetone concentration in the environment for health and workplace for safety.

1.2.5. Chlorinated hydrocarbons

Trichloroethane, trichloroethylene, tetrachloroethylene, methylene chloride carbon tetra chloride and chloroforms are main chlorinated hydrocarbons comes under VOCs. They are mainly used as a solvent, dry cleaner, fabric finisher, degreaser, paint and stain remover and chemical intermediate. Moderate to high doses of halocarbons, are associated with a number of noncancer toxicities. Tetrachloroethylene induced hepatic injury to human upon exposure to high concentration. CCl_4 produced oxidative stress in brain and increased lipid peroxidation (LPO), protein carbonyls (PC) content and glutathione (GSH) depletion are observed upon exposure to CCl_4 [26].

1.2.6. Formaldehyde

Formaldehyde is widely used in the industrial and medical fields, and employees in these sectors are frequently exposed to it. Formaldehyde has neurotoxic characteristics and systemic toxic effects [27]. It is hypothesized that inhalation of FA, during the early postnatal period, is linked to some neurological diseases that occur in adults. It is a potent sensitizer and a probable human carcinogen. Malaise, headache, sleeping disturbances, irritability, and impairment of dexterity, memory, and equilibrium may result from high level exposure to formaldehyde. Formaldehyde exposure has been weakly associated with increased risk of nasal cancer and nasal tumors were observed in rats chronically inhaling formaldehyde.

Table 1.2: Primary effected site of some VOCs.

VOCs	**Primary affected site**	**IDHL(immediately dangerous to life or health)**	**TVL(threshold limit value)**
Benzene	Bone marrow	500 ppm	1 ppm
Toluene	Brain	500 ppm	100 ppm
Xylene and ethylenzene	Liver and kidney	3300 ppm	100 ppm
Formaldehyde	Nasal sinus, bronchus	20 ppm	0.75 ppm
Chlorinated hydrocarbons	Liver	1000 ppm	10 ppm
Acetone	CNS	20000 ppm	750 ppm

1.3. VOCs as exhale breath biomarker

Our exhale breath contains minuscule amount of over 200 different types of VOCs besides CO_2, N_2, oxygen and water. VOCs are produced in the human body from different biological processes, most of them are related to liver enzymes, carbohydrate metabolism, oxidative stress, lipid metabolism and cytochrome P450 [28]. Alteration of these VOCs concentration in exhale breath is an indication of metabolic and physiological disorder. The detection and identification of VOCs in exhaled breath may be helpful for advancement of novel, noninvasive diagnostic methods for a wide range of diseases, such as different types of cancers [29-32], liver failure [33], kidney failure [34], diabetics [35] perkinson [36]etc. This kind of breath analysis is, now considered to be futuristic, low cost and sensitive technique for early detection of diseases. A disease can be recognized by its specific pattern of VOCs. Among the diverse compounds in exhaled breath, 20 to 30 VOCs are important for disease diagnosis. For examples, alterations of the concentrations of pentane and acetone are indicator of heart disease and diabetes respectively. Similarly alternation of concentration of ammonia in breath related to kidney malfunction. n-pentane concentration is found to be altered in breath in case of lipid peroxidation, and related to a variety of pathological disorders [37]. Acetone and n-propanol, are recognized as markers of lung cancer [38], and 2-propanol as breast cancer [39]. Table 1.3 summarises some VOC biomarkers released in case of some diseases. In general, VOCs are analyzed using gas chromatography mass spectroscopy (GC-MS) [40], FT-IR spectroscopy and HPLC, but such techniques suffer from complexity, non-portability and are of high cost and time consuming [41, 42]. There are many different approaches that can be used to synthesize portable sensors for VOC field detection, viz surface plasmon resonance, chemiresistivity, surface acoustic wave and quartz crystal microbalance. Among them Chemiresistive sensors have many advantages over others in terms of cost, response time, ease of production, real-time monitoring and the possibility of an easy integration into a chemiresistive array [43, 44].

Table 1.3: Exhale breath biomarkers for various diseases.

Type of disease	Major VOC biomarker
Diabetes[45-47]	Acetone, Ethanol, Isopropanol
Lungs cancer[38, 48, 49]	Pentanal, ethylbenzene, Isoprene, benzene, toluene. 1-butanol , 3-hydroxy-2-butanone.
Breast cancer[39]	Heptanal, hexanal, nonane, 5-methyl tridecane,
Kidney diseases[34, 50, 51]	Ammonia, dimethyldisulfide, isoprene
Gastric cancer [52]	2-methylpentane, menthol, hexanol, hexane

1.4. Different sensing methods for VOC

On the basis of operating principles detection of VOCs can be divided into following groups:

(1) Chromatography and Spectrometry, (2) Electrochemical sensors, (3) Mass (SAW and Cantilever) sensors, (4) Optical sensors, (5) Thermal sensor and (6) Chemiresistive sensors.

1.4.1. Chromatography and spectrometry

By far most common methods for determination of VOCs are sorbent based sampling of VOCS followed by Gas Chromatography (GC) using flame ionization (FID), electron capture (ECD), or photoionization detection (PID)[53, 54]. In GC technique separation of a complex mixture of analytes is achieved by passing the mixture of analytes through an adsorbing medium. Consequently the adsorbing medium selectively interacts with analytes of interest resulting separation of complex mixtures. Due to the different in interaction kinetics of adsorbing medium and analytes, the different components in injected mixture travel down the chromatographic column at different time. Therefore components have arrived at the end of the column according to the interaction with column materials. Gas chromatography/mass spectrometry (GC/MS) is becoming an increasingly common tool in environmental laboratory due to its high sensitivity when operated in selected ion monitoring (SIM) mode, and its unique ability of chemical structure analysis [55-58]. Analysis time in case of GC is generally 10–60 minutes with conventional capillary columns depending on the complexity of sample and the experimental conditions. Such a long analysis time, non-portability, high cost and dependence on handling efficiency of individual be the main disadvantages of GC based technique. By including the attachments like ion-mobility spectrometry and mass spectrometry with Chromatography the technique become excellent in terms of selective discrimination of analytes, but like the gas chromatographs, they are currently not useful for in-situ applications.

1.4.2. Electrochemical sensors

Electrochemical gas sensors are one of the oldest and widely used for concentration measurements of VOCs [59]. There are different kinds of electrochemical sensors based on different basic principles. Based on different measured parameter (either voltage or current) electrochemical sensors can be classified as potentiometric sensors and amperometric sensors. The electrochemical sensing process is based on the chemical reaction that happens on electrodes and the transportation of charge throughout the electrolyte gives sensing response. The electrolyte can be a solid, gel-like, liquid or gaseous. Electrochemical sensors can be made more selective compare to others by tuning them to a specific electrochemical reaction. The electrodes composition also gives selectivity and sensitivity to diffuse target gases [60, 61]. Electrochemical sensors are low cost, low power, compact and their response time is short. However, these devices are not widely used for detection of VOCs at gaseous state; they are mainly used to detect VOCs in liquid medium.

1.4.3. Mass sensors

Mass sensors generally rely on the change of mass of the sensors due to accumulation of VOC molecules at surface. The detection can be done by measuring the change in resonance frequency of device.

1.4.3.1. Surface Acoustic Wave (SAW) Sensor

The surface acoustic wave (SAW) sensor is one type of mass sensor that is sensitive to mass change of sensor device [62, 63]. In SAW sensor a piezoelectric substrate is used. Usually a quartz plate is used as piezoelectric materials. Surface acoustic wave is generated as a result of oscillating electric field and the wave transmitted across the whole surface of piezoelectric material. The wave creates a resonance frequency. The characteristic resonance frequency is highly dependent on the on the mass of the oscillating plate. Considerable change in the resonance frequency is being observed by adsorption of gas molecules into the surfaces of active material of SAW sensor. Generally resonance frequency decrease with adsorption of VOC molecules. By quantifying the change in resonance frequency it is possible to quantify the amount of gas molecules adsorbed into the sensors.

1.4.3.2. Cantilever Sensor

Cantilever sensors are one type of potential mass-sensitive vapour sensor. Chemically sensitive polymers are coated into cantilever device that have been used for VOC detection

[64, 65]. The base of the cantilever is securely attached to a silicon support. The free-standing cantilever end which is coated with a chemically sensitive layer selectively absorbs analyte molecules from the gas phase. Every cantilever has its own characteristics resonance frequency. Upon absorption of VOC molecules the ass of cantilever change and that reflects in change in the resonance frequency.

1.4.4. Optical sensors

Operating principles of optical sensors are based on the change in light absorbance, transmittance and reflectance upon interaction with analytes. By detect such change in optical parameter it is possible to determine the concentration of VOCs. In a general arrangement of optical sensor, the monochromatic radiation passes through a sample and its properties are examined at the output. Alternatively, the sample may respond with a secondary radiation (induced luminescence) which is also measured. Applications of FTIR were reported for remote VOC sensing [66, 67]. Compared to other vapour transducers, most optical sensor usually exhibited lower sensitivity.

1.4.5. Thermal sensors

Adsorption and desorption of VOCs molecules into any sorbents accompanied by enthalpy changes. The enthalpy changes occur during the sorption of VOC can be detected by thermopile (series of thermocouples). Thermocouple made of platinum has a significant increase of resistance with increasing temperature caused by the combustion of gas on the surface. The change of resistance is directly proportional to the concentration of gas present. For biochemical sensing of analytes semi conductive thermistors are also used as thermal transducer. Application of thermocouple to VOC detection has also been reported [68, 69].

1.4.6. Chemiresistive sensors

Chemiresistivity is a phenomenon wherein significant change in the resistance is observed when a chemiresistor material exposed to a particular analyte [70-72]. Such a chemical concentration dependent change in resistance can therefore be utilized to develop a wide range sensor for VOCs. Chemiresistors have been extensively reported for sensitive and selective measurement of VOCs as well as normal gas (like NH_3, NO_2, CO, CH_4 etc.) sensors [73-78]. There are several types of chemiresistive sensor using different shape and size of metal oxide sensing materials.

1.4.6.1. Metal oxide based sensors

Mostly inorganic semiconductor oxides have been used as sensing materials for chemiresistive sensors [79, 80]. These sensors can react with the target VOCs by redox reaction. As a result of oxidation/reduction of metal oxide, electron exchange between analytes and sensor matrix happens which leads to change in resistivity of chemiresistive matrix. Typically the change in resistance also known as sensing response is proportional to the concentration of the analyte gas. Metal oxide based sensors are classified as; n-type (zinc oxide, tin dioxide, titanium dioxide or iron (III) oxide) and p-type (nickel oxide, cobalt oxide). n-type metal oxide based sensors exhibited better interaction with reducing type gases p-type sensors shows better response for oxidizing gases. Vaishanv et al. have developed indium tin oxide based sensors for methanol, ethanol, butanol, and acetone [81]. Shao et al. reported porous SnO_2 based sensors for acetone vapour [82]. However, the applications of metal oxides based chemiresistors have been restricted considerably due to high power consumption, high cross sensitivity towards water vapour, poor selectivity and high operational temperature despite the highly sensitivity of metal oxide based sensors. Also these types of sensors detect gases that are redox reactive, therefore many VOCs which are not participate in redox reaction, cannot be detected by them.

1.4.6.2. Intrinsically conducting polymer (ICP) sensors

Intrinsically or conjugated Conducting polymers (ICP) [83-85] such as polyaniline (PANi) [86], polypyrrole (PPy) [87] and polythiophene (PTH) [88], poly(3,4-ethylenedioxythiophene) (PEDOT) are used as the sensing layer of gas sensors. Upon exposure to gases or analytes the ICPs show significant changes in conductivity due to changes in charge mobility and the number of charge carrier in the conducting films. Upon interaction with gaseous species it can act either as an electron donor or an electron acceptor depending upon electron density of conducting polymers and analytes and sensing environment. The whole conductivity increases when a p-type ICP donates electrons to the gas. On the other hand, its conductivity decreases when the same ICP acts as an electron acceptor. Intrinsically conductive polymers have advantageous morphological and structural properties that are critical to the sensitivity and selectivity of gas sensors. Due to conformational changes of the polymer backbone during the course of interaction with analyte molecule there will be some change in the number of carriers which leads to change in bulk mobility. David W. Hatchett and M. Josowicz have reviewed the sensing properties of many ICPs and their composites [89]. Hosono et al. have investigated sensing properties of plasma polymerized highly conducting polypyrrole thin films [90]. However, ICP based sensors have poor oxidation stability and over time their sensing responses decreased. Another disadvantage is that electrical conductivity and flexibility of ICP can’t be tuned according to target specific application. All these inherent disadvantages and nonflexibility in terms of electrical conductivity have limited the practical application of ICP based sensors.

1.4.6.3. Conducting polymer nanocomposites (CPC) based chemiresistor

Conductive polymer nanocomposites (CPC) are polymer composite materials having a polymer matrix which is insulator and a conducting filler in nanoscale size. CPC can be capable as a chemoresistive [78], piezoresistive [91] or thermoresistive [92] matrix depending upon the nature of external stimulation. In case of CPC based chemiresistors, upon exposure to VOCs with good thermodynamic interactions with a polymer, the polymer chains relax, thereby inducing disruptions in the percolated conducting network. Such disruptions of conducting pathway due to chemical induced internal stress lead to change in the resistivity of the matrix. Increased in resistivity may believed due to increase in separation between conducting aggregates or agglomerates or due to the reduction in conducting network density [93] as a result of interaction with VOCs. These CPC based chemiresistive sensor offers some distinct advantages in terms of cost effectiveness, response time, ease of production, realtime monitoring and the possibility of an easy integration into a chemiresistive array. Particularly, CPC based chemiresistors in addition to cost-effective, can be used at ambient temperature and, generally, do not have cross-sensitivity to humidity. The chemiresistivity of CPC based chemiresistors does not depend on the chemical reactions as well (e.g. redox). Unlike metal oxide based sensors, where a support matrix is needed, polymer based CPC chemiressitor can be produced in very thin film and use them as standalone sensing materials. Another advantage is that interaction of analytes and polymer can be tuned by changing the chemical structure of polymer. Polymeric sensors are capable of giving rapid, reversible, and reproducible responses. Additionally, sensor array can be constructed by incorporating diverse sets of polymer nanocomposites. In an array of chemiresistor, each array of sensor contains chemically different polymer, which allow discriminating analytes based on the differences in interaction between analyte vapour and polymer matrix. The variable selectivity governs by chemiresistor array provides useful information for pattern-recognition analysis [94]. Kumar et al. have reported several conducting polymer nanocomposites (CPC) and studied chemiresistive properties against different analytes [95-97]. Han et al. have used PMMA/SWNT electrospun composites nanofibers combined with inter-digitated electrodes printed on the surface for sensing of methanol vapour [98]. Alizadeh and Soltani have reported a Poly(methyl methacrylate)/graphene composites based chemiresistive sensor for formaldehyde field detection [77]. Kessick and Tepper have reported an electrospun polymer composite microsensor array with four different polymer and carbon black as filler and used them for 1,5-dichloropentane, methanol, toluene and trichloroethylene vapour sensor [99]. Compatible polymer blend system of poly(vinyl acetate) and poly(methyl methacrylate) with carbon black have also been explored by Brett J. Doleman et al. for chemiresisitive sensors [100]. In another work Zhang et al have used in-situ polymerization of Styrene and CNT to form bridge-like conduction networks and that have been used for VOCs detection [101]. All these studies explicitly established that CPC based chemiresistive sensors are potential materials for designing room temperature, low cost and portable sensor for VOCs in chemical field as well as for biomarker detection.

1.5. Carbon nanomaterials

Owing to their high surface-to-volume ratio various nano materials having dimension ranging from 0D (nanoparticles) to 1D (nanowires, nanorods and nanotubes) and 2D (nanofilms, nanolayers, and nanocoatings) have been explored as sensing materials. Among them significant attention have been attracted by Carbon nanomaterials for various applications [102], thanks to their exceptional electronic, optical, thermal, mechanical, and chemical properties. Sp2 bonded graphitic carbons are building block of carbon nanomaterial. They are found in all reduced dimensionalities such as zero-dimensional fullerenes, one-dimensional carbon nanotubes, and two-dimensional graphene [103], [104]. Graphite being the most thermodynamically stable form of carbon at room temperature, consists of a layered two-dimensional structure [105] where each carbon layer consist of honeycomb like structure of sp2 bonded carbon atoms with a C–C bond length of 0.142 nm. The weak interlayer bonding in graphite implies that single graphene layers can be exfoliated via mechanical or chemical methods. Carbon nanotube (CNT) belongs to the family of fullerene structures. The name CNT is derived from their long and hollow structure with the walls formed by graphene sheets. These graphene sheets are rolled in a particular direction to give hollow structure. There are several types of nanotubes they are single-walled carbon nanotubes (SWNT), double-walled carbon nanotubes (DWNT) and multiwalled carbon nanotubes (MWNT). A single-walled carbon nanotube consists of one wall of graphene sheet. Multi-walled carbon nanotubes consist of multiple concentric graphene sheets roll together. In MWNT there may be two (DWNT) to as many as hundred of tubes with increasing diameter. Each tube is held at a certain distance from either of its neighbouring tubes by interatomic forces. Individual CNTs align themselves into "ropes" held together by van der Waals forces. Nanocarbon blacks (NCB) are another allotrope of carbon which is widely used for developing conducting nanocomposites for over current protection devices [106] vapour sensing [107] and various other applications [108]. Carbon black is virtually pure elemental carbon in the form of colloidal particles that are produced by incomplete combustion or thermal decomposition of gaseous or liquid hydrocarbons under controlled conditions. Carbon black is chemically and physically distinct from soot and black carbon, with most types containing greater than 97 % elemental carbon arranged as aciniform particulate.

1.5.1. Carbon nanomaterials based chemiresistors

Nano carbon and their nanocomposite materials are most emerging materials used for gas and vapour sensing applications. Most of the atoms in case of nano-dimensional carbon materials are exposed to environment offering high. This high specific surface area is gives high sensitivity due to the effective adsorption of vapour molecules. Therefore, there is an increased interest in development of nanocarbon based sensors with fast response time, high sensitivity, selectivity, portability and process ease. Among other nanocarbon conducting nanocarbon black (NCB) [42], Carbon nanotube(CNT) [109] and graphene [110] are the most promising materials for developing nanocarbon based chemiresistor, owing to their low cost and high conductivity.

In case of NCB based chemiresistive sensors NCB are dispersed into polymer matrix to produce an electrically conductive film. NCB imparts electrical conductivity where as polymer gives mechanical strength and chemical diversity to interact with analyte molecules. In presence of vapour the percolated network formed by NCB disrupts giving a change in electrical conductivity. Usually the change in conductivity directly relates the concentration of analyte vapours. Ha et al. have reported a sensor array consisting of eight different polymer and carbon black composites responded diversely when they were exposed to various chemical vapours [111]. Principal component analysis (PCA) demonstrated that the gas sensor array could identify individual vapours. Mark C. Lonergan and co-workers have proposed an array of chemiresistor elements consist of different polymer and carbon black composites which give distinct signal patterns in presence of various organic vapours [112, 113]. Talik et al. studied composite of polyvinyl chloride and carbon black for room temperature sensing of carbon tetrachloride, chloroform and methylene chloride [114].

Since the discovery in 1991 by Iijima [115], scientific world has put a great effort to the application of CNTs. The usefulness of CNTs as gas and vapour sensor was first reported by Collins and Kong [116, 117]. There are several review articles regarding gas and vapour sensing properties of CNTs [118-121]. The local chemical environment has found to influence the electronic properties of CNTs greatly, because the conduction channel in CNT is composed almost entirely of surface atoms, and even a small changes in the local chemical environment will result in measurable changes in resistance of CNT [122]. Ma et al highlighted that Polyaniline and CNT based composites demonstrated fast and reversible room-temperature response to trimethylamine, triethylamine, NH3, and HCl [123]. CNTs based sensors can also being used for detection of explosives and nerve agents. For example, Li et al and Novak et al. reported a detection limit of ppb level of 3-nitrotolune and sub-ppb level of DMMP respectively using bare SWNTs dropcast onto interdigitated electrodes [124, 125].

For sensing application SWNT and MWNT both can be applied, while MWNT exhibited several advantages over SWNT. Mass production, low product cost, and enhanced chemical and thermal stability thus better preservation of inherent physical properties make MWNT better candidate for sensing applications over SWNT. Because of these advantages of MWNT over SWNT and owing to the low cost of NCB, MWNT and NCB were used to make CPC based chemiresistor in this thesis.

1.6. Nanocarbon based conducting polymeric nanocomposites (CPC) based chemiresistors

Most of these studies discussed above are vapour sensing properties of either pristine CNTs or covalently functionalized CNTs, where the sensors are fabricated with the help of a support/substrate. It may be noted that polymer composite based sensors offer distinct advantages in terms of standalone sensor. In comparison to the substrate based sensors, the standalone sensors are expected to offer advantages such as independence of substrate-sensor interface characteristics, availability of larger surface area and fabrication ease [126]. Kumar et al. have reported that poly(caprolactone) and CNT based CPC can be used for sensing VOCs like toluene, THF and chloroform [78]. In another work they have highlighted that poly lactic acid/CNT composites can give selective response for chloroform in a mixture of chloroform, methanol, toluene and water [127]. Cattanach et al. reported polyethylene terephthalate (PET) and SWNT based flexible composites for sensitive detection of dimethyl methylphosphonate (DMMP) and diiso-propyl methylphosphonate (DIMP) [128]. Wei et al. demonstrated that vertically aligned CNT–poly(vinyl acetate) films showed reversible sensitivity to hexane, THF, cyclohexane, acetone, $CHCl_3$, ethyl acetate, methanol, toluene, DMF, and CCl_4 [129]. Recently Yucel et al. have demonstrated that electrospun PVDF, polystyrene and PMMA incorporated with MWCNT based microfluidic cartridge based hand held breath analyser give sensing response for acetone in 35 ppb - 3 ppm range and 1 ppb - 10 ppm for toluene [130]. Incorporating of hybrid nanofiller has been a simple yet profound technique to synthesise CPC aiming excellent combination of electrical and mechanical properties [131, 132]. Interestingly, there are emerging evidences suggest that the use of hybrid fillers can improve the sensing response of chemiresistors; for example, Kaniyoor and Ramaprabhu have reported that graphene nanoplatelets and CNT hybrids can enhance sensitivity for hydrogen detection along with excellent stability and repeatability [133]. Recently Li et al have reported melt mix Polycarbonate/MWCNT/CB based hybrid nanocomposites sensors for detection of organic vapours. They have established the critical role of two nanofillers in formation of conducting networks which tune the sensitivity of matrix [132]. In another hybrid system, SWCNT bundle layers with indium tin oxide (ITO) nanoparticles were reported to result in a threefold sensitivity increase [134]. It is understood that hybrid fillers in a polymer matrix might provide unique opportunity of controlling the CNT network and inter-tube interconnections and thus could be a route of designing advanced chemiresistors with improved detection range, sensitivity and detection limit.

1.6.1. Shear/Melt compounding and radiation technology for CPC based chemiresistor preparation

The conventional methods for preparation of polymer composites are solution casting, in-situ polymerization and melt/shear compounding. In solvent casting method, nanofiller and the polymer are dispersed in a common solvent and mixed thoroughly; nanocomposites can be obtained after evaporation of the solvent. In case of in situ polymerization nanofiller and a precursor of polymer (monomer or oligomer) are mixed together then polymerization is carried out to obtained nanocomposites. Melt/shear compounding is done in an extruder or in an internal mixer. The required amount of polymer and the nanofiller are added in internal mixer and mixed together by means of intense mixing at higher temperature. Melt/shear compounding does not involve any solvent or toxic chemicals and easily can be upscaled. This approach is effectively employed to develop conducting polymer composites during the course of the study. However, electrical percolation threshold (minimum quantity of filler required to obtain threshold electrical conductivity) for nanofiller in compounding techniques is much higher than in-situ polymerization or in sonication assisted solvent dispersion method. Thus innovative strategies such as hybrid fillers, functionalization of filler are used to achieve desired electrical conductivity and better sensing properties of nanocomposites.

Since the discovery of X-ray in 1895, Radiation Technology has been contributing in advancement of science and technology. It is also responsible for development of new materials for various applications in industry, health care and agriculture. High energy radiation can produce cross-linked networks in a polymer matrix [135]. It forms linkages in the polymer and polymer-filler interface. High energy irradiation forms free radicals on filler surface, interface of polymer-filler and in the bulk which initiate reactions to bring changes in the polymer composites. Cross-linked networks are expected to improve dimensional stability under chemiresistive pressure and thus providing an important contribution for the development of a standalone chemiresistor.

1.6.2. Characteristics of CPC chemiresistors

There are several sensing characteristics based on which sensing performances can be evaluated for a chemiresistive sensor. Sensitivity and selectivity are two most important criteria which mainly dictates sensing characteristic of chemiresistors. Besides that response time, recovery time, reproducibility, reversibility, stability, limit of detection and range of detection are also important parameter to discuss in order to get proper understanding of sensing performances.

Sensitivity is defined by the change in signal output upon unit change in input parameter. In case of chemiresistor sensor sensitivity can be given by change in relative change in resistance upon change in concentration in analyte. Thus, Sensitivity **(S) = (ΔR/R$_0$)/C,** where ΔR, R_0 and C are change in resistance, initial resistance of chemiresistive sensor and concentration of analytes respectively.

Selectivity of a sensor governs how much target analyte is favoured over other present analyte by sensor. Selectivity can be measured by taking ratio between sensing responses of analyte and interfering element.

Response time is the time taking by sensor to reach 90% of maximum signal at a particular concentration analyte. **Recovery time** is the time takes to return within 10 % of baseline value.

Reproducibility can be defined by regeneration of sensing signal in successive cycles. **Reversibility** of chemiresistive sensors signal said that how close resistance comes back to its original value after removal of analye.

Limit of detection, It is the lowest concentration of analyte detected by one particular sensor. It can be quantified from signal to noise ratio of sensor (LOD= 3 x signal to noise ratio).

Stability of a sensor is the ability to retain all sensing characteristics over a period of time.

1.6.3. Current Status and Future need of CPC chemiresistors

Chemiresistive sensors based electronic nose has the potential to be miniaturized to small device that gives fast response compared to traditional gas analysis methods, such as gas chromatography mass spectrometry (GC-MS) and Fourier transform infrared (FT-IR) spectrometry [44]. Commercially available chemiresistive electronic nose instruments are mostly priced from Rs. 10 to 50 lakh. The electronic noses of most manufacturers are realized by fixing gas collectors and detecting devices to personal or notebook computers, and weigh between 15 and 75 kg. Therefore, the high price and non-portability mean that electronic noses are only affordable by companies, organizations, and research institutions. With the rise of intelligent electronic products, cell phones have developed increasingly powerful functions; therefore, a method for using smart phones to develop an electronic nose system has attracted a considerable amount of interest. The design of electronic noses and general electronic products is closely related to the pursuit of inexpensive micro-scale devices, high compatibility with other consumer electronics and low power consumption. In [136] the authors predicted that the price of an electronic nose will be $1 by 2020. In summary, electronic nose products are available on the market, and currently provide solutions to a wide range of tasks in various areas. However, the electronic nose has not achieved its full potential as a commercial device; the bulky size and high price restrict its applications in daily life. Fortunately, the appearance of new sensing materials, development of fabrication technologies, and evolution of data processing methods offer the possibility of creating the next generation of electronic noses. As polymeric nanocomposites based chemiresistive sensors are inexpensive and light weight thus they have the potential to be used for developing low cost, portable electronic nose device.

1.7. Scope of Study

Sensitive and selective detection and identification of hazardous VOCs are desired not only to counter the health hazards associated with it but also to early stage diagnosis of various diseases by analysis of VOCs in exhale breathe. CPC based chemiresistive sensors are particularly useful for detection and identifications of VOCs owing to their low cost, ease of production and room temperature and simple operation. Melt compounding and shear compounding do not involve any solvent or toxic chemicals and readily can be upscaled. In this work these approaches have been employed to develop nano carbon based CPC with different polymer matrices and explored their chemiressitive properties. Radiation technology is found to be helpful to modify polymer matrix without external additives. Co-60 gamma radiation was utilised to crosslink the CPC in present study. Mechanical, electrical and vapour sensing characteristics of the prepared CPCs have been thoroughly studied. Morphology of the composites was characterized by optical imaging and SEM techniques. Rheological and Dielectric spectroscopy was done to better understand the interaction of filler with polymer chain which could affect sensing properties of chemiresistors.

In present study our objective has been to develop radiation crosslinked CPC based chemiresistive sensor for sensitive detection of VOCs. Different elastomeric (Fluorocarbon elastomer, polydimethyl siloxane and Natural rubber) and thermoplastic (Polyvinyl butyral) materials have been chosen as polymeric phase for chemiresistor preparation.

Fluorocarbon elastomer (Viton®, contains 66% fluorine; a copolymer of vinylidene fluoride (VF2) and hexafluoropropylene (HFP)).

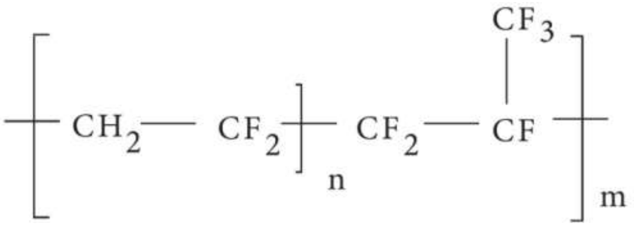

Figure 1.1: *Structure of Viton rubber.*

Viton is a brand of FKM, a synthetic rubber and fluoropolymer elastomer commonly mostly used in O-rings, chemical-resistant gloves, and other molded or extruded goods. There are several grades of Viton rubber depending upon the amount of fluorine contain. Mostly Viton rubbers are used in harsh chemical environment. They have excellent compatibility towards hydrocarbons but incompatible with ketones and esters solvents. In this study radiation crosslinked Viton rubber is used for making chemiresistive sensor for acetone. Upon irradiation C-H bond breaks and produce H and C radicals which further reacts with other macromolecules to form covalent bond.

Natural Rubber is an elastic substance obtained from the latex sap of trees, especially those trees which belong to the genera Hevea and Ficus. Natural rubber latex is an aqueous colloidal dispersion of cis-polyisoprene and is widely used in production of gloves, catheters, rubber bands etc. Reversible and reproducible sensing response needs crosslinking of polymer matrix which can be achieved by different approaches, use of high energy radiation is one of them.

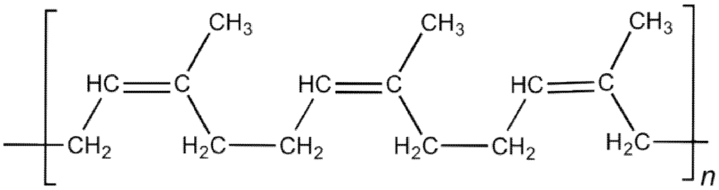

Figure 1.2: *Structure of Natural rubber.*

High energy gamma radiation is a useful tool to crosslinked natural rubber (NR) without adding chemicals. The crosslinking mechanism as follows

NR-H $\xrightarrow{\gamma\ \text{radiation}}$ NR-H*

NR-H*-----> $\text{NR-H}^{+} + e^{-}$

NR-H*-----> $\text{NR}^{\cdot} + \text{H}^{\cdot}$

$\text{H}^{\cdot}$ + NR-H-----> $\text{NR}^{\cdot} + H_2$

$\text{NR}^{\cdot} + \text{NR}^{\cdot}$----->NR-NR (Crosslinked rubber)

Polyvinyl butyral is mostly used for applications that require strong binding, optical clarity, adhesion to many surfaces, toughness and flexibility. It is prepared from polyvinyl alcohol by reaction with butyraldehyde. The major application is laminated safety glass for automobile windshields. C-H bonds break upon irradiation with high energy and forms C-C bond with other macromolecules to form 3D crosslinked structure.

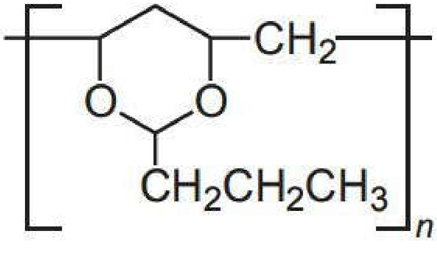

Figure 1.3: *Structure of Polyvinyl Butyral.*

Poly(dimethylsiloxane) (PDMS) is an elastomeric matrix and can be easily processed. It has good temperature and chemical resistance while it is also biocompatible in nature. PDMS widely used for electronic and biomedical applications.

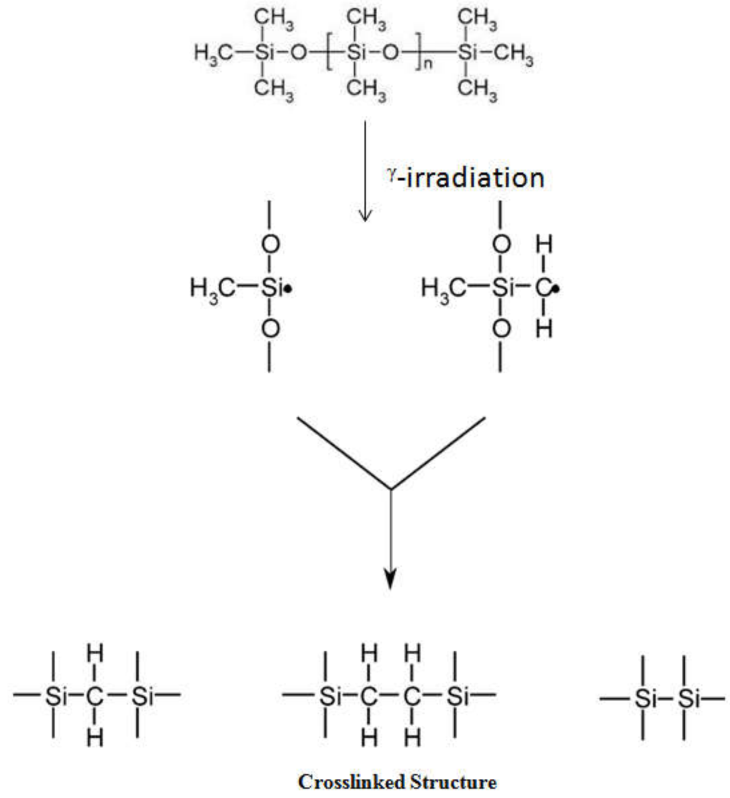

Figure 1.4: *Structure of PDMS rubber. And Crosslinking mechanism of PDMS*

By gamma irradiation both Si$^{\cdot}$ and C$^{\cdot}$ radicals are formed and three types of crosslinked network are observed [137].

The VOCs selected for the studies included Benzene, Toluene, Xylene, Ethyl benzene, Acetone, Isoprene and Ethanol. Brief descriptions of chapters are given below.

Chapter 2: This chapter describes the preparation of different polymeric CPCs by shear compounding method. The details of all the instruments used for characterizing the CPCs are discussed in this chapter. Fabrications of sensing elements and vapour sensing setup both static as well as dynamic have been discussed in details.

Chapter 3: First section of this chapter highlights development of a stand-alone radiation crosslinked chemiresistive sensor for acetone vapour. The chemiresistor showed a highly selective response for acetone whereas a considerably lower response was noted for benzene, toluene, xylene, ethanol, methanol and water. In the second section of this chapter preparation of a novel CNT induced coagulated natural rubber latex (NRL) nanocomposites is described. The crosslinked NRL/ CNT based chemiresistors shows good selective response towards Isoprene vapour and negligible response was obtained for water, methanol and ethanol. Chemically crosslinked polyvinyl butyral/CNT based chemiresistor for ethanol sensor has been discussed in the last part of this chapter.

Chapter 4: This chapter presents chemiresistive behaviour of poly(dimethylsiloxane) (PDMS)/carbon nanotube (CNT) and nanocarbon black (NCB) based hybrid CPCs. Efforts were made to understand how two geometrically different nanocarbons can affect the sensing response. These hybrid sensors demonstrate high sensitivity and reversible response for benzene, toluene, ethyl benzene and xylene (BTEX) under dynamic flow as well as under static vapour conditions. It was found that addition of CNT improves temperature stability and detection limit while sensitivity did not change significantly.

Chapter 5: This chapter describes the effect of the CNT-functionality on chemiresistive behaviour of the PDMS/ functionalized CNT nanocomposite sensors. The result elucidates that polymer-filler interactions were modified by gamma irradiation and that in turn affected chemiresistivity of the matrix. It was found that PDMS/carboxylic functionalized CNT shows significantly higher chemiresistivity than PDMS/amine functionalized CNT chemiresistors.

Dielectric, CNT percolation and XPS analysis also revealed marked variations in CPCs' properties with change in functional groups on CNT.

Finally in Chapter 6 summary and conclusive remarks have been discussed. This chapter described overall finding of the current study and indentifies potential aspects of future studies. It was found that melt/shear compounding along with radiation technology offers unique advantage to tailor made CPC based chemiresistive sensors for VOC. Judicial chose of polymer matrix and a combination of conducting fillers and/or functionalized carbon nanotube was found to be useful to make such sensor. Additionally, it was also found that optimizing crosslinking density, conducting network between NCB - CNT and CNT functionality has distinct effect on chemiresistive behaviour of CPC chemiresistors.

CHAPTER 2

Experimental Methods and Characterization techniques.

2.1. Introduction:

In this chapter preparation of polymer nanocomposite, different characterization techniques and vapour sensing setup used during the course of this study are discussed in details. The present study involved preparation of polymer nanocomposites by solvent free shear compounding method and the nanocomposites were crosslinked with high energy gamma radiation. Co-60 gamma radiation was used to irradiate the sample. These irradiated nanocomposites were thoroughly characterized by various techniques. The physico-mechanical properties of the nanocomposties were studied using tensile test and dynamic mechanical thermal analysis (DMTA). Surface functionality and morphology of nanocomposites were studied by X-ray photo electron spectroscopy (XPS), surface energy measurement and Scanning Electron Microscopy (SEM). Crosslinking density and gel fraction of the composites was elucidated by sorption study in suitable solvents. Rheology is an important characterization technique to understand flow behaviour of polymers and their composites. It provides valuable information regarding interactions between polymers and filler particles. Both linear and nonlinear rheological study was conducted to elucidate the polymer- polymer and polymer-filler interactions in nanosomposites. Dielectric spectroscopy was used to study the effect of nanofillers on the dynamics of the segmental mobility of the polymer chains in the nanocomposites. The vapour sensing studies were carried out in static setup as well in dynamic setup. Principles of each technique are discussed in the trailing section of this chapter.

2.2. Preparation of nanocomposites by melt compounding

Melt compounding, a well established polymer processing method, involves breakdown of aggregated fillers into nano level by shear force and ensuring a proper mixing of polymers and nanofillers. Hydrodynamic force between polymer chains and fillers are mainly responsible to achieve homogeneous mixing in this technique [138]. The melt mixing process for synthesis of polymer nanocomposites is emerging as a suitable alternative of other conventional processes due to its inherent advantages. Main advantage is that it does not involve any solvents or added chemicals and thus environmental friendly. Compatibility with modern industrial processes such as extrusion and moulding which are suitable for large scale production in comparison to solution processing and in situ polymerisation.

In present study nanocomposites were prepared by melt/shear compounding method using a Brabender Plasticorder fitted with an internal mixer with two counter rotating screws. Mixing was done at high temperature depending upon polymers melting temperature and variable speed of screw to achieve uniform mixing. Considering the bulk density, desired amount of polymers and nanofillers were taken to ensure proper filling of mixer chamber (40 cc, 80% of the maximum capacity). The homogeneous mixtures obtained after uniform mixing were taken out and cut into small pieces and compressed into sheets of 10 x 10 cm^2 of different thicknesses using compression-molding machine at 150 kg/ cm^2 for 30 min at elevated temperature. These compress moulded sheets were crosslinked in GC-5000 ^{60}Co Gamma Chamber and used as chemiresistor.

2.3. Cobalt-60 Gamma Source (GC-5000)

GC-5000 ^{60}Co Gamma Chambers, Board of Radiation & Isotope Technology, Mumbai, India was used for irradiations of the samples. GC-5000 gamma chamber contains stationary ^{60}Co source in a cylindrical container surrounded by a lead shield. ^{60}Co emits β particle followed by two γ-rays having energy of 1.33 MeV and 1.17 MeV (Figure 2.1). β

radiation were cut out by walls of metal container having ^{60}Co isotopes. Figure 2.2 shows one of the gamma chambers used for present studies.

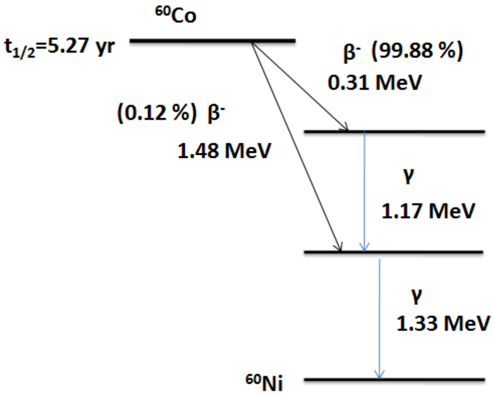

Figure 2.1: *Decay scheme of ^{60}Co radioisotope.*

The material for irradiation was placed in a shaft located in chamber. The shaft can move up and down with the help of a motor to enables precise positioning of sample in radiation filed.

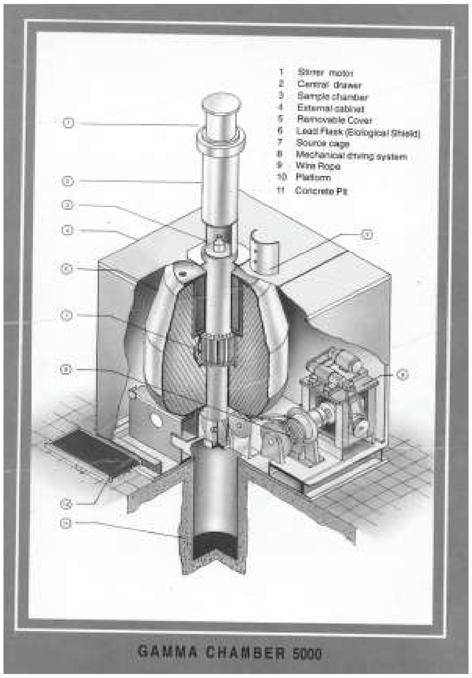

Figure 2.2: *Schematic diagram of GC-5000 gamma chamber.*

2.3.1. Radiation dose measurement (Dosimetry) of GC-5000 Gamma Chamber and irradiation of samples.

Dose rate of the gamma chamber was ascertained by dosimetry before carrying out irradiation. In general, Fricke dosimetry was used to measure the dose rate of gamma chamber. The standard Fricke dosimeter comprises of an aerated solution of 1.0 x 10^{-3} mol.dm^{-3} ferrous ammonium sulphate, 1.0 x 10^{-3} mol.dm^{-3} NaCl and 0.4 mol.dm^{-3} sulphuric acid (pH= 0.46). The basic principles of Fricke dosimetry is formation of ferric ion by radiation induced oxidation of ferrous ions in presence of oxygen at low pH solution [139]. The reactions involved in the Fricke dosimeter are summarized under reactions (2.1) – (2.7) [140]

$$H_2O \xrightarrow{\gamma \text{ radiation}} e_{aq}^{-}, H^{\cdot}, {}^{\cdot}OH, H_2, H_2O_2, H_3O^{+} \tag{2.1}$$

$$e_{aq}^{-} + H^{+} \longrightarrow H^{\cdot} \tag{2.2}$$

$$H^{\cdot} + O_2 \longrightarrow HO_2^{\cdot} \tag{2.3}$$

$$Fe^{2+} + {}^{\cdot}OH \longrightarrow Fe^{3+} + OH^{-} \tag{2.4}$$

$$Fe^{2+} + HO_2^{\cdot} \longrightarrow Fe^{3+} + HO_2^{-} \tag{2.5}$$

$$HO_2^{-} + H^{+} \longrightarrow H_2O_2 \tag{2.6}$$

$$Fe^{2+} + H_2O_2 \longrightarrow Fe^{3+} + OH^{-} + {}^{\cdot}OH \tag{2.7}$$

The radiation chemical yield of ferric ion is related to the primary radical and given by equation (2.8)

$$G(Fe^{3+}) = 2\,G(H_2O_2) + 3\,\{G(e_{aq}^{-}) + G({}^{\bullet}H) + G(HO_2^{\bullet})\} + G({}^{\bullet}OH) \tag{2.8}$$

By substituting the G values of the primary radicals the G(Fe^{3+}) is calculated as 15.5. The spectrophotometric method was used to measure the concentration of ferric ion formed during the course of irradiation. Maximum absorbance of Fe^{3+} ion was found at 304nm. To minimize adventitious oxidation, spectrophotometric data were taken as soon as possible after irradiation. The mean absorbed dose (D_D) for the volume occupied by dosimeter solution is given by Eq. 2.9.

$$D_D = \frac{9.684\ x\ 10^6\ \Delta A_D}{\varepsilon l p G(P)} \mathrm{Gy} \tag{2.9}$$

where, ΔA_D is the change in absorbance of dosimeter solution before and after irradiation. G(P) is yield (number of molecules per 100 eV) of ferric ions due to irradiation was calculated to be 15.5, ε is molar extinction coefficient of ferric ions (2201 M^{-1} cm^{-1}) at the measuring wavelength 304 nm, ρ is the density of dosimeter solution (1.06 g/cc), l is the path length (1 cm).All samples were irradiated under nitrogen atmosphere. The samples were packed in a plastic bag and sealed it in presence of nitrogen to avoid any radiolytic oxidation during irradiation with Co-60 gamma ray.

2.4. Mechanical properties measurement

Polymers and polymers nanocomposites displayed a wide range of mechanical properties. Different polymers and their nanocomposites exhibited different stress-strain behaviour depending upon various factors like molecular weight, crosslinking density, filler concentration, crystalinity of polymers, interaction of polymer chain with filler particles etc. Thus measuring mechanical properties such as Young's modulus, tensile strength, elongation at break, are important in order to characterise polymers and polymer nanocomposites properly.

a) Young's modulus: Young's Modulus or tensile modulus is the stress required to create unit tensile strain in a material. Young's modulus can be calculated from the slope of stress–strain graph in the linear elastic region (Figure 2.3). If a rectangular bar of sample of cross-sectional area A is pulled by a force F at each end, the bar stretches from its original length L_0 to a new length L_n. The applied tensile stress due to the force F is the ratio between force and the cross-sectional area, or F/A. The strain (ε) or relative deformation is the change in length, ΔL divided by the original length, or $(L_n - L_0)/L_0 = \Delta L/L_0$. Thus Young's modulus may be expressed mathematically as

$$Youngs\ Modulus = \frac{Stress}{Strain} = \frac{F/A}{\varepsilon} = \frac{F/A}{\Delta L/L_0} \tag{2.10}$$

Elastic modulus is a measure of the stiffness of the material.

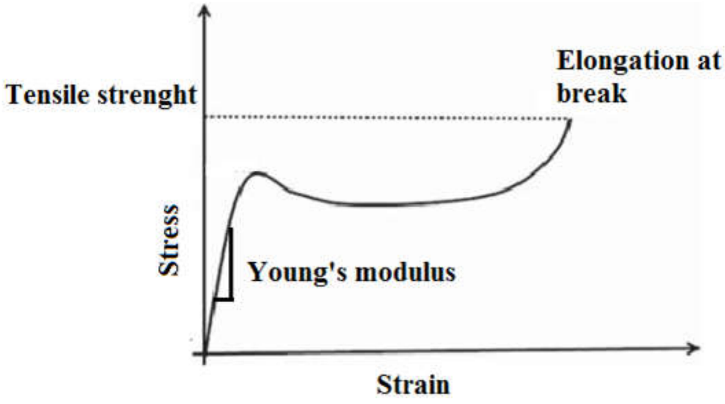

Figure 2.3: *Representative Stress- strain graph of polymer.*

b) Tensile strength: Tensile strength is the stress required to break the sample. Tensile strength is the measure of maximum stress sample can withstand before failure. In general Crosslinking of polymer and addition of filler into polymer increases tensile strength of polymer matrix.

c) Elongation at break: It is the maximum strain in the material on its breakage. Elastomeric polymers have very high elongation while glassy polymers have low elongation at break. Elongation at break of polymers decreases upon addition of filler and crosslinking of polymer matrix.

During the course of this study, for mechanical properties measurement, at least five dumbbell shaped specimens were cut from composite sheets using a sharp edged steel die of standard dimensions. The thickness of the samples were determined to the nearest of 0.1 mm. The Young's modulus, tensile strength and elongation at break were measured at room temperature using a universal testing machine supplied by M/s Hemetek, MUMBAI, India.

2.5. Rheology and Dynamic mechanical Analysis (DMA)

Rheology involves the study of the deformation and flow of materials. Rheological properties are extremely sensitive to very small changes in the structure of polymer. This makes rheological study an important tool for characterization of polymer and their composites. There are two extreme behaviour of material upon deformation, Elastic deformation and viscous deformation. Elastic deformation termed also as elasticity, is the ability of a material to store deformational energy, and can be viewed as the capacity of a material to regain its original shape after being deformed. Viscous deformation or viscosity, is a measure of the ability of a material to resist flow, and reflects dissipation of deformational energy through flow. In rheological study, the force required for deformation is expressed as the stress, or force per unit area. The degree of deformation caused due to the stress applied to a material is called the strain.

An ideal solid obeys Hooke's law. The stress (σ) response is proportional to the imposed strain (γ) and is independent of the strain rate. Thus stress can be given as

$$\sigma = G\gamma \qquad \textbf{(2.11)}$$

where, the proportionality constant G is termed as the shear modulus. It manifests the stiffness of the material or the materials ability to resist deformation. In an ideal solid material the energy supplied in form of deformation force is fully conserved. Where as an ideal liquid also called as Newtonian fluid follows Newtonian law of viscosity where the stress (σ) is proportional to the imposed strain rate ($\dot{\gamma}$) and given by

$$\sigma = \eta\dot{\gamma} \qquad \textbf{(2.12)}$$

where, η is the coefficient of viscosity. The deformation energy is completely dissipated in a Newtonian fluid [141]. In general, polymer poses both elastic as well as viscous behaviour, termed as viscoelasticity.

Rheological study can be done under both steady and oscillatory deformation. In steady deformation study, the sample's viscosity is measured as a function of shear rate. Normally at low shear rates a plateau in viscosity value is observed called Newtonian plateau whereas, viscosity decreases at higher shear rate. Nevertheless, steady−shear measurements are not that much sensitive compare to oscillatory measurements when more detailed microstructural study has to be done. In an oscillatory measurement the material is subjected to a sinusoidal stress or strain and the strain or stress response is measured. When the small amplitude oscillatory shear technique is used, the sample is subjected to a sinusoidal shear strain, γ, and the resultant shear stress, σ, is measured. If the strain is sufficiently small (linear response regime), the stress response will also have an oscillatory behaviour with the same frequency but with a phase angle shift of δ depending upon viscoelastic nature of the material (Figure 2.4). The stress signal generated by a viscoelastic material can be separated into two components: an elastic stress (σ′) that is in phase with strain, and a viscous stress (σ″) that is in phase with the strain rate (dγ/dt or $\dot{\gamma}$) but 90° out of phase with strain.

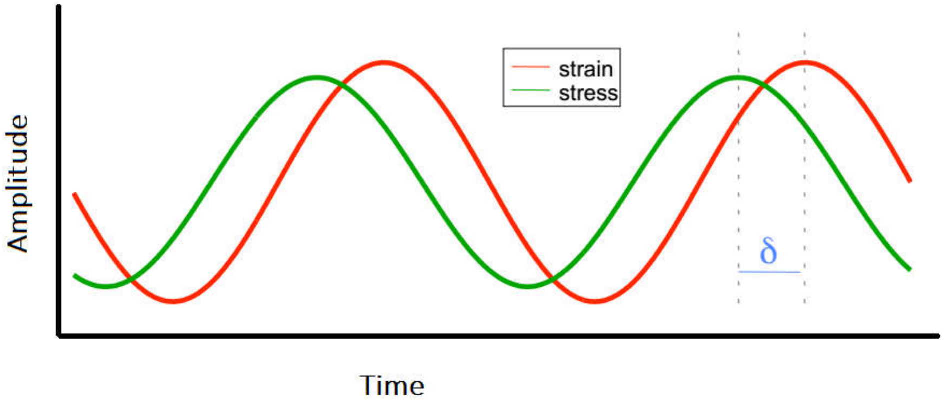

Figure 2.4: *Oscillatory stress and strain of Viscoelastic materials.*

The elastic and viscous stresses are sometimes referred to as the in-phase and out-of-phase stresses, respectively. The elastic stress is a measure of the degree to which the material behaves as an elastic solid. The viscous stress is a measure of the degree to which the material behaves as an ideal fluid. The stress and strain are used to calculate a complex (G*), real (storage modulus, G′) and imaginary (loss modulus, G″) parts of the shear modulus.

Mathematical expression of strain which is a function of frequency ω is given by

$$\gamma(t)= \gamma_0 \sin(\omega t) \qquad \textbf{(2.13)}$$

the stress response will be of the form

$$\sigma(t) = G'\gamma_0 \sin(\omega t) + G''\gamma_0 \cos(\omega t) \qquad \textbf{(2.14)}$$

where G′ and G″ are given by

$$G' = \frac{\sigma}{\gamma} cos\delta \;\; and \; G'' = \frac{\sigma}{\gamma} sin\delta \qquad \textbf{(2.15)}$$

The storage modulus, G′, and the loss modulus, G″, are the real and the imaginary component of the complex modulus, G*, respectively,

$$G^* = G' + iG'' \qquad \textbf{(2.16)}$$

A parameter often found in literature is the loss tangent or loss factor tanδ, which is defined as the ratio between loss and storage modulus,

$$\frac{G''}{G'} = tan\delta \qquad \textbf{(2.17)}$$

Loss factor provides the ratio of viscous to elastic response of a material, indicates which one is the dominant one. The elastic and viscous properties of the material are equal when tanδ is equal to 1. Loss factor less than 1 means elastic property dominates and greater than 1 implies viscous property dominates. The value of Loss factor for polymeric systems related to various molecular relaxations within the material.

Complex viscosity η^*, as the ratio of the shear stress σ to the rate of shear $\dot{\gamma}$, and is given by

$$\eta^* = \eta' - i\eta'' \qquad \textbf{(2.18)}$$

where $G' = \eta''\omega$ and $G'' = \eta'\omega$.

Considering the special case of the Maxwell model the dynamic moduli given by two following equations

$$G' = \frac{\eta\tau\omega^2}{1+\omega^2\tau^2} \qquad \textbf{(2.19)}$$

$$G'' = \frac{\eta\omega}{1+\omega^2\tau^2} \qquad \textbf{(2.20)}$$

Where η is viscosity and τ is relaxation time. Typical shapes of the storage and loss modulus as a function of angular frequency are shown in Figure 2.5. Where, storage modulus is proportional to ω^2 in the low frequency region, and attains a constant value at high frequency. The loss modulus is proportional to ω at low frequency, and proportional to 1/ω at high frequency. At low frequency G′<G″, i.e the material is liquid like. Both the modulus increase with increase in frequency until the crossover point ω_c is reached. The reciprocal of this crossover frequency ω_c denotes relaxation time of the polymers. In the intermediate frequency region G′ reaches a constant value known as rubbery plateau ($G' \approx G^0_N$).

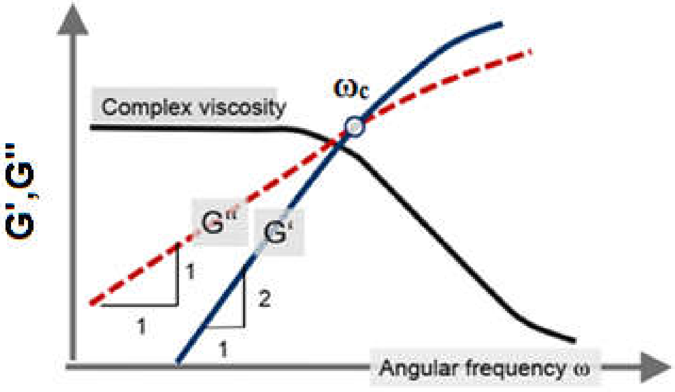

Figure 2.5: *Frequency response of Storage and loss modulus of typical polymer.*

In the rubbery plateau the modulus (G^0_N) is independent of the molecular weight of polymers and only depends on chemical structure of polymer. Both G′ and G″ again increase at higher frequency. The response observed at such high frequencies, which correspond to small time scales, will only be due to small parts of the polymer chains (i.e. few monomeric units). Dynamic mechanical analysis or dynamic mechanical thermal analysis (DMTA) measures the change in the elastic modulus (E′) and loss modulus (E″), as well as the ratio of these two tanδ (E″/E′), with temperature. The value of glass transition temperature can be probed either from peak of tanδ or peak of E” (Figure 2.6). Often some literature has estimated the T_g from onset temperature drop of E’. DMTA is about 10 to 100 times more sensitive to changes occurring at the T_g than other thermal technique such as DSC. It is therefore very much useful to detect a weak glass transition.

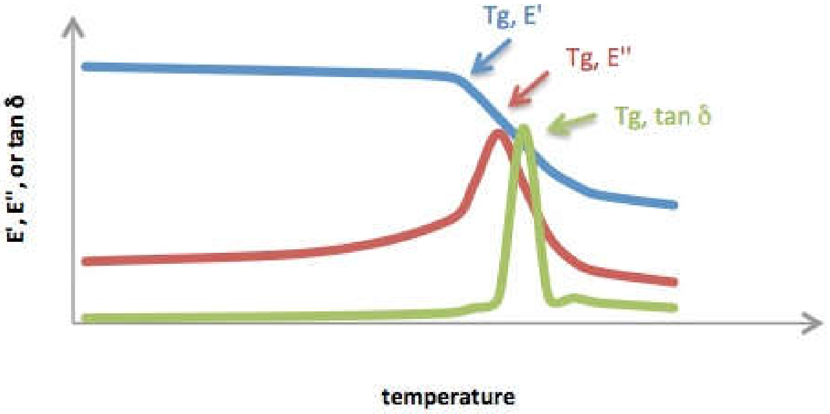

Figure 2.6: *Representative DMTA graph of polymer.*

2.6. X-ray photo electron spectroscopy (XPS)

X-ray photoelectron spectroscopy (XPS) is used for investigating the surface chemistry of electrically conducting and non-conducting samples [142]. It provides useful information about the chemical environment of the surface of polymer and composites. During the XPS analysis, the surface of sample is irradiated with X-rays in vacuum. The X-ray photon strikes out the core shell electron of atoms of sample by transferring its energy. Kinetic energy of emitted electron (photoelectron) depends upon the energy of the incident X-ray and binding energy of the atomic orbital from which it originate. The energy and intensity of the emitted photoelectrons are analysed to identify and determine the concentrations of the elements present in a sample. In the photoelectron spectrum, which represents the distribution of emitted photoelectrons as a function of their binding energy, peaks can be observed which are related to individual elements present on the sample surface. For each element there will be a characteristic binding energy associated with each core atomic orbital i.e. each element will give rise to a characteristic set of peaks in the photoelectron spectrum. Incident photon energy and the respective binding energies of atomic orbital will determine the kinetic energies of the emitted electron. These photoelectrons originate from a depth of <10 nm, therefore the information obtained is from within this depth. During the analysis, two types of XPS spectra are usually recorded. Firstly, a spectrum through a wide energy range is acquired, in which the peaks of present elements are identified. In addition to wide energy range spectra, high energy-resolution spectra for characteristic peaks of the elements like C 1s, O 1s and others (N 1s, S 2p, Cl 2p, F 1s, Si 2p …) are recorded through a narrow energy range. From the shape and binding energy peaks within these XPS spectra, the chemical bonding of surface elements can be identified with the help of data from the literature. During present study XPS analysis of the samples was performed at 4354 eV photon energy on the PES-BL14 beamline (BARC) at Indus-2, RRCAT, Indore, India.

2.7. Surface energy measurement

Contact Angle measurement is adapted to measure surface energy of polymer composites by analysing drop shape of polar and non polar solvents. A liquid droplet (1.5-2.5 μl) was allowed to fall on the samples to be studied from a software-controlled syringe. An image sequence was taken through a CCD camera of goniometer from GBX instruments, France which was connected to a PC computer and interfaced to image capture software (Windrop++, GBX instruments). In this work, the Owens and Wendt [143] method was used to calculate surface energy of composites. They assumed the total solid surface tension γ to be of the general form

$$1 + cos\theta = 2\sqrt{\gamma_s^d}\left(\frac{\sqrt{\gamma_l^d}}{\gamma_{lv}}\right) + 2\sqrt{\gamma_s^p}\left(\frac{\sqrt{\gamma_l^p}}{\gamma_{lv}}\right) \qquad \textbf{(2.21)}$$

In this equation, θ is contact angle, the subscripts s and l refer to the solid and liquid surface tension respectively; the superscripts d and p coincide with dispersive and polar components of total surface tension, where sum of these two values are equal to the total surface tension. The γ_s^d and γ_s^p are needed to be resolved. Therefore two independent contact angles were needed to be measured by two different liquid whose surface tension components are known. Water and diiodomethane were chosen for this purpose and contact angle for both solvent were measured. Polar and dispersive components of surface tension were taken from literature and are given in the table 2.1.

Table 2.1: Dispersive (γ_l^d) and Polar (γ_l^p) components of the surface tension (γ_{lv}) for water and diiodomethane at 25 °C.

Solvents	γ_l^d (mN/m)	γ_l^p (mN/m)	γ_{lv} (mN/m)
Water	21.8	51.0	72.8
Diiodomethane	49.5	1.3	50.8

2.8. Scanning electron microscopy (SEM)

The scanning electron microscope (SEM) employs a focused high energy beam of electrons to generate a variety of signals at the surface of solid specimens. The signals generated from the interaction of electrons with sample atoms carried information about surface morphology, composition, and orientation of different components within the sample

[144, 145]. SEM is routinely used to characterise polymers, polymer blends and polymer composites. Morphology of cryofractured polymer composites was studied using SEM in this thesis. During SEM operation, a beam of electrons is focused on a spot volume of the sample specimen, different interactions between electrons and sample atoms happen (Figure 2.7) during the energy transfer. These bombarding electrons, known as primary electrons, dislodge electrons from the specimen itself. The dislodged electrons, also known as secondary electrons, are attracted and collected by a positively biased grid or detector, and then translated into a signal. To produce the SEM image, the electron beam is swept across the area being inspected, producing many such signals.

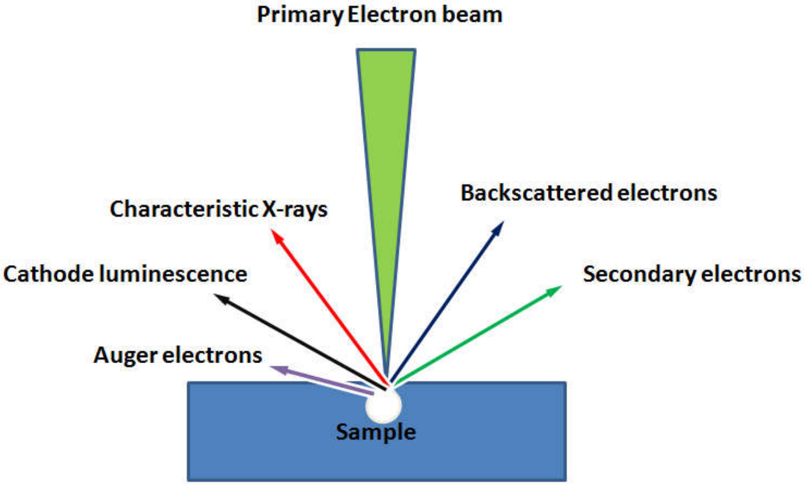

Figure 2.7: *Interaction of primary electrons and signal generation.*

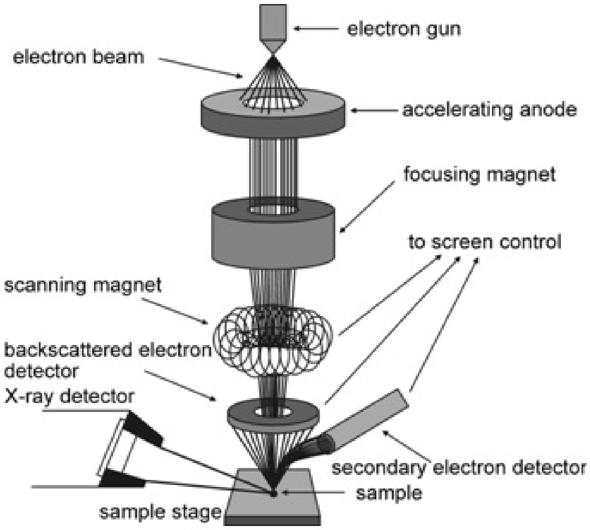

Figure 2.8: *Schematic diagram of SEM.*

These signals are then amplified, analyzed, and translated into images of the topography of the inspected sample. Different components of a typical SEM are shown in Figure 2.8.

2.9. Electrical conductivity and Dielectric spectroscopy

Polymers are electrically insulator in nature but with addition of conducting filler become electrical conductor. Electrical conductivity of polymer composites can be measured by measuring resistance of the composite. DC electrical conductivity (σ_{DC}) of polymer nanocomposites can be given by

$$\sigma_{DC} = \frac{1}{\rho} = \frac{Rl}{A} \tag{2.22}$$

Where ρ is resistivity, R resistance, l and A are sample thickness and area respectively.

Dielectric spectroscopy is now a well-established technique for understanding molecular dynamics of polymers and their composites. It can provide information such as miscibility of composites and blends, flow behaviour, molecular relaxations, thermal transitions, and polymerization reaction rates. Molecular dynamics of composites are different that of base polymer material due to the interaction of polymer chain with filler particles. As dielectric spectroscopy is sensitive to molecular relaxation, it provides useful information about the interaction between polymers with nanofiller [146, 147].

Among various geometry, parallel plates geometry is mostly used for dielectric measurement. Dielectric materials store energy when an external electric field is applied. The atomic and molecular charges of the dielectric material are displaced from their equilibrium positions upon applied electric field and the material is polarized. Usually the magnitude of this polarization is directly proportional to the applied field. In polymeric materials two types of polarization can happen; one is the polarization due to charge migration and other is polarization due to orientation of permanent dipoles. Each of these polarizations has characteristic relaxation frequency. The proportionality constant is called the permittivity (ε). Generally the permittivity is expressed as relative permittivity or dielectric constant. It is a ratio between permittivity of the material (ε) and permittivity of vacuum and given by

$$\varepsilon_r=\varepsilon/\varepsilon_0 \qquad \textbf{(2.23)}$$

where ε_0 is the permittivity of a vacuum (= $8.854 \times 10^{-12}\ J^{-1}\ C^2\ m^{-1}$).

Oscillating electric field is applied during dielectric measurements. An oscillating voltage is applied across the electrode and the corresponding current is measured along with the phase shift (δ). Complex Permittivity is represented by

$$\varepsilon^*=\varepsilon_r'-i\varepsilon_r'' \qquad \textbf{(2.24)}$$

ε_r' and ε_r'' are the real part and imaginary or loss part of permittivity respectively. The loss factor is associated with energy absorption by the polymer. Another important parameter is dissipation factor or loss tangent (D). It is the ratio between loss and real permittivity

$$D = \tan\delta = \varepsilon_r'' / \varepsilon_r' \qquad \textbf{(2.25)}$$

This loss tangent is a convenient quantity for qualitative comparison between DMTA and dielectric data since it is directly analogous to the mechanical loss tangent. It is also directly calculable from the measured impedance data without knowing the geometrical dimensions of the electrodes.

The AC conductivity can be expressed in terms of DC conductivity and frequency (ω) by following relation

$$\sigma_{AC} = \sigma_{DC} + \omega\varepsilon'' \qquad \textbf{(2.26)}$$

ε'' is loss permittivity.

2.10. Zeta potential measurement

The zeta potential (ζ-potential) is defined as the potential difference between solids and liquids across the phase boundaries. It is a measure of the electrostatic charge between suspended particles and one of the fundamental parameters to affect stability of colloidal solution. Due to the net charge that develops at the particle surface affects the distribution of counter ions nearby the surface of solid particles, facilitate the formation of electrical double layer. The zeta potential is a key parameter which dictates the stability of colloidal dispersions. Typically, higher the zeta-potential more stable is the colloid. When the zeta-potential of colloids equals to zero, the solid particles will precipitate. Colloids with higher zeta potential value (negative or positive) are electrically stabilized while colloids with low zeta potentials tend to coagulate or flocculate. In general, when the zeta potential of a colloid is high, the repulsive forces between particles exceed the attractive forces between them, resulting in a relatively stable system.

Zeta potential can be measured indirectly by measuring electrophoretic mobility of particles. Particles having zeta potential will migrate toward the opposite-charged electrode. The rate of migration is proportional to the zeta potential. Consequently by measuring the velocity of charged particles under electric filed one can determine the Zeta potential. The calculation is based on a theory described in 1903 by Marian Smoluchowski [148]. Smoluchowski's theory is valid for any concentration or shape of dispersed particles. Measurement of zeta potential gives an insight of electrical charge present in surface of particles thus one of the fundamental interest for studying coagulation process and stability of colloidal solution. Malvern Zetasizer nano ZS was used to determine zeta potential of samples.

2.11. Dynamic and static vapour sensing setup

Chemiresistive behaviour of CPC based sensors against different analyte vapours is determined in dynamic flow as well static vapour condition. Dynamic flow measurements were used to determine the sensing response over a broad concentration range. Figure 2.9 shows the setup used for dynamic measurements. At a particular rate dry nitrogen gas was bubbled into the analyte contained in a 50 ml glass vessel maintained at isothermal conditions. The analyte vapours were carried by nitrogen into a mixing chamber where the vapours get diluted by another inlet of nitrogen to the desired extent. The diluted vapours are then carried to the sensing chamber. Real-time chemiresistive response of chemiresistors was monitored by measuring the relative change in resistance due to the exposure of VOCs. For 5 min chemiresistors was exposed into VOC vapour and then dry nitrogen was purged for 5 min to clean the chamber hence sensing response of chemiresistors was recorder for

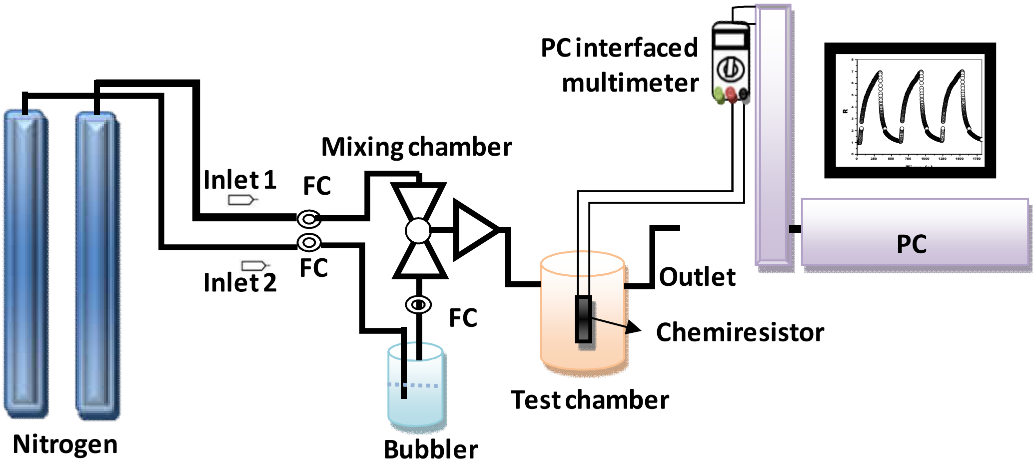

Figure 2.9: *Schematic diagram of dynamic vapour sensing setup.*

successive cycles of VOC and nitrogen. The relative change in resistance ($A_r = \Delta R/R_0$) was recorded for different concentrations by using PC connected multimeter. PTFE guides were used to hold chemiresistors, without blocking the exposure and to minimize vibrations due to vapour flow. Although Real-time measurements simulate the real exposure conditions however it has limitation. In dynamic setup, vapour pressure of analytes at amibient temperature plays a crucial role in final concentration of analyte. To overcome this issue, a static system was used to get vapour pressure independent concentration of VOCs. In static measurement setup, chemiresistor was kept inside a 2 litre closed glass container. Different concentration of VOC was introduced inside the container by injecting required volume with the help of a syringe, and then resistance of chemiresistor was measured for 5 min under VOC filed by computer controlled multimeter. After 5min VOC vapour was removed by suction through vacuum pump allowing dropping of resistance of chemiressitor. Sensing response was recorded as relative change of resistance ($A_r = \Delta R/R_0$). Schematic diagram of static vapour sensing setup is shown in Figure 2.10.

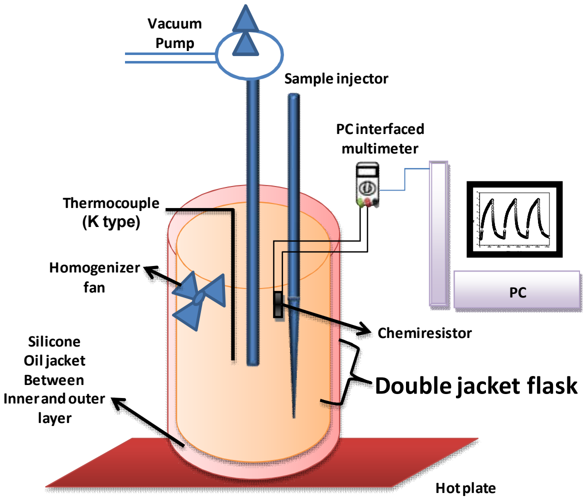

Figure 2.10: *Schematic diagram of static vapour sensing setup.*

2.12. Principle Component Analysis (PCA)

It is impossible to graphically represent large number of raw data when number of samples and sensors are more than three. So it is a challenging task to reduce dimensionality of data without losing important information associated with it. In this context, Principle component analysis (PCA), a statistical technique, can be useful to reduce dimensionality of data with maximum retention and easy visualization of related information [149-151]. PCA decompose a set of data produced by an array (m x n, where m is no of sensors and n is different types of vapour) into more simple components called principle components by linear transformation. Each principle components are orthogonal to each others. For simplification consider 3 sensor system having change of resistance ΔR_1, ΔR_2 and ΔR_3 for three different VOCs. Then first principle component PC_1 is a linear combination of resistance change by three sensors and can be represented by

$$PC_1 = a_{11}\Delta R_1 + a_{12}\Delta R_2 + a_{13}\Delta R_3, \text{ where } a_{11}^2 + a_{12}^2 + a_{13}^2 = 1 \qquad \textbf{(2.27)}$$

The data has largest variance along first principle component. The second principal component, PC_2, is in the direction perpendicular to PC_1 and results in the second largest variance. The third principal component, PC_3, is perpendicular to both PC_1 and PC_2 and results in the third largest variance. From these components the most distinctive components are selected to feature the final plot [151].

CHAPTER 3

Nanocarbon black and Carbon nanotube based Conducting Polymeric Composites for Chemiresistive application.

Introduction:

Nanocarbon black (NCB), carbon nanotubes (CNT) and graphene are three conducting allotropes of carbon having different shapes and geometries. They are also different in terms of physical, mechanical and thermal characteristics. Graphene is sp^2 hybridized carbon in the form one atom thick sheet. It has exceptionally high electrical conductivity, thermal conductivity and mechanical strength, making it suitable in various advanced applications such sensors and actuators, super capacitors, batteries, aircraft components and hydrogen storage [152, 153]. CNTs can be visualized as an assembly of several concentric graphene tubes, having excellent electrical, mechanical and thermal characteristics [154-156]. Application domain CNTs are vast owing to their excellent electrical conductivity and inertness towards harsh chemical processing. On the other hand, Nanocarbon blacks are another allotrope of carbon having grapes like structure forming by some spherical particles. NCB are widely used for developing conducting nanocomposites for over current protection devices [157] and various other applications [158-160].

For developing chemiresistive sensors electrical conductivity and a responsive polymer phase are two prerequisite components. Several kinds of thermoplastic and elastomeric polymers have been investigated so far as a responsive polymer matrix to develop CPC based chemireistive sensors [71, 77]. Nanocarbon based conducting polymer nanocomposite materials are one of the most promising materials to develop low cost, flexible, room temperature and standalone chemiresistive sensors [96, 161]. Chemiresistivity of several conducting polymer nanocomposites based on poly(caprolactone)/carbon nanotube [78] acrylate copolymer latexes/CNT [162], polylactic acid/CNT [127] and polymethyl methacrylate/CNT [70] are studied against different analytes. Han et al. have used PMMA/SWNT electrospun composites nanofibers combined with inter-digitated electrodes printed on the surface for sensing of methanol vapour [98]. All these studies along with several other highlights the potential of conducting nanocarbon for the development of novel chemiresistive sensors [43, 163]. Owing to its low cost high conductivity, high surface area conducting nanocarbon black (NCB) is an excellent choice as a conducting phase [164, 165]. Two elastomeric polymers namely Fluorocarbon elastomer (FCE) and Natural rubber (NR) and one thermoplastic polymer as Polyvinyl Butyral (PVB) have chosen to develop chemiresistive sensors for acetone, isoprene and ethanol respectively. Chemiresistivity of these three different nanocomposites have been discussed in subsequent section of this chapter.

3a. Development of radiation cross-linked FCE/NCB nanocomposite based chemiresistor for acetone detection:

3.1a. Introduction

Acetone is one of the main exhaled breath biomarker in case of various diseases like diabetes and lung cancer. Its concentration increased by several fold in breath in case of diabetes ketoacidosis [166, 167]. Another fact is that acetone has wide range of uses in different industries and laboratory. Acute inhalation of acetone produces several negative effect on human health [168]. Thus analysis of acetone concentration may be helpful for rapid and early detection of disease associated with it and monitoring the exposure of acetone. Therefore availability of small, reversible, room temperature and low-cost acetone field detector is expected to be highly helpful in order to early detection of disease and ascertaining of exposure of acetone within permissible limits.

Like other Volatile organic compounds (VOCs) acetone is generally analyzed using gas chromatography (GC), FT-IR spectroscopy and HPLC. But high cost, complexity, time consuming and nonportability has limited their use. Among many other techniques chemiresistors offer many advantages over other techniques in terms of cost, response time, ease of production, real-time monitoring and the possibility of an easy integration into a chemiresistive array. Note worthily, though many works have been carried out in low range detection of acetone by mainly metal oxide based chamiresistors [169, 170], there are limited informations about higher level detection of acetone vapour associated with diabetic kitoacidisis.

For polymeric nanocomposites based chemiressitors selection of polymer matrix is critical because primary sensitivity towards a particular analyte depends upon interaction parameter between polymer chain and analyte. Fluorocarbon elastomer (FCE) is an excellent choice for this purpose as they have solubility parameter close to acetone. FCE are generally used in harsh chemical and temperature condition though there is little information available on its use for chemiresistor development [171, 172]. For achieving good sensing characteristics of CPC base chemiresitors crosslinking of polymer matrix is required. Crosslinked networks of polymer matrix are responsible to increase dimensional stability when chemiresistive stress is being applied by VOCs. Furthermore, crosslinked matrix has changed diffusion behaviour of analytes without significantly affecting polymer-filler interactions. High energy radiation is a clean and effective tool to crosslink polymer without external additive. Such crosslinked nanocomposites can be used as standalone chemiresistor. Thus radiation crosslinked CPC based standalone chemiresistive sensors are expected to offer advantages such as independence of substrate-sensor interface characteristics, availability of larger surface area and fabrication ease.

First section of this chapter elaborates the preparation of fluorocarbon elastomer (FCE)/nano carbon black (NCB) nanocomposites by shear compounding method. Different fractions of NCB loaded composites were prepared in order to establish percolation profile of NCB in polymer matrix. Different crosslinking densities were achieved by using high energy gamma radiation and the effect of crosslinking density on AC and DC conductivity was estimated by impedance analysis and resistance measurements. The effect of crosslinking density and NCB loading on acetone sensing characteristics was evaluated.

3.2a. Materials and experimental method

3.2.1a. Materials

Fluorocarbon elastomer (Viton®, contains 66% fluorine; a copolymer of vinylidene fluoride (VF2) and hexafluoropropylene (HFP)) and Nanocarbon black (NCB) (size 50 nm, surface area 70 m^2/g, density 1.8 g/cc) were procured from M/s TA Corporation, Mumbai, India. Acetone, benzene, xylene, toluene, ethanol and methanol used were of AR grade (purity $> 99.9\%$) and were procured from local supplier M/s SD Fine Chemicals, Mumbai.

3.2.2a. Preparation of FCE/NCB composites:

Shear compounding method was employed to prepare FCE/NCB nanocomposites in Brabender plasticorder. Considering the bulk density different amounts of NCB and FCE were taken and were mixed homogenously in Brabender plasticordar at 100 ^{o}C, 30 rpm for 20 min. After taken out from plasticorder the homogeneous mixture was cut into small pieces. Then these pieces were compressed moulded at 120 ^{o}C for 30 min at 150 kg/cm^2 into 10 cm × 10 cm sheet with different thicknesses (100 μm–500 μm). Co-60 gamma radiation was used to crosslink the chemiresistors for desired absorbed doses. Figure 3.1 represents the schematic of sample preparation by shear compounding and crosslinking by exposing to gamma radiation. Prior to irradiation the dose rate of gamma chamber was ascertained by Fricke dosimetry and it was found to be 1.0 kGy/h. The samples in the study were mentioned as VTX^{Y} where X is the wt% of the NCB in the composite and Y is the absorbed dose. NCB content was varied from 10 wt% to 40 wt%. Table A1 in appendix summarises the composition of FCE/NCB nanocomposites.

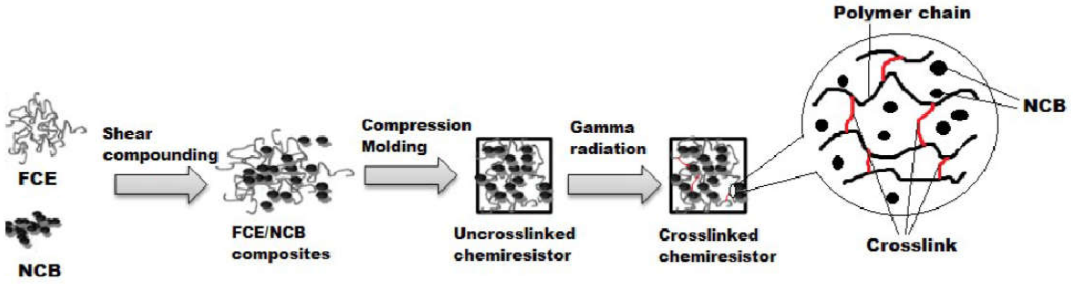

Figure 3.1: *Schematic for preparation of radiation crosslinked FCE/NCB chemiresistor (Red lines depicts cross-linking).*

3.2.3a. Mechanical properties evaluation of nanocomposites by tensile and DMTA test

Mechanical properties like elastic modulus and elongation of break of nanocomposites were evaluated by uniaxial tensile test. Five dumbbell shaped specimens were cut from composite with the help of a sharp edged steel die of standard dimensions and used them for tensile test. The thickness of the samples were determined to the nearest of 0.1 mm. The tensile strength and elongation at break were measured using a universal testing machine supplied by M/s Hemetek, MUMBAI, India at crosshead speed of 100 mm/min at room temperature. DMTA measurements were performed on an MCR 102 Rheometer (Anton Paar, Austria) in SRF mode. Samples dimensions were 25mm x 12mm x 1mm (l x b x t) for all samples. Temperature sweep was carried out in the temperature range. -70 to 30 ^{o}C, rate 3 ^{o}C /min to monitor storage modulus, loss modulus and loss factor in glassy and rubbery states, at 1 Hz frequency and 1% strain.

3.2.4a. Sorption study of nanocomposites

For sorption studies, cross-linked samples were Soxhlet extracted for 12 h to remove any sol content using acetone as a solvent. The remaining gel part was then dried under room temperature and later under vacuum at 40 ◦C. The obtained dried nanocomposites were cut into uniform circular pieces of 1 cm diameter using a sharp-edged die and further used for swelling studies. For swelling study pre-weighed samples were placed in a 200-mesh stainless steel compartment and immersed in an excess of acetone. The swollen samples were periodically removed, blotted free of surface solvent using laboratory tissue paper, weighed on an analytical balance (accuracy 0.00001 g) from M/s AND, India, in stopper bottles and returned to the swelling medium. Until sample reaches equilibrium swelling weight measurement was done. Acetone uptake was defined as the ratio of the weight of the swelled sample to its initial weight.

3.2.5a. AC and DC electrical conductivity

For AC and DC conductivity measurement samples of circular disk shape with diameter of 15mm were cut from compression moulded sheet of 1 mm thickness. The surfaces of the specimen samples were polished with 800-grit sandpaper and were coated with conducting silver paste in order to get good contact between sample and electrodes. The DC conductivity of the samples was measured by recording the resistance of the samples by a two-probe arrangement. A mega ohm meter was employed when samples having resistance higher than 10^6 Ohm. For each composition, at least three specimens were tested. The dielectric measurements were conducted by HIOKI 3570 Impedance Analyzer (Japan) over the frequency range of 4Hz–5MHz. All measurements were performed at ∼24 ◦C and relative humidity of 55%.

3.2.6a. Dynamic and static vapour sensing

To determine the sensing characteristics of chemiresistive sensors both dynamic setup and static vapour setup were used. Figure 2.9 and 2.10 depicts dynamic and static vapour measurement system respectively. A carrier gas as nitrogen is bubbled trough the acetone contained in a glass container (50 ml) maintained under isothermal conditions (298 K). The acetone vapours were diluted to desire extent by mixing with another inlet of nitrogen (0-150 ml/min). The vapour was then transferred to a sensing chamber contains chemiresistor. In dynamic tests, the acetone vapours concentration was expressed in terms of dilution (v/v). The real-time sensing response of chemiresistive sensor was tested for successive exposures of VOC vapours and nitrogen as background. First acetone vapour was purged for 5 min in the sensing chamber followed by flushing with nitrogen for 5 min. The relative change in resistance ($A_r = \Delta R/R_o$) was recorded for different concentrations of analytes. For static measurements, a fixed volume of the acetone was placed in a 2 lit closed glass container and recorded the resistance for 5min then flush with nitrogen to remove the acetone vapours. Relative change in resistance was recorder as sensing response of chemiresistors.

3.3a. Results and Discussion

3.3.1a. Mechanical properties and gel fraction of irradiated FCE/NCB composites:

3.3.1.1a. Effect of radiation dose on mechanical properties:

Elastic modulus of Fluorocarbon elastomer (FCE)/nanocarbon black (NCB) nanocomposites increased significantly with the increase in the radiation dose as well as with increase in NCB fraction (Figure 3.2). Elongation at break (EB) for different FCE/NCB nanocomposites has been shown in Figure 3.3. Pristine FCE and 30% NCB loaded nanocomposites (VT30) both showed drastic decrease in EB with the absorbed gamma radiation dose. With increase in weight fraction of filler, elongation at break was expected to decrease, as the polymer-filler interface is expected to act as crack propagation site; moreover at higher filler loading filler agglomeration can also accentuate the failure [173, 174]. On the other hand, high energy radiation such as gamma radiation is expected to either crosslink or degrades the polymer matrix. As reflected from the modulus value (Figure 3.2), FCE predominantly undergoes rapid crosslinking on irradiation. Increase in crosslinking density can account for the observed precipitous fall in the EB (Figure 3.3). Higher the crosslinking density lesser will be inter and intra chain slippages since most of the polymer chains are interconnected through covalent bonding. A similar trend has been reported earlier for other filled elastomeric and polymeric systems [174, 175].

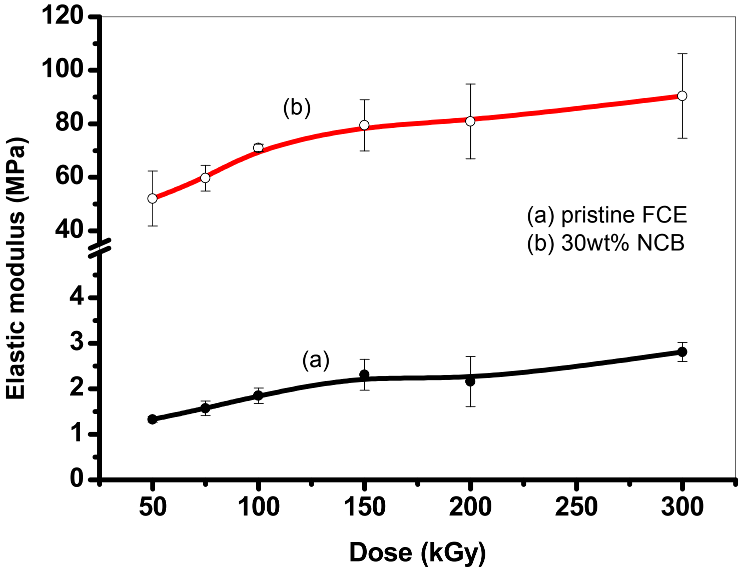

Figure 3.2: *Effect of absorbed dose and NCB incorporation on modulus of FCE (a) 0% and (b) 30% NCB loading (VT30).*

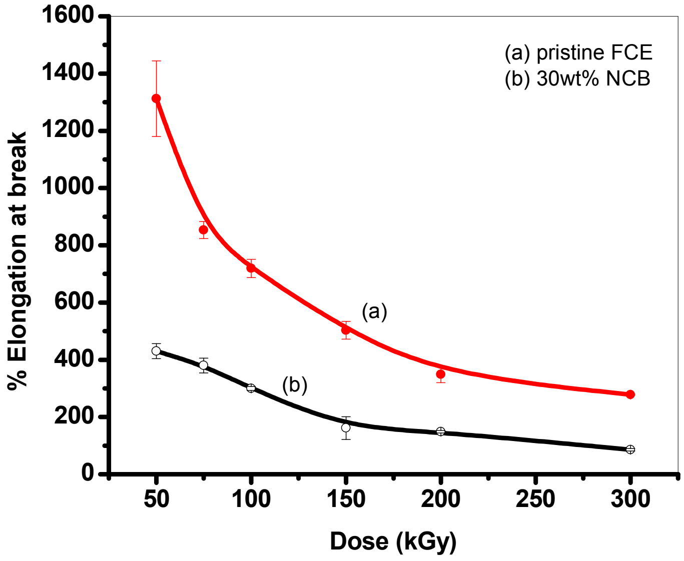

Figure 3.3: *Effect of absorbed dose and NCB incorporation on elongation at break of FCE (a) 0% and (b) 30% NCB loading (VT30).*

3.3.1.2a. Effect of radiation dose on gel fraction and crosslinking density:

The gel fraction and crosslinking density of the nanocomposites was varied by using gamma radiation induced crosslinking. Changes in the gel fraction of filled and unfilled FCE have been shown in Figure 3.4 & its inset. The gel fraction increased with dose, both for 35 % NCB filled (VT35) and unfilled FCE. Maximum gel fraction was around 0.89 for unfilled FCE and around 0.80 for VT35 composite. For different filler loading and total absorbed doses of 50 and 100 kGy the reduction in gel fraction is in the range 7-10% (Inset Figure 3.4). From Figure 3.4 & its inset it is clear that there is a slight reduction in gel fraction at all doses for all compositions compare to pristine FCE. These results show that NCB reduces the efficiency of radiation crosslinking in FCE, marginally but consistently at all doses and at all NCB loadings.

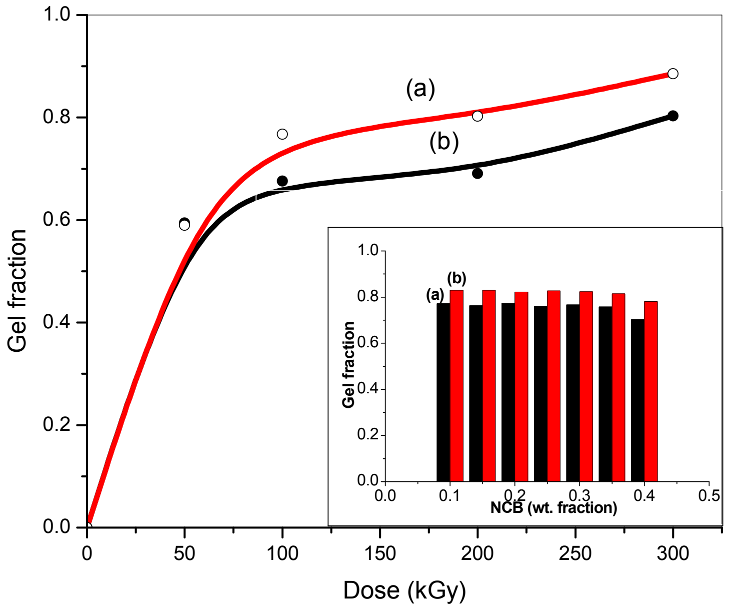

Figure 3.4: *Effect of absorbed dose on gel fraction (a) pristine FCE (b) VT35 nanocomposite. Inset: Gel fraction of FCE/NCB composites at different doses (a) 50 kGy (black) (b) 100 kGy (red).*

The crosslinking density was calculated from estimation of the molecular weight between cross-links (M_c) using the following relation which is based on the theory proposed by Flory and Rehner can be presented as

$$\overline{M_c} = -V_1\rho_p \frac{\phi_p^{1/3} - 1/2\phi_p}{\ln(1-\phi_p) + \phi_p + \chi\phi_p^2} \qquad \textbf{(3.1)}$$

where V_1 is the molar volume of the solvent, ρ_p is the polymer density; φ_p is the volume fraction of the polymer in the swollen matrix and χ is the Flory–Huggins interaction parameter between solvent and polymer which can be calculated using following relation

$$\chi = \beta + \frac{V_1}{RT}(\delta_s - \delta_{p,T})^2 \qquad \textbf{(3.2)}$$

where, δ_s and $\delta_{p,T}$ are the solubility parameters of the solvent and the polymer, β is the lattice constant, R is the universal gas constant and T is absolute temperature. φ_p was calculated using following relation

$$\phi_p = \frac{(w_d - f w_i)/\rho_p}{(w_d - f w_i)/\rho_p + w_s/\rho_s} \tag{3.3}$$

where w_s and ρ_s are the weight and density of the solvent respectively; f is filler weight fraction and w_d and w_i are initial and dried weight respectively. The crosslinking density has been reported as $1/2M_c$. Crosslinking density of the pristine FCE and FCE/NCB nanocomposites is shown in Figure 3.5. It is clear from the figure that for both unfilled and filled FCE crosslinking density increased with absorbed radiation dose. Similar behaviour was observed for gel fraction; though there was slight difference in the trend, which may be attributed to the fact that increase in gel fraction would be negligible at higher doses when most of the chains are interlinked, whereas crosslinking density will keep increasing as the chains get further interlinked. The crosslinking density of the filled composites was slightly higher than the unfilled FCE, this can be attributed to the contribution of physical crosslinking by nanoparticulate filler. A similar behaviour was observed in elastic modulus (Figure 3.2). One of the plausible explanations for the increase in the elastic modulus and crosslinking density of FCE/NCB nanocomposites with NCB loading might be good interaction between NCB and FCE interfaces. Therefore, interactions between NCB and FCE were assessed using Kraus equation:

$$\frac{V_{r0}}{V_{rf}} = 1 - m\left(\frac{\phi_f}{1-\phi_f}\right) \tag{3.4}$$

Where V_{r0} is the volume fraction of the polymer in the swollen rubber, V_{rf}, volume fraction of polymer in the swollen filled system and ϕ_f is the volume fraction of the filler in the filled composite. To access the polymer filler interaction, V_{r0}/V_{rf} was plotted against $\phi_f/(1-\phi_f)$. A linear profile with negative slope obtained suggested high reinforcement by filler (Inset figure 3.5a). The polymer-filler interaction parameter C (Kraus constant) was calculated using the Kraus equation (equation 3.5) by putting “m” value obtained from plotting suitable parameters of equation 3.4.

$$C = \frac{m - V_{r0} + 1}{3(1 - V_{r0}^{1/3})} \tag{3.5}$$

The C value for the system was found to be 1.03±0.2 suggesting good interaction between NCB and FCE.

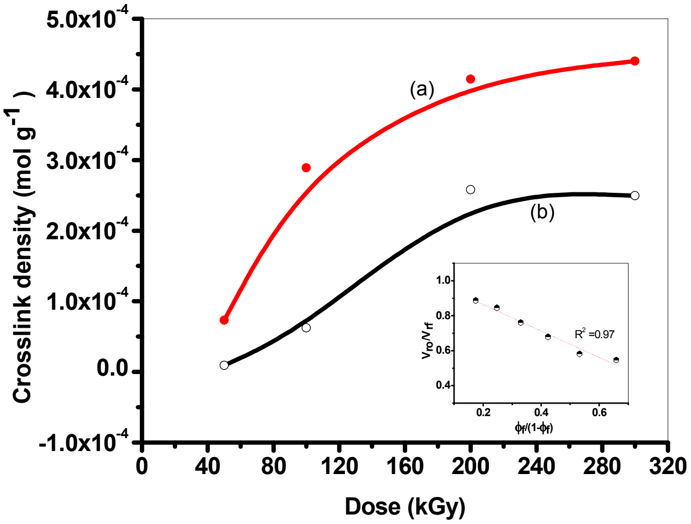

Figure 3.5: *Effect of absorbed dose on crosslinking density (a) VT35 composites (b) pristine FCE. Inset: Kraus plot for FCE-NCB composites.*

3.3.1.3a. Effect of radiation dose on dynamic mechanical properties:

Dynamic mechanical properties were investigated to understand effect of radiation dose on segmental motions of FCE polymer molecules. The radiation dose was found to have a significant effect on the dynamic mechanical properties (Figure 3.6). The storage modulus increased with increase in absorbed radiation dose. The increase in radiation dose influenced the glass transition and the loss factor (tan δ), suggesting marked influence of radiation on the segmental dynamics. In the glassy region, the difference in storage modulus with radiation doses was significant (Figure 3.6a). The matrix irradiated to 300 kGy doses showed highest elastic modulus, suggesting highest cross-linking density of the matrix. Variation in tan δ with an increase in temperature has been presented in Figure 3.6b. The glass transition was observed at around –13 °C. With the increase in radiation dose, there was shift in glass transition, suggesting a reduction in the segmental motion.

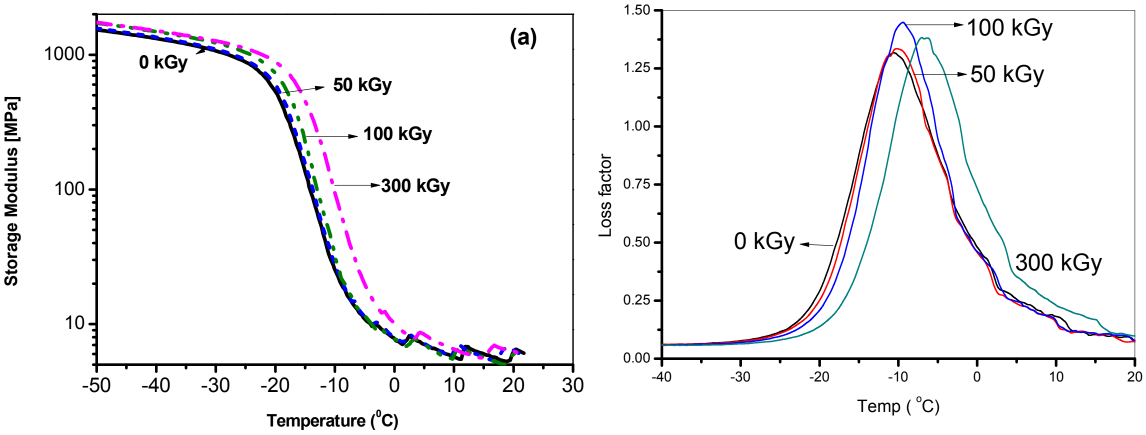

Figure 3.6: *Variation of (a) Storage modulus (b) tan δ with temperature for pristine FCE.*

3.3.2a. Electrical properties of FCE/NCB composites:

3.3.2.1a. DC and AC electrical conductivities of nanocomposites:

DC electrical conductivity of composites as a function of NCB fraction has been shown in Figure 3.7. Upto 0.2 weight fraction of NCB there was hardly any change in conductivity after that a dramatic increase in conductivity (~ in order of 10^6) was observed. The conductivity behaviors of the composites is often governed by a power law [176, 177]:

$$\sigma = \sigma_f(\varphi_f - \varphi_c)^t \tag{3.6}$$

where ϕ_f is the volume fraction of the filler, ϕ_c is the percolation threshold, σ_f is the filler conductivity and t is the critical exponent. It can be shown from inset of Figure 3.7 that the above power law equation fitted very well with experimental data. The power law fitted experimental data gives values of ϕ_c and t as 0.15 and 2.57 respectively. FCE/NCB composites showed significantly lower percolation threshold than other elastomeric nanocomposites containing NCB; though it was higher than what is commonly observed for anisotropic conducting fillers such as MWNT, SWNT, carbon fibers and graphene [178]. In this context it may be noted that, though the employed melt compounding process offers several advantages in terms of process efficacy and environmental friendliness, it is expected that such process offers higher percolation threshold than other conventional methods. The value of critical exponent, t, in equation 3.6 reflects the dimensionality of conduction and suggests 3D conduction within the system [179].

The variation of AC electrical conductivity at room temperature of FCE/NCB nanocomposites with the frequency in the frequency range 100 Hz to 1 MHz is shown in Figure 3.8. From the figure it can be seen that the AC conductivity varies significantly with increase in frequency as well as with NCB loading. AC electrical conductivity increase with increase in NCB loading of nanocomposites. It indicates that formation of additional conducting network with addition of NCB into composites. Nanocomposites containing 0.1 weight fraction of NCB shows significantly different behavior of AC electrical conductivity than other nanocomposites. Almost linear increase in AC conductivity with frequency was observed for 0.1 weight fraction nanocomposites. Whereas 0.2 and 0.3 weight fractions NCB containing nanocomposites displayed quite stable σ_{AC} with increase in frequency. Interestingly however, σ_{AC} decreased significantly for the composite containing 0.35 weight fraction of NCB (VT35) when the frequency increased beyond 0.1 MHz. Huge difference in the AC conductivity was observed at 100 Hz between VT10 nanocomposites (0.1 weight fractions NCB) and rest of the nanocomposites. The linear increase in the conductivity with increase in frequency for the VT10 nanocomposite suggests that till 0.1 weight fraction of NCB the nanocomposite of FCE/NCB act as an insulating material, corroborating our result on the percolation threshold of FCE/NCB nanocomposites [180].

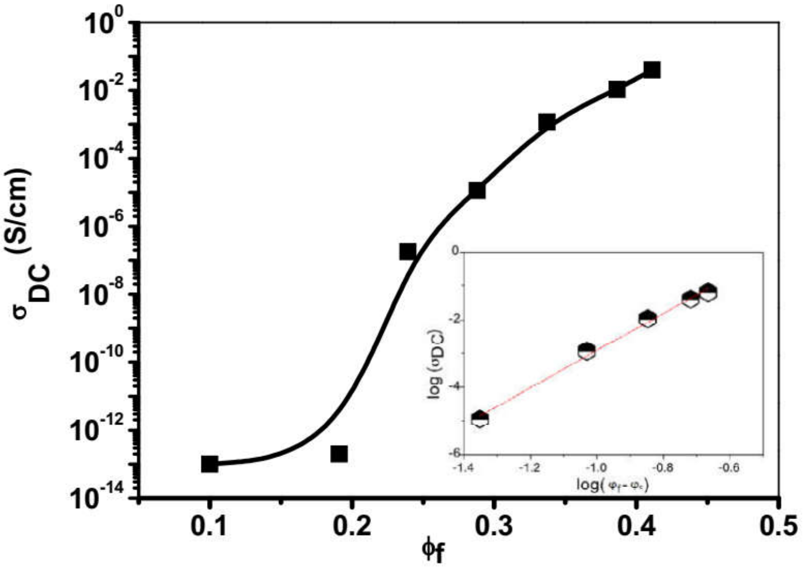

Figure 3.7: *Variation of DC conductivity of unirradiated composites with NCB loading.*

Inset: log-log plot for σ_{DC} *vs* (φ_f-φ_c).

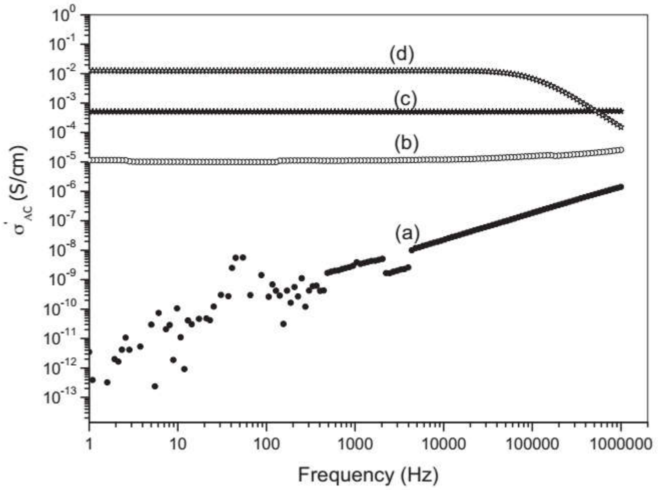

Figure 3.8: *Variation in AC conductivity with frequency of unirradiated composites (a) VT10; (b) VT20; (c) VT30; and (d) VT35.*

3.3.2.2a. Effect of Crosslinking density on DC and AC electrical conductivities:

Effect of crosslinking density on AC conductivity and DC conductivity are represented in Figure 3.9 and 3.10 for VT35 nanocomposites respectively. It can be seen that with increase in crosslinking density (radiation dose) both AC and DC electrical conductivities decreased significantly. The highest change was observed between crosslinking densities 73 µmol/g (50 kGy) and 290 µmol/g (100 kGy). There was further decrease in conductivity at higher crosslinking density. Though at higher dose the decrease in AC and DC conductivities were marginal. There was a precipitous fall in σ_{AC} values in the frequency region 10 kHz - 200 kHz for nanocomposites having different crosslinking densities. At very high frequency value (above 0.5 MHz) the AC conductivity values for all composites were near about same, reflecting conductor to insulator transition at this frequency.

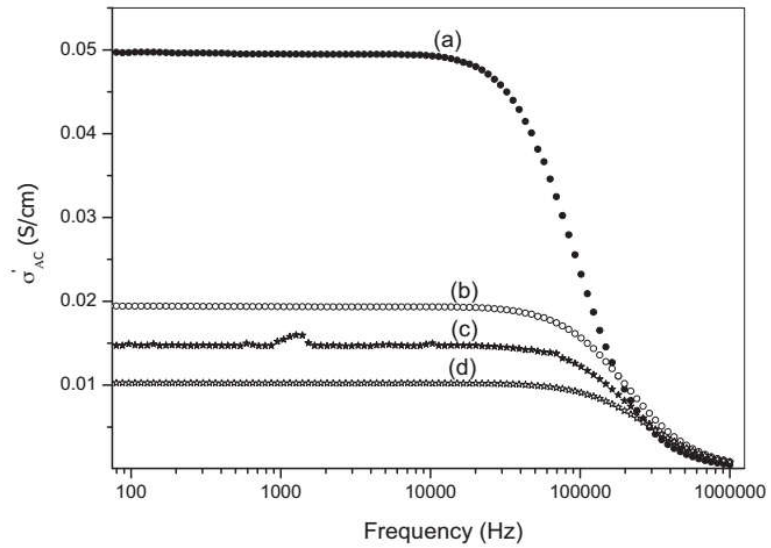

Figure 3.9: *Variation in AC conductivity with frequency of VT35 nanocomposite at different doses (a) 50 kGy; (b) 100kGy ;(c) 200kGy; (d) 300kGy.*

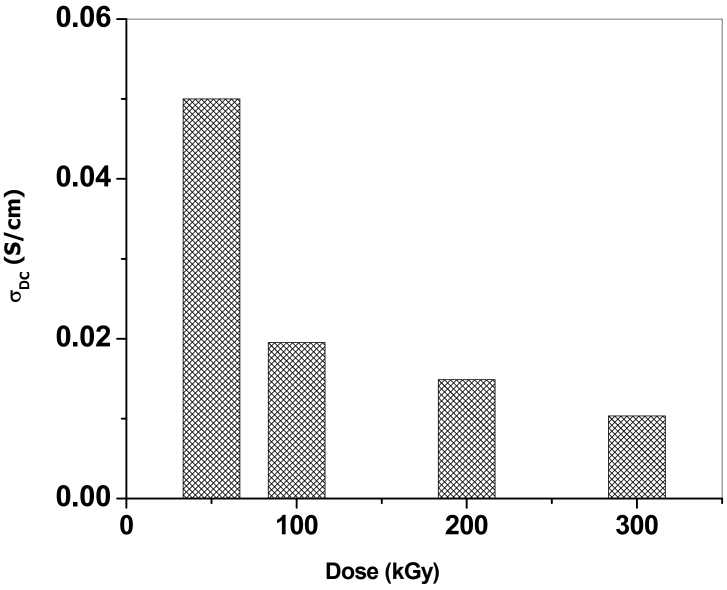

Figure 3.10: *Change in DC conductivity for VT35 nanocomposite with radiation dose.*

For conducting nanocomposites, the conductivity remains constant till a certain range (known as DC plateau) and decrease thereafter [181, 182]. This phenomenon is generally attributed frequency dependent changes in polarization of permanent and induced dipoles in the nanocomposite matrix [180, 181]. The observed decrease in conductivity with radiation dose can be attributed to the formation of rigid crosslinked network of polymer by high energy radiation which hindered electron transport. With increase in frequency dipoles get less time for reorienting themselves in the direction of applied filed thus reducing polarization effect. It is therefore quite probable that at lower frequency current flows throw NCB aggregates resistor network, whereas at high frequencies capacitor admittance of insulating polymer matrix plays a critical role in electrinic conduction in nanocomposites[181, 183].

The change in DC conductivity with increase in the network density is shown in Figure 3.10. It can be seen that the conductivity decreases significantly with an increase in radiation dose (i.e. increase in network density). The decrease in the conductivity is generally attributed to the residual changes in the free volume/density at polymer–filler interface, affecting electron tunnelling and hopping mechanisms [184-186].

3.3.3a. Chemiresistive behaviour of FCE/NCB nanocomposites:

3.3.3.1a. Effect of NCB loading on chemiresistivity:

Chemiresistivity of different nanocomposites from percolation profile of FCE/NCB were investigated to establish the effect of NCB loading on chemiresistivity of FCE/NCB nanocomposites towards acetone vapour. Nanocomposites with NCB fraction 25% (VT25, limited conductivity region), 30% (VT30, intermediate conductivity region) and 35% (VT35, high conductivity region) were chosen. All of these chemiresistors showed significant sensing response for acetone vapour at room temperature. Among these chemiresistor VT25 showed too non-reproducible response to be of practical application. Thus VT25 was discarded and VT30 and VT35 were selected for further study. Figure 3.11 shows the sensing response of VT30 and VT35 irradiated at 100 kGy dose for different vapours fractions of acetone. Both chemiresistors showed a concentration-dependent increase in the resistance; notably, $VT35^{100}$ chemiresistor had markedly higher response than $VT30^{100}$ chemiresistor. Langmuir–Henry-Clustering (LHC) model is often used to explain such chemiresistive response. It can be described as follows

$$A_r = \frac{b_L(f''-f)f}{1+b_L f} + k_H f + (f - f')f^{n'} \tag{3.7}$$

where A_r is a relative change in resistance ($\Delta R/R_o$), f is the vapour fraction of acetone, f' is the acetone fraction over which clustering takes place and f″ is the acetone fraction where Henry's diffusion takes precedence over Langmuir's diffusion, b_L is the Langmuir's affinity parameter, k_H is Henry's diffusion parameter and n′ is the average number of solvent molecules per cluster [162].

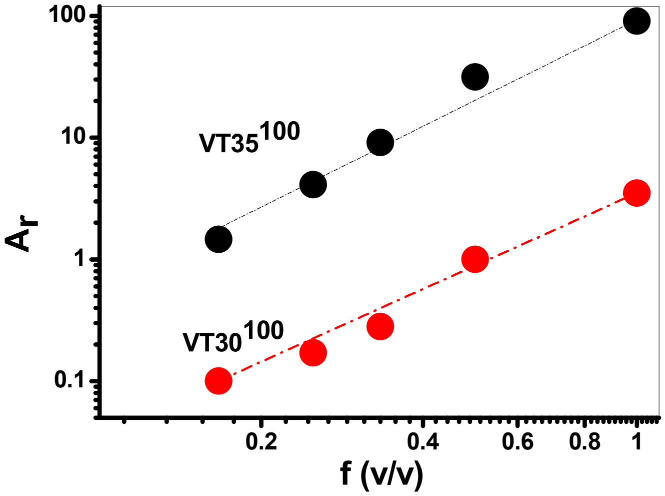

***Figure 3.11**: Dependence of sensing response A_r on the vapour fraction of acetone for $VT35^{100}$ and $VT30^{100}$.*

$VT35^{100}$ and $VT30^{100}$ both chemiresistors followed a log–log dependence on the vapour concentration. The slope of the curve which actually represents sensitivity of the chemiresistors was found to be 2.2 for $VT35^{100}$ and 1.9 for $VT30^{100}$. The power-law dependence between A_r and vapour fraction of acetone can be explained by considering the dominance of vapour clustering. However the clustering hypothesis fails to explain the higher response of $VT35^{100}$ in comparison to $VT30^{100}$. As equilibrium uptake of acetone was lower in $VT35^{100}$ than $VT30^{100}$ and thus clustering is expected to be more in $VT30^{100}$ composite. Additionally, diffusion kinetics experiments did not show much difference between these two chemiresistors.

3.3.3.2a. Effect of radiation dose sensing response:

Sensing response can be significantly affected by absorbed radiation dose. Figure 3.12 shows relative change in resistance ($A_r = \Delta R/R_o$) in presence of 50% diluted acetone vapour and nitrogen cycles for VT35 chemiresistors irradiated to two different radiation doses, 100 and 300 kGy. $VT35^{100}$ showed 400% increase in the resistance while the $VT35^{300}$ chemiresistor showed 300% increase in the resistance. Both unirradiated and irradiated chemiresistors were exposed to undiluted acetone vapours to further probe the effects of radiation dose and compare the sensing response (Figure 3.13). Without acetone field resistance was stable and increase rapidly once the chemiresistors were exposed to acetone. Again the resistance come back close to original value once acetone was replaced by nitrogen. The un-irradiated matrix $VT35^{00}$ was found to be unsuitable for sensing application, because response was not reversible and also considerably less than that of $VT35^{100}$ and $VT35^{300}$. Resistance of un-irradiated chemiresistor didn't come back to original value once acetone was removed. Interestingly, though the $VT35^{300}$ chemiresistor showed a decrease in resistance, it took more than 150 sec to reduce it to half of the peak value. While the same reductions has been achieved within 30 sec for VT35^{100}chemiresistor.

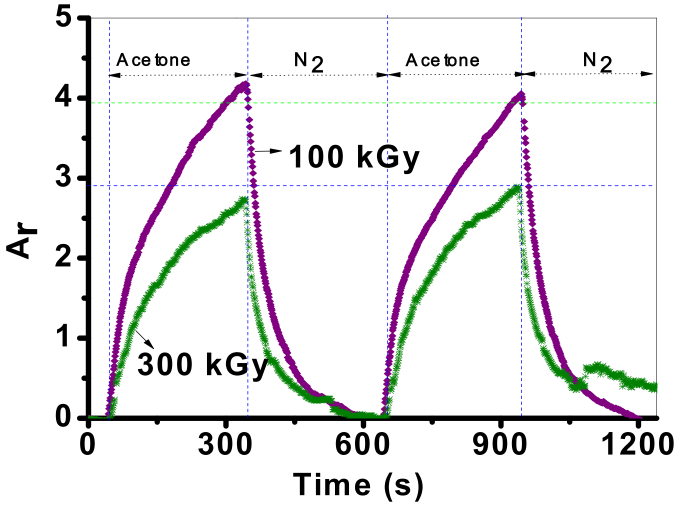

Figure 3.12*: Variation in resistance for VT35^{100} and VT35^{300} chemiresistors in presence of 50% diluted acetone vapour.*

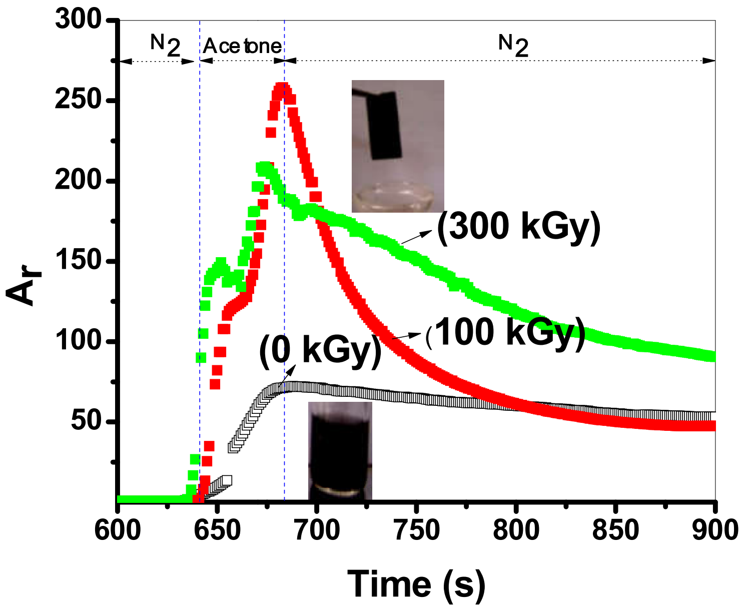

Figure 3.13*: Variation in resistance for VT35^{00}, VT35^{100} and VT35^{300} chemiresistors in presence of saturated acetone vapour. Figure also shows the photographs, showing disintegration of VT35^{00} and retention of integrity of VT35^{100} chemiresistors after putting in acetone for 30 min.*

Physical examination showed an irreversible change in dimension of un-irradiated chemiresistors ($VT35^{00}$) upon exposure to acetone vapour. The reason of irreversible change in dimension may be that the un-irradiated chemiresistors do not have inter-macromolecular linkages between polymer chains; therefore, they don't restore back to original position once deformed by chemiresistive stress. This permanent change in dimension was responsible for irreversible change in resistance of unirradiated matrix by acetone vapour. $VT35^{00}$ composite completely disintegrates within 30 min when immersed in acetone; whereas, $VT35^{100}$ maintained its integrity (Figure 3.13, photographs). The matrix integrity of the chemiresistors irradiated to 100 kGy and 300 kGy was tested for an extended time. It was found that irradiated matrices do not disintegrate up to 2 days of continuous immersion in acetone. Irreversibility of un-irradiated chemiresistor ($VT35^{00}$) attributed to the absence of cross-linked networks in FCE/NCB chemiresistor matrix. FCE chain relaxed in presence of chemiresistive stress and expands the matrix, leading to an increase in the bulk resistivity. The un-irradiated matrix has no elasticity since the matrix was not covalently crosslinked, which would enable it to recover its original conducting network once the chemiresistive stress is removed (Figure 3.14). Reversibility was also compromised significantly in $VT35^{300}$ chemiresistors and the reduction of resistance was not rapid compare to $VT35^{100}$ chemiresistor after the removal of acetone vapour field (Figure. 3.13). This increase in recovery time in case of $VT35^{300}$ chemiresistors may be attributed to the reduction of diffusion of acetone molecules into chemiresistor matrix due to the formation of the rigid polymer network. Essentially, the prime reasons for the radiation dose-dependent changes in the sensing response could be alterations in acetone diffusion behaviour in chemiresistor and variations in the disaggregation dynamics of NCB aggregates under chemiresistive stress. These factors lead to changes in the chemiresistive stress induced expansion of FCE chains and in the contact resistance between NCB aggregates.

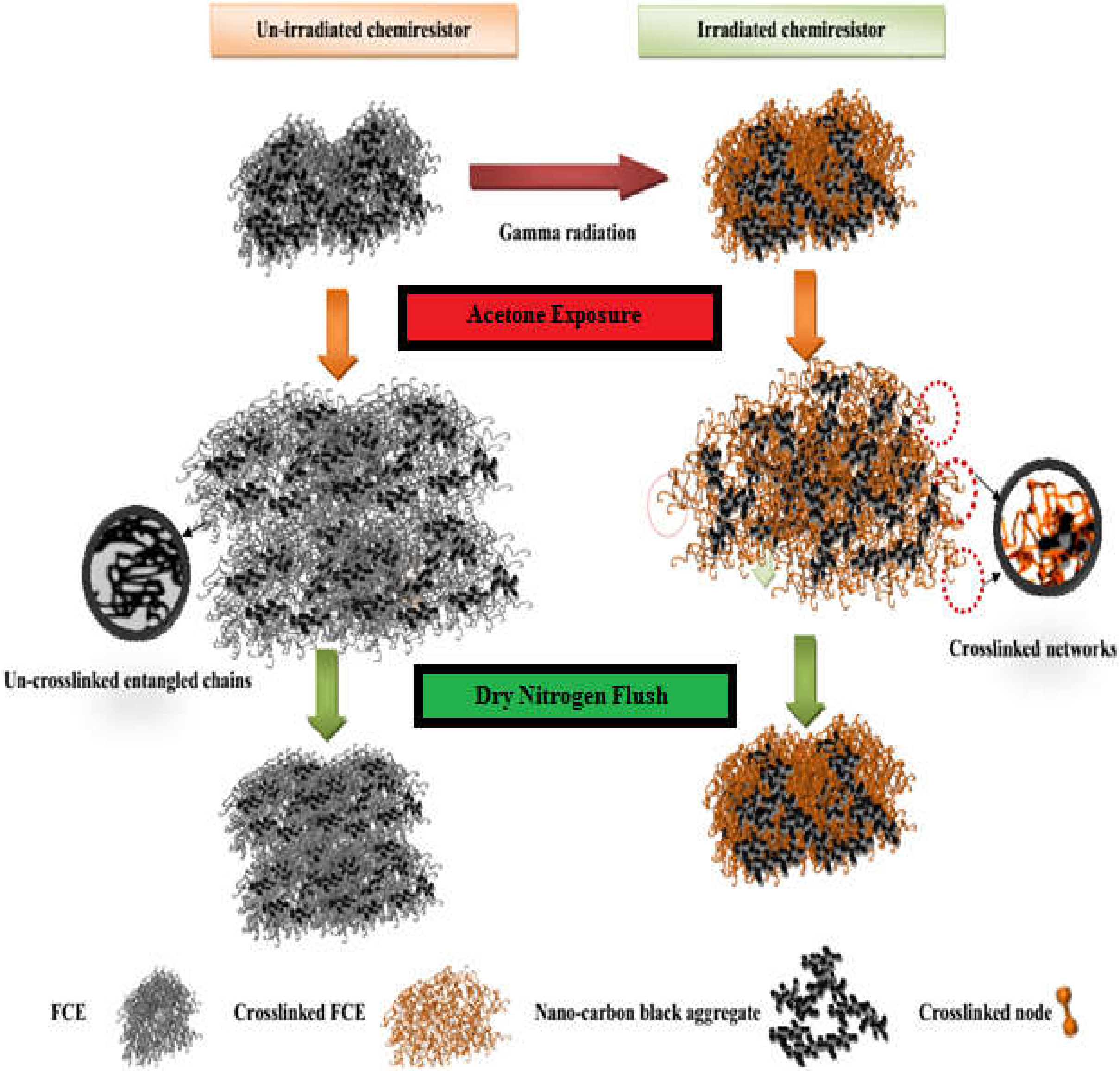

Figure 3.14: *Schematic showing the response of un-irradiated and irradiated FCE/NCB chemiresistors for acetone vapours-nitrogen flush cycle. Under chemiresistive stress, the matrix expansion of irradiated chemiresistor was relatively less and it had enough elasticity to restore original shape once acetone vapour field is removed.*

3.3.3.3a. Effect of radiation dose and NCB loading on acetone diffusion behaviour:

To probe the impact of radiation dose and NCB loading onto FCE chain relaxation and acetone diffusion behaviour, acetone uptake kinetics of chemiresistors was investigated [187, 188]. Acetone uptake was quantified by taking ratio of swelled weight at particular time and initial weight of chemiresistors and equilibrium uptake is given by wt at equilibrium swelling in acetone/initial weight of chemiresistors. Uptake kinetics of unfilled FCE, VT35^{100}, VT35^{300} and VT30^{100} is represented in 3.15 (a) and 3.15 (b).

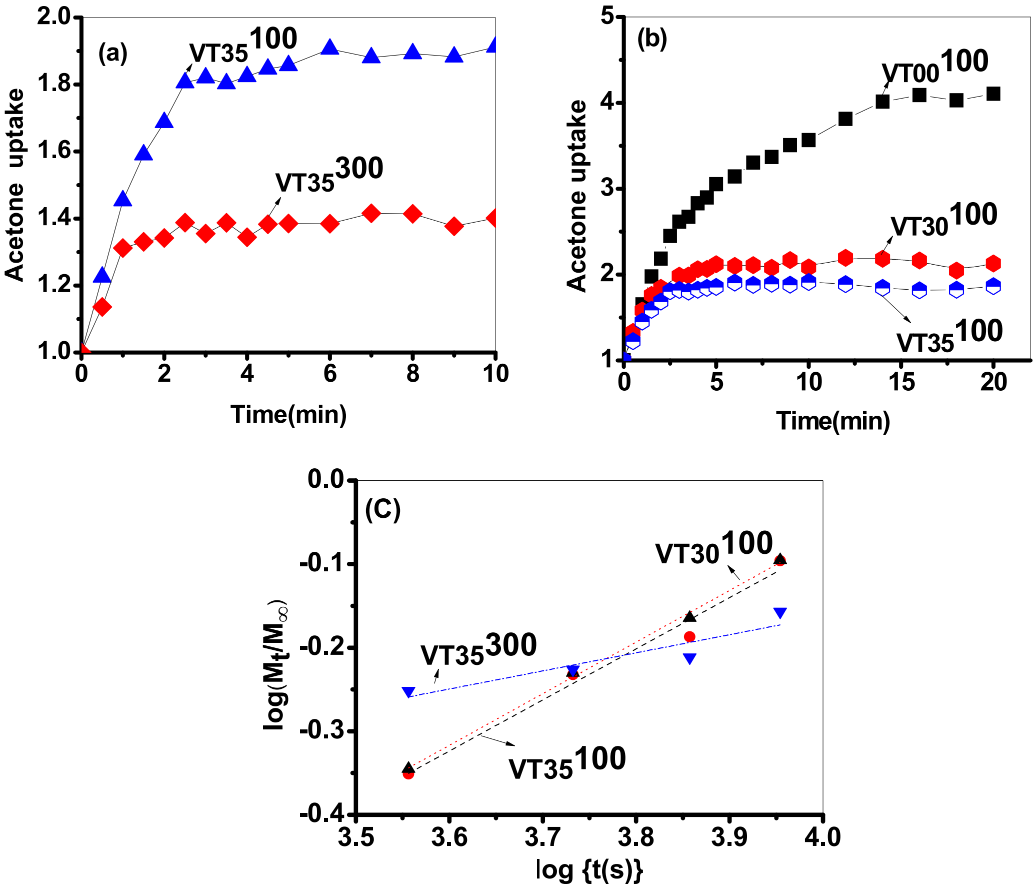

Figure 3.15: *Effect of radiation dose and NCB loading on the acetone uptake by FCE/NCB chemiresistors. (a) VT35^{100} and VT35^{300} (b) VT00(FCE), VT30 and VT35 at a fixed dose of 100 kGy (c) Uptake kinetics data fitted in equation 3.8.*

Relative eqilibrium uptake of acetone (EUA) decrease with ratiation dose and with addition of filler. At 100 kGy dose for VT35 composites EUA was 1.8; whereas, at 300 kGy it was about 1.3. EUA decreased to half of its value from unfilled FCE by addition of 30 wt% NCB to FCE. While furthur addition of NCB (30wt% to 35wt%) did not significantly change EUA (~25%). This is due to the radiation induced grafting of the FCE elastomer chains onto NCB surface [189, 190]. In this context its worth highliting that there was a substantial increase in electrical conductivity (~1000%) by increasing NCB loading from 30 wt% to 35wt%. This observation has confirmed contribution from radiation grafting of FCE onto NCB and of physical crosslinking. To fully understand the diffusion and relaxation process the sorption data was further analyzed using Fickian diffusion model.

$$M_t/M_\infty = kt^n \tag{3.8}$$

where M_t=mass of solvent absorbed at time t, M_∞ = mass of solvent absorbed at equilibrium, k is a constant depending upon the characteristics of the polymer network and the solvent, n is an empirical number called as transport or diffusion exponent. $VT35^{300}$ composite has displayed quasi- Fickian behaviour with n value 0.22, while $VT35^{100}$ and $VT30^{100}$ composites follow non-Fickian diffusion behaviour with n>0.5 (Figure 3.15 c). It suggests that in case of $VT35^{100}$ and $VT30^{100}$ the relaxation of polymer chains plays an important role in acetone diffusion. For $VT35^{300}$, the quasi-Fickian behaviour suggests that the relaxation of polymer chains are more restricted in $VT35^{300}$ composite [191]. The observed relatively better acetone sensing response of $VT35^{100}$ than of $VT35^{300}$ therefore can be attributed to the radiation dose assisted changes in the FCE chain relaxation dynamics [192, 193].

3.3.3.4a. Effect of acetone concentration:

In the previous section (3.3.3.1a), it was observed that VT35^{100} and VT30^{100} composites show log-log linear relationship between the sensor response and acetone concentration (v/v) in dynamic setup. Static setup was used to confirm these results, wherein a different concentration of acetone was generated in a 2 litre closed container and relative change in resistance was observed as sensing response. The results are shown in Figure 3.16. It can be seen that the response at different concentration was reversible and the signal-concentration relationship was log–log linear (Inset Figure 3.16). Often Langmuir–Henry-Clustering (LHC) model is used to explain such chemiresistive response (equation 3.7). Feller et al. have found applicability of all three components of LHC model i.e. adsorption, diffusion and clustering in PMMA/CNT based chemiresistor [70]. However, LHC model did not adequately explain the sensing response of FCE/NCB chemiresistors. LHC model basically base on the underlying assumptions of Henry's and Langmuir's model, states maximum monolayer coverage by analyte molecules which was clearly not in the case of standalone FCE/NCB sensor. LHC isotherms do not effectively accounts the diffusion of analyte into the chemiresistor which is subjected to three-dimensional exposure to the analyte. Han et al. also observed similar finding on electro spun PMMA- SWNT composite sensors for methanol [98]. Another major fact is that the dynamic changes taking place in the chemiresistor due to acetone and FCE interactions. Thus the enhanced sensitivity of standalone FCE/NCB chemiresistors may be ascribed as the three-dimensional (3-D) sensing which was not possible in top-layer sensing used in printed layer by layer assembly or coated electrodes. In addition to 3-D sensing, there were some distinct aspects of FCE/NCB chemiresistor matrix which could able to influence the sensing response. The standalone chemiresistors used in this work were prepared by shear compounding followed by compression moulding and crosslinking using high energy radiation to impart sufficient strength to function as a standalone sensing film. The sensing response (A_r) of FCE/NCB chemiresistors would as well depend on various other attributes such as crosslinking density, physical crosslinking by NCB, acetone diffusion kinetics and overall network architecture of NCB aggregate.

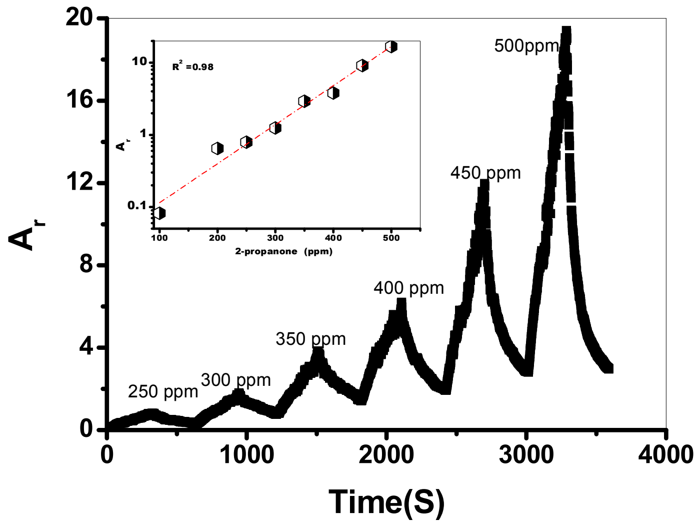

Figure 3.16: *Variations in the* A_r *with an increase in acetone concentration for VT35*^{100} *chemiresistor under static vapour condition. Inset shows log– linear fitting.*

3.3.3.5a. Selectivity of chemiresistor:

Selectivity of chemiresistors is another aspect besides sensitivity which enables the chemiresistors to distinguish target analytes from others. Selectivity of sensor was tested against 500 ppm of different VOCs in static setup and results are shown in Figure 3.17. The response for acetone was about 22 folds higher than the response for ethanol and was about 52 fold higher than the response for water. Cross sensitivity (Response for interfering VOC/Response of targeted analyte) is an important characteristic for developing VOC sensor. To qualify as acetone sensor for breath analysis this cross sensitivity towards water and ethanol should be less than 10%. Table 3.1 gives a brief overview of some literatures regarding the cross sensitivity between acetone and ethanol/methanol vapour. Figure 3.17 shows response of VT35^{100} chemiressitors for different VOCs. The response for water, ethanol, methanol and aromatic hydrocarbons are less than 10% than that of acetone response. In current study the cross sensitivity for ethanol and methanol was found to be 0.045 and 0.038 respectively. This is an important advantage of FCE/NCB chemiresistors to act as an exhaled breath analysis for acetone.

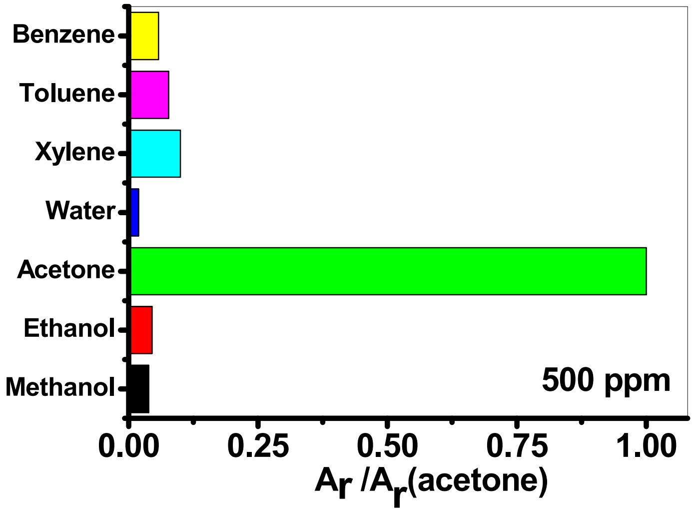

Figure 3.17: Variation in relative change in response compare to acetone for VT35^{100} chemiresistors against different VOCs. (500 ppm, static setup).

Efforts were made to understand the mechanism behinds the selectivity of FCE/NCB nanocomposites for acetone vapours. Selectivity of CPC based chemiresistive sesnors primarily comes from the interaction of analyte molecules and polymer matrix. Both kinetics and thermodynamic aspects may be considered in order to interpret the interaction between analyte and polymer chain. At first analyte molecules diffused inside polymer matices and relaxed polymer chains. This build a chemiresistive stress within matrix and disrupt transport of electron between conducting fillers, leading the increase in resistivity of conducting polymer composites based chemiresistors. The magnitude of interaction between polymer and analyte molecules can be expressed in terms of Flory-Huggins interaction parameter (χ_{12}), which is a thermodynamic measure of polymer-analyte interaction [127].

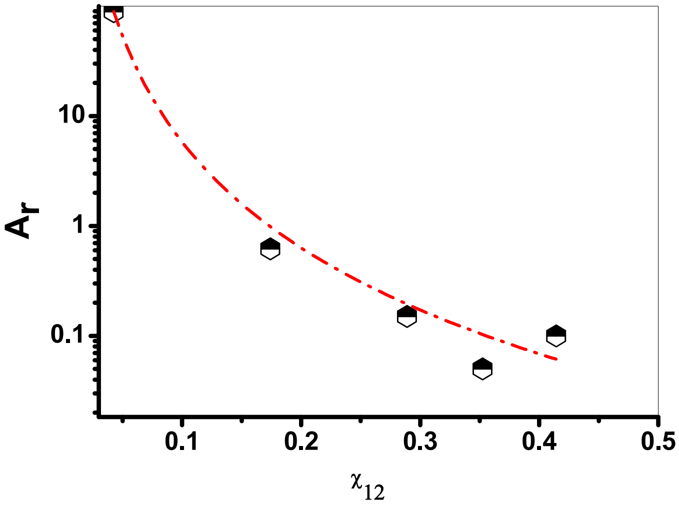

Figure 3.18*: Variation in relative change in resistance with χ_{12}; the dotted line shows fitting of the equation 3.9.*

χ_{12} depends on the solubility parameter of the polymer and the analyte (equation 3.2). χ_{12} governs the relaxation of polymer chains in a particular analyte and is related to the sensing response of a chemiresistive sensor for particular analyte by following relation

$$\frac{\Delta R}{R_0} = ae^{b(\chi_{12})^{-n}} \quad \textbf{(3.9)}$$

where a, b and n are constants [162]. The sensing response of $VT35^{100}$ chemiresistor is plotted against χ_{12} in Figure 3.18 for benzene, ethylbenzene, toluene, xylene and acetone (50% dilution with nitrogen). It can be seen that the sensing response decreased with an increase in χ_{12}. The Eq. (3.9) fitted well for the composite $VT35^{100}$ ($R^2 = 0.98$). The value of n was found to be 3, suggesting a profound dependence of the A_r on polymer-filler interaction parameter. Therefore, the high selectivity towards acetone can be attributed to the good thermodynamic interaction between FCE chains and acetone molecules. Such interactions relax the polymer chains and builds stress within the matrix, increasing inter-aggregate distance within the percolated NCB networks.

Table 3.1: Comparison of key feature of FCE/NCB chemiresistor sensors with various reported composite matrices.

Material	Synthesis procedure	Operation temperature	Cross-sensitivity (Ethanol or methanol signal / acetone signal)	Concentration range	Reference
ZnO nanosheets	Precipitation	300 °C	0.36	5-1000 ppm	[194]
Ultrafine -Fe_2O_3 nanoparticles	Micro-emulsion	340 °C	0.5	20-3000 ppm	[195]
Stabilized zirconia and $Co_{1-x}Zn_x$ Fe_2O4	Sol-gel	650 °C	0.7 (for methanol)	5-100 ppm	[196]
Titanium dioxide nanoparticles	Low-temperature hydrothermal	270 °C	0.67	0.5-1000 ppm	[197]
SnO_2 nanofibers	Electrospinning	200 °C	0.33	1-100 ppm	[198]
Triple-shelled $ZnO/ZnFe_2O_4$ heterojunctional hollow	Precipitatation	140 °C	0.69	5-500 ppm	[199]

microspheres					
$Fe_2O_3/CuFe_2O_4$ heterostructure	Template	225 to 375 ^{o}C	0.71	0.1-2 ppm	[200]
Calix4pyrrole-decorated carbon nanotubes on paper	Non-covalent functionalization of SWCNT	RT	0.5	20- 500 ppm	[201]
Yolk-shell $LaFeO_3$ microspheres	Hydrothermal	225 ^{o}C,	0.6	25.5-100 ppm	[202]
3D-printed poly(vinylidene fluoride)/carbon nanotube composites	3-D printing	RT	0.33 (for methanol)	Saturated acetone vapours	[71]
MHDA-Functionalized Multiwall Carbon Nanotubes	CNT functionalization	RT	16.3	5-30 ppm	[203]
FCE/NCB composite	Melt/shear compounding	RT	0.045 (ethanol) 0.038 (methanol)	100-500 ppm 0.1-1 (v/v)	This work

3.3.3.6a. Detection limit, Reproducibility, Response time and stability of chemiresistor:

The detection limit was determined from standard deviation (SD) of response at 100 ppm and the slope(S) of the calibration curve (3.3 SD/S) in the linear region of the Inset Fig. 3.16. The detection limit was found to be 18.2 ppm for acetone. The reproducibility of the signal was estimated at 100 ppm by using four successive measurements for VT35^{100} chemiresistors (Fig. 3.19A). It is clear from the figure that sensing response was reversible and reproducible in nature. The response time and recovery time were also gauged at 100 ppm in the static setup (Figure 3.19B). 50% of the peak response was attained in 27.8 sec and 90% of the peak response was attained in 131.6 sec. t_0 was the time assumed to be when vapours are homogeneously dispersed in the sensor chamber. 50% recovery was attained in 58.2 sec and almost 90% background response was attained in 153 sec. The stability of the sensor response during 1-h exposure to 100 ppm acetone vapours is shown in Figure 3.19C. It can be seen that the sensor shows a stable response for 1 hr under 100 ppm acetone vapour.

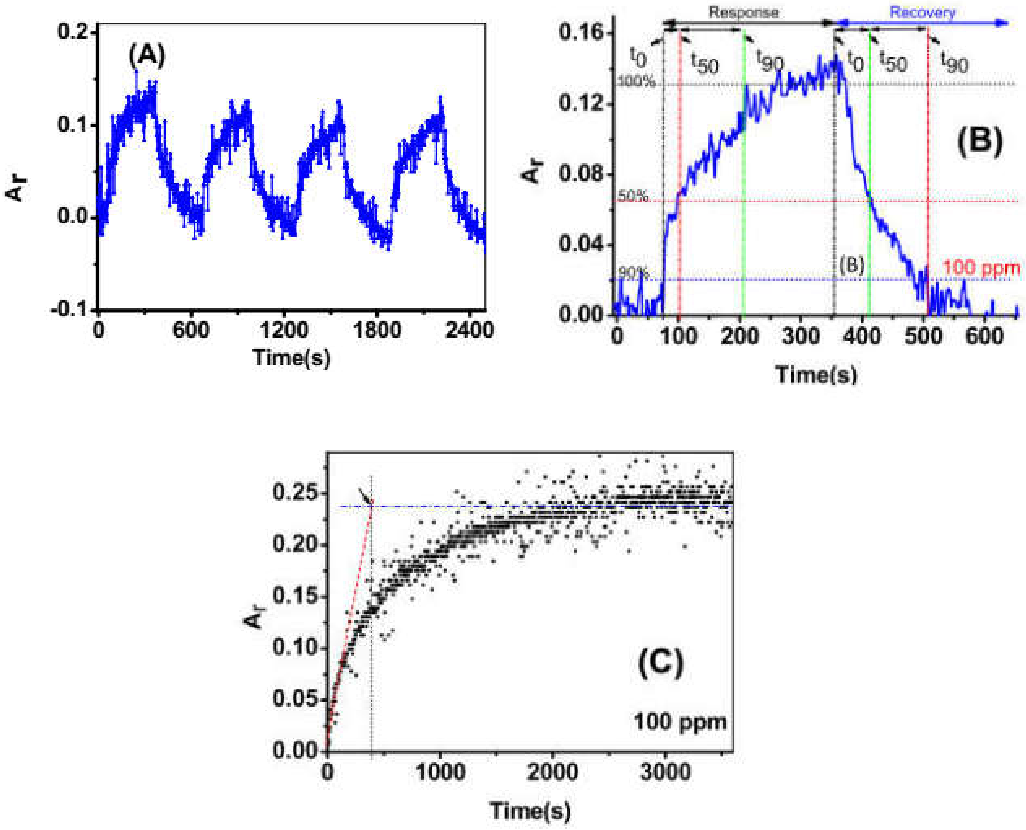

***Figure 3.19**: (A) Reproducibility of the $VT35^{100}$ sensor for four successive cycles of 100 ppm acetone (B) Sensor response and recovery time at 100 ppm acetone in a static setup (C) sensor response for 1hr at 100 ppm acetone.*

3.4a. Conclusions

A novel radiation crosslinked FCE/NCB based chemiresistor was developed for rapid, selective and reversible detection of the acetone vapour at room temperature. Nanocomposites of different crosslinked network densities were obtained using high energy gamma radiation. The crosslinked network was found to have a profound effect on the sensing response of the chemiresistor. The change in conductivity with increase in NCB content was found to be governed by the power law. The chemiresistor showed a highly selective response for acetone and the substantially lower response was recorded for benzene, toluene, xylene, methanol, ethanol and water. It was found that the sensing response had a strong correlation with the FCE – acetone interaction parameter (χ_{12}). Acetone uptake kinetics underscored the significance of heterogeneities in the crosslinking network and the sensing response of FCE/NCB chemiresistors.

3b. Investigation of coagulated natural Rubber Latex (NRL)/CNT nanocomposite based chemiresistor for Isoprene detection:

3.1b. Introduction

Exhaled breath analysis has emerged as an effective tool for early detection of various life threatening disease like cancer, diabetics etc. There are more than 200 biomarkers in exhaled breath of human among them isoprene is second most abundant VOC after acetone [30]. In human body isoprene has formed as a by product of cholesterol synthesis through mevalonic pathway [204-206]. Alteration of isoprene concentration in exhaled breath is an indication of lungs cancer [207], end-stage renal disease [208], liver disease patients with advanced fibrosis [209] and various condition of oxidative stress [210]. Thus sensitive, real time, low cost and effective detection of isoprene is important for non invasive detection of metabolic disorder, various disease conditions and possible screening of lungs cancer at early stage. Various approaches have been adopted for making sensors for isoprene, among them polymer nanocomposites based chemiresistive sensors have unique advantages over others in terms of their room temperature operation, flexibility and low cost .

Electrical conductivity and a responsive polymer phase are two most essential requirements for the development of chemiresistive sensors. Carbon nanotube (CNT) is one of the most electrically conducting allotrope of carbon and expected to have high potential in such applications [115]. Natural rubber latex is an aqueous colloidal dispersion of cis-polyisoprene and is widely used in production of gloves, catheters, rubber bands etc. Reversible and reproducible sensing response needs crosslinking of polymer matrix which can be achieved by different approaches, use of high energy radiation is one of them. Being an additive free tool, high energy radiation makes it possible to impart different crosslinking densities in a polymer matrix without affecting their chemical properties which are very much essential to get good sensing characteristics of chemiresistors.

This study reports synthesis of NR/CNT based nanocomposite chemiresistive matrix by CNT induced coagulation of NRL. Zeta potential study was conducted to investigate the CNT induced coagulation mechanism of NRL. High energy radiation was used to crosslink the nanocomposites. Dielectric and DMTA measurements were done to elucidate the effect of interaction between CNT and natural rubber matrix. The sensing response of radiation crosslinked chemiresistors was investigated against isoprene vapour.

3.2b. Materials and experimental method

3.2.1b. Materials

Natural rubber latex (NRL, 60phr) was procured from M/s TA Corporation, India. Multiple walled CNTs (unfunctionalized and hydroxyl functionalized (2.36-2.6 wt % CNT-OH), OD: 10-30 nm; Length: 1-2 μm SSA: 100-130 m^2/g) were purchased from Otto Chemie Pvt. Ltd, Mumbai India. Isoprene, acetone, methanol and ethanol used were of Analytical grade (purity >99.9%) and were procured from M/s SD Fine Chemicals, Mumbai.

Gamma chamber GC-5000 having Co-60 gamma radiation source, supplied by M/s BRIT, India having a dose rate of 8 kGy /hr as measured by Fricke dosimetry was used for irradiation purpose.

3.2.2b. Preparation of NRL/CNT composites:

Natural rubber/CNT nanocomposite was prepared by CNT induced coagulation of natural rubber latex (NRL). At first required amount of CNT was well dispersed in 1% ammonia solution by the aid of ultrasonication for 1hr. Sonication process was performed with horn sonicator (Oscar Ultrasonic processor, Mumbai) with a cylindrical tip (13 mm end cap diameter). The output power was fixed at 90 W. During sonication the beaker containing CNT was placed in an ice bath in order to prevent heating during the dispersion. Then NRL was added to this solution with constant stirring. Surface charge present in natural rubber particles interacts with CNTs and help to coagulated together to form nanocomposites (Figure 3.20). Then these coagulated nanocomposites were separated, cut into small pieces and dried for overnight at 60 °C under vacuum. The dried nanocomposites were compressed moulded at 150 kg/cm^2 at 100 °C into different thicknesses (100 µm–500 µm) with an area of 10 cm × 10 cm. Coagulated NR/CNT chemiresistors were cross-linked by exposing them to Co-60 gamma radiation in a gamma chamber (GC-5000) for desired absorbed dose. Table A2 in appendix summarises the composition of NR/CNT nanocomposites.

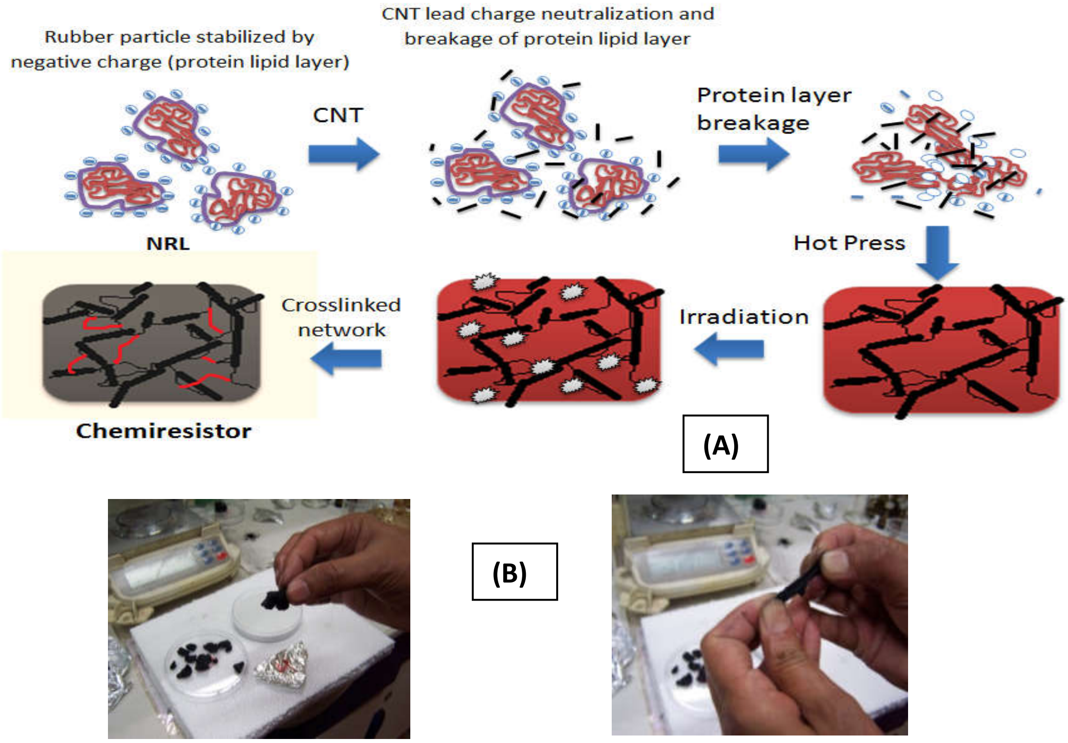

Figure 3.20: *(A) Schematic of NR/CNT nanocomposites preparation by CNT induced coagulation of natural rubber particles. (B) Pictures showing flexibility of composite.*

3.2.3b. AC and DC electrical conductivity and impedance analysis

For AC and DC conductivity measurement samples of circular disk shape with diameter of 10 mm were cut from compression moulded sheet. To ensure good electrical contact surfaces of the specimens were polished with 800-grit sandpaper and conductive silver paste was applied at both surfaces of samples. The DC conductivity of the samples was measured by standard two-probe electrode using a Keysight 34410A source meter at room temperature. For each composition, at least three specimens were tested. The impedance and AC conductivity measurements were conducted by HIOKI 3570 Impedance Analyzer (Japan) over the frequency range of 4 Hz–5 MHz. All measurements were performed at room temperature and relative humidity of 55%.

3.2.4b Dynamic mechanical analysis (DMTA)

DMTA measurements were performed on an MCR 102 Rheometer (Anton Paar, Austria) in SRF mode. Samples dimensions were 25 mm x 10 mm x 1.5 mm (l x b x t) for all samples. Temperature sweep was carried out in the temperature range. -100 to 30 ^{o}C at 3 ^{o}C /min heating rate at 1 Hz frequency and 1% strain.

3.2.5b. Dynamic and static vapour sensing

Dynamic flow measurements and static vapour setup were used to determine the sensing response of NR/CNT chemiresistor over a broad concentration range. The procedure was discussed in section 3.2.6a in details; instead of acetone isoprene was used as analyte vapour. The real-time chemiresistive response was tested against successive exposure of VOC vapours and nitrogen (background). The relative change in resistance ($A_r = \Delta R/R_o$) was recorded for different concentrations of isoprene. For static measurements, a fixed volume of the isoprene was placed in a 2 lit closed glass container with heating and homogenizer arrangement for the vapours.

3.3b. Results and Discussion

3.3.1b. Effects of CNT on coagulation process

Natural rubber latex is a suspension of rubber particles in water. It is composed of two phases; aqueous or serum phase contains water, some water soluble protein, carbohydrate and minerals while rubber phase contains cis-1,4-polyisoprene hydrocarbon chains which are surrounded by rubbery membrane and negatively charged protein phospholipid layer [211]. In current study the used NRL contains about 60% rubber hydrocarbon. Rubber particles are stabilized by negatively charged protein lipid bi-layer in colloidal suspension. Zeta potential of NRL in aqueous ammonia solution was found to be -91.3 mV. CNT neutralized the surface charge of NR particles leading to coagulation of natural rubber particles to form NR/CNT nanocomposites [212]. Figure 3.21 shows coagulated mass of nanocomposites as a function of CNT weight fraction. It is clear from the figure that the coagulated mass increases significantly beyond threshold CNT volume fraction of >0.014. After that there was a systematic increase in coagulated weight by further addition of CNT. Initially a minimum concentration of CNT is required to break the protein lipid layer and neutralize the surface charge of NR particles.

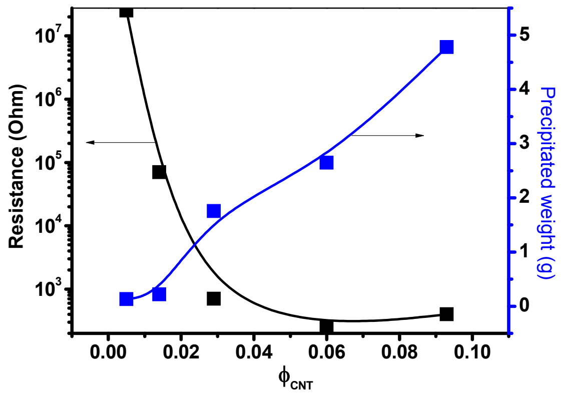

***Figure 3.21**: Variation of resistance and coagulated mass of nanocomposites as a function of CNT volume fraction.*

Once charge neutralization was completed CNT induced coagulation proceeds rapidly. Upto ϕ_{CNT} 0.014 the nanocomposite was acting as an insulator (resistance in mega ohm range). By further addition of CNT electrical resistance drops three orders of magnitude. It can be safely attributed that percolation of CNT to form a continuous networks happens in this region. Once percolation concentration of CNT was reached no significant change in resistance was observed on further addition of CNT.

Table 3.2: Zeta potential values of CNT, CNT-OH and NRL.

	Zeta potential (mV)	**Difference in zeta potential value from NRL (mV)**
CNT	4.38	95.68
Hydroxyl functionalized CNT(CNT-OH)	-50.8	40.5
Natural rubber latex	-91.3	-

To further gauge the effect of functional group in surface of CNT, hydroxyl functionalized CNT was also used for preparing nanocomposites. It was found that CNT-OH has failed to

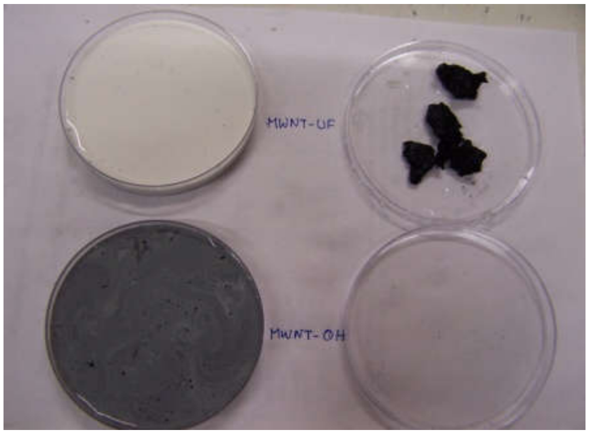

***Figure 3.22**: Pictures of unfuctionalized CNT induced coagulated nanocomposites(upper) and CNT-OH failed to coagulate natural rubber particles (lower).*

coagulate the natural rubber particles. Indeed difference in zeta potential (Table 3.2) with rubber latex is more for unfunctionalized CNT than CNT-OH, resulting efficient coagulation of natural rubber particles by unfunctionalized CNT. Figure 3.22 illustrate this fact, it can be seen that in case of unfunctionalized CNT almost all the rubber particles get coagulated by CNT whereas for CNT-OH almost all CNT-OH remains in aqueous phase.

3.3.2b. Electrical properties of nanocomposites

The variation of AC electrical conductivity at room temperature of NR/CNT nanocomposites as a function of frequency in the range of 4 Hz to 5 MHz for different CNT contained composites are shown in Figure 3.23A. Below ϕ_{CNT}=0.014 the nanocomposite shows frequency dependent conductivity, behaviour like insulator materials. However, above ϕ_{CNT} =0.014 nanocomposites shows frequency independent behaviour below a critical frequency (ω_c) after that frequency dependency observed. Furthermore, this critical frequency shifted towards higher values as CNT loading increases.

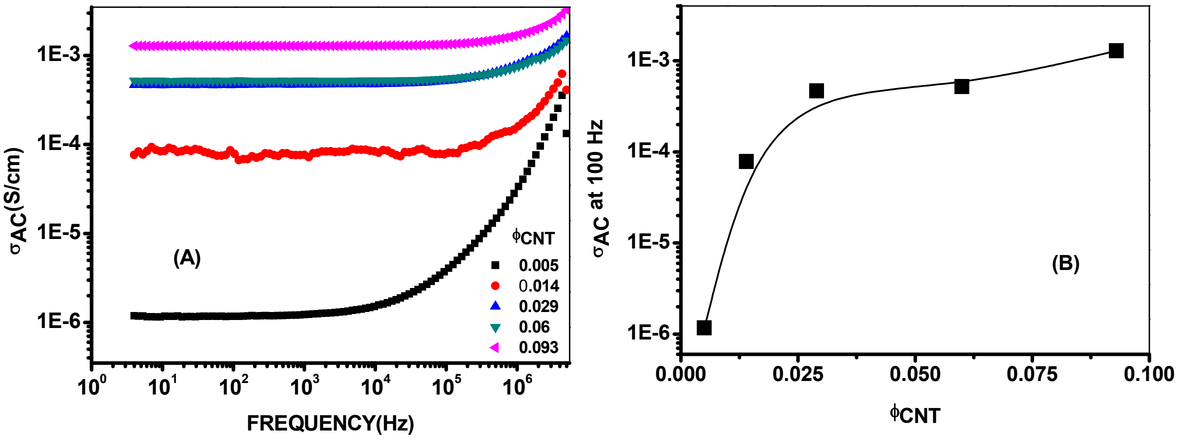

***Figure 3.23**: (A) AC electrical conductivity of NR/CNT nanocomposites with increasing frequency. (B) AC conductivity at 100 Hz as a function of CNT content.*

The frequency–independent behaviour at lower frequency region is a characteristic of a nondielectric behaviour of nanocomposite as the electron polarization is negligible in lower frequency. Similar kind of behaviour was observer by Barrau et al. for CNT–epoxy resin nanocomposites [213].

Low frequency conductivity which governs as DC conductivity found to increase with CNT fraction. Figure 3.23 B shows the AC conductivity at 100 Hz (low frequency) for different CNT loading. It can be seen that conductivity increase abruptly in the region of $\phi_{CNT}>0.014$. More than two decades of increase in conductivity was observed when ϕ_{CNT} increase from 0.005 to 0.03. This huge increase in conductivity has been anticipated in previous section as the formation of continuous conducting network of CNT in NR matrix. At this stage, the electrical conductivity of the nanocomposite was controlled by the conducting CNT networks. High aspect ratio and asymmetrical nature of CNT were mainly responsible for such a low percolation threshold. Note that symmetrical filler such as nano carbon black has relatively high percolation threshold values; this has been observed in FCE/NCB system.

The change in dielectric permittivity (ε') and loss permittivity (ε'') with frequency has been shown in Figure 3.24 A-B. It can be observed that dielectric permittivity increase with increase in ϕ_{CNT}. Such an increase in ε' was due to the presence of micro capacitor inside the matrix formed by conductive nanotubes domains [214]. With increase in frequency, ε' decrease due to the relaxation of permanent dipoles in nanocomposite. At higher frequency this dipole could not cope up with the change in electric field hence dipole relaxes and dielectric constant decrease. This decreased in ε' was very obvious in higher loading of CNT especially above percolation. Above percolation, the filler network hindered dipole orientation by reducing the segmental mobility of polymer chain, thus charge separation was reduced which eventually reduced the ε' value. Figure 3.24B shows loss permittivity (ε'') as a function of frequency for different NR/CNT nanocomposites. The loss permittivity increased with increase in ϕ_{CNT}. As the dielectric loss is an indicator of leakages through electron transport, hence it was expected that with increase in CNT loading dielectric loss will also increase.

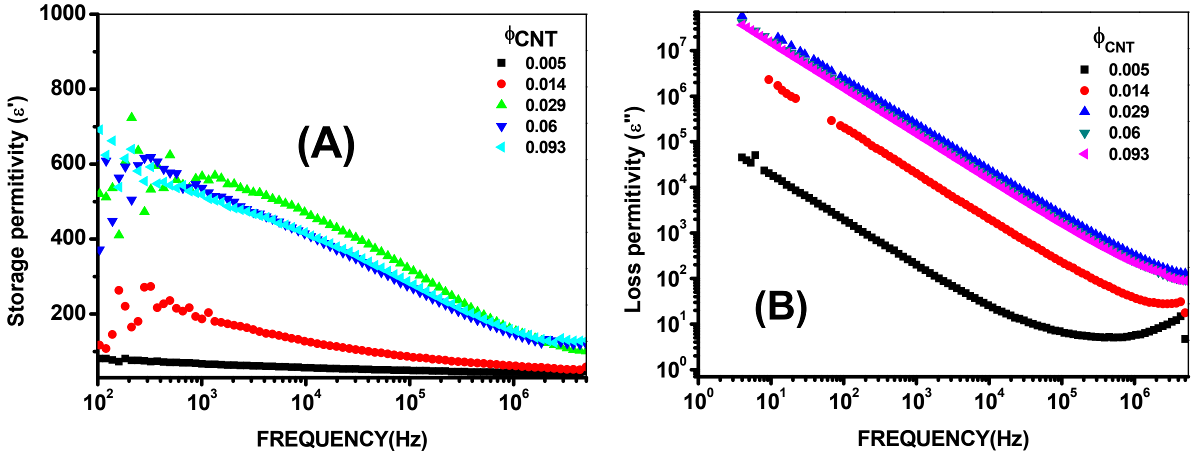

***Figure 3.24**: (A) Dielectric permittivity and (B) Loss permittivity as a function of frequency of NR/CNT nanocomposites.*

3.3.3b DMTA of NR/CNT nanocomposites

Figure 3.25 A-C shows temperature dependent storage modulus, loss modulus and loss factor (tan δ) of NR/CNT nanocomposites. It was found that CNT loading affects the dynamic modulus of the nanocomposites. With an increase in the CNT loading, the storage modulus increased while the intensity of loss factor decreased. In can also be seen that in the glassy region ($T < T_g$) the difference in the storage modulus of nanocompositeswith different CNT loading was not significant; however in the rubbery region ($T > T_g$) storage modulus increase with increase in CNT loading. At low temperature, modulus of nanocomposites mainly governs by polymer and not much effect of CNTs was observed in this region. So at low temperature all nanocomposites show more or less same modulus value. However, at higher temperature (T>T_g, rubbery region) more than three decades drops of storage modulus was observed for prinstine NR. In this region polymers become soft enough and can't overcome forces due to frinction between the CNTs [215]. In rubbery region increase in modulus with CNT loading was due to formation of percolated CNT-CNT network. The glass transition temperature was probed form peak of loss modulus curve. Unfilled NR shows glass transition at -61.5 °C which is suggestive of amorphous domain of polyisoprene segments [216].

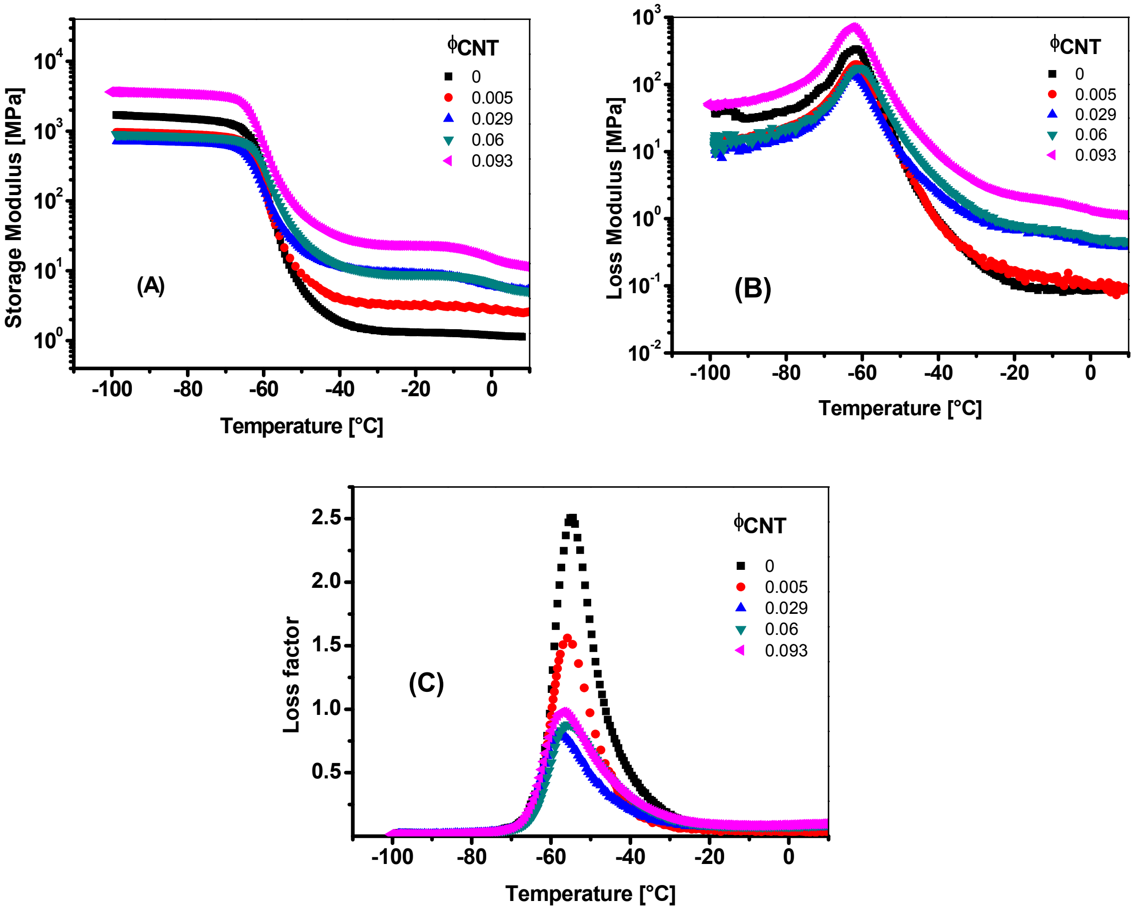

Figure 3.25: *(A) Storage modulus (B) Loss modulus and (C) Loss factor as a function of temperature for NR/CNT nanocomposites.*

It was observed that glass transition temperature didn't change much with addition of CNTs. But the intensity of tanδ decreased with increase in CNT loading (Figure 3.25 C). In nanocomposites system this decrease in loss factor with filler loading is an indication of interfacial interaction between polymer chain and filler. Because of the better interaction of polymer with filler the segmental motions of polymer chain near interface will reduced compare to bulk. Furthermore, formation of percolation networks of CNT-CNT also affects the segmental motion of polymer. Hence decrease in loss factor with CNT loading in NR/CNT nanocomposites system not only indicates better interfacial interaction between NR molecules with CNTs but also confirming the fact that CNT-CNT percolative network was formed in lower fraction of CNT which positively affects the sensing characteristics of nanocomposites based chemiresistors.

3.3.4b. Chemiresistive behaviour of NR/CNT nanocomposites

Figure 3.26 shows sensing response of irradiated NR/CNT (ϕ_{CNT} 0.03, 50 kGy) against 100 ppm of isoprene vapour under static condition. The chemiresistor was exposed to successive cycles of isoprene vapour and dry air and change in resistance (R/R_0) was monitored as sensing response with time. It can be observed that the relative resistance of chemiresistor increase when exposed to isoprene vapour and reversibly change back to original resistance when atmosphere changed to air. Completely reversible sensing response was obtained for 100 ppm isoprene vapour. Typically response time (90 % of the peak response, t_{90}) was found to be 35 sec, the resistance dropped rapidly to the half of the peak value t_{50} within 50 sec. The mechanism behind the change in the resistance in NR/CNT based conducting chemiresistors was that, upon exposed to isoprene vapour conducting network architecture get disturbed due to polymer chain relaxation induced chemiresistive stress generate in matrix, consequently resistance of chemiresistor increased. Conducting network of CNT reformed back while isoprene vapour was removed giving a reversible change in resistance.

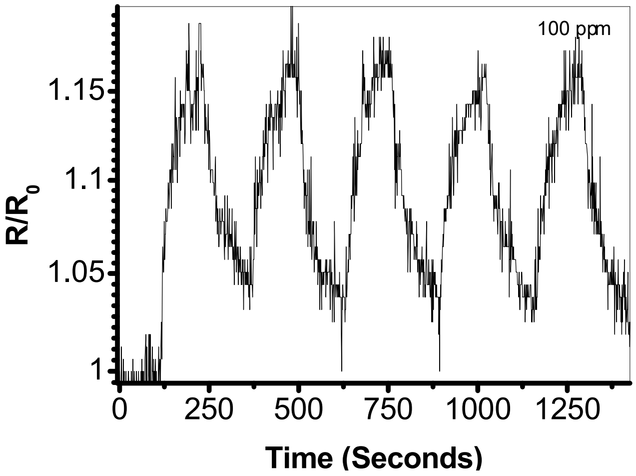

***Figure 3.26**: Sensing response of NR/CNT nanocomposites for 100 ppm isoprene vapour.*

Figure 3.27 A-B shows sensing response for increasing concentrations of isoprene under static condition. Sensing response was found to be linear with concentration of isoprene vapour. In CPC based chemiresistors often exponential increase in sensing response was obtained due to clustering of analyte vapours [217]. But in present study the chemiresistor was prepared by coagulating of NRL by CNTs, which have much higher aspect ratio than the conventional conducting filler such as carbon black and metallic powders. Due to the higher aspect ratio more long-range interconnectivity of conducting CNT-CNT junctions is possible in CNT based chemiresistors. Such an increased range of interconnectivity allows electrical conduction even at higher concentrations of the isoprene, and a linear chemiresistive response was observed over a wide concentration range. Sensitivity can be gauged from the slope the curve (3.27 B) and was found to be 8.8 ppm^{-1}. Detection limit of the NR/CNT chemiresistor was calculated by 3σ method and found to be 50 ppm.

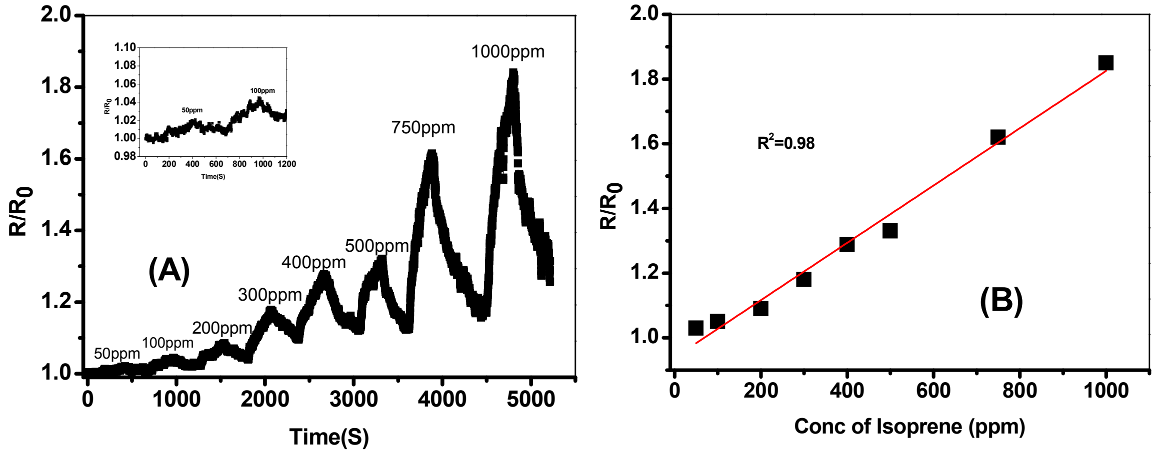

***Figure 3.27**: (A) Sensing response of NR/CNT nanocomposites for increasing concentration of isoprene (50-1000ppm). (B)Sensing response-concentration relationship for isoprene (red line depicts linear fitting).*

Selectivity and stability of sensor has been depicted in Figure 3.28 A and B. It can be seen that response for isoprene was about 3 folds higher than the response for methanol and almost 4 times higher than the response for water. Selectivity of CPC based chemiresistive sensors primarily depends upon interaction between the polymer chain and analytes. The magnitude of interaction between isoprene and natural rubber can be described by Flory-Huggins interaction parameter (χ_{12}). It was previously discussed that sensing response was inversely proportional to χ_{12} and related by the equation 3.9. As natural rubbers are basically cis-1,4 poly isoprene thus solubility parameters of natural rubber and isoprene are near to each other. This low value of χ_{12} between NR and isoprene was primarily responsible for observing maximum sensing response towards isoprene compare to other analytes. Stability of sensing response was tested under 50% diluted isoprene vapour under dynamic setup and shown in Figure 3.28 B. It can be seen that the sensing response remain stable for 30 min under vapour condition , only less that 10 % decrease in sensing response was observed after 30 min.

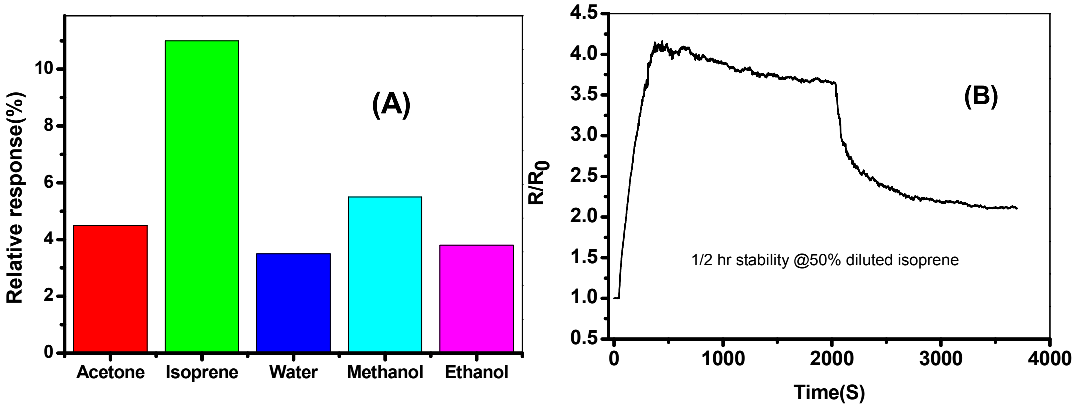

***Figure 3.28**: (A) Selectivity of NR/CNT chemiresistors towards different analyte vapours (100 ppm). (B) Stability of sesning response for 30 min under 50% diluted isoprene vapour in dynamic setup.*

3.4b. Conclusions

Radiation crosslinked NR/CNT nanocomposite based chemiresistor can be useful in designing reversible chemiresistive sensor for the real-time detection of Isoprene. Surface functionality of CNT played a crucial role to destabilize the natural rubber latex and by breaking the lipid layer help coagulation process to form NR/CNT composites. Zeta potential measurement of NR particles and CNTs help to understand the underlying mechanism behind the coagulation method. The ac and dc electrical properties of nanocomposites reveal that percolation of CNT occurs at very low loading of CNT and conductivity of composites shows power law dependence on CNT loading. The radiation crosslinked coagulated NR/CNT nanocomposties were able to show sensitive, selective and linear response for isoprene vapour. Detection limit and sensitivity of the chmiresistors were found to be 50 ppm and 8.8 ppm^{-1} respectively. It was also found that sensing response has a strong correlation with Flory-Huggins interaction parameter (χ_{12}).

3c. Polyvinyl Butyral (PVB)/CNT nanocomposite based chemiresistor for ethanol sensor:

3.1c. Introduction

Alcoholism and driving under the influence of alcohol causes fatal injuries and sometimes death. Drinking and driving is a crime under law also. Ethanol is a major breakdown fermented product of high carbohydrate containing food such as grain, potato, fruits etc [218]. Therefore, sensitive, real time low cost and room temperature ethanol detection is of prime interest now days [219]. In general metal oxide semiconductor based sensors [219, 220], capacitive sensors[221] and gas chromatography [222, 223] have been used for sensitive detection of ethanol. But all these sensors have inherent disadvantages. There is some literature reports which used acid or oxide doped intrinsic conducting polymer based sensor for alcohol detection [224, 225]. Stewart at al. have used NiO and ZnO doped poly (2,5-dimethyl aniline) as radio frequency identification (RFID) sensor for transdermal ethanol detection [226]. In another work Kar et al. have reported room temperature sensing characteristics of sulphuric acid doped poly (m-aminophenol) for aliphatic alcohol [227].

However, conducting polymer composites (CPC) based VOC sensors have attract much more attention due to some inherent advantages such as simple formulation based properties adjustment, flexibilities in terms of shapes and geometry, easy processing and room temperature operations. Here in this study reports polyvinyl butyral and CNT based melt processed conducting nanocomposites based chemiresistive sensors for room temperature detection of ethanol vapours. Electrical conductivity and rheological studies were conducting in order to fully characterize the as prepared nanoconposites in terms of electronic conducting mechanism in nanocomposites. Rheological study gives an insight to CNT-CNT network formation and wrapping of CNTs with polymer molecules which gives much enhanced chemiresistivity towards ethanol vapours. Crosslinking of nanocomposites was found to improve sensing characteristics.

3.2c. Materials and experimental method

3.2.1c. Materials

Polyvinyl butyral (PVB) and vinyl trimethoxy silane (VTMS) were obtained from Sigma Aldrich. Multiple walled CNT (OD: 10-30 nm; Length: 1-2 μm SSA: 100-130 m^2/g) was purchased from Otto Chemie Pvt. Ltd, Mumbai India. Ethanol, acetone, methanol and ethanol used were of Analytical grade (purity >99.9%) and were procured from M/s SD Fine Chemicals, Mumbai.

3.2.2c. Preparation of PVB/CNT nanocomposites:

PVB/CNT nanocomposites were prepared by melt compounding method. Different amount of CNT and PVB were taken considering their bulk density and was mixed homogenously in Brabender plasticordar at 180 ^oC, 30 rpm for 20 min. During mixing VTMS was added to crosslink the matrix [228]. The PVB modified with VTMS was compression moulded to different thickness in a hydraulic press at 150 kg/cm^2 for 10 min. Then, the sheets were stored in an atmosphere saturated with moisture at 60 ^oC to complete the crosslinking process. Table A3 in appendix summarises the composition of PVB/CNT nanocomposites.

3.2.3c. AC and DC electrical conductivity study

AC and DC conductivity of nanocomposites were measured with sample of circular disk (diameter 15 mm). DC resistance was measured using Keysight 34410A multimeter and for AC conductivity measurement HIOKI 3570 Impedance Analyzer (Japan) was used over a frequency range of 4 Hz-5 MHz. All measurements were performed at room temperature and relative humidity of 55%.

3.2.4c. Rheological measurement

Rheology measurements were performed on an MCR 102 Rheometer (Anton Paar, Austria) using parallel plate fixture of 25 mm diameter. All measurements were conducted in the linear viscoelastic regime. Frequency sweep study was conducted over 500-0.1 rad/s frequency range with shear strain of 1 % at 180 ^{o}C temperature. Nitrogen atmosphere was maintained to avoid oxidative degradation of samples during experiments.

3.2.5c. Dynamic and static vapour sensing

Dynamic flow measurements and static vapour setup were used to determine the sensing response of chemiresistor over a broad concentration range. The procedure was discussed in section 3.2.6a in details. Here ethanol vapour was used instead of acetone. The real-time chemiresistive response was tested against successive exposure of VOC vapours and nitrogen (background). The relative change in resistance ($A_r = \Delta R/R_o$) was recorded for different concentrations.

3.3c. Results and Discussion

3.3.1c. AC and DC electrical properties of nanocomposites

Optical and electron microscopies are often unable to identify the state of dispersions of CNT in polymer nanocomposites. Due to the extreme differences in carbon nanotubes radial and axial dimensions and their complex shapes, it is difficult to observe an entire CNT and distinguish between CNTs [179]. Electrical properties measurement however gives an insight of CNT networks formation, dispersion of CNTs into polymer matrix and electron conduction mechanism of nanocomposite. DC electrical conductivity as a function of CNT loading has been shown in Figure 3.29. DC conductivity was observed to increase with increase in CNT loading. Upto ϕ_{CNT}=0.017 no significant change in DC conductivity was observed after that conductivity suddenly increase by four order of magnitude (~10^4) by increasing the ϕ_{CNT} to 0.034.

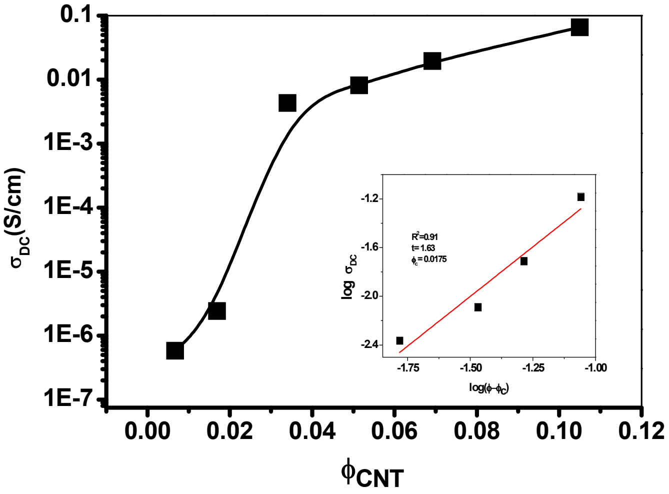

Figure 3.29*: DC electrical conductivity of PVB/CNT nanocomposites. Inset: log-log fitting of σ_{DC} vs(ϕ_f-ϕ_c)for same composites, straight line represents best fit line of data in equation 3.6.*

This sudden increase in DC conductivity is an indication of formation of percolating network by CNT in PVB matrix. DC conductivity values fitted well in equation 3.6 (inset of Figure 3.29) giving percolation threshold ϕ_c and t as 0.0175 and 1.63 respectively. Exceptionally low percolation threshold of CNT indicates excellent dispersion of CNTs in PVB matrix. In percolation theory the value of t reflects dimensionality of conducting networks. In general, the value of t in between 1.6-2.0 reflects 3D conducting network formation [229]. For PVB/CNT nanocomposites t value of 1.63 suggests that 3D percolation network formation and the formed percolation networks associated with less amount of "dead ends" [229, 230].

It is understood that in conducting polymer composites electrical conductivity is limited upto a certain limit due to wrapping of CNT by polymer chains. These wrapped polymer chains act as a potential barrier to inter-nanotube hopping and/or tunnelling of electrons, limiting the electrical conductivity. There are several literatures that discussed about the tunnelling mechanism in polymer–CNT nanocomposites [229, 231, 232]. The conductivity due to tunnelling of electron in nanocomposite system can be expressed as

$$\sigma_{DC} \propto \exp(-AD) \tag{3.10}$$

where, A is tunnel parameter and D represents tunnelling distance. Assuming that the polymer is homogeneous in nature and for a random distributed CNTs tunnelling distance among nanotube will be proportional to $\phi^{-1/3}$[231]. Figure 3.30 shows the experimental data fitting well in equation 3.10. Good agreement of the experimental data with above equation suggest that the presence of tunnelling conductivity in PVB/CNT nanocomposites.

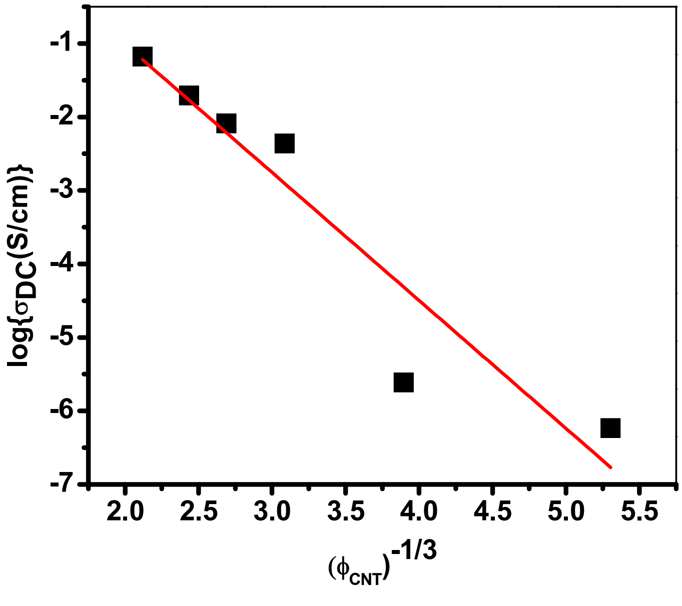

Figure 3.30*: Linear variation of log(σ_{DC}) vs $\phi^{-1/3}$for PVB/CNT nanocomposites. Red line depicts linear fitting of expt data in equation 3.10.*

The variation of AC electrical conductivity at room temperature has been shown in Figure 3.31 for PVB/CNT nanocomposites as a function of frequency in the range of 4 Hz to 5 MHz. The figure shows a gradual increase in AC conductivity with increase in frequency for CNT loading upto 0.017 (ϕ_{CNT}=0.017), reflecting a typical insulator like behaviour. After that a drastic increase in conductivity was observed at low frequency, confirming the formation of percolation network by CNT as discussed in previous paragraph. Nanocomposites beyond percolation concentration of CNTs show more or less similar behaviour, a plateau at lower frequency followed by frequency dependent increase in conductivity after a critical frequency. Additionally this critical frequency shifted towards higher values with increase in CNT concentration in nanocomposites, because at higher frequency dipoles gets less time to orient themselves makes polarization effect insignificants.

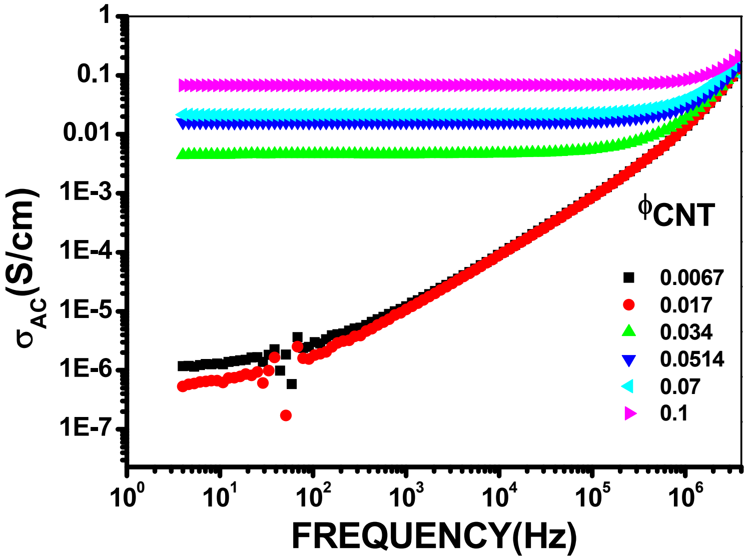

***Figure 3.31**: AC conductivity of PVB/CNT composites as a function of frequency.*

3.3.2c. Rheological properties of nanocomposites

Rheological study of pure PVB and PVB/CNT nanocomposites were performed in order to probe critical information about interaction of polymers and fillers interaction and formation of filler-filler networks regardless of electrical conductivity. This polymer chain and filler interactions have positive affects in chemiresistivity of chemiresistors [233]. Figure 3.32 shows complex viscosity of PVB/CNT nanocomposites with angular frequency (ω) for different loading of CNTs. All nanocomposites show frequency dependent viscosity, but with CNT addition the frequency dependency increase specially at low frequency. Pristine polymer shows typical Newtonian plateau at low frequency but this plateau diminishes as CNT loading increase. For pure PVB and nancomposites upto ϕ_{CNT} 0.017 there was hardly any differences in complex viscosity value at 0.1 rad/s frequency while complex viscosity increases rapidly as CNT loading increase further highlighting reinforcing effect of CNTs in nanocomposites [234, 235].

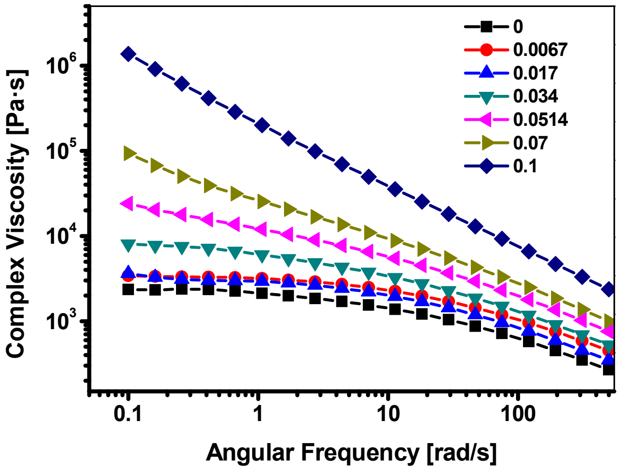

***Figure 3.32**: Complex viscosity of PVB/CNT nanocomposites for different loading of CNT with angular frequency at 180 °C.*

Regardless of electrical properties measurement CNT-CNT network formation was also probed by measuring storage modulus (G') and loss modulus (G") as a function of angular frequency and showed in Figure 3.33. Both storage as well as loss modulus increases with increase in frequency and CNT loading. As CNT loading increases the frequency dependency decease for both storage and loss modulus but the effect was more obvious for storage modulus than loss modulus. Pure and uncrosslinked polymers said to have typical terminal region with viscoelastic behaviour. The slope of G' and G" at terminal region can be given by 2 and 1 respectively ($G' \propto \omega^2$ and $G'' \propto \omega^1$). With increase in CNT more solid like behaviour emerges and that was reflected by decrease in slope for both G' and G". Slopes of G' and G" are listed for in Table 3.3 for different nanocomposites.

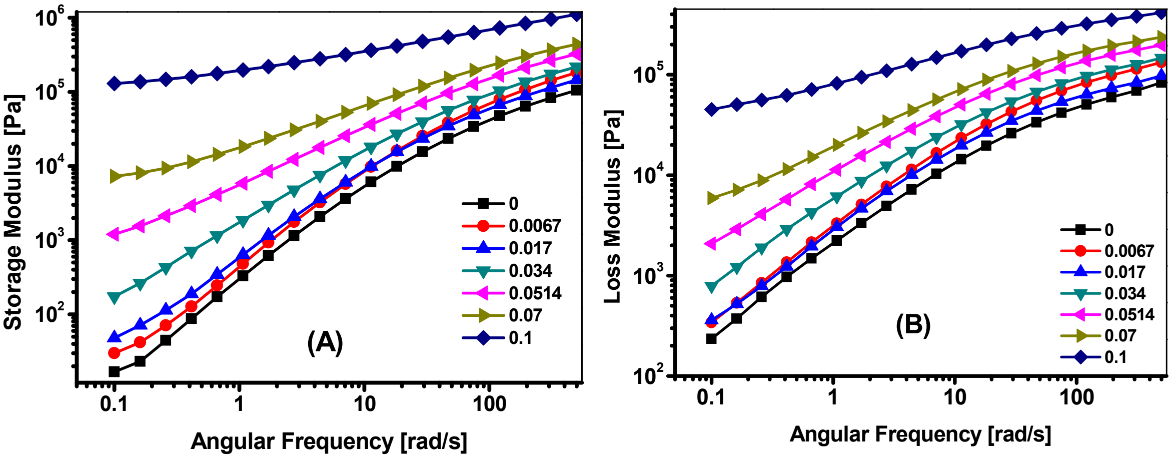

***Figure 3.33**: (A) Storage modulus and (B) Loss modulus as a function of angular frequency for PVB/CNT nanocomposites at 180 °C.*

Table 3.3: Slopes of storage and loss modulus at terminal region of PVB/CNT nanocomposites.

CNT volume fraction (ϕ_{CNT})	Slope of G′	Slope of G"
0	1.266	0.98
0.0067	1.22	0.97
0.017	1.03	0.89
0.034	1.01	0.89
0.0514	0.65	0.72
0.07	0.36	0.49
0.1	0.16	0.24

The slopes of pure PVB are 1.266 and 0.98 for storage and loss modulus respectively. The values did not change much in ϕ_{CNT}= 0.0067composites suggesting CNT network was still not formed and liquid like behaviour of polymer was still there. When ϕ_{CNT} reaches to 0.017 drastic decreases in slope for both G’ and G” was observed. This decrease in slope highlights the formation of CNT-CNT network in nanocomposite which was previously anticipated in electrical conductivity measurements. Indeed at a critical concentration of CNT the significant decrease in frequency dependency of modulus value due to the formation of CNT-CNT network is known as rheological percolation [236].

3.3.3c. Chemiresistive behaviour of PVB/CNT nanocomposites

Figure 3.34 shows sensing response of PVB/CNT (ϕ_{CNT}=0.1) against 50% diluted ethanol vapour under dynamic condition. The chemiresistor was exposed to successive cycles of ethanol vapour and dry nitrogen and relative change of resistance ($\Delta R/R_0$) was monitored as sensing response with time. Rapid change in resistance was observed once the chemiresistor exposed to ethanol vapour and resistance decrease almost instantaneously when ethanol vapour was removed. This phenomenon is often called positive vapour coefficient (PVC) [162]. Sensing responses were found to be reversible and reproducible for successive cycles of ethanol and dry nitrogen. Response time which was gauged from 50% change in relative resistance was obtained in 40 sec, 90% change in relative resistance was in 65 sec. While recovery time was found to be 20 sec for 50% change of base resistance (t_{50}) and 80 sec for 90% change of base resistance (t_{90}). It is noteworthy that response time found for current system is less compare to other metal oxide based ethanol sensors [237]. Crosslinking of polymer matrix is crucial in order to get reversible and stable response for VOCs [238]. Crosslinked ϕ_{CNT}=0.1 chemiresistor shows 170% change in resistance for 50% diluted ethanol vapour. Figure 3.35 A shows sensing characteristics of uncrosslinked chemiresistors. It can be seen that though response was high for uncrosslinked chemiresistor (~ 260% for 50% diluted ethanol vapour) but the responses of successive cycles are too non reproducible.

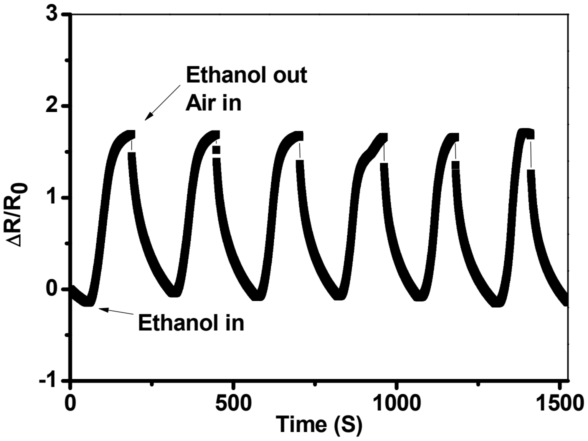

Figure 3.34: *Sensing response of crosslinked PVB/CNT (ϕ_{CNT}=0.1) nanocomposites for 50% diluted ethanol vapour.*

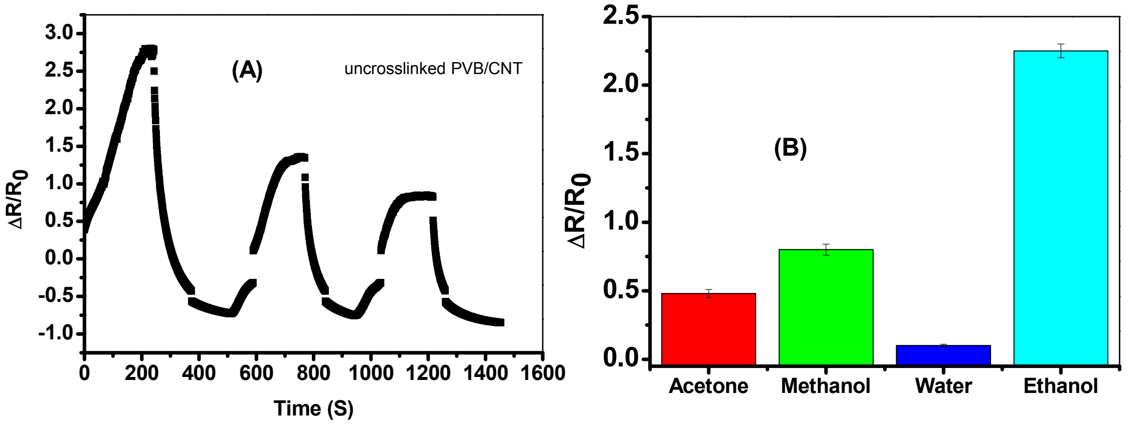

***Figure 3.35**: (A) Sensing response of uncrosslinked PVB/CNT chemiresistors. (B) Selectivity of PVB/CBT chemiresistors for 50 % diluted vapor.*

In presence of analyte vapours under chemiresistive stress PVB chain relaxes. The relaxation of polymer chains result an increase in inters CNT distances, leading to increase in resistivity of chemiresistor matrix. Crosslinking of matrix ensures reversibility of this mechanism when analyte vapours were removed. Since un-crosslinked matrix don't have the inter-molecular linkage, thus once deformed they don't restore back to original position giving non reproducible response towards analyte vapours.

Discrimination of different vapour, known as selectivity is an important aspect for chemiresistive sensors. Selectivity of chemiresistors was evaluated by determining sensing responses of different kind of VOCs having different polarity and interaction with polymer chain. In this study water, methanol and acetone were chosen for this purpose. It was found that selectivity of PVB/CNT follows the order ethanol > methanol > acetone > water (Figure 3.35B). Selectivity of CPC based chemiresistive sensors primarily depends upon interaction between the polymer chain and analytes. The interaction between polymer and analyte molecules can be gauged from Flory-Huggins interaction parameter (χ_{12}). Previously it was discussed that the sensing response for a particular analyte was inversely proportional with χ_{12} i.e. sensing response was high for the analyte having low χ_{12} value with PVB. Again χ_{12} depends upon solubility parameter of polymer and solvent vapour (equation 3.2). Total solubility parameter (δ_T) consist of three different types of intermolecular interaction in molecules. They are dispersive (δ_d), polar (δ_p) and hydrogen bonds (δ_H). Each of these interactions play vital role in controlling the diffusion of vapours and hence sensing responses. Thus it can be attributed that CPC having polar polymer gives better response for polar vapours where as CPC with nonpolar polymer gives better results for nonpolar vapours [239, 240]. Table 3.4 summarises Hildebrand solubility parameters for different solvents and PVB polymer. It can be found that total Hildebrand solubility parameter (δ_T) for PVB is close to ethanol than methanol and water thus sensing response for ethanol is high compare to methanol and water which is coherent with experimental observation.

Table 3.4: Solubility parameters of VOCs and PVB polymer [241].

Solvents	**δ_d (MPa$^{1/2}$)**	**δ_p (MPa$^{1/2}$)**	**δ_H (MPa$^{1/2}$)**	**δ_T (MPa$^{1/2}$)**
Ethanol	15.8	8.8	19.4	26.6
Methanol	29.6	15.1	12.3	37.9
Water	15.5	16	42.4	47.9
Acetone	15.5	10.4	7	19.9
PVB	15.5	6.5	10.4	19.7

δ_d :energy from dispersion bonds between molecules.

δ_p :energy from polar bonds between molecules.

δ_H :energy from hydrogen bonds between molecules.

δ_T :total energy from bonds between molecules can be calculated from following equation

$$\delta_T^2 = \delta_d^2 + \delta_p^2 + \delta_H^2 \qquad \textbf{(3.11)}$$

However, selectivity for acetone was less though δ_T of acetone is 19.9 and that for PVB is 19.7 whereas for ethanol it is 26.6. Such types of behaviour were also reported by Castro et al. and Bouvree et al [78, 242]. Formation H-bonding between PVB molecules and ethanol may be the reason for such a discrepancy in selectivity. Indeed for ethanol molecule formation of H-bonding is far more effective than acetone which helps better diffusion of ethanol molecules and swelling of polymer chain consequently disturbing the electron conduction in chemiresistor matrix. Based on this observation sensing mechanism of PVB/CNT for ethanol vapour and higher selectivity towards ethanol compare to other analytes can be represented as Figure 3.36.

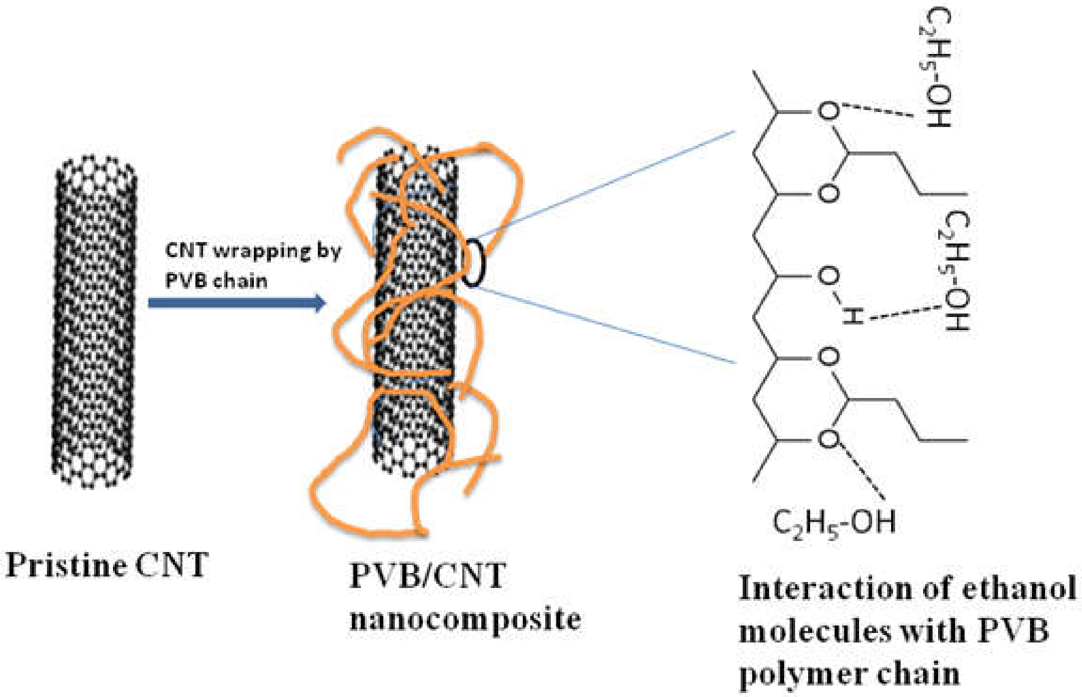

Figure 3.36: *Schematic representation of sensing mechanism of PVB/CNT nanocomposites.*

3.4c Conclusions

Poly vinyl butyral (PVB)/CNT nanocomposites were prepared by solvent free melt compounding methods. These nanocomposites were characterized by frequency dependent AC and DC electrical conductivity and rheological measurement. Electrical studies revealed that extremely low percolation threshold of CNTs in PVB matrix and also give critical information about electron tunnelling mechanism in nanocomposites. Reinforcing effect of CNT was confirmed from complex modulus measurement in rheological study. Furthermore, rapid increase in storage and loss modulus and less dependency of these parameters with frequency corroborate formation of CNT-CNT network at extremely low concentration of CNT in nanocomposites. These PVB/CNT based CPC gives sensitive, selective and rapid sensing response towards ethanol vapour at room temperature. It was also found that crosslinking of matrix is essential in order to obtain stable and reproducible sensing response. Various interactions of analytes and polymer have a strong dependence on chemo-electrical behaviour of chemiresistors and that in turn tune the selectivity of matrix.

CHAPTER 4

Hybrid Nanocarbon black and Carbon nanotube based Conducting Polymeric Nanocomposites for detection of aromatic hydrocarbon.

4.1. Introduction

Detection of VOCs like benzene, toluene, ethyl benzene and xylene (BTEX) is of utmost interest in order to avoid negative health effects on human and reduce environmental pollution associated with them [243, 244]. Some members of BTEX family have been identified as toxic, carcinogenic and mutagenic at low concentration level. Apart from that exposure of BTEX produces several health effects such as irritation to skin and sensory organs, CNS break down, dizziness, memory loss, and respiratory problem [3, 5, 245]. Especially benzene have been identified as type I carcinogenic compound and likely to be responsible for myeloid leukaemia [246]. The main sources of BTEX into the environment are the petroleum, chemical industries, rubber industries, leather industries paints etc. Cigarette smoke is mainly responsible for indoor concentration of BTEX. They are also reported in exhaust gases of vehicles as a incomplete combustion of fossil fuels. Thus there is an obvious need to develop a fast, responsive and low cost BTEX detection system to counter health consequences and protect environment [247-249].

Till date various sensing approaches are adopted for detection of BTEX vapour [250-253]. Among them CPC based chemiresistive sensors have attracted much attention due to some inherent advantages such as low cost, portability, low power consumption etc. Many scientific groups have reported usefulness of hybrid nano carbon based chemiresistive sensors for BTEX and other VOCs [133, 134]. However all these studies have relied on intrinsic properties of hybrid filler and not much work is reported on the hybrid nanocarbons/ polymer nanocomposites based sensors. It is well understood that hybrid fillers in a polymer matrix might provide unique opportunity of controlling the CNT network and inter-tube connections and thus could be a route of designing advanced chemiresistors with improved detection range, sensitivity and detection limit.

Environmental friendly methods like melt and shear compounding for preparing polymer composites don't involve any solvents but electrical percolation threshold of conducting filler in compounding techniques is much higher than other techniques like in-situ polymerization and solvent assisted dispersion. With the use of nanofiller, the amount typically required to develop conducting composites has come down drastically however, there are still a major hurdle in terms of process efficacy, stable conductivity and reproducible response. Synergistic advantages in terms of enhanced conductivity and mechanical properties can be achievable by judicial choice of hybrid nanofillers and selective percolation of fillers. Prasad et al. have reported exceptional synergy between the uses of nanocarbons [254]. Dubey et al. have reported advantages of hybrid fillers and selective percolation in terms of better electromechanical response, higher conductivity, mechanical properties and positive temperature coefficient behaviour [189, 255, 256]. However, little is understood how two geometrically different nanofillers would affect the sensing response of a chemiresistive matrix. Further, little attention has been paid to utilize solvent free polymer processing technologies that are energy efficient and can be easily up-scaled.

Poly(dimethylsiloxane) (PDMS) is an elastomeric matrix and can be easily processed. It has good temperature and chemical resistance while it is also biocompatible in nature. PDMS widely used for electronic and biomedical applications [257-259]. PDMS and CNT based flow injection micro fluid device has been reported by Karuwan et al. [260]. In another work PDMS and CNT based DNA sensor has been reported by Juwan et al. [261]. However, there is little research on the chemiresistive response of PDMS/nanocarbon nanocomposites particularly via a solvent free route.

Current study reports development of CNT and NCB based hybrid filler contained PDMS nanocomposites based chemiresistive BTEX sensor. These nanaocomposites were prepared by shear conmpounding techniques and crosslinked by using high energy gamma radiation. FE SEM was used in order to characterize morphology of nanocompoiste materials. Polymer-BTEX interaction and BTEX diffusion behaviours were elucidated to understand sensing behaviour of irradiated composites. The effect of CNT addition into sensing response was also investigated.

4.2. Preparation of PDMS/NCB/CNT hybrid chemiresistors:

4.2.1. Materials

Carbon nanotube (CNT) (Multiple walled, OD: 8-20 nm; Length: 1-2 μm specific surface area: 130-180 m^2/g) was procured from Otto Chemie Pvt Ltd, Mumbai India. Nano carbon black (NCB) (size 50nm, specific surface area 70 m^2/g, and density 1.8g/cc) was purchased from M/s TA Corporation, Mumai, India. PDMS (Hardness = 60; density = 1.13 ± 0.05 g/cc, containing vulcanizator 2,5-dimethyl-2,5-bis(tert-butyl peroxy) hexane (0.65%)) was procured from M/s DJ silicone, China. Benzene, Toluene, Xylene and Ethyl benzene used were procured from M/s SD Fine chemicals, Mumbai and used without further purification.

4.2.2. Preparation of nanocomposites

Electrically conducting PDMS/NCB/CNT nanocomposites were prepared according to the composition given in table no 4.1. In brief PDMS/NCB composite with 30wt% of NCB was prepared as master batch through shear compounding method in Brabender Plasticordar. Then required amounts of CNT were added in to this master batch to get composites of 1,2 and 3 wt% of CNT. Mixing was done at 120 ^oC temperature for 20 mins at screw speed of 30 rpm. Amount of components were carefully chosen in order to completely fill 40 cc volume of mixture. The so obtained homogeneous mixture was cut into small pieces and compressed moulded into 10 x 10 cm^2 of 100 micron thick sheets using a compression moulded machine at 150 kg/ cm^2 for 30 min at 120 ^oC .

Table 4.1: Composition of PDMS/NCB/CNT nanocomposites.

Composition	Wt % of PDMS	Wt% of NCB	Wt % of CNT
M0	70	30	0
M1	69	30	1
M2	68	30	2
M3	67	30	3

4.2.3. Irradiation of nanocomposites

Irradiation was carried out under aerated condition using a gamma chamber 5000 (GC-5000) having Co-60 gamma source supplied by M/s BRIT, India. The dose rate of the gamma chamber was ascertained to be 1.0 kGy/h using Fricke dosimetry prior to irradiation of samples.

4.3. Characterization of nanocomposites:

4.3.1. Mechanical, electromechanical and crosslinking density evaluation

The tensile strength and elongation at break of nanocomposites were measured using a universal testing machine of M/s Hemetek, MUMBAI, India at crosshead speed of 100 mm/min at room temperature. During electromechanical measurement uniaxial strain was applied to the nanocomposites and electrical resistance of the nanocomposites was measured via a computer coupled multimeter having data acquisition rate of 0.5 sec^{-1}. The electrical contacts were made by applying conducting pastes on both ends of the samples.

To elucidate crosslinking density, radiation cross-linked nanocomposites were Soxhlet extracted for 12 h to extract any sol content using xylene as a solvent. The insoluble gel part was then dried initially under room conditions and later under vacuum at 40 ^{o}C. The dried composites so obtained was cut into uniform square pieces (1 cm x 1 cm) using a sharp edged die and used for swelling studies. Pre-weighed samples were placed in a 200-mesh stainless steel compartment and immersed in xylene. The swollen samples were periodically removed, blotted free of surface solvent using laboratory tissue paper, weighed on an analytical balance (accuracy 0.00001 g) from M/s AND, India, in stopper bottles and returned to the swelling medium. Measurements were taken until the samples reached constant weight (equilibrium swelling).

The crosslinking density was determined by estimating the molecular weight between cross-links (M_c) using Flory and Rehner relation. The procedure has been discussed in details in chapter 3.

4.3.2. Morphological study by Field Emission Scanning Electron Microscopy (FE-SEM)

Morphological analyses of cryo-fracture nanocomposites were determined by Field Emission Scanning Electron Microscopy (FE-SEM). FE-SEM studies were done using Zeiss Ultra 55 FE-SEM with acceleration voltage of 5 kV.

4.3.3. AC and DC electrical conductivity and temperature coefficient of resistivity

For AC and DC electrical conductivity measurement was conducted with disk (15 mm dia) shaped samples. DC conductivity of the samples was measured by recording the resistance of the samples by using a four-probe arrangement. For the samples having resistance higher than 10^6 ohm, a mega ohm meter was used. AC conductivity was measured by using a HIOKI 3570 Impedance Analyzer (Japan) over the frequency range of 4 Hz–5 MHz. All measurements were performed at 25 ^{o}C and relative humidity of 55%. Temperature coefficient on resistivity of nanocomposites was measured in a four probe setup with controlled heating arrangement.

4.3.4. Dynamic and static measurements of BTEX

Sensing characteristic of hybrid chemiresistors have been evaluated by using static as well as dynamic vapour setup as discussed in chapter 2. Real time sensing response was obtained by cyclic exposure of BTEX vapour and nitrogen for two minutes cycles. Sensing response was determined as the relative change in resistance ($A_r = \Delta R/R_o$) over exposure to analyte vapours. To obtain vapour pressure independent response, sensing response of each analyte was normalized with respect to vapour pressure and expressed as concentration normalized response (CNR= A_r/C). For static measurements, a fixed volume of the BTEX was placed in a 2 litre closed glass container with heating and fan arrangement for the rapid homogenization of BTEX vapours. The relative change in resistance ($A_r = \Delta R/R_o$) was recorded for different concentrations of different analytes.

4.4. Results and Discussion:

4.4.1. Mechanical and Electrical properties of PDMS/NCB/CNT nanocomposites

4.4.1.1. Effect of radiation dose on mechanical properties and crosslinking density

Different irradiation doses were employed to crosslink the PDMS matrix to have different extent of crosslinking in the matrix. Elastic modulus of the PDMS/NCB 30 nanocomposites containing different weight fraction of CNTs is shown in Figure 4.1 for different radiation doses. It can be seen that at 50 kGy the elastic modulus is lowest for all the nanocomposites whereas it was highest for 200 kGy. This increase in elastic modulus can be attributed to the increase in crosslink density of PDMS matrix with radiation dose, leading to increase in the resistance to tensile deformation [262]. In aerated condition PDMS get crosslinked by high energy gamma radiation through both H-type and Y-type mechanism [263].

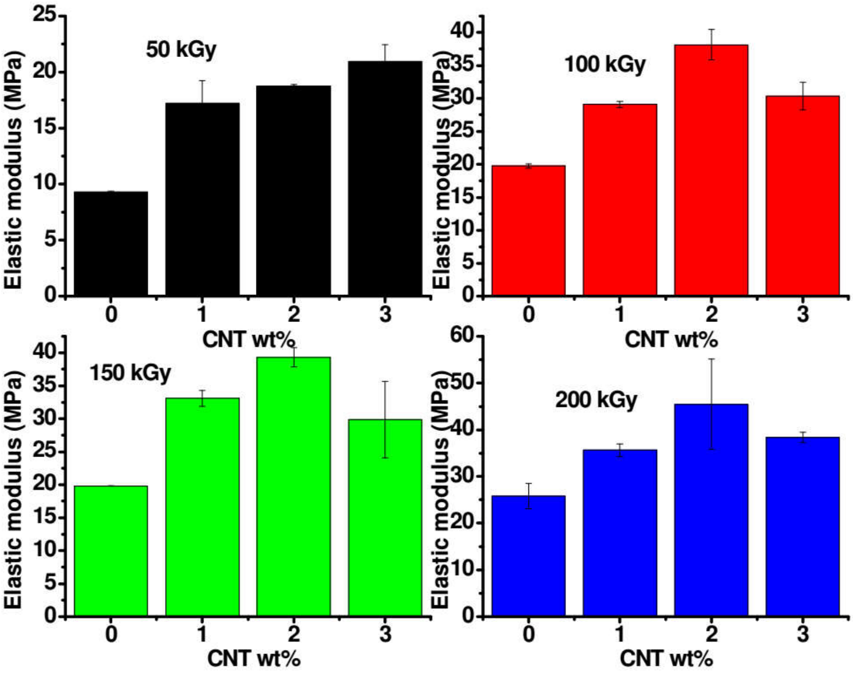

Figure 4.1: Elastic modulus of the PDMS/NCB 30 nanocomposites containing different fractions of CNTs at different radiation doses.

With increase in CNT content the elastic modulus increased for all radiation doses. For all the doses except 50 kGy, the elastic modulus showed an increase up to 2 wt% CNT and decrease at higher fraction. This variation in trend with increase in radiation dose can be attributed to formation of graft networks at filler and polymer interface. From stress- strain graph it is clear that addition of CNT increases modulus of matrix and decrease elongation at break decrease (Figure 4.2). Increase in modulus with CNT may be attributed the formation of higher number of physical crosslinking network with polymer chains and CNT. CNT is known as reinforcing filler because effective load transfer can occur between polymer chain and CNT. Thus more force will be required to induce same amount of deformation in higher CNT containing nanocomposites. Decrease in elongation at break is probably due to the fact that interface of CNT and polymer chains act as an effective crack propagation site and at sufficiently high strain this leads to the failure.

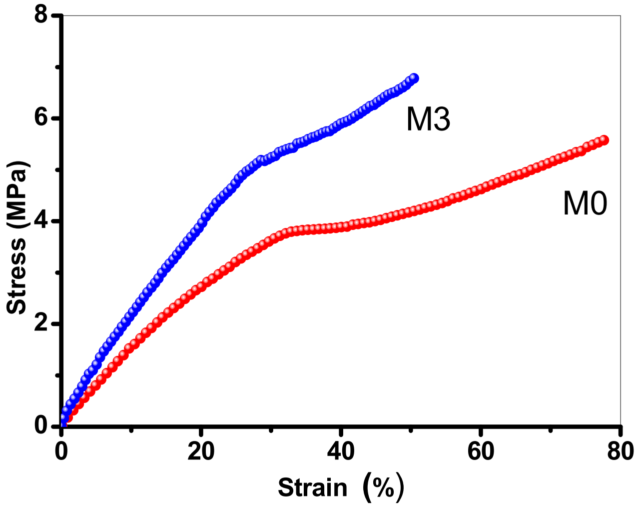

Figure 4.2: *Stress vs strain graph of PDMS/NCB 30 nanocomposites for two CNT loading at 100 kGy radiation dose.*

Variation in crosslinking density with radiation dose has been shown in figure 4.3 for different CNT wt%. The figure shows that crosslinking density increased with absorbed radiation dose. High energy radiation expected to form 3D crosslinked network in PDMS matrix. Crosslinking density was higher for 2 and 3 wt% than 1 wt% CNT. There was no appreciable difference in crosslinking density in 2 wt% and 3 wt% CNT containing nanocmposites. This result supports the hypothesis of increase in elastic modulus due to synergistic effect of CNT and radiation crosslinking. At every dose slightly higher number of crosslinked networks formed with the addition of CNT. Since efficacy of radiation crosslinking depends on the localized free volume, the radiation and nanofillers are expected to act synergistically.

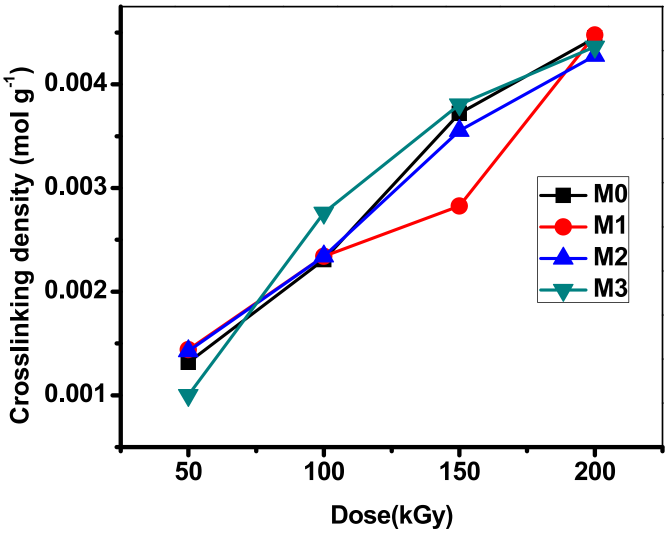

Figure 4.3: *Variation in crosslinking density of PDMS/NCB30/CNT nanocomposites with radiation dose at different CNT loading.*

4.4.1.2 AC and DC conductivities

Figure 4.4 shows the DC conductivity of the composites having different amount of CNT. It can be seen that even at 1 wt% addition of CNT the conductivity increased to about four times and with 3 wt% addition of CNT it increased to almost 10 times with respect to the nanocomposites without CNT. This observation clearly pointed out formation of better conducting network with addition of CNT into PDMS/NCB composites. Figure 4.5 represents effect of CNT content on the AC conductivity as a function of frequency. It can be seen that with addition of CNT the AC conductivity increase. With the increase in frequency, there was a precipitous fall in the AC conductivity at around 100 kHz. The AC conductivity for all composites was almost same between 1 MHz to 10 MHz reflecting conductor to insulator transition. This phenomenon is generally attributed to frequency dependent changes in polarization of permanent and induced dipoles in the nanocomposite matrix [229, 264]. The observed change in conductivity can be attributed to frequency dependent variation in the polarization and charge accumulation, since with increase in frequency, dipoles gets less time for reorienting themselves in the direction of applied field, reducing polarization effect. The frequency dependence of AC conductivity of conducting composites often gets affected

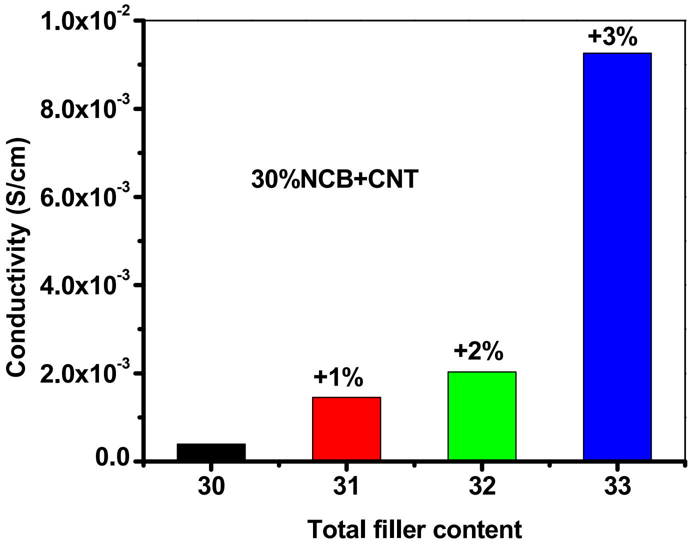

Figure 4.4: *DC electrical conductivity of PDMS/NCB30/CNT nanocomposites (100 kGy).*

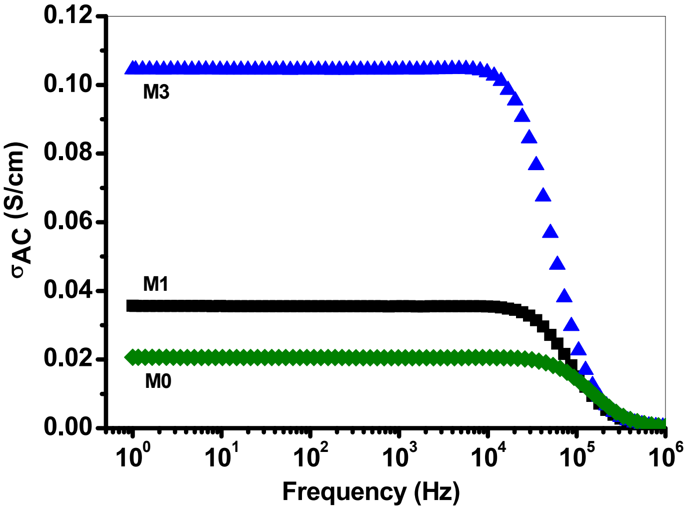

Figure 4.5: *AC electrical conductivity of PDMS/NCB30/CNT nanocomposites (100 kGy).*

with the loading of filler, as the number and morphology of conducting pathways change with increase in filler concentration. However it can be inferred that there is a change in the conduction domains with increase in frequency, at lower frequency current flows through NCB aggregates resistor network, whereas at high frequencies insulating polymer matrix plays a critical role in conduction [265].

4.4.2 Chemiresistive behaviour of PDMS/NCB/CNT hybrid nanocomposites

4.4.2.1 Effect of CNT on real time sensing response

Concentration normalized dynamic sensing response of the PDMS/NCB chemiresistors having different wt% of CNT irradiated to 100 kGy for BTEX vapours has been shown in Figure 4.6. It can be seen that significant change in resistance was observed in all chemiresistors by exposure of BTEX. Sensing response was completely reversible in nature and 90% change of resistance (t_{90}) was observed within 10 sec. During recovery, it took only 5-10 sec to come back to 50% of its original value. It may be noted that in case of colorimetric and metal oxide VOC sensors significantly higher response time is observed compare to the response time observed in this study [42]. The magnitude of sensing response was different for different analytes (Figure 4.7). It can be seen that benzene gives lowest response while xylene gives highest response for all chemiresistors. For M0 chemiresistor, the response for xylene was around 2.15 times higher than the response for ethyl benzene, 4.05 times higher than the response of toluene and 19 times higher than that for benzene. There was a significant reduction in the response for all VOCs upon addition of CNT. From M0 to M1, the decrease in response was ~42% for benzene, ~51% for toluene, ~28% for ethyl benzene and ~56% for xylene. Further decrease in responses was observed when CNT was added to the nanocomposites form 1 wt% to 3 wt%.

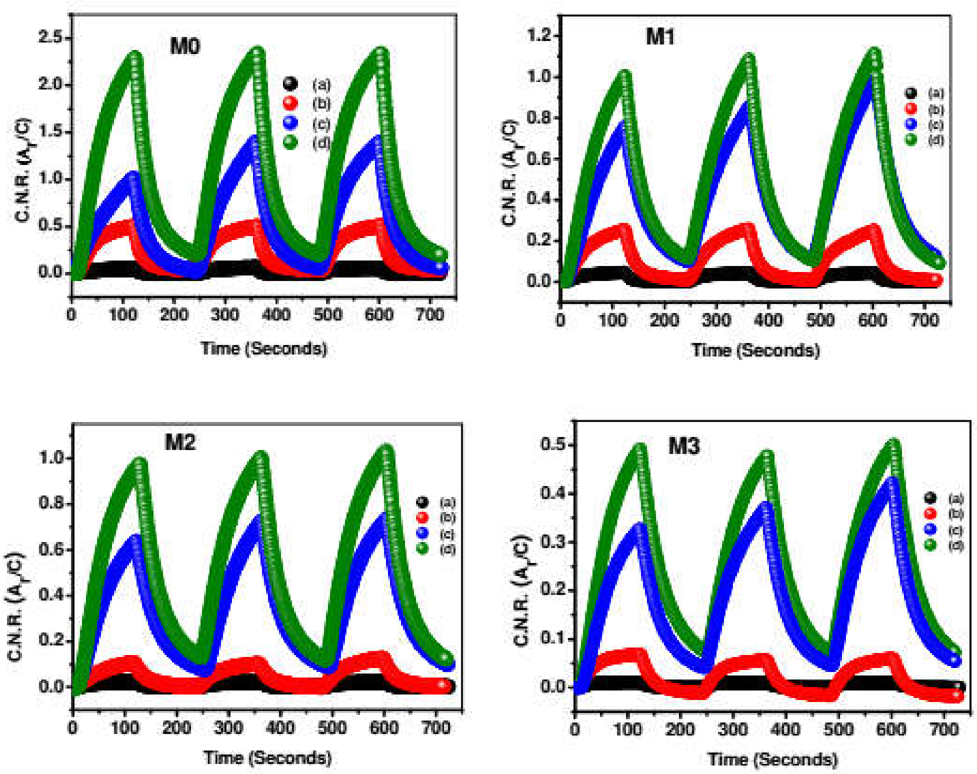

__Figure 4.6__: Concentration normalized relative change in the resistance (C.N.R) for different nanocomposites (a) Benzene (b) Toluene (c) Ethyl benzene (d) Xylene. The BTEX flow rate was 100ml/min.

This is an interesting observation suggesting that the CNT loading affects sensing response towards each analyte differently. It may be highlighted that the factors governing sensing response is polymer matrix-analyte interaction (χ_{12}) as well as the diffusion kinetics of analytes into the chemiressitor matix. As all these analytes have different solubility parameter thus interaction parameter with PDMS matrix will be different which in turn affects sensing response. There is also kinetic factor, since CNT has coil like structure it induces additional hindrance in diffusion of analytes into chemiresistor matix [266]. Thus it is probable that presence and quantity of CNT affects sensing response by affecting diffusion of analytes. All these aspects are described in details in subsequent sections.

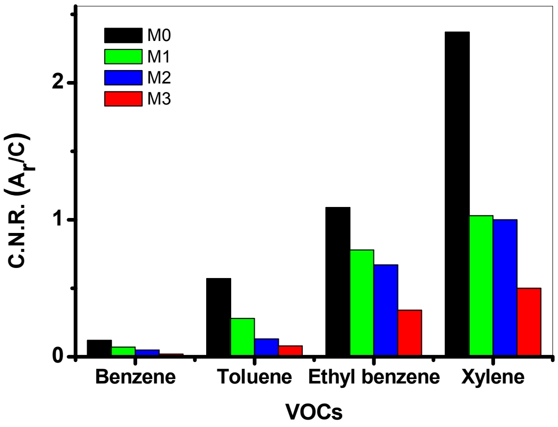

Figure 4.7*: Concentration normalized relative change in the resistance (C.N.R) for BTEX vapour for different nanocomposites.*

4.4.2.2. Selectivity of the hybrid nanocomposites

Selectivity for a particular analyte comes from the interaction of analytes with polymer matrix in sensing elements. Upon interaction with analyte molecules polymer chains get relax that produced a stress inside nanocomposite sensor. This chemiresistive stress induced disruption of conducting network leading to increase in electrical resistance of chemiresistive sensor. It was reported that CPC having polar polymer gives better sensing response for polar analytes and nonpolar polymer based CPC gives better response for nonpolar vapour [267, 268]. The magnitude of interaction between analyte and polymer nanocomposites can be governed by Flory-Huggins interaction parameter (χ_{12}). The relation of χ_{12} and sensing response ($A_r = \Delta R/R_0$) for a particular analytes for chmemiressitve sensors can be expressed by

$$A_r = ae^{b(\chi_{12})^{-n}} \tag{4.1}$$

where a, b and n are constants. From the relation it is clear that sensing response has an inverse relation with χ_{12}. The sensing response of different sensors is plotted against χ_{12} in Figure 4.8 for different analytes at 50 ppm. From the plot it can be seen that the sensing response decreased with increase in χ_{12}. The highest response was for xylene which has lowest χ_{12} with PDMS and the lowest for benzene which has highest χ_{12} with PDMS. Interestingly, sensing response decreased with increase in CNT wt% in chemiresistors for all analytes. And the highest decrease was observed for xylene which has lowest χ_{12}. The equation fitted well for composites M0, M1, M2 however the fitting for M3 was very poor ($R^2 < 0.8$).

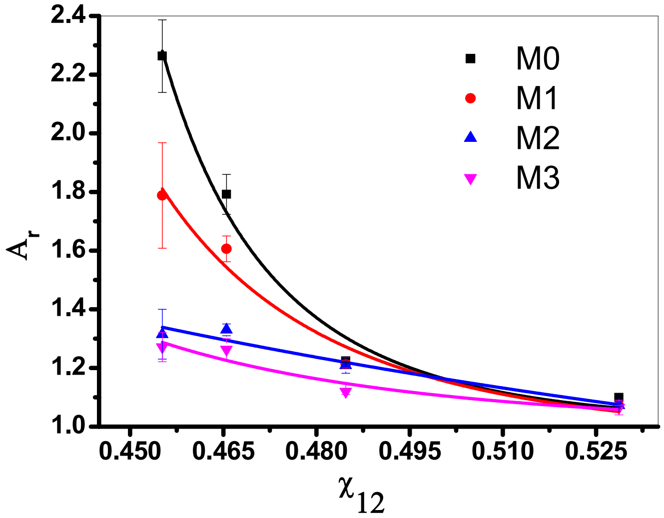

***Figure 4.8**: Variation in relative change in resistance with χ_{12} for different nanocomposites. Conc of analytes are 50ppm. Solid line represents fitting of data in eq 4.1.*

Table 4.2: a, b and n values obtained from fitting equation 4.1 in the data shown in figure 4.8.

CNT wt%	a	b	n	R^2
0(M0)	1.01	4.081E-7	18.43045	0.96
1(M1)	0.96	2.53E-5	12.87376	0.92
2(M2)	0.68	0.0692	2.95247	0.98

With addition of 2 wt% CNT into PDMS/NCB matrix the value of n decreased from 18.4 to 2.9 (Table 4.2). Due to the coil like structure of CNT diffusion of analytes gets hindered therefore affect the diffusion of analyte and polymer chain relaxation, decreasing the sensing response. Furthermore, the deviation of M3 from the equation no 4.1 suggests that the sensing response of CNT filled chemiresistors not only dependent on thermodynamics parameter, $\chi_{12,}$ but also diffusion related kinetic aspects play critical role.

4.4.2.3. Diffusion behaviour of hybrid nanocomposites

In order to understand the effects of CNT on diffusion kinetics and sensing response, mass absorption study was done for M0 and M3 nanocomposites taking benzene and xylene as solvents. Figure 4.9 shows equilibrium mass absorption data. It can be seen that for both the nanocomposites equilibrium uptake of xylene was higher than that of benzene. For xylene the extent of swelling and swelling kinetics both change significantly with addition of CNT. While in case of benzene the extent of equilibrium swelling did not change much but there was considerably reduction in swelling kinetics. To fully understand the effects of CNT on the diffusion parameter the data was further analyzed using Fickian diffusion model

$$M_t/M_\infty = kt^n \qquad \textbf{(4.2)}$$

where M_t mass of solvent absorbed at time t, M_∞ mass of solvent absorbed at equilibrium, k is a constant depends on the structural characteristics of the polymer network and dictating interaction with the solvent, n is an empirical number called as transport or diffusion exponent. Initial stage of swelling plots between $\ln(M_t/ M_\infty)$ vs ln(t) gives a straight line up to $M_t/M_\infty \leq 0.7$. Slope and intercepts of the plot yields n and k values respectively (Figure 4.10a -d). A value of n = 0.5 denotes the process is Fickian diffusion also known as Case-I transport where the rate of relaxation of polymer chain is higher compared to the diffusion rate of the solvent. In other way, for Case II transport, n= 1.0 states the diffusion is relaxation controlled where chain relaxation is slower compare to diffusion of solvents. When the value of n lies down between 0.5 to 1.0, it is classified as anomalous diffusion. Diffusion coefficient (D) of the nanocomposites under investigation was calculated using following relation [269]

$$D = \pi\left(\frac{h\theta}{4M_\infty}\right)^2 \quad \textbf{(4.3)}$$

where h is the sample thickness, θ is the slope of the linear portion of the sorption curves, and M_∞ is the mass uptake at equilibrium swelling. All samples displayed quasi Fickian diffusion with $n < 0.5$. With increasing CNT fraction, diffusion coefficient reduced for benzene and xylene (Table 4.3). This CNT induced reduction of diffusion kinetics is responsible for the observed reduction in sensing response. Due to the coil like structure, CNT has restricted the relaxation of macromolecular chains and reduced solvent diffusion. Furthermore, CNTs can also act as a barrier to the solvent penetration in the nanocomposite matrix leading to a slower swelling kinetics. It is emphasized that in the present system, the sensing element is subjected to 3-D exposure; therefore thermodynamic interactions between BTEX and PDMS matrix and diffusion kinetics both might influence the observed sensing response.

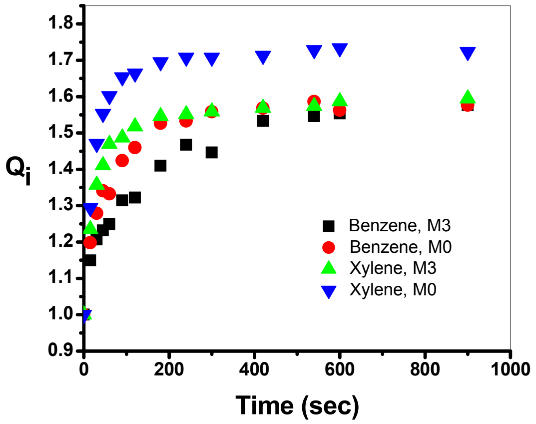

Figure 4.9: *Equilibrium mass uptake (Qi=Uptake at equilibrium/initial mass) by M0 and M3 nanocomposites against benzene and xylene.*

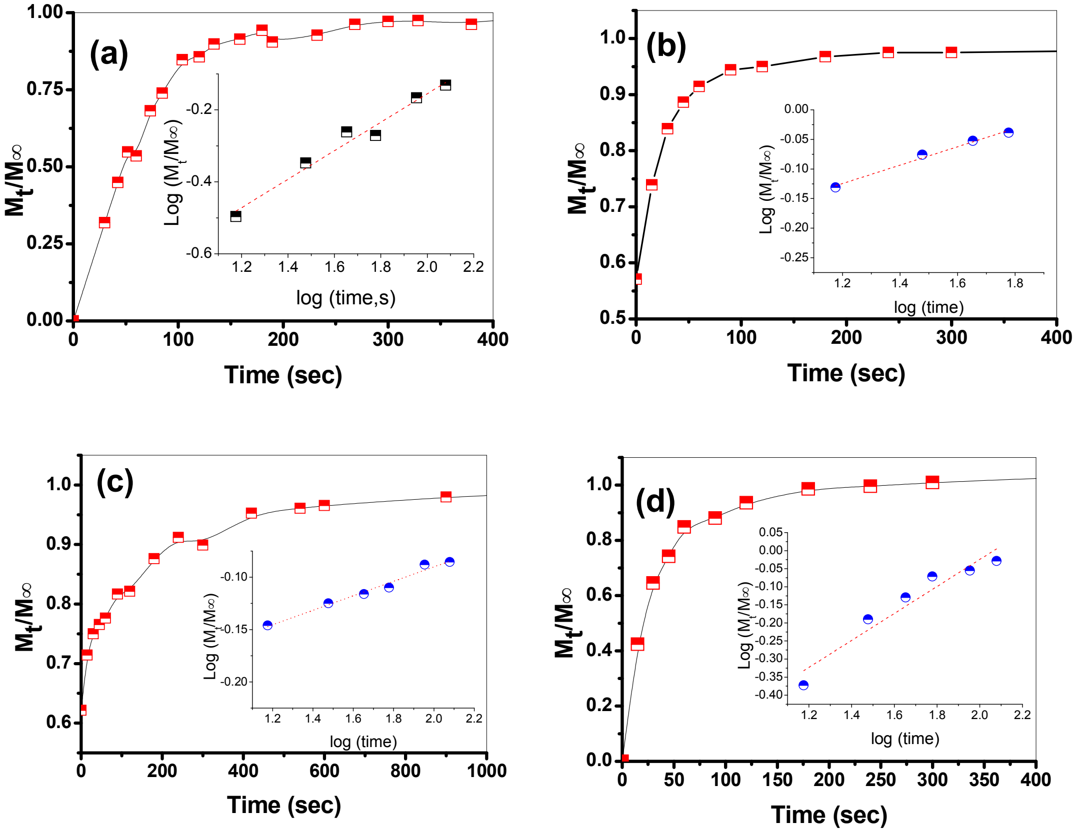

Figure 4.10: *Solvent uptake kinetics of nanocomposites for benzene and xylene (a) M0, benzene (b) M0, xylene (c) M3, benzene (d) M3, xylene. Inset all: Linear fitting of logarithmic data for*$M_t/M_\infty < 0.7$.

Table 4.3: Swelling parameters of composites for different analytes.

	Benzene				Xylene			
	lnk	n	R^2	Diffusion Coefficient (D) (cm2 s^{-1})	lnk	n	R^2	Diffusion Coefficient (D) (cm2 s^{-1})
M0	-0.94715	0.39605	0.96	1.71E-8	-0.31116	0.15547	0.98	1.49E-6
M3	-0.22834	0.06914	0.97	5.4E-9	-0.77087	0.37325	0.91	3.11E-8

4.4.2.4. Effect of analytes concentrations on sensing response

Concentration dependent change of sensing response of the nanocomposites for benzene and toluene under dynamic condition for different chemiresistors has been shown in Figure 4.11. Nonlinear relationship between sensing response and vapour concentration was observed for both the analytes. Chemiressitor containing 3 wt % CNT showed lowest response whereas 0wt % CNT containing chemiresistor showed highest response. Langmuir-Henry-Clustering (LHC) model is often used to explain the relation between sensing response and analyte concentration of conducting polymeric nanocomposites based chemiresistors and can be described as

$$A_r = \frac{b_L(f''-f)f}{(1+b_L f)} + k_H f + (f - f')f^{n'} \qquad \textbf{(4.4)}$$

where A_r is relative change in resistance ($\Delta R/R_0$), f is the vapour fraction i.e molar ratio of analyte vapour and nitrogen. f' is the solvent fraction over which clustering takes place and f'' is the solvent fraction where Henry's diffusion takes precedence over Langmuir's diffusion, b_L is the Langmuir's affinity parameter, k_H is the Henry's diffusion parameter and n′ is the average number of solvent molecules per cluster.

A series of chemiresistive sensors have been investigated by Lu et al. and Kumar et al. and they have found that LHC model adequately explain the relation between analyte vapour concentration and sensing response [127, 162]. However, for the PDMS/NCB and CNT based hybrid chemiresistors the LHC model was not found suitable for any of the analytes. It is evident from the fact that with increase in vapour concentration the sensing response did not saturate rather an exponential increase in response was observed in dynamic as well as in static vapour sensing setup (Figure 4.12).

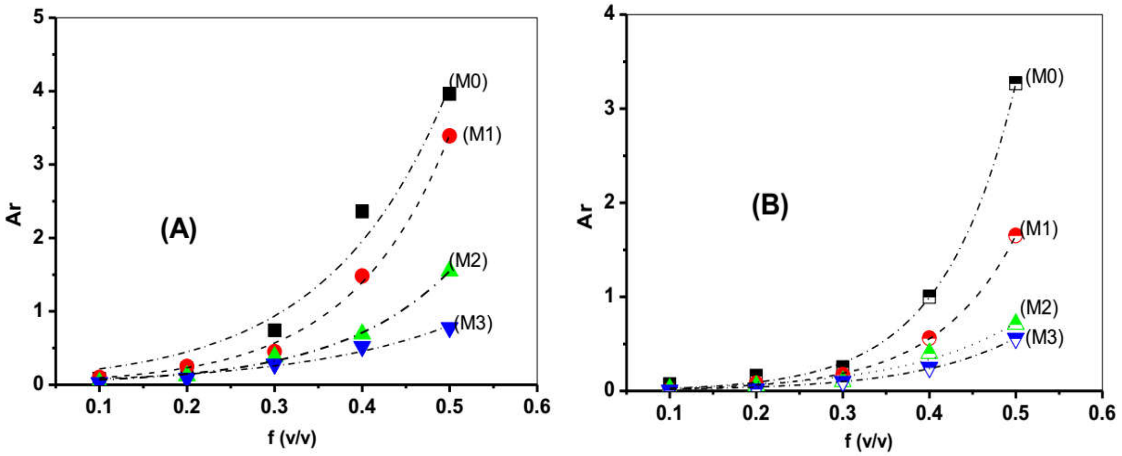

***Figure 4.11**: Concentration dependent change of sensig response for different chemiresistors under dynamic flow conditions (A) Toluene (B) Benzene. The dotted lines shows fitting of the equation 4.5.*

Langumir adsorption assumes maximum monolayer coverage by vapour molecules; whereas, in Henry's isotherm it is assumed that surface coverage depends on vapour pressure of the analyte. It must be highlighted that chemisorptions phenomena of polymer nanocomposites depends on short and long range bonding between polymers and analyte and follows Henry's or Langumir's adsorption isotherms only in ideal cases [270]. However, diffusion of analytes into a 3-D matrix does not sufficiently represented by these isotherms. Fan et al. have reported an exponential increase in sensing response with vapour concentration for analytes having good interaction with polyurethane polymer matrix [271]. Han et al. have recently reported sensing response similar to that observed in the present study in electrospun polymer/carbon nanotube based chemiresistors [98]. They also found an exponential variation of sensing response with an increase in analyte concentration. This sensitivity enhancement can be attributed as an effect of 3D sensing mechanism where sensor matrix was exposed by analyte molecules from all direction. It was impossible in sensor having layer by layer structure in screen printed electrode. In present study, chemiresistors were compressed moulded and crosslinked by high energy radiation to impart sufficient strength thus it was possible to use them as standalone sensing film where 3D sensing can be achievable. Furthermore, being an elastomer PDMS has very little crystalline domain; and thus expected to have higher sensitivity than thermoplastics such as polycaprolactone, PMMA and polystyrene. The data of Figure 4.11 for toluene and benzene was fitted in the exponential model given by

$$A_r = \mathrm{a} * e^{(bf)} \tag{4.5}$$

where a and b are constants, f is the vapour fraction and A_r is the relative change in resistance. The parameter b represents the sensitivity of chemiresistor and can be seen that the value of parameter b reduces with addition of CNT (Table 4.4). These results clearly point out reduction in sensitivity with addition of CNT.

Table 4.4: a and b parameters obtained for different composites against different analytes.

	Toluene			Benzene		
	a	b	R^2	a	b	R^2
M0	0.008±0.001	11.9±0.47	0.99	0.10±0.05	7.35±1.08	0.97
M3	0.007±0.001	8.69±0.49	0.99	0.05±0.02	5.72±0.80	0.97

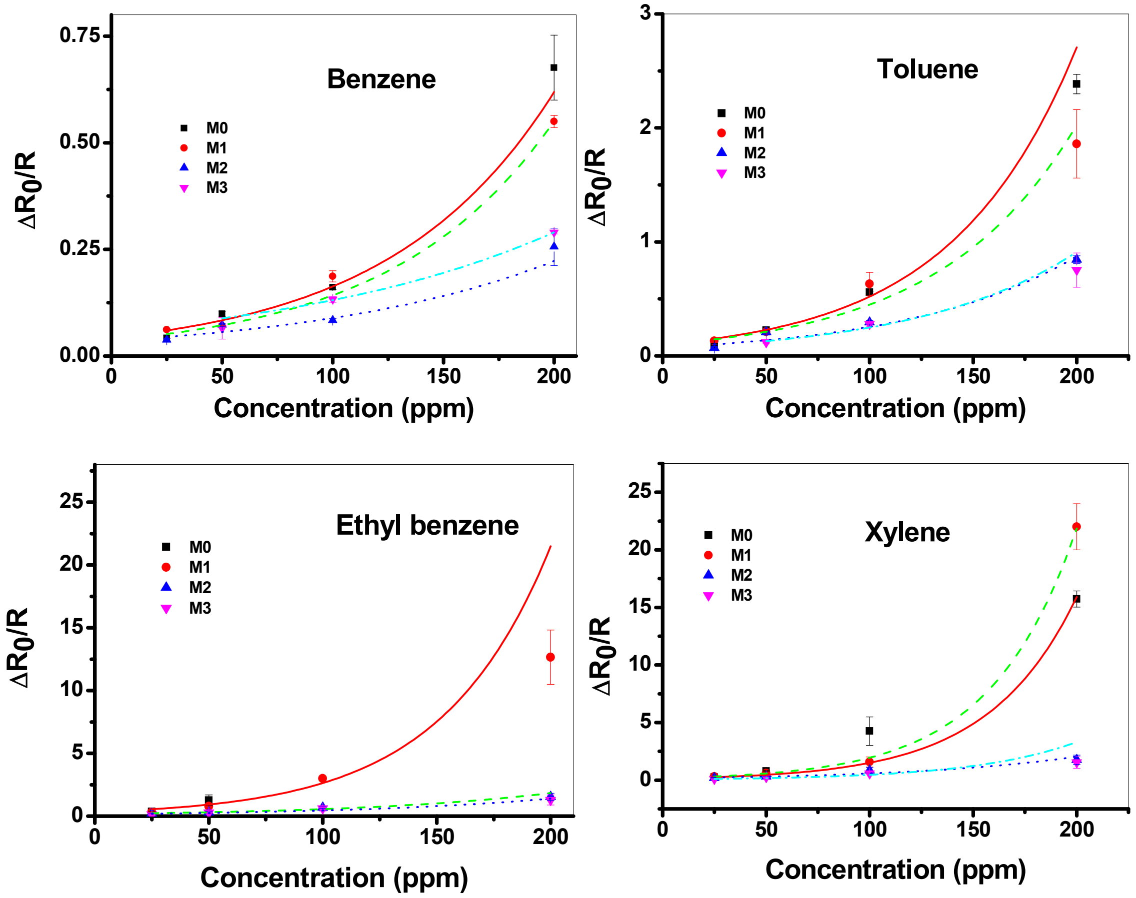

Figure 4.12*: Variation in relative change in the resistance for different composites under static condition. Concentration range of analytes 25-200 ppm,*

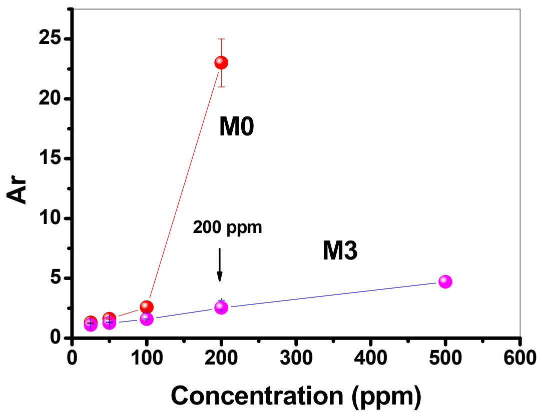

Figure 4.13: *Effect of higher concentrations of ethyl benzene on composites M0 and M3 under static condition.*

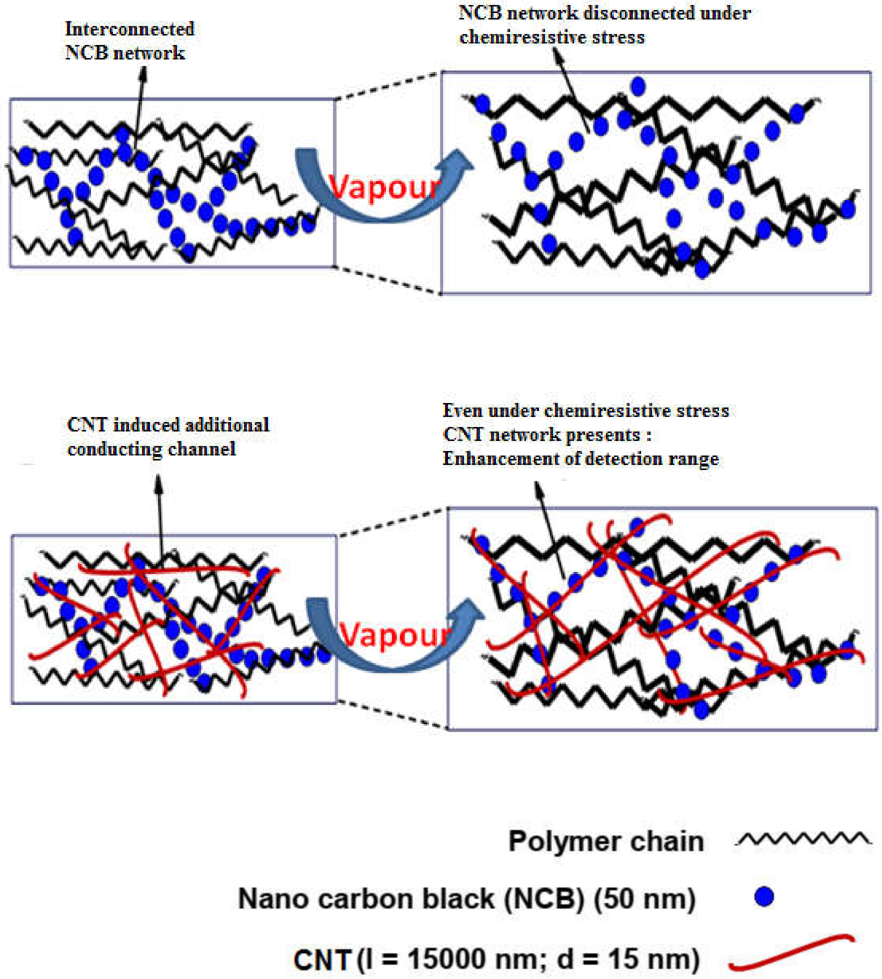

Figure 4.14: *Schematic representation showing additional CNT networks help to enhance detection range of chemiresistors.*

However, by addition of CNT, the detection range of chemiressistors was found to be extended. Figure 4.13 represents the extended range showed by M3 composites against ethyl benzene vapour compare to M0 composites. The sensor M3 showed extended range up to 500ppm while M0 went out of range at >200 ppm ethyl benzene vapour. The mechanism of enhancement of detection range can be explained with the help of schematic diagram shown in Figure 4.14. Addition of CNT into PDMS/NCB matrix forms additional conducting network, which implies more chemiresistive pressure (more concentration of vapour) will be needed to disrupt these additional network forms by CNT. This favours enhanced detection range. The detection limit was determined using the conventional definition by IUPAC [272]. It says that lower limit of detection (LOD) can be determined from signal to noise ratio S/N. For M0 the LOD was 9 ppm, 6 ppm, 12 ppm and 50 ppm for benzene, toluene, xylene and ethyl benzene respectively. For M3 the LOD increased for all VOCs except for ethyl benzene. It was 18 ppm, 12 ppm, 21 ppm and 27 ppm for benzene, toluene, xylene and ethyl benzene respectively. This suggests that there is minor reduction in terms of sensitivity but significant increase in terms of detection range with increase in CNT content.

4.4.2.5. Principle component analysis (PCA)

PCA was used for pattern recognition of analytes by using an array of chemiresistive sensors [273, 274]. It helps to visualize whether change in sensing response due to CNT can be useful to recognize an individual BTEX using a sensor array. An array was constructed by taking four sensing elements M0, M1, M2 and M3 and the sensing response for BTEX were recorded in the concentration range 30-50 ppm. After conducted PCA the result is shown in Figure 4.15. The graph shows that the two principal components are enough to represent 96.3 % of total variance of data. Among this 85.9 % variance is described by first principle component (PC_1) and 10.4 % variance can be described by second principle component

(PC_2). It was observed that benzene is well separated from other three VOCs ; however, there was a significant clustering between ethylbenzene and xylene. These results highlight good discrimination of benzene. Nonetheless, these hybrid nanofiller based chemiresistor are expected to be useful as field detectors and can offer different sensitivity and detection limits to suit different applications.

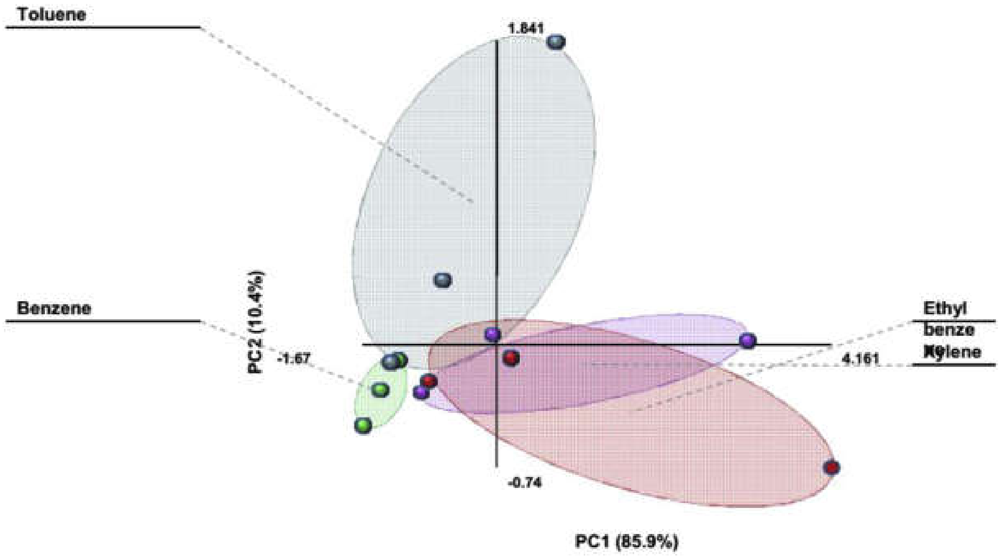

***Figure 4.15**: Principle component analysis using an array of M0, M1, M2, and M3 in the concentration range 30-50 ppm of BTEX.*

4.4.3. Temperature dependence on resistivity

Temperature dependence on resistivity is an important parameter to investigate for CPC based chemiresistive sensors along with other sensing characteristics. In general, conducting polymer based nanocomposites showed positive temperature coefficient (PTC) before melting temperature of base polymer [275, 276]. Figure 4.16 shows the positive temperature coefficient behaviour M0 and M3 chemiresistors in the temperature range 323-393 K. M0 shows significant increase (400%) in the resistance, whereas a considerably less increase (50%) in resistance was observed for M3 in the experimental temperature range. Also for M3, relatively stable response was obtained in middle temperature range. The temperature coefficient of resistivity was found to be 10.0 x 10 $^{-3}$ Ω cm.K^{-1} and 2.7 x 10 $^{-3}$ Ω cm.K^{-1} for M0 and M3 respectively. From Figure 4.4 it was clear that addition of CNT significantly improves the electrical conductivity of nanocomposites. Relatively stable resistance over temperature range of 323- 393 K suggests formation of additional conducting channels by CNTs in M3 in comparison to M0. This observation supports our hypothesis that more chemiresistive pressure will be needed to disrupt these additional channels formed by CNT, favoured enhancement of detection range of chemiresistor.

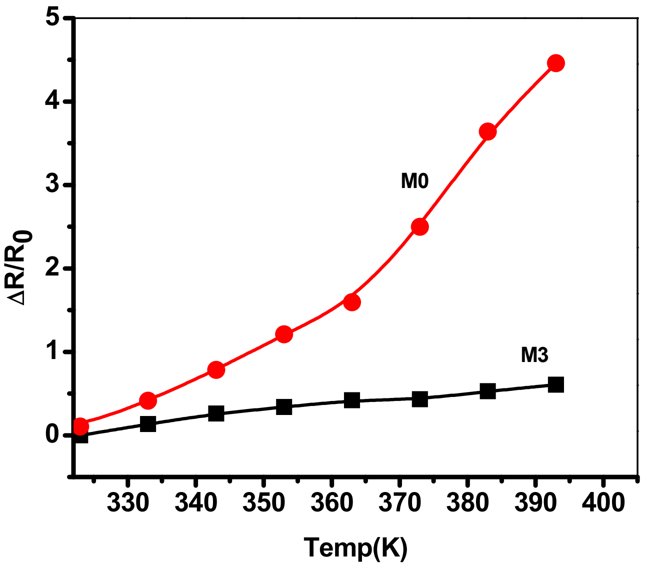

Figure 4.16: *Effect of temperature on the relative change in the DC resistivity for M0 and M3.*

4.4.4. Morphological and electromechanical analysis of nanocomposites

Morphological characterization of cryo-fractured samples was done by FE-SEM and presented in Figure 4.17 (a-e). The cryo-fractured samples demonstrate brittle failure for all composites. It can be seen that for M0, around 50-100 nm spherical NCB domains were homogenously embedded in the entire matrix. With addition of 2 wt% CNT, more prominent NCB domain were observed and also projected out of the matrix surface.

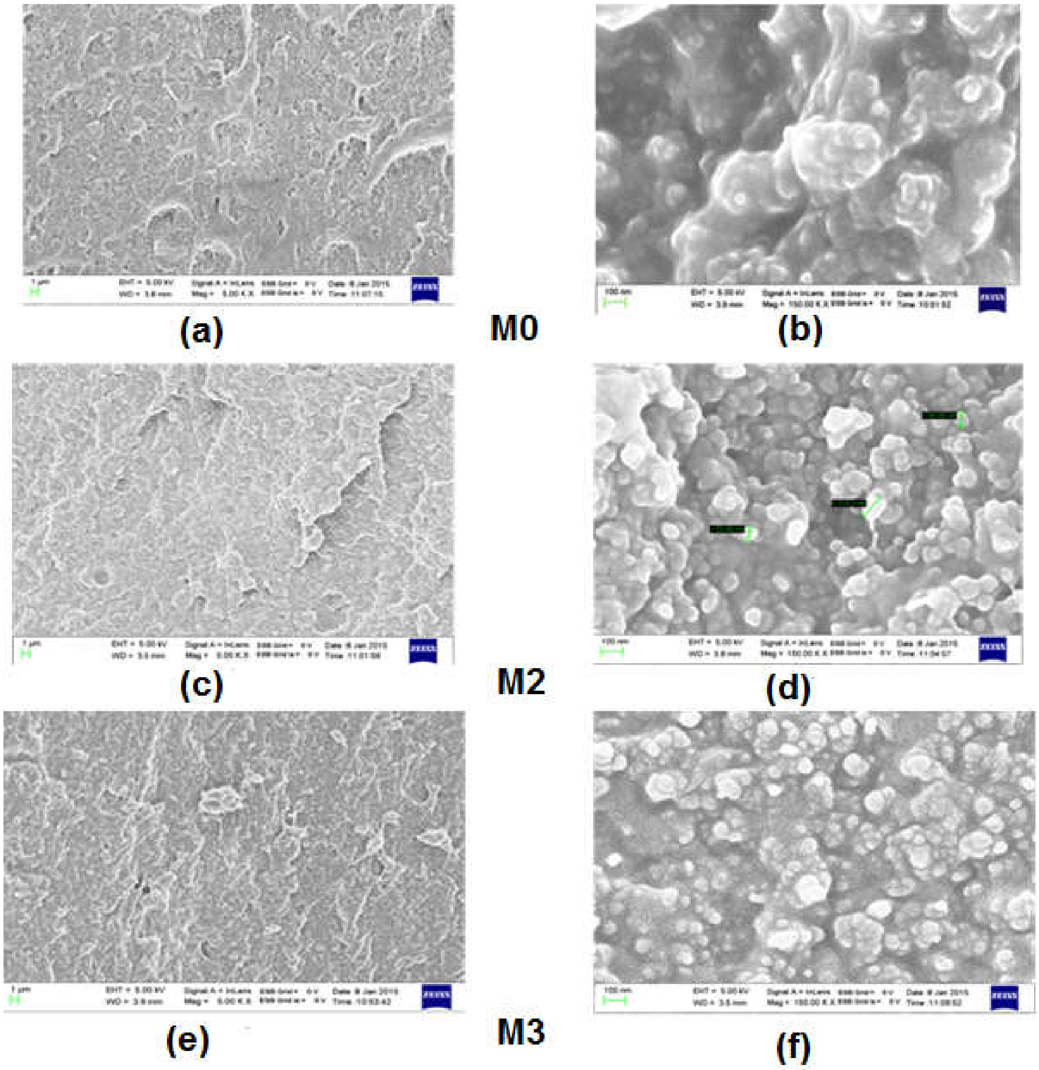

Figure 4.17*: FE-SEM images of cryo-fractured nanocomposites (a) M0, 5 kX (b) M0,150kX (c) M2, 5 kX (d) M2, 150kX (e) M3, 5 kX (f) M3, 150kX.*

Due to the contrast limitation, isolated CNT structure or projected out CNT domains were not visible. This may be due to the fact that weight fraction of CNT is significantly lower than NCB weight fraction. More NCB domains were noticeable when CNT increase to 3wt%; also the size of the domains of NCB reduced further and the morphology seems completely pushed out of the matrix, in contrast to the embedded morphology observed in M0. This pushed out domains of NCB suggests enhanced percolation of NCB and thinning of interfacial layer and can be attributed to the increased conductivity of chemiresistors on the addition of CNT.

In spite of the fact that CNTs and their nanocomposites are extensively researched for the development of chemiresistive sensors, still there is a lack of understanding in the mechanism behind the sensing response specially in terms various sensing parameter like sensitivity, selectivity, detection range of chemiresistors, conducting network structure and diffusion of analyte and relaxation of polymer chain [277]. Boyd et al., have recently proposed that both CNT network and inter-tube interconnections play a crucial role in the sensing response [278]. They elucidated that the changes in the junction and contact, as a result of chemiresistive pressure due to interaction of analyte, increased resistivity of composites. They have established that if J/C (where J is no. of junction and C is the no of CNTs between electrodes) is higher than 4 nanotube junctions play a crucial role. In the present work, there are three types of conducting networks: NCB-NCB, CNT-CNT and CNT-NCB. As hypothesized, under chemiresistive pressure NCB-NCB networks disrupts easily though NCB-CNT networks are relatively long ranged and retains conductivity even when chemiresistive pressure is high. To further test this hypothesis, both M0 and M3 were subjected to uni-axial tensile stress and recorded electromechanical response (Figure. 4.18). It was found that, linear increase in resistance only up to 10% strain in M0, whereas, in case of

M3 the resistance increases linearly up to more than 25% strain. These results highlighted that the presence of long range inter-connections in the nanocomposites containing CNT. The reason for the increase in resistance due to uni-axial stain is the increased physical separation between two conducting interconnections that exceeds tunnelling barrier. It can be suggests that, with addition of CNTs (1000-2000 nm) which have much higher length than NCB (50 nm), provide long range interconnections to the primary conducting networks formed by percolated NCB thus giving a longer linear region than pure NCB containing nanocomposites.

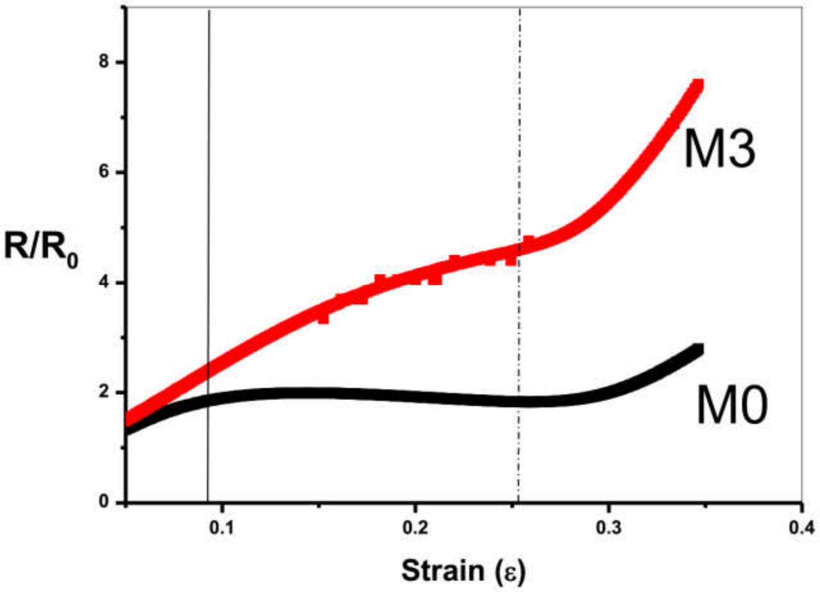

***Figure 4.18**: Electromechanical response of M0 and M3 under uni-axial tensile strength. The nanocomposites were put under strain using a universal tensile machine and relative change in resistance was monitored in real time. Solid vertical line depicts strain sensing limit for M0 and dashed line depicts strain sensing limit for M3.*

Kaniyoor et al., used a hybrid graphene nanoplatelets and multiwalled carbon nanotubes system and found that enhanced sensitivity with excellent stability and repeatability for hydrogen detection; this result was attributed the importance of the morphology of the hybrid carbon nanostructure [133]. In another hybrid system Rigoni et. al. found that SWCNT bundle layers with indiumtin oxide (ITO) nanoparticles increased the sensitivity of ammonia gas by three fold [134]. All these studies along with the results of this work highlight the fact that hybrid fillers can not only improve sensing characteristics but also decrease the temperature sensitivity by incorporating additional network of filler with high aspect ratio.

4.5. Conclusions

PDMS/NCB and CNT based hybrid nanocomposites based chemiressitors have been prepared by melt compounding and crosslinked by high energy gamma radiation. Mechanical and electrical properties were found to be improved by radiation dose as well as with CNT wt %. These radiation crosslinked hybrid nanocomposite base chemiresistors showed sensitive and reversible sensing response for BTEX vapour. Highest response was observed for xylene where as lowest for benzene. The sensitivity showed strong dependence on polymer-solvent interaction parameter (χ_{12}). It was also found that addition of CNT improves the dispersion of NCB in the PDMS matrix and affects the interfacial layer of PDMS which in turn help to increase electrical conductivity of hybrid nanocomposite. Detection range of chemiresistors was increased significantly due to the formation of additional long range networks of CNT which also improves temperature dependence of resistivity. These results highlight the usefulness of hybrid nanocarbons in VOC field detection, and suggest that, using hybrid fillers, different sensitivities and detection ranges can be achieved in chemiresistors to target different applications. Furthermore, CNT induced enhancement in electrical conductivity along with good stretchability and low positive temperature dependence of conductivity are expected to be useful in stretchable electronics and for other applications where flexibility, electrical conductivity and light weight are desired.

CHAPTER 5

Enhancement of Chemiresistivity of CPCs by using functionalized CNT-polymer nanocomposites.

5.1. Introduction

CNT based conducting polymer nanocomposites (CPC) were first reported back in 1994 by Ajayan et al [279]. Since then remarkable attention has been paid to fabricate CPC containing CNT with superior mechanical and electrical properties along with several other functional properties and applications [280-284]. Efficient dispersion of CNTs and good interfacial interaction between polymer and CNTs are prerequisite condition to get better target properties. Unfortunately, strong CNT-CNT interaction, CNT agglomeration, chiralities, presence of impurities has hampered the final properties of CNT based CPC [280, 285]. Furthermore, incorporation of high amount of conducting filler is often needed to form percolation network of CNTs in polymer composites [286, 287]. But loading of higher amounts of fillers sometimes poses challenges in terms of increased viscosity, agglomeration, and morphological instabilities. Uses of hybrid nanofiller, covalent and non covalent functionalization of CNT, preferential percolation of CNT in multiphase polymer composites are some of the strategy which could bring down the percolation concentration [255, 288, 289]. Among them covalently functionalizes CNT have been proved to be quite successful to prepare CPC with relatively lower concentration of filler due to better dispersion of nanotubes and efficient thermodynamic wetting of nanotubes with polymer matrices [283, 290].

Chemiresistivity of CPC depends on the structure of conducting network formed by conducting fillers and the characteristics of polymer chains. Covalently functionalized CNTs have been demonstrated to improve the interfacial compatibility, percolation, and micromechanics [285, 291]. And since the surface properties of CPCs are greatly affected by the nature of functional groups present in CNT, it is quite probable that the chemiresistivity of functional CNT based CPCs also get affected. Crosslinking of CPC introduces intermolecular linkages between polymer chains and thus profoundly affects the vapour permeability, solvation and mechanical properties of a polymer [135, 292]. It is worthwhile to mention that for filled systems, such as CPCs, both physical and chemical crosslinking may take place. High energy radiation such as electron beam and gamma ray is an effective additive-free tool to crosslink polymers and its composites at room temperature. It has potential to forms linkages not only between the polymer chains but also at polymer-filler interface [293]. This is mainly possible due to the radiolytic efficiency and penetrating power of high energy radiation, enabling the formation of free radicals on the filler surfaces, interface and in the bulk. Functionalized CNTs together with optimal radiation dose thus can be useful in improving the interface, integrity and the chemiresistivity of CPCs.

In this work CNT functionality and gamma radiation were used to modify polymer-filler interfacial interactions. Particularly, attention has been paid to varying filler functionality and strengthening polymer-filler interfacial interactions using high energy radiation, with a focus on enhancement in chemiresistivity. For that different proportion of PDMS/ functional-CNT CPCs were prepared by shear compounding method. Non-linear oscillatory rheology was used to estimate CNT-polymer interactions and the impedance spectroscopy was used to understand electron conduction in CPC. Chemiresistivity was investigated with respect to CNT-functionality, CNT volume frcation, and radiation dose. Surface energy, functional groups (x-ray photoelectron spectroscopy), gel content and morphology of the CPCs were also analyzed in the context of observed chemiresistivity.

5.2. Preparation of PDMS/NCB/CNT hybrid nanocomposites

5.2.1. Materials

Poly(dimethylsiloxane) (PDMS) (Hardness= 60; density= 1.13±0.05 g/cc) was procured from M/s DJ silicone, China. Multiple walled CNTs [unfunctionalized (CNT-UF), amine functionalized (2-3 wt %; CNT-NH2), hydroxyl functionalized (2.36-2.6 wt %; CNT-OH), and carboxylic functionalized (1.47-1.63 wt %; CNT-COOH); OD: 10-30 nm; Length: 1-2 μm SSA: 100-130 m^2/g] were purchased from Otto Chemie Pvt. Ltd, Mumbai India. Benzene, toluene, acetone, chloroform, methanol and ethanol used were of Analytical grade (purity >99.9%) and was procured from M/s SD Fine Chemicals, Mumbai.

5.2.2. Sample preparation

PDMS/CNT (un-functionalized, hydroxyl, amine and carboxylic group functionalized) nanocomposites were prepared by the shear compounding of constituent materials in Brabender plasticorder at 70 ^{o}C at 40 rpm for 30 min. After mixing, the homogeneous mixture was taken out, cut into small pieces and compress moulded to the different thickness (100 -1000 μm) at 150 kg/cm^2 for 20 min at 70 ^{o}C. These moulded sheets were crosslinked by high energy Co-60 gamma irradiation (GC-5000, M/s BRIT, India). Before irradiation, the dose rate of gamma chamber was ascertained by Fricke dosimetry and was found to be 8.0 kGy/h. The samples in the study are mentioned as PDMS/CNT-UF (PDMS/unfunctionalized CNT), PDMS/CNT-COOH (PDMS/carboxyl functionalized CNT), PDMS/CNT-OH (PDMS/hydroxyl functionalized CNT) and PDMS/CNT-NH2 (PDMS/amine functionalized CNT), depending upon the type of CNTs used. Table A5 in appendix summarises the composition of PDMS/CNT and PDMS/ fun-CNT nanocomposites.

5.3. Characterization of nanocomposites

5.3.1. Mechanical characteristics, diffusion behaviour and Scanning Electron Microscopy

For tensile strength measurements, at least five dumbbell shaped specimens were cut from composite sheets using a sharp edged steel die of standard dimensions. The thickness of the samples were determined to the nearest of 0.1 mm. The tensile strength and elongation at break were measured using a universal testing machine supplied by M/s Hemetek, MUMBAI, India at crosshead speed of 100 mm/min at room temperature. For sorption studies, radiation cross-linked composites were Soxhlet extracted for 12 h to extract any sol content using xylene as a solvent. The insoluble gel part was then dried initially under room conditions and later under vacuum at 40 ^{o}C. The dried composites so obtained was cut into uniform square pieces (1 cm x 1 cm) using a sharp edged die and used for swelling studies. Pre-weighed samples were placed in a 200-mesh stainless steel compartment and immersed in xylene. The swollen samples were periodically removed, blotted free of surface solvent using laboratory tissue paper, weighed on an analytical balance (accuracy 0.00001 g) from M/s AND, India, in stopper bottles and returned to the swelling medium. Measurements were taken until the samples reached constant weight (equilibrium swelling).

The morphology of composites with different CNT content was investigated using a scanning electron microscope (Model PS-230, Pemtron, S. Korea). The cryo-fractured specimen was used to observe fractured morphology and dispersion of CNT. The acceleration voltage of 5 kV was used for recording micrographs.

5.3.2. Surface energy and X-ray photoelectron spectroscopy (XPS)

The radiation-induced modification of surface was characterized by its wetting angle measurements. In this work, the Owens and Wendt method was used. Details of the method have been discussed in chapter 2. The measurement of contact angles of the sample was carried out by sessile drop technique using image analysis software. A liquid droplet (1.5- 2.5 μl) was allowed to fall on the samples to be studied from a software-controlled syringe. An image sequence was taken through a CCD camera of goniometer from GBX instruments, France which was connected to a PC computer and interfaced to image capture software (Windrop++, GBX instruments).

XPS analysis of the samples was performed at 4354 eV photon energy on the PES-BL14 beamline (BARC) at Indus-2, RRCAT, Indore, India.

5.3.3. Impedance spectroscopy

The impedance of the samples was measured at room temperature using an LCR meter (HIOKI IM3570) in the frequency range 4 Hz to 5 MHz. All samples were of disc shape (Diameter = 15 mm; thickness = 0.5 mm). To minimize contact resistance the surface of the samples were coated with conducting silver paste. For ensuring good electrical contact, the surfaces of the specimens were polished with sandpaper and conductive silver paste was applied between the electrodes and the specimen. For each composition, at least three specimens were tested. All measurements were performed at ~24°C and relative humidity of 55%.

5.3.4. Rheological measurement

Rheological measurements were performed on MCR 102 Rheometer (Anton Paar, Austria) using parallel plate (25 mm diameter) geometry at different angular frequencies.

Samples dimensions were 25 mm diameter and 1 mm thickness. All measurements were conducted in the linear viscoelastic regime. N_2 atmosphere was maintained to avoid oxidative degradation of samples. Frequency sweep measurements were conducted at 1% strain and strain sweep experiments were conducted at 1 rad/s angular frequency.

5.3.5. Vapour sensing measurements

A fixed volume of the volatile organic compound (VOC) was placed in a 2000 ml closed glass container with heating and homogenizer arrangement for the vapours 31. The relative change in resistance ($A_r=\Delta R/R_0$) was recorded for different concentrations. Baseline corrected peak response was represented as $A_{r,p}$. The chemiresistors used in this work were prepared by compression moulding (Thickness~100 μm) followed by crosslinking by high energy radiation to impart sufficient strength to function as a standalone sensing film. The electrodes were prepared by piercing gold coated pins in the 100 μm thick PDMS/CNT composite sheet. PTFE guides were used to hold chemiresistors, without blocking the exposure and to minimize vibrations due to vapour flow.

5.4. Results and Discussion

5.4.1. Electrical properties of PDMS/ functional-CNT nanocomposites

DC electrical conductivity of PDMS/functional-CNT nanocomposites has been shown in Figure 5.1. PDMS/CNT-OH (hydroxyl functionalized) shows very poor conductivity where as PDMS/CNT-UF (unfunctionalized), PDMS/CNT-COOH (carboxyl functionalized) PDMS/CNT-NH_2 (amine functionalized) nanocomposites showed good conductivity. The type of functional groups on CNT was found to play a critical role in the electron transport in nanocomposite. PDMS/CNT-OH was found unsuitable for chemiresistive sensors due to this lower conductivity. Impedance is a measure of cumulative effect of inductance, capacitance and resistance present in a matrix. Its variation with AC frequency can provide important information about the type of electrical circuitry in matrix and conduction mechanism. AC conductivity value was measured for all nanocomposites and shown in Figure 5.2. PDMS/CNT-NH2 composites had the least impedance whereas PDMS/CNT-OH composites showed the highest impedance. It can be seen that impedance values were decreased with increase in frequency. Noteworthy, insulator type behaviour was observed in PDMS/CNT-OH composites over entire loading of CNT-OH (even at ϕ_{CNT}=0.004-0.06). On the other hand, all others nanocomposites having CNT-UF, CNT-COOH and CNT-NH_2 shows decrease in impedance values with increase in CNT loading. Impendence results clearly indicate a lower percolation threshold of CNT-NH2, CNT-COOH and CNT-UF than of CNT-OH in PDMS matrix. After ϕ_{CNT} =0.009, the impedance of PDMS/CNT-UF, PDMS/CNT-COOH, and PDMS/CNT-NH2 composites showed a plateau followed by a rapid decline after a particular frequency. This behaviour is attributed to the capacitive effect of the matrix at higher frequencies. This observation suggests that functionalization dependent changes in the development of a percolated network of CNT in the PDMS matrix.

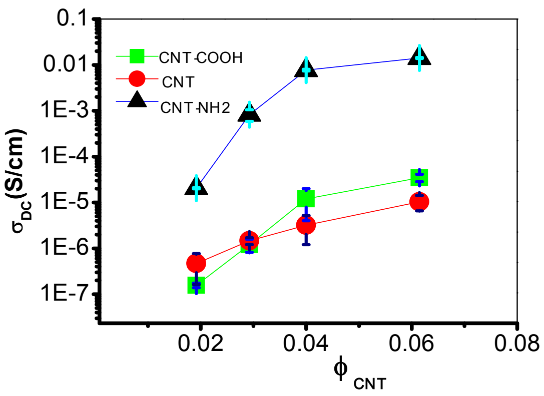

Figure 5.1: *DC electrical conductivity of PDMS/CNT nanocomposites containing different functionalized CNT.*

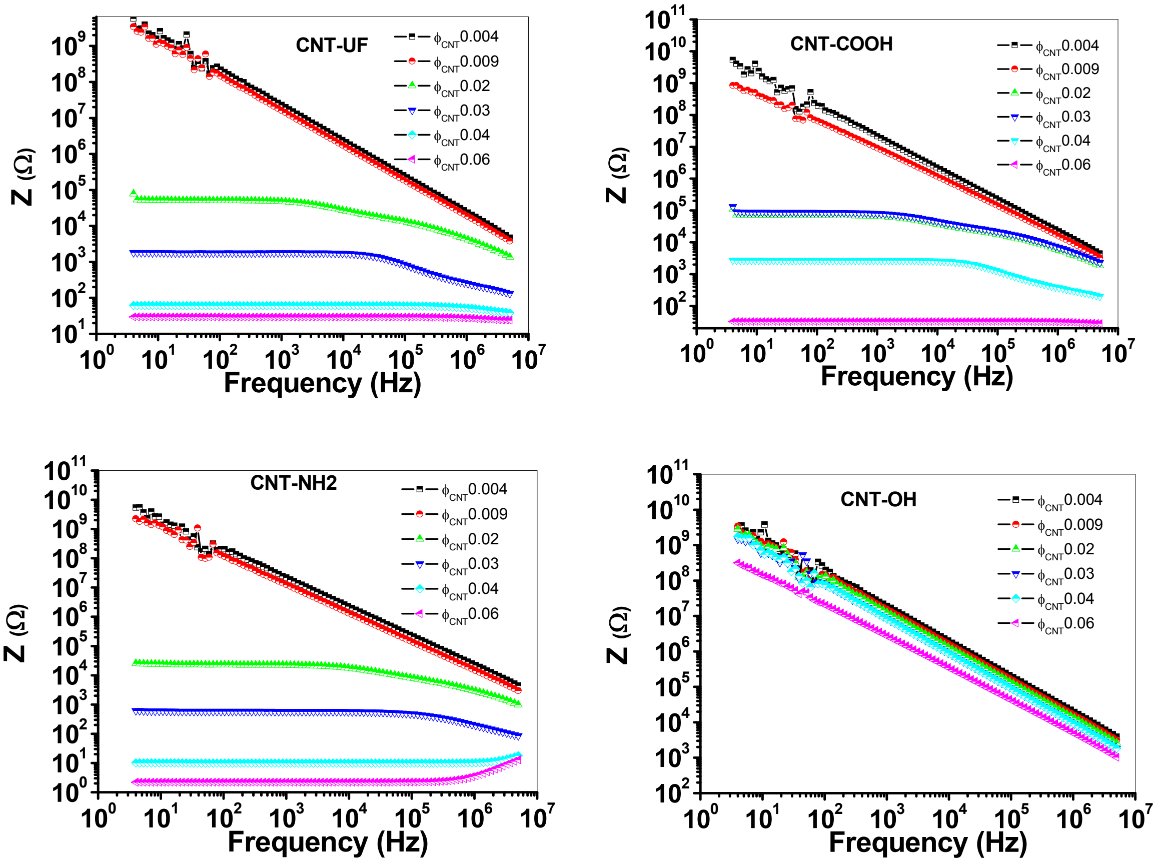

Figure 5.2: *AC impedance values of PDMS/functional-CNT nanocomposites having different volume fraction of CNTs with frequency.*

Furthermore, the critical frequency (ω_c) (i.e. the frequency after which rapid decline in the AC impedance was observed) was different for the composites of different functionalities, even at the same ϕ_{CNT}. For example, at ϕ_{CNT}=0.03, for PDMS/CNT-COOH CPC ω_c was 12.7 kHz whereas, for PDMS/CNT-UF CPC, it was 76.8 kHz and for PDMS/CNT-NH2 53.2 kHz. This difference in critical frequency reflects different mechanism of the electron transport in different CPCs. This is particularly important, as the emergence of the capacitive effect at an early frequency reflects inefficiency in terms of electron transport via tunnelling or hopping.

To understand the effects of CNT functionalities on electron transport and dielectric loss storage permittivity (ε') and loss permittivity (ε") were also evaluated. Figure 5.3A shows storage and loss permittivity with increasing frequency for CPCs having different functional CNTs. PDMS/CNT-OH CPCs had around 40 fold lower storage permittivity at 1 kHz than PDMS/CNT-COOH or PDMS/CNT-NH_2 CPCs. Nonetheless, in comparison to PDMS (storage permittivity~2.3, 1 kHz) the storage permittivity of PDMS/CNT-OH CPC (storage permittivity~6.2, 1 kHz) was about 3 fold higher. Generally CNT embedded in an insulating matrix is expected to behave as a microcapacitor and with the increase in the number of such microcapacitors, dielectric permittivity is expected to increase [294]. The markedly low storage permittivity of PDMS/CNT-OH CPCs can be attributed to the poor dispersion of hydroxyl functionalized CNTs in PDMS matrix, as was evident from the SEM analysis and high impedance. It may be noted that the agglomeration of CNT will reduce the overall surface area and thus the boundary layer responsible for capacitive effects.

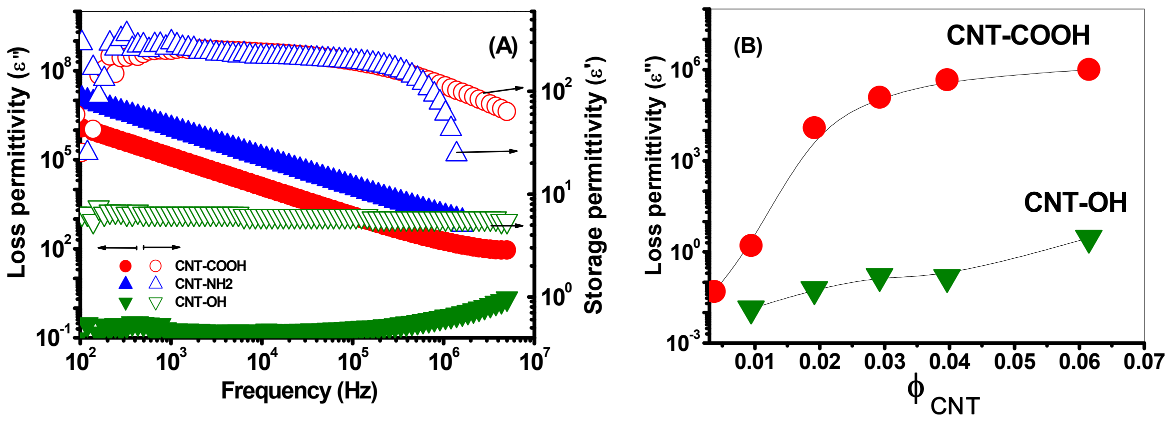

Figure 5.3: *(A) Effect of CNT functionality on Storage (ε') and Loss (ε") permittivity of PDMS/CNT composites. (B) Loss permittivity as a function of CNT loading.*

The loss permittivity increased with increase in ϕ_{CNT} (Figure 5.3 B). This increase may be attributed due to formation of more CNT-CNT interjunctions with increase in CNT concentration, as the dielectric loss is an indicator of leakages through electron transport. However, the dielectric loss of PDMS/CNT-NH_2 CPC was higher than that of PDMS/CNT-COOH CPC over entire frequency range, though the both of them had comparable storage permittivity between 1000 Hz- 0.1 MHz (Figure 5.3 A). In the experimental frequency range, 10 Hz- 10MHz, Maxwell–Wagner polarization and the contribution of dipole relaxations are expected to be negligible and mobility of electrons via tunnelling or hopping through CNT mainly responsible for the high dielectric loss [295, 296]. The major factor in facilitating electron transport within CPC is the interface between polymer and conducting filler, thus all these results points out better interfacial characteristics in PDMS/CNT-COOH CPCs than in PDMS/CNT-NH_2 CPCs. At higher frequency (>0.1 MHz), where the capacitive effect due to the matrix are prominent, there was the significantly lower rate of storage permittivity decline in PDMS/CNT-COOH than in PDMS/CNT-NH_2 CPC.

5.4.2 Linear and nonlinear rheology: Molecular entanglement and CNT-CNT network

Rheological analysis was expected to reveal critical information about the formation of the CNT percolated network in PDMS matrix, irrespective of electron transport (conductivity). Figure 5.4 shows the storage modulus values of unirradiated CPCs for different functionalized CNT. It can be seen that storage modulus (G') increase with increase in angular frequency for all CPCs. At higher frequency composite behave like solid and viscous or liquid like behaviour emerges at lower frequency. As ϕ_{CNT} increases this frequency dependence decreases gradually due to formation of CNT network and incomplete relaxation of polymer chains.

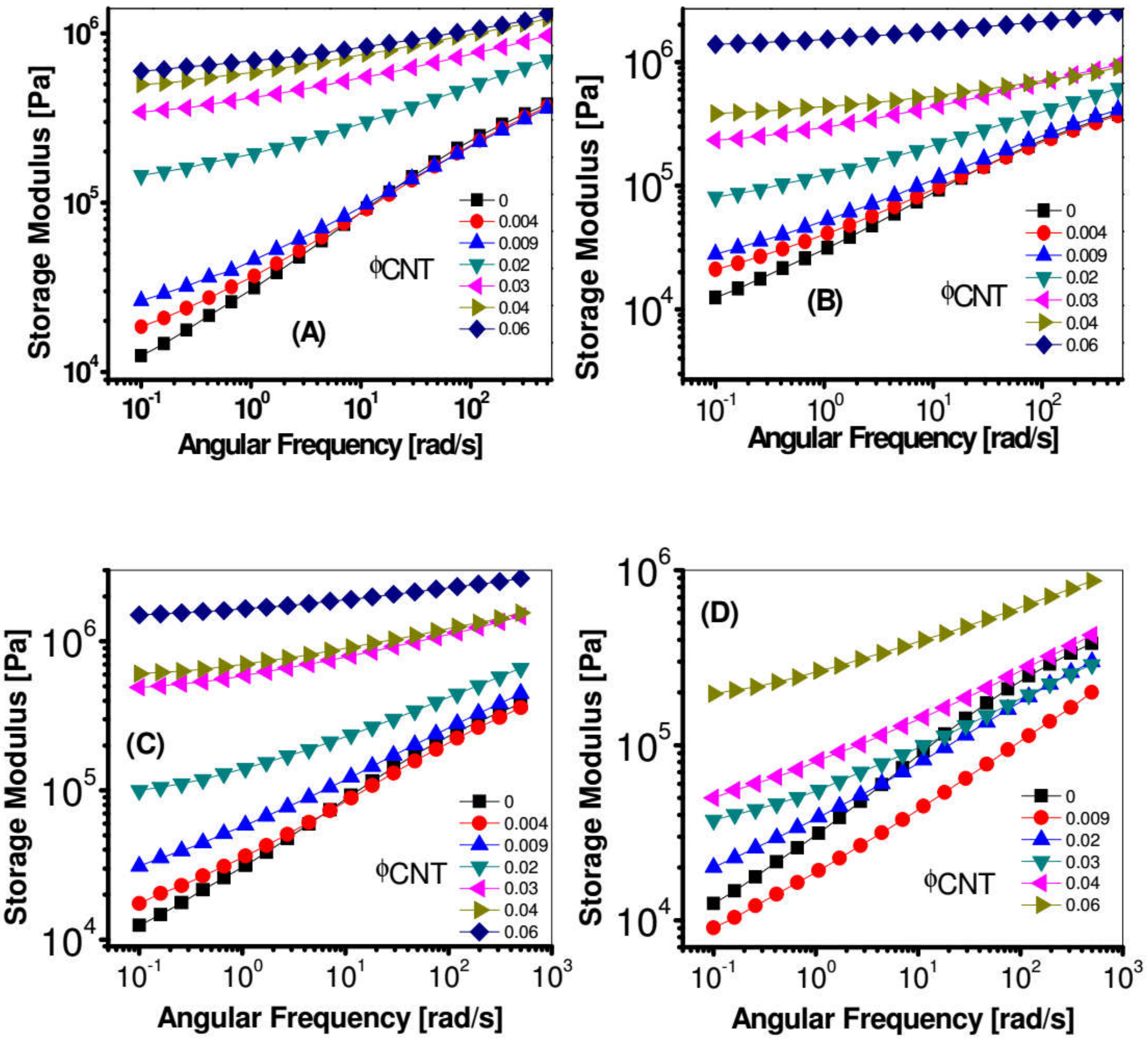

Figure 5.4: *Storage modulus of PDMS/functional-CNT nanocomposites containing different volume fractions of CNT of different functionalities, shear strain 1%, temperature 70 °C. (A) PDMS/CNT-UF (B) PDMS/CNT-NH_2 (C) PDMS/CNT-COOH (D) PDMS/CNT-OH.*

Figure 5.5 represents the changes in the shear storage modulus (G′) with an increase in CNT volume fraction for PDMS/CNT-OH and PDMS/CNT-COOH composites. It can be observed that PDMS/CNT-COOH composites had markedly higher storage modulus than PDMS/CNT-OH composites. This confirms better interactions between CNT-COOH and PDMS and the formation of the percolated network of CNT-COOH at lower fraction in PDMS/CNT-COOH nanocomposites.

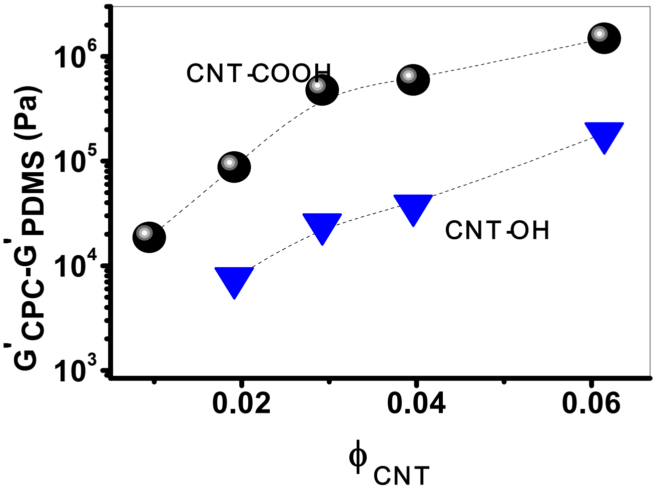

Figure 5.5: *Increase in storage modulus (G') with volume fraction of CNT for PDMS/CNT-COOH and PDMS/CNT-OH nanocomposites.*

Interfacial grafting and interaction of reinforcing filler with polymer chains are affecting stiffness of polymer composites which in turn governs entanglement of polymer chains in nanocomposites [297-299]. Linear oscillatory shear rheology data were further analysed to gauge the changes in the molecular entanglements in different CPCs. Molecular weight between entanglement (M_e) and shear modulus is related by following relation

$$M_e = {}^{\rho RT}\!/_{G'_0} \quad \textbf{(5.1)}$$

Where ρ is mass density, R is gas constant, T is absolute temperature and G'_0 is the shear storage modulus at angular frequency 0.1 rad/s. Density of such entanglement can be estimated by

$$\nu_e = {}^{\rho}\!/_{M_e} \quad \textbf{(5.2)}$$

It was found that with the increase in CNT vol fraction, an increase in entanglement density was observed for all CPCs with different functional CNTs (Figure 5.6). Highest entanglement was observed for PDMS/CNT-COOH and PDMS/CNT-UF where as lowest was for PDMS/CNT-OH nanocomposites. PDMS/CNT-NH_2 nanocomposites also have significantly lower entanglement densities compare to PDMS/CNT-COOH and PDMS/CNT-UF. These results highlight the significance of CNT functionalities on formation of entanglement and extend of physical crosslinking induced by CNTs.

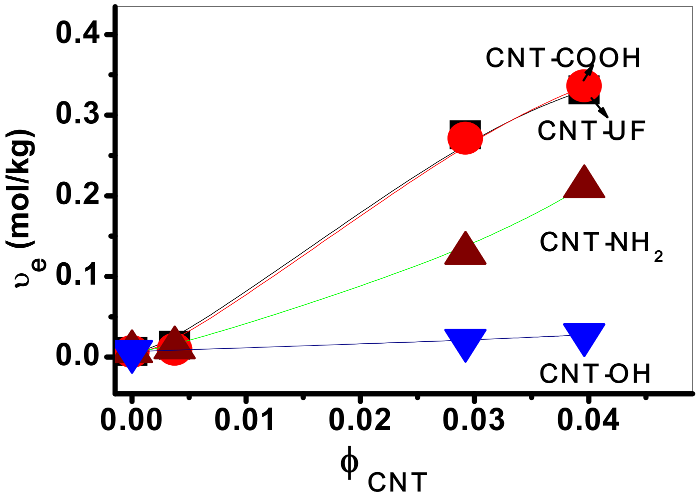

Figure 5.6: *Change in entanglement density as a function of CNT volume fraction.*

Nonlinear rheological measurement was employed to further analyze the finer difference between PDMS/CNT-UF and PDMS/CNT-COOH nanocomposites in terms of CNT-CNT network formation and structural break down. Dependence of the shear storage modulus with stain amplitude is presented in Figure 5.7. It can be seen that with increase in shear strain value storage modulus initially does not change much, after a critical strain modulus decrease precipitously and attain a plateau at higher strain. The quantitative extend of filler-filler and polymer- filler interface breakdown can be obtained by fitting the datas in phenomenological Kraus model [300]. This model is based on the agglomeration and deagglomeration of filler networks under shear strain and given by

$$G'(\gamma) = G'_{\infty} + \frac{G'_0 - G'_{\infty}}{1+(\gamma/\gamma_c)^{2m}} \qquad \textbf{(5.3)}$$

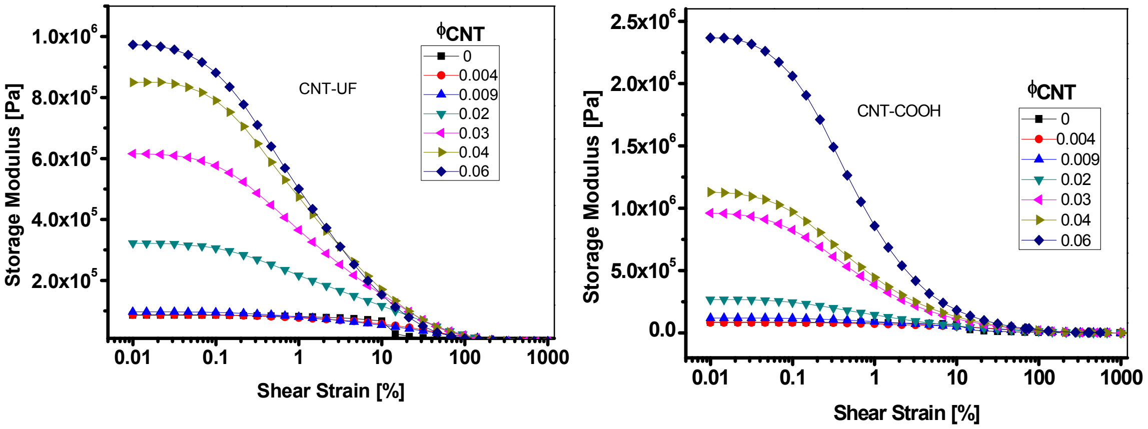

Figure 5.7: *Dependence of Shear storage modulus with shear strain for PDMS/CNT-UF and PDMS/CNT-COOH nanocomposites. Angular frequency 1 rad/s and temperature 70 °C.*

where G′(γ) is the shear storage modulus at shear strain γ ; G'_0 and G'_{∞} are shear storage modulus at very low and very high strain respectively, γ_c is the critical strain at which G′(γ) decreases to a value half of $(G'_0-G'_\infty)$. The number density of CNT interconnection changes in response to applied strain and depends on γ_c. The structure factor m is related to the fractal dimension and depends on the geometric quality of filler network. The experimental data for all composites fitted well with the Kraus model (Figure 5.8A in all cases: $R^2>0.99$). For PDMS/CNT-UF and PDMS/CNT-COOH CPCs critical strain γ_c as a function of ϕ_{CNT} is plotted in Figure 5.8B. It was observed that critical strain shifted to lower values with increase in CNT loading. Noteworthy, PDMS/CNT-COOH has higher critical strain than that of PDMS/CNT-UF CPCs for all CNT vol. fractions. Higher critical strain of PDMS/CNT-COOH nanocomposites means the composites can withstand more strain or deformation without disruption of CNT-CNT network irreversibly. The result highlights better interfacial interactions between CNT-COOH and PDMS compare to unfuctionalized CNT and PDMS [301]. It is evident that more chemiresistive stress is required to break CNT-CNT network in PDMS/CNT-COOH CPC than PDMS/CNT-UF composites highlighting better chemiresistive behaviour.

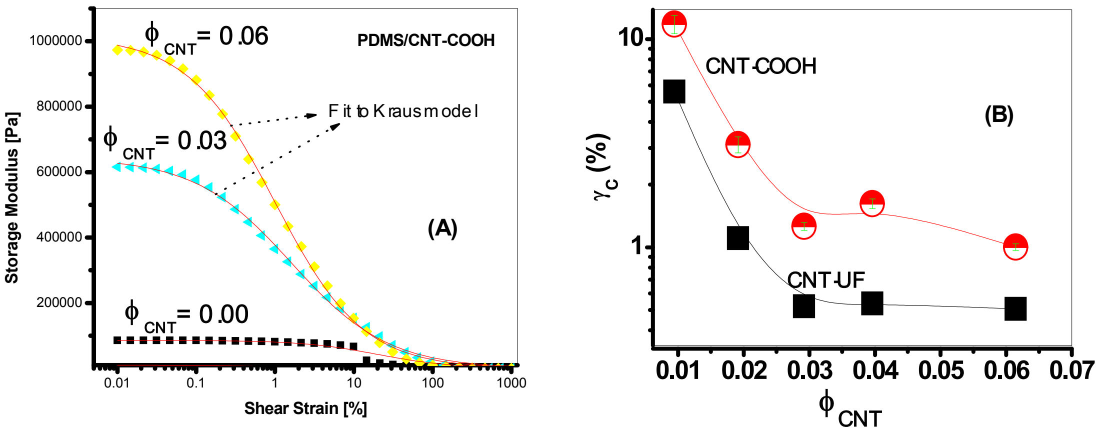

Figure 5.8: *(A) Kraus model fitted data for PDMS/CNT-COOH nanocomposites. (B) Change in critical strain with CNT vol fraction in PDMS/CNT-UF and PDMS/CNT-COOH nanocomposites.*

5.4.3 Effect of radiation dose on gel content and mechanical properties of nanocompoistes

The linear and nonlinear oscillatory rheological studies were performed on unirradiated CPCs, therefore only provides information about the physical crosslinks and interfacial characteristics. However, high energy radiation induced crosslinking of matrix and interfacial modification of chemiresistors which were ascribed to be main factor to enhance the chemiresistivity of PDMS/CNT-COOH CPCs (discussed in subsequent section). To evaluate this effect of high energy radiation, the gel content and the mechanical properties were estimated. The gel content of the irradiated chemiresistors (100 kGy) containing different CNT functionalities is shown in Figure 5.9 A. It can be observed that in both loading of CNTs gel fraction 0.8 was lowest for PDMS/CNT-NH_2 CPC; whereas highest for PDMS/CNT-COOH CPC (0.92). Additionally with increase in radiation dose gel fraction

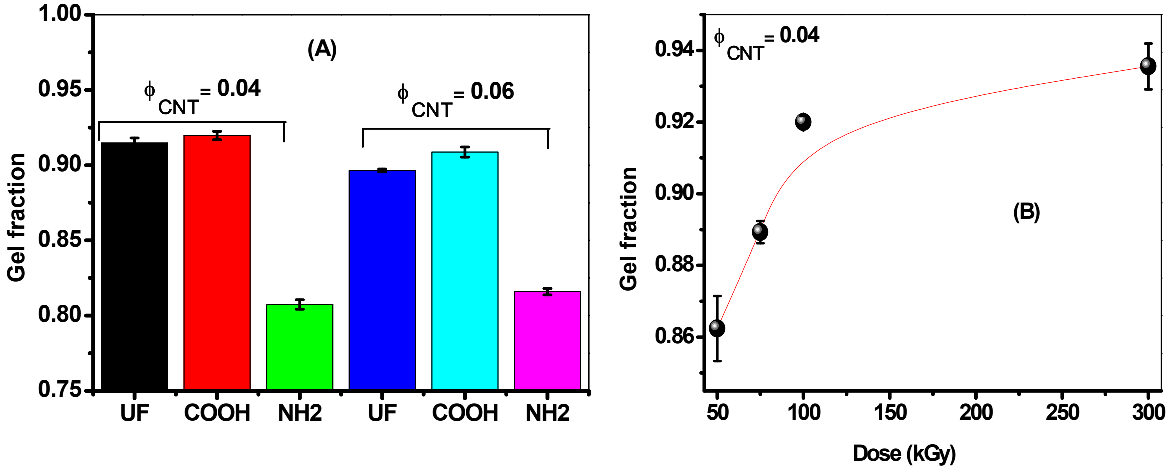

Figure 5.9: *(A) Gel fraction of PDMS/CNT nanocomposites irradiated to 100 kGy with different CNT functionalities. (B) Gel fraction as a function of radiation dose for PDMS/CNT-COOH nanocomposites*

increased upto 100 kGy after that it get saturated (Figure 5.9B). The gel fraction is an indicator of covalent crosslinking of polymer chains. It may be noted that high energy radiation induces covalent crosslinking in PDMS; whereas entangle density (ν_e) reflects only physical crosslinking/chain stiffening related factors. Around 12% lowering in gel content in PDMS/CNT-NH_2 composites than that of PDMS/CNT-COOH composites indicates the changes in the CNT-PDMS interfacial region. It worthwhile to mention that, diffusion of radicals forms in CNTs to bulk matrix are difficult considering the high viscosity of composites and short time frame of radiolytic transformations. Thus alternation (inhibition or acceleration) of radiation induced crosslinking by CNT is expected to be localized effect. Aromatic amines are well-known for inhibition of radical recombination [302-304]. A possible mechanism could be hydrogen abstraction by polymer radicals formed during the course of radiation from amine groups (Figure 5.10). Thus lower gel fraction obtained in case of amine functionalized CNT containing composite could be due to the fact that radiation induces radical formation and hydrogen abstraction from amine group. Since CNT has a large surface area, such effects are expected to play a major role in lowering gel contained in whole PDMS/CNT-NH_2 composites. On the contrary, better gel content and good interfacial interaction between polymer chain and filler obtained in PDMS/CNT-COOH and PDMS/CNT-UF was due to formation of better graft network of polymers into CNT surfaces and is primarily responsible for enhanced chemiresistivity. Uniaxial tensile stress-strain profiles of irradiated PDMS/CNT composites are shown in Figure 5.11. It can be seen that with radiation dose tensile modulus increase for all nanocomposites corroborating the radiation induced crosslinking of PDMS. While at a fixed radiation dose PDMS/CNT-NH_2 nanocomposite has lowest modulus and PDMS/CNT-COOH nanocomposite has highest modulus.

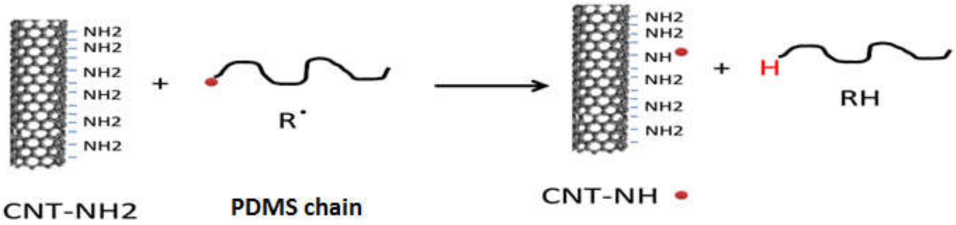

Figure 5.10: *Schematic representation of amine induced quenching of radicals via hydrogen abstraction in PDMS/CNT-NH_2 nanocomposites.*

It may be noted that all these nanocomposites have same loading of CNT only different is that they have CNT with different functionalities. These results highlighting that CNT functionality plays an important role in modification of radiolytic transformation of PDMS/CNT nanocomposites.

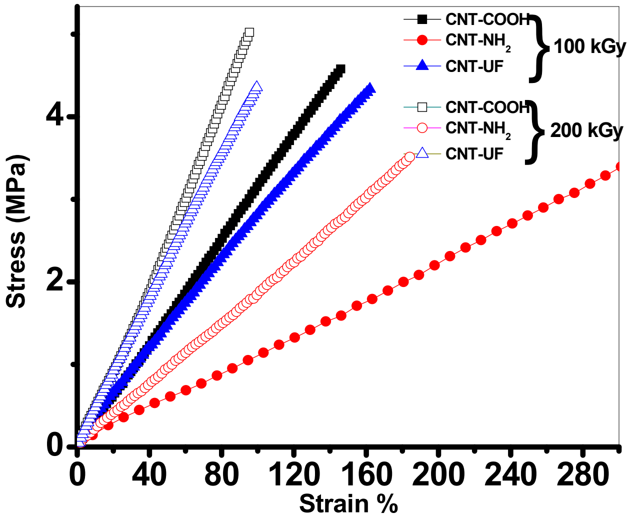

Figure 5.11: *Stress-strain profiles of irradiated (100 kGy and 200 kGy) PDMS/functionalized-CNT nanocomposites (ϕ_{CNT}=0.02).*

The departure of elasticity from ideal behaviour due to interfacial grafting and physical crosslinking in nanocomposites was estimated using Mooney-Rivlin equation [305].

$$\frac{\sigma}{(\lambda-\frac{1}{\lambda^2})} = 2C_1 + 2\frac{C_2}{\lambda} \qquad \textbf{(5.4)}$$

where σ is the tensile stress at the elongation ratio λ is ratio to final to initial length ($l/l_0=\varepsilon+1$). C_1 and C_2 are constants, reflecting characteristics of network. The value of C_2, which is an indicator of departure from ideal elastomeric behaviour due to interfacial grafting and physical crosslinks [306]. To make contribution of strain hardening negligible [307] low strain data of two nanocomposites, PDMS/CNT-COOH and PDMS/CNT-NH_2 were fitted to the above equation (eq. 5.4) and shown in Figure 5.12. It was found that the value C_2 for PDMS/CNT-COOH is 0.70 and for PDMS/CNT-NH_2 is 0.28. However, it may be noted that the applied strain range in tensile measurements is much higher than the shear strain imposed in linear rheology (1%). Together all these results, linear/ non-linear rheology and Mooney-Rivlin analysis revealed better interfacial interaction and better entanglement density and higher covalent linkages in PDMS/CNT-COOH CPCs.

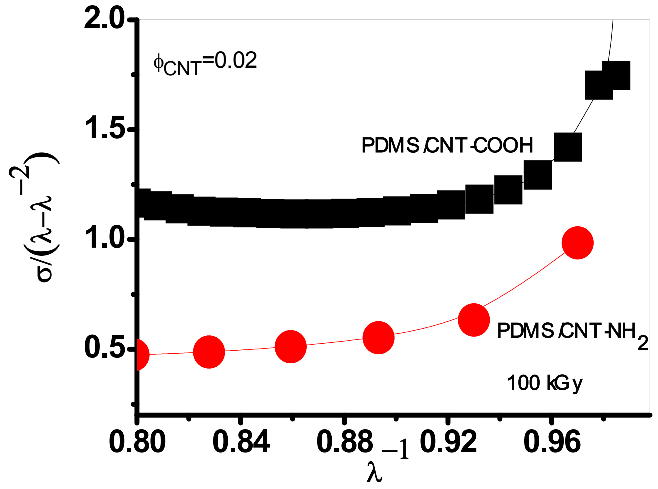

Figure 5.12: *Mooney-Rivlin plot for PDMS/CNT-COOH and PDMS/CNT-NH_2 CPC irradiated at 100 kGy.*

5.4.4 Surface energy, XPS analysis and morphological analysis of nanocompoistes

All of the above analysis pointed out the critical role of CNT functionalities in mechanical and electrical properties of nanocomposites. It must be noted that the variation in functional groups in CNT can not only affects electrical properties of CPCs but also the affinity towards other chemicals. However in subsequent section it will be pointed out that the major mode of chemiresistivity in PDMS/CNT CPCs is due to the interaction between analyte vapour and PDMS chain thus ruling out a significant contribution of functional group led intrinsic change in CNT. Surface energy is an important parameter playing a key role in determining the interactions of two matrices with different chemical potential, such as a chemiresistor and the chemical vapours [308]. The surface energy of the composites was therefore measured to understand the possible effect of functionalities of CNTs (Table 5.1). Figure 5.13 shows the relative change in the surface energy of the CPCs with the inclusion of functionalized CNT (ΔSurface Energy = Surface energy $_{\text{PDMS/CNT functionalized CPC}}$ –Surface energy $_{\text{PDMS/CNT-UF}}$). It was found that PDMS/CNT-NH_2 composites had the highest surface energy whereas the PDMS/CNT-COOH composites had the least. This lowering of surface energy further suggests better polymer-filler interactions in PDMS/CNT-COOH CPC [309].

Table 5.1: Contact angles, dispersive, polar and total surface energy of PDMS/CNT nanocomposite.

Sample	**Water contact angle (^{o})**	**CH_2I_2 contact angle (^{o})**	**Surface Energy (mJ/m^2)**	**Dispersive (mJ/m^2)**	**Polar (mJ/m^2)**
PDMS/CNT-UF	100.5±1.05	70.6±1.09	24.08±0.21	22.54±0.17	1.52±0.04
PDMS/CNT-COOH	109.6±0.66	83.4±2.66	16.66±0.42	15.79±0.37	0.87±0.06
PDMS/CNT-OH	108.5±0.61	62.6±5.80	27.17±1.09	27.08±1.08	0.09±0.04
PDMS/CNT-NH_2	109.7±0.2	53.7±3.50	32.19±0.70	32.10±0.6	0.01±0.01

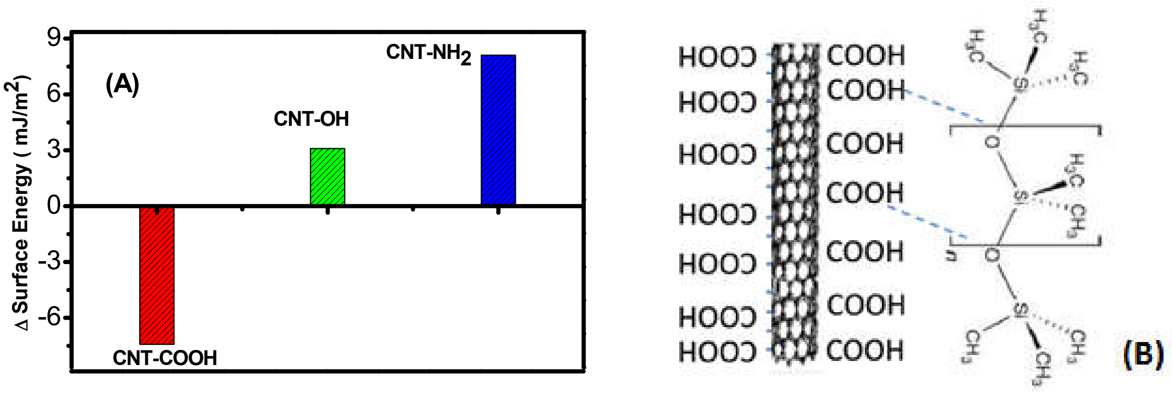

Figure 5.13: *(A) Change in the surface energy of different CPCs with functionalized CNT, with respect to PDMS/CNT-UF nanocomposite;* $\phi_{CNT}=0.06$. *(B) Schematic representation of possible polar-polar interactions between CNT-COOH and PDMS*

It was expected that COOH group is involved in dipolar interaction with oxygen atom presented in PDMS. This allows wrapping of CNT-COOH surfaces by PDMS polymer chains and leading to better interfacial characteristics. It may also be noted that such wrapping by PDMS chains will lead to encapsulate the polar groups of CNT and leaving nonpolar methyl groups at the outer surface (Figure 5.13B). Lowering of the surface energy of PDMS/CNT-COOH nanocomposites corroborates this assumption also. Similar results were also observed by Khare et al. on the effect of carbon nanotube functionalization in transferring the mechanical load across the matrix-filler interface in a cross-linked nanocomposites [310]. The chemiresistivity of a CPC, essentially, relies on the efficiency of the stress transfer from the matrix to the filler i.e. the overall disruption of conducting networks due to chemical-induced relaxation of polymer chains. When a matrix-filler interface is very weak, the interface region in the nanocomposites becomes more compressible thereby attenuating the effect of chemical-induced relaxation of polymer chains and vice-versa.

XPS analyses were performed to understand the differences in the functional groups present at the surface PDMS/CNT composites. Figure 5.14 shows wide scan XPS spectra of different composite and also the characteristics peaks of O1s (529.3 eV), C1s (282.4 eV), Si 2s (152.0 eV) and Si 2p (101.0 eV) are identified [311, 312]. Since C1s is expected to include information about functional groups on CNT, a detailed analysis of C1s spectra was done from the deconvolution of functional groups peaks which can be clearly recognized (Figure 5.15 A-D). Gaussian curve fitting reveals four distinct peaks of C 1s depending upon chemical environment of carbon atom; (i) C-C, C=C, and C-H were appeared at 284.6 eV [312] (ii) C-O, C-N and C-Si were appeared at 285.8eV [312, 313] (iii) C=O was at 286.8 eV [312] and (iv) COO was at 288.9 eV [312].

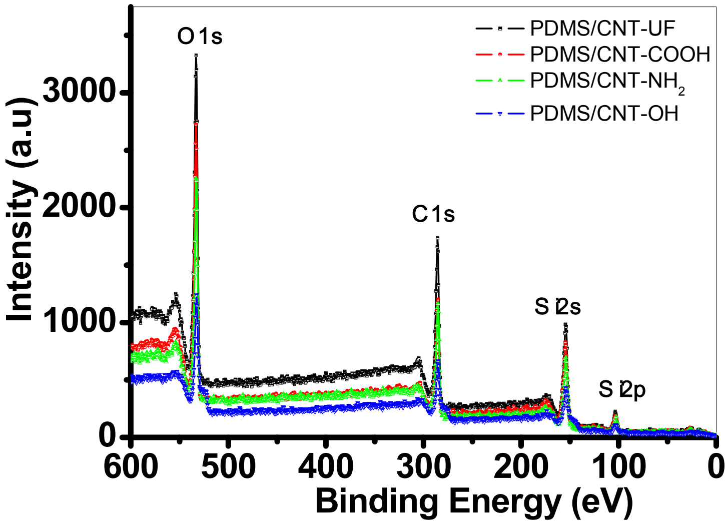

Figure 5.14: *Wide scan XPS spectra of PDMS/CNT composites with different CNT functionalities.*

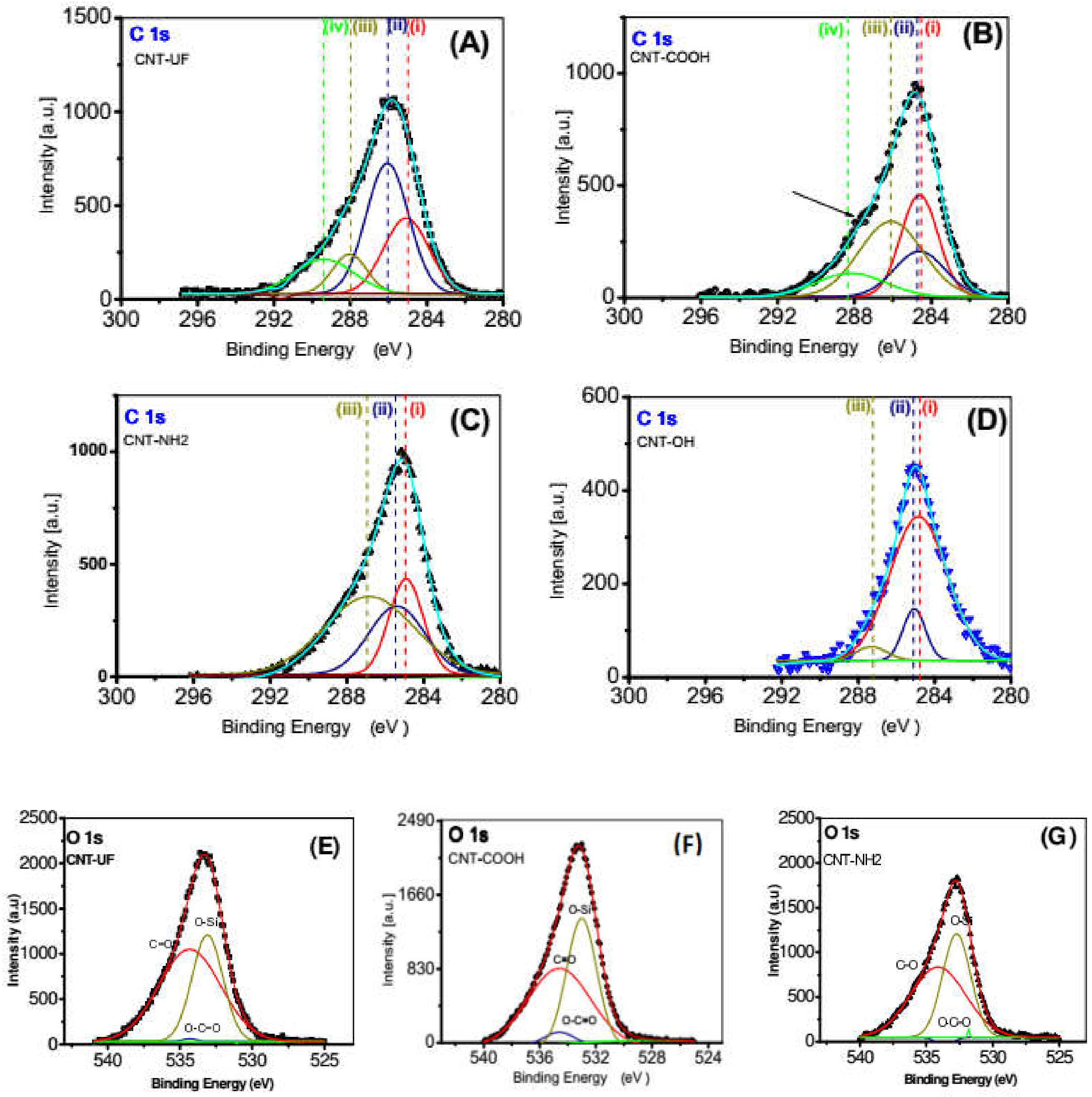

Figure 5.15: *Deconvolouted XPS spectra of PDMS/CNT nanocomposites (A) C1s CNT-UF (B) C1s CNT-COOH (C) C1s CNT-NH_2 (D) C1s CNT-OH (E) O1s CNT-UF (F****)*** *O1s CNT-COOH (G) O1s CNT-NH_2* **.**

In addition to the main peak at 285 eV significant additional photoemission at higher binding energy was observed for all nanocomposites except PDMS/CNT-OH. Notably, the asymmetry of the main peak around 285 eV is clearly evident for all nanocompostes. Among them PDMS/CNT-COOH CPCs gives most asymmetrical shape having a shoulder in higher binding energy and PDMS/CNT-OH nanocomposite gives most symmetrical one. Analysis of O 1s spectra reveals presence of carboxylic group in in surface of CNT-UF and CNT-COOH nanocomposites. Whereas, this peak was absent in PDMS/CNT-NH_2 and PDMS/CNT-OH based chemiresistors [314]. As discussed in the previous section that, even at the fixed CNT loading the dispersion and distribution of CNT in the PDMS matrix can be greatly varied. Therefore, no attempt was made to correlate the observed peak with the concentration of a functional group in the composites.

Cryofracture SEM images of PDMS/CNT-COOH and PDMS-OH composites are shown in Figure 5.16 A-D. It is evident from the micrograph that CNT-OH forms agglomerated domains within the PDMS matrix; whereas, CNT-COOH was well distributed. The optical micrographs also confirm the poor dispersion of CNT-OH in PDMS (Figure 5.16E and F). The good dispersion of CNT-COOH in PDMS matrix is also predicted by surface energy and electrical conductivity results of composites. The better dispersion of CNT-COOH not only increase electrical conductivity, lowering percolation of CNT-COOH into PDMS matrix but also enhances the chemiresistivity towards toluene vapour compare to other nanocomposites. On the other hand the poor dispersion of CNT-OH is mainly responsible for poor electric conduction and hence unsuitability of such composites for chemiresistive applications. Also markedly low storage permittivity and high impedance value of PDMS/CNT-OH CPCs can be attributed to the poor dispersion of hydroxyl functionalized CNTs in PDMS matrix as was evident from the SEM analysis.

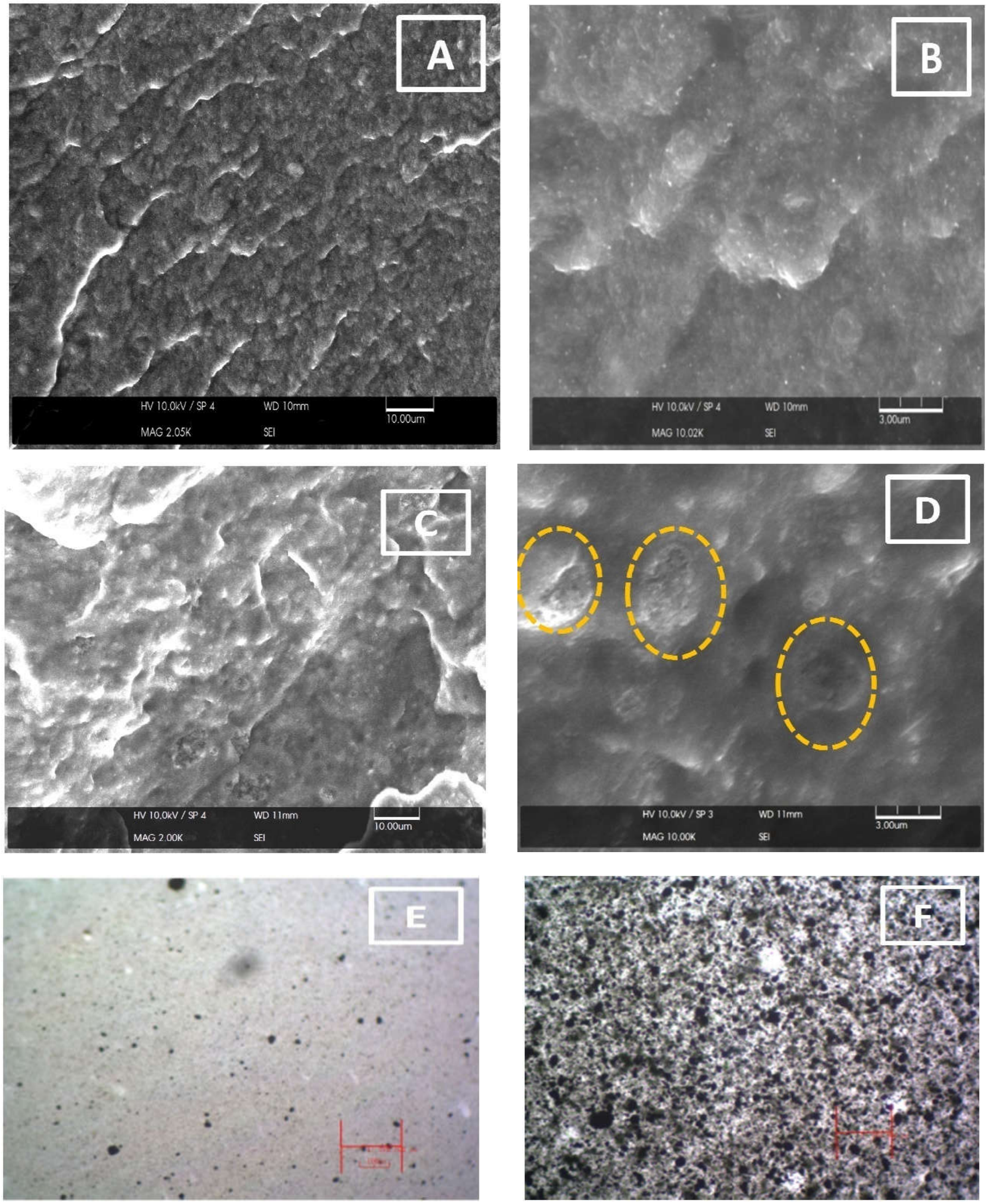

Figure 5.16: *SEM of cryo-fractured PDMS/CNT composite, ϕ_{CNT}=0.06 (A) PDMS/CNT-COOH, 2kX (B) PDMS/CNT-COOH, 10kX (C) PDMS/CNT-OH, 2kX(D) PDMS/CNT-OH, 10kX, Optical image of (E) PDMS/CNT-COOH (F) PDMS/CNT-OH.*

5.4.5. Chemiresistive behaviour of nanocomposites

5.4.5.1. Effects of different functionality of CNT on chemiressitivity

Radiation crosslinked PDMS/CNT-UF, PDMS/CNT-COOH and PDMS/CNT-NH2 CPCs exhibited reversible chemiresistive behaviour for toluene vapour. All of these CPCs on exposure to toluene vapours showed a concentration-dependent increase in the resistance. Figure 5.17A shows the relative changes in the resistance of crosslinked CPCs with CNTs having different functional groups. All chemiresistors were exposed to the successive cycles of toluene vapour (100 to 1000 ppm) and air. The signal was reversible in nature as the atmosphere changed from toluene vapours to air. Typically response time (90 % of the peak response, t_{90}) was found to be 90 sec, the resistance dropped rapidly to the half of the peak value t_{50} within 30 seconds. The response of chemiresistor containing carboxyl functionalized CNT was considerably higher at all concentrations than those containing un-functionalized CNT or amine functionalized CNT. Figure 5.17B shows the baseline corrected peak sensing response ($A_{r,p}$) of different chemiresistors for the different toluene concentrations.

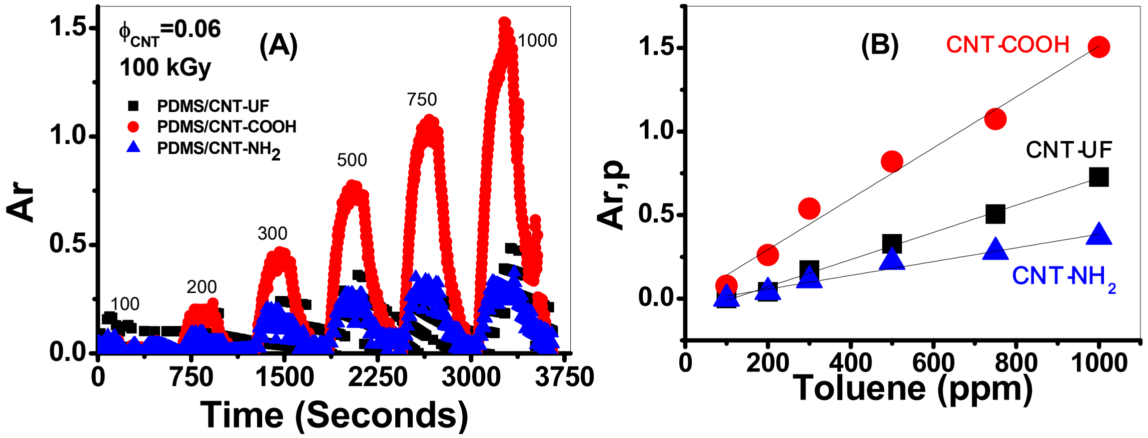

Figure 5.17: *(A) Chemiresistivity of PDMS/CNT nanocomposites having different functionalized CNT (B) Linear fit of base line corrected peaks.*

In the studied concentration range (100-1000 ppm) the sensing response was found to be linear. The sensitivity of the sensor was estimated from the slopes of respective graph. It can be seen that sensitivity was followed the order: CNT-COOH>CNT>CNT-NH_2. At 1000 ppm, about 6 times higher responses were observed for PDMS/CNT-COOH chemiresistor than for PDMS/CNT-NH_2 based chemiresistor. The basic mechanism behind the change in resistance in CPC based chemiresistors is the changes in the conducting network architecture due to the strain imposed by the relaxation of polymer chains resulting from polymer chain-chemical vapour interactions. In CPC based chemiresistors, power-law dependence of sensing response on the vapour concentrations is often advocated considering adsorption, diffusion and clustering. But in current study CNT percolated chemiresistors were used, which has much higher aspect ratio than the conventional conducting filler such as carbon black and metallic powders thus more long-range interconnectivity of conducting CNT-CNT junctions is possible. Such an increased range of interconnectivity allows electrical conduction even at higher concentrations of the toluene, entailing a linear chemiresistive response over a wide concentration range.

Measurement of AC impedance values of CPC based chemiresistors under toluene field give an insight into electrical conduction mechanism and sensing mechanism of chemiresistive matrix. Impedance Z includes imaginary and real component. The real component Z' is the measure of resistance of the composites and the imaginary component Z'' reflects the reactance of the composites. The plot two components is a semicircle and can be represents by following relation.

$$\left(Z' - \frac{2R_a + R_c}{2}\right)^2 + Z''^2 = \left(\frac{R_c}{2}\right)^2 \qquad \textbf{(5.5)}$$

where R_c is contact resistance and R_a is the resistance of CNT aggregates. Figure 5.18 shows the effect of toluene field on the electrical impedance of the PDMS/CNT-COOH chemiresistor. The presence of a single semicircle in all chemiresistors is an indication of single relaxation time.

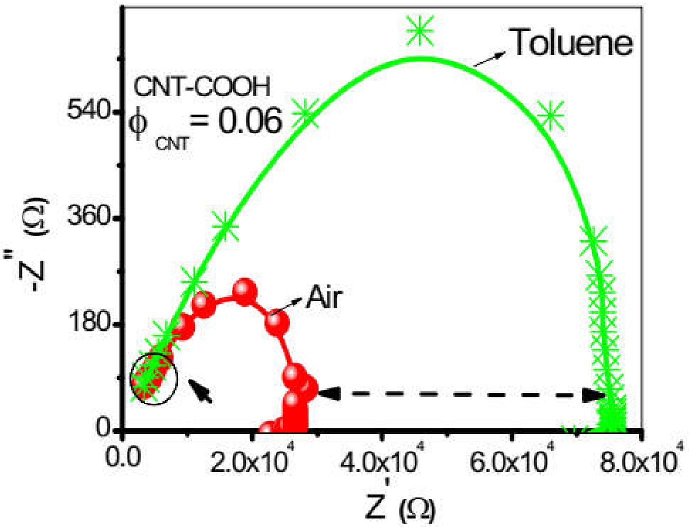

Figure 5.18: *Imaginary and real part of impedance under air and toluene vapour for PDMS/CNT-COOH chemiresistor.*

In the percolation region of a conducting composite the electrical conduction can be described as resistor-capacitor series. The electrical conductivity of such chemiresistors depends upon several factors such as contact resistance (R_c), the resistance of CNT aggregates (R_a) and the gap between aggregates (d_a). The contribution of d_a in the electronic transportation of chemiresistor can be represented by parallel plate capacitor. The capacitance of such a capacitor depends on the material's dielectric constant, the contact area and the separation between the CNT aggregates. It is obvious from the Figure 5.18 that both curves overlap in the initial region but in the terminal region significantly departure was observed (marked with arrows). The results entails that there was a significant change in R_c while changing the environment from air to toluene. R_c in case of an semicircle can be estimated from its radius whereas R_a can be estimated from the position of its centre (Eq. 5.5). As PDMS and toluene both have similar dielectric constant, there should not be any significant change in dielectric constant of the medium that could affect capacitive resistance at high frequency. Therefore, the observed chemiresistivity is primarily responsible for higher value of R_c. The CPCs upon exposure to toluene leads to higher contact resistance by increasing the gap between CNTs, thereby hindering the electron transport [315].

5.4.5.2 Effects of CNT loading on chemiressitivity

Figure 5.19 shows chemiresistive behaviour of PDMS/CNT-COOH composites for two different loading of CNT-COOH against toluene vapour (100-1000 ppm). Both of these composites give linear increase in response with increase in toluene concentration. However, it can be seen that higher response was observed for lower loading of CNT-COOH. Indeed sensitivity, which was gauged from the slope of the curve showing in Figure 5.19B, was three times higher for $\phi_{\text{CNT-COOH}}=0.03$ than $\phi_{\text{CNT-COOH}}=0.06$ chemiresistor. Notably, it is expected that the cumulative interfacial layers length as well as the tendency to form agglomerates increase with increase in CNT-COOH loading. In addition to that the number of CNT-CNT interconnections was expected to be higher at higher loadings, as was evident from the lower resistance of $\phi_{\text{CNT-COOH}}=0.06$ than $\phi_{\text{CNT-COOH}}=0.03$. In case of higher loading, where more CNT-CNT interconnections are present, more chemiresistive stress will required to disturb the electron conduction thus decreasing the sensitivity. The relative change in the impedance with an increase in frequency for $\phi_{\text{CNT-COOH}}=0.03$ and $\phi_{\text{CNT-COOH}}=0.06$ chemiresistors under toluene and air is shown in Figure 5.19C. It was anticipated that the critical frequency (where impedance value decrease sharply) was much higher at higher loading; interestingly, however, under the toluene field, at $\phi_{\text{CNT-COOH}}=0.03$ there was a significant change in critical frequency but at $\phi_{\text{CNT-COOH}}=0.06$ the change is not that sharp. Such effect confirms that chemiresistive effect was more pronounced in the $\phi_{\text{CNT-COOH}}$ =0.03 composites. This can be attributed to the fact that the density of the CNT-CNT network is lower at lower loading of CNT-COOH; such chemiresistors are therefore more prone to substantial change in resistance due to the increased gap between CNTs under toluene field [316]. It may be noted that the decrease in gel content with increase in CNT-COOH from 0.03 to 0.06 was negligible (~0.01 i.e. <2%); therefore, the changes in the gel content are not expected to contribute much to the observed higher chemiresistivity of at 0.03 $\phi_{\text{CNT-COOH}}$.

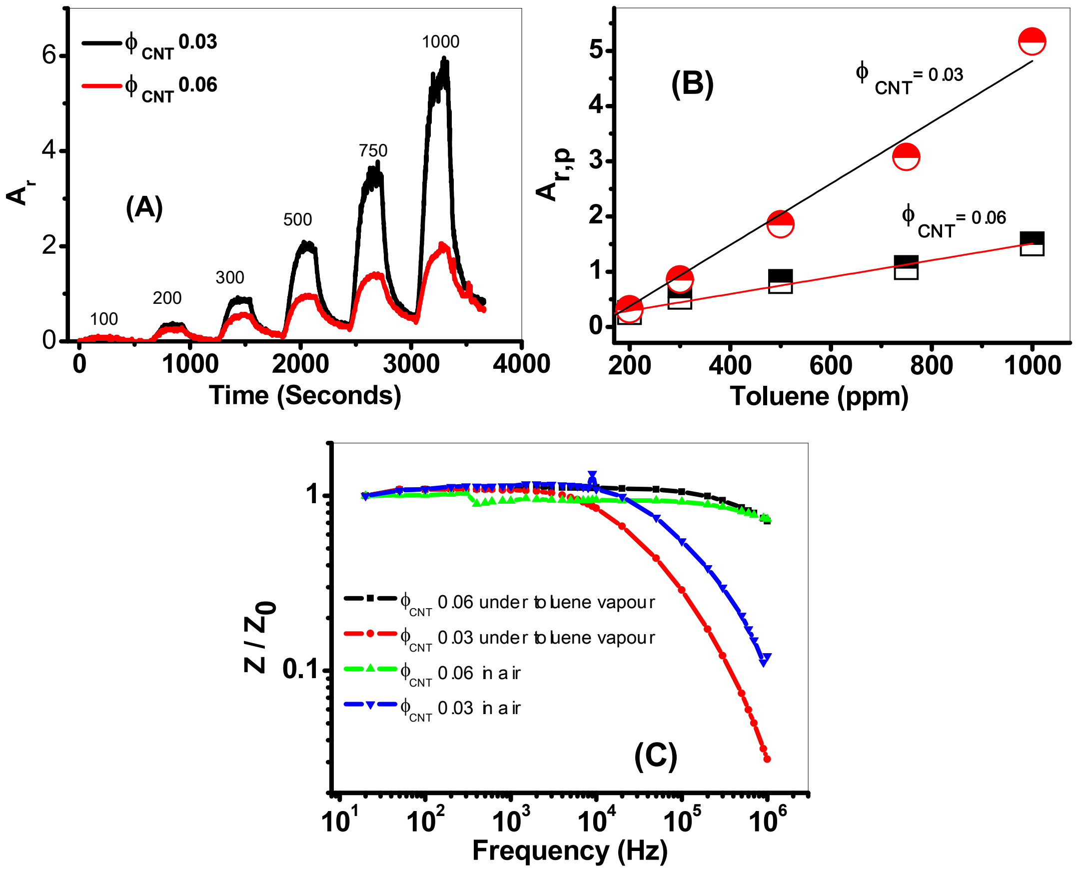

Figure 5.19: *Effect of CNT-COOH volume fraction on chemiresistivity (A) Sensing responses for PDMS/CNT-COOH CPCs with increasing concentrations of toluene (B) Relative peak change in resistance at different concentrations and linear fit of the data (C) Relative change in impedance in air and in the presence of toluene.*

5.4.5.3 Effects of radiation dose on chemiresistivity

Effect of radiation dose on chemiresistive behaviour of PDMS/CNT-COOH chmiresistors is shown in Figure 5.20A-C. The chemiresistors irradiated to different radiation doses were exposed to several cycles of toluene-air with increasing concentration of toluene. It was observed that upto 100 kGy, there was a significant increase in sensing response and then response get saturates (Fig 5.20B). The sensitivity of the chemiresistor was estimated from the slope obtained after a linear fit of sensing response (A_r) versus concentration curve and presented in Figure 5.20C. It can be seen that the sensitivity increases up to 100 kGy and saturates thereafter.

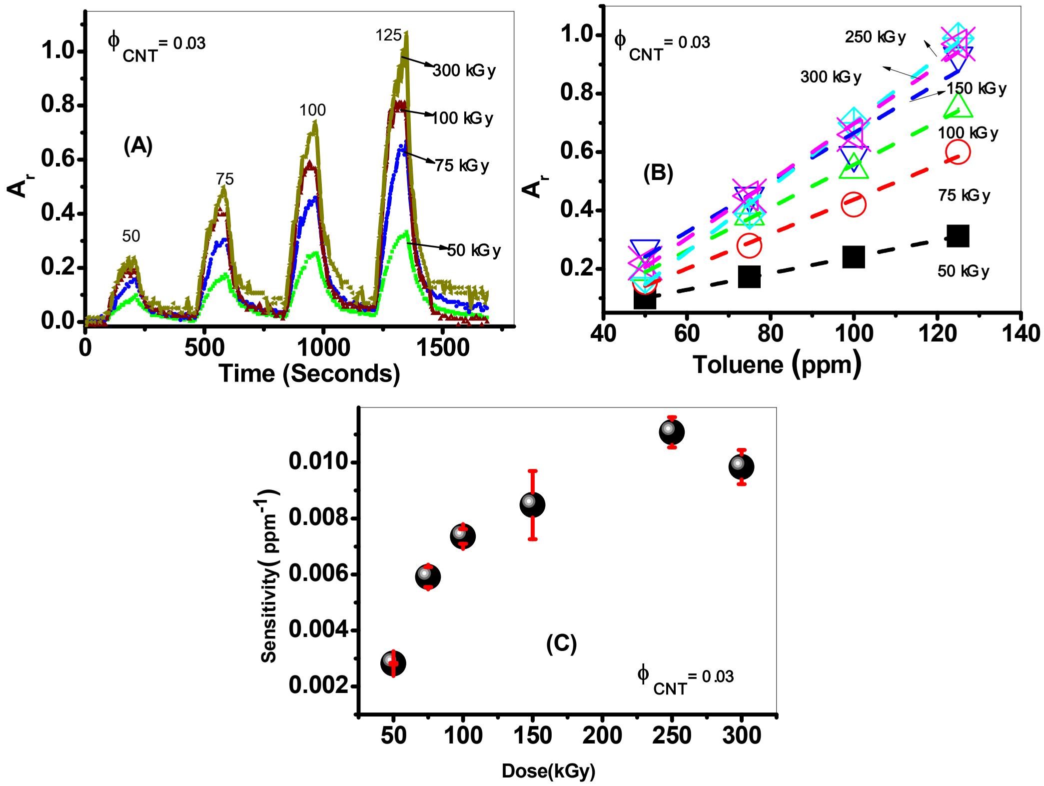

Figure 5.20: *Effect of radiation dose on chemiresistivity (A) Sensing responses of PDMS/CNT-COOH composites irradiated at different radiation doses. (B) Relative peak change in resistance at different concentrations at different doses and linear fit of the data (C) Variation of sensitivity with radiation dose.*

Generally with radiation dose the crosslinking density and gel content is expected to increase. Theoretically gel content can attain a value of 1 whereas crosslinking density keeps on increase with dose. At high crosslinking density mesh size decreases which results a decrease in permeability of analyte molecules inside polymer matrix as well. In PDMS/CNT-COOH chemiresistor gel content increased up to 100 kGy (Figure 5.9B) and saturates thereafter. This close similarity between gel content-dose and the sensitivity-dose profiles supports the hypothesis that radiation assists the formation of PDMS-CNT linkages. It can be stressed that radiation can generate radicals both on CNT and on polymer chains which may subsequently recombine to form crosslinking network in bulk and/or may lead to form grafting of polymer chain in CNT surfaces (Figure 5.21 A).

In previous section it was found that in PDMS/CNT naocomposites, there were formations of physical crosslinks, molecular entanglements and/or immobilization of polymer chains at CNT interface. It was also suggested that upon irradiation radiaolytic transformations in bulk was different from the interfaces thus polymer chain density/arrangements at the CNT interface will be different from bulk. To confirm this, effects of chemiresistive behaviour of unfunctionalized chemiresistors were also monitored (Figure 5.21B). Sensing response was found to increase with radiation dose for PDMS/CNT-UF chemiresistors as well, although the magnitude of response was much less than that of PDMS/CNT-COOH chemiresistors. This observation further confirms that the enhancement in chemiresistivity was primarily due to CNT-PDMS interfacial characteristics and was not much dependent on the bulk characteristics of irradiated CPCs. The impedance profile of the composites irradiated to different doses is shown in Figure 5.21C. It can be found that with the increase in radiation dose, the critical frequency shifted to a lower value, confirming the radiation-induced modifications of the interface and dominance of capacitive effects due to radiation-induced grafting/crosslinking at CNT-polymer interface.

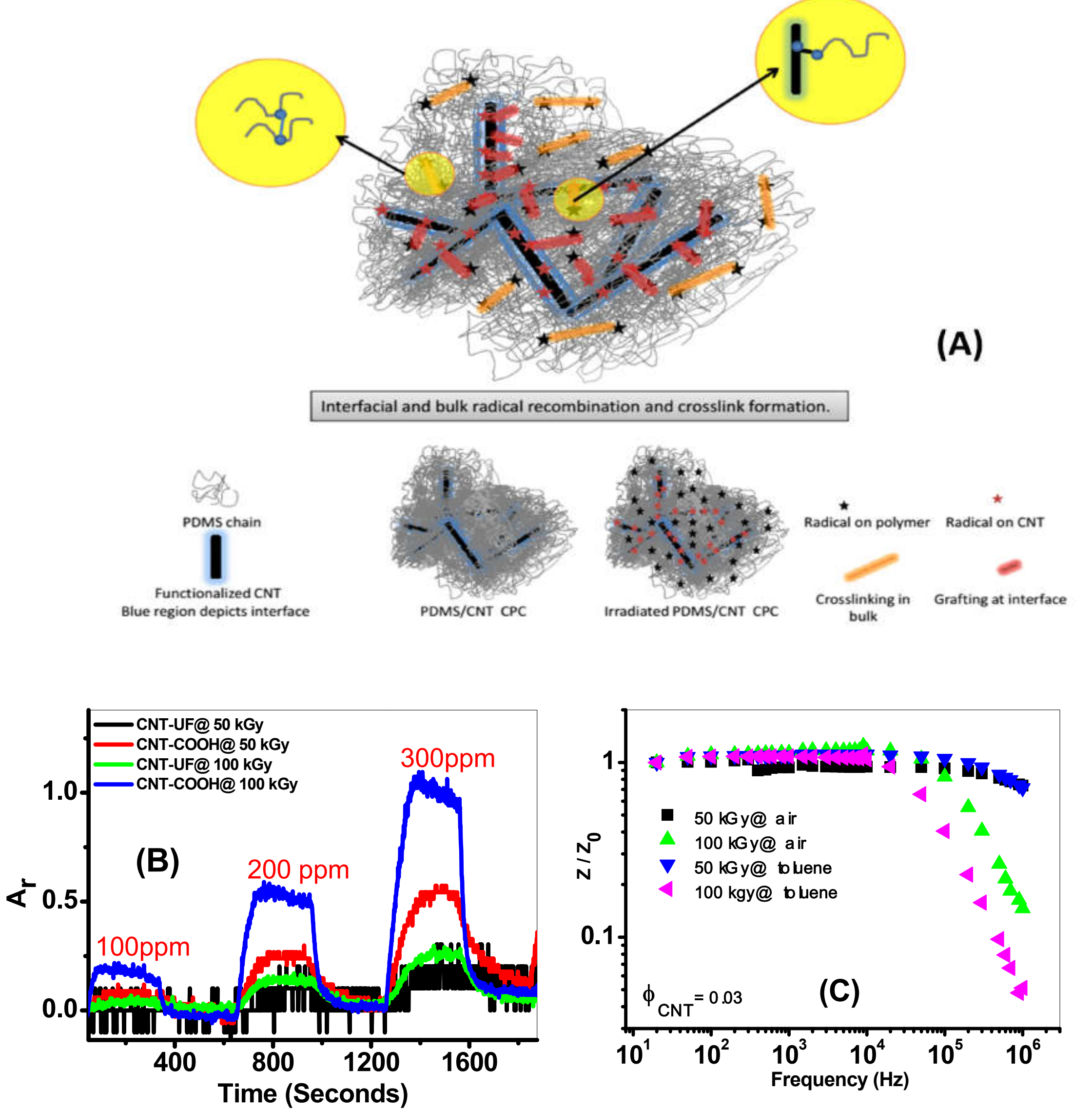

Figure 5.21: *(A) Schematic representation of PDMS/CNT interface and crosslinks in bulk and interface. (B) Relative change in resistance for irradiated PDMS/CNT-COOH and PDMS/CNT-UF chemiresistors with increasing concentrations of toluene vapour (C) Relative change in impedance in air and in the presence of toluene (500 ppm).*

5.4.5.4 Selectivity, reproducibility and detection limit of the chemiresistor

The response of PDMS/CNT-COOH chemiresistor against different analyte vapours is shown in Figure 5.22A-B. Upon exposure to different VOC vapours, the sensing response builds up rapidly and saturated in about 100 seconds. It was observed that toluene exhibited highest response and then followed by benzene, chloroform, acetone, ethanol, and methanol. Negligible response was obtained for water (does not show in graph). The saturated response of an analyte relative to that of toluene is shown in Figure 5.22B. The cross sensitivity of chemiresistors which was obtained by normalising the sensing response of other VOCs with respect to the response toluene vapours. It was about 0.4 for benzene and was less than 0.1 for other VOCs.

The interaction of an analyte with the polymer composite based chemiresistive matrix depends on both kinetic and thermodynamic factors. Primarily, a chemiresistive stress within the CPC matrix was developed due to the diffusion of analyte molecules and relaxation of the polymer chains. This disrupts the electron transport in the matrix and leading to an increase in the resistivity of the matrix. The magnitude of the interaction between polymer and analyte can be expressed in terms of Flory-Huggins interaction parameter (χ_{12}). χ_{12} depends on the solubility parameter of the polymer and the analyte and related to sensing response by

$$A_r = ae^{b(\chi_{12})^{-n}} \tag{5.6}$$

The sensing response of PDMS/CNT-COOH is plotted against χ_{12} in Figure 5.22B inset. It can be seen that the sensing response decreased with an increase in χ_{12}. The equation 5.6 fitted well (R^2>0.99) for composites, suggesting the dependence of the response of the sensor on the polymer-filler interaction parameter. Since polymer filler interactions originate from the thermodynamics of the system, the high selectivity towards toluene can be attributed to the relaxation of the PDMS chains under toluene atmosphere. Such a relaxation will build stress within the matrix, increasing inter-aggregate distance within the percolated CNT networks [317].

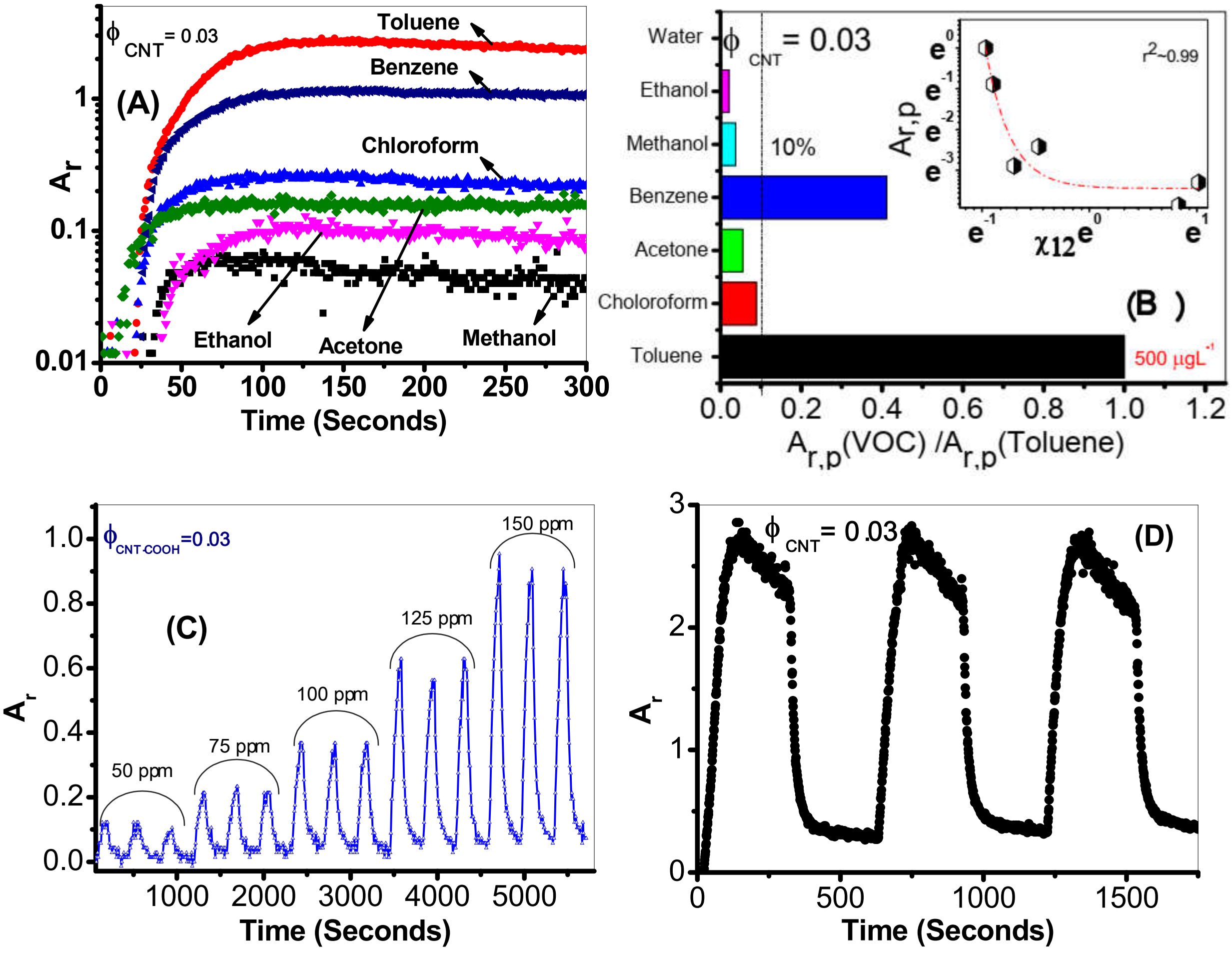

***Figure 5.22**: Selectivity and reproducibility of the chemiresistor (A) Sensing response for PDMS/CNT-COOH chemiresistors in the presence of vapors of different VOCs (500 ppm) (B) Normalized response of different VOCs with respect to the response of toluene (A_r(VOC)/A_r(toluene)) ; inset shows fitted data in eq.5.6 (C) Change in A_r after exposure to successive air-toluene cycles, three cycles of a fixed concentration were used followed by increased concentrations. (D) Reproducibility of PDMS/CNT-COOH chemiresistors against toluene vapour.*

Sensitivity and reproducibility of the sensor are presented in Figure 5.22C and D respectively. The chemiresistor was exposed to three successive exposure cycles of a fixed concentration followed by three successive cycles of increased concentration. The signal was reversible and reproducible. The sensor attained 90% of peak response in about 90 seconds and 50% of the signal was recovered in about 30 seconds. The reproducibility of the signal was estimated from the relative standard deviation and was found to be 0.049 (4.9%). The sensitivity of the chemiresistors was found to be 0.008 ppm^{-1}. The detection limit was gauged from $3.3\sigma/s$ and was found to be 1.5 ppm.

5.5 Conclusions

The present study highlighted the effects of functional groups on CNT on the chemiresistivity of PDMS/ functionalized CNT nanocomposite based chemiresistors. It was observed that CNT-COOH has better interfacial interaction with PDMS polymers compare to other functionalized CNT based composites. The better interfacial interaction of CNT-COOH leads to a marked enhancement in the sensitivity of the chemiresistor. Surface energy and XPS studies help to establish the CNT-COOH induced modification of PDMS filler interfaces. The PDMS/CNT-COOH chemiresistor showed good selectivity for toluene and had a wide detection range and good reproducibility. These results highlight the impact of the functional group driven changes at the CNT/polymer interface, on the electron transport within the matrix and its profound effect on the chemiresistivity. Furthermore, as the sensors exhibit reversible and reproducible response for multiple cycles, such chemiresistors will be useful as the standalone field sensors for volatile organic compounds.

CHAPTER 6

Summary and Future Studies

6.1 Summary

The objective of this thesis was to investigate high energy radiation processed conductive polymeric nanocomposites based chemiresistive sensors for sensitive detection of volatile organic compounds. Such chemiresistive sensors possess high prospect in the field of medical diagnosis as well as in environmental monitoring. A sensor has to be sensitive and selective enough towards target analyte to be viable used for biomarker sensor. Therefore in order to fabricate highly sensitive and selective towards a particular VOC, the implementation of different methodologies for the synthesis of conductive nanocomposite was strongly emphasized. For this purpose carbon nanomaterials such as NCB, CNT, hybrid nanofiller and different functionalized CNTs were used as the basic conducting material for chemiresistive sensors fabrication. The selectivity of the chemiresistors was imparted by judicial choice of polymer matrix because primarily analyte vapour interacts with polymer matrix only. Being an additive free tool high energy radiation was used to introduce optimum crosslinking and sometimes it can also being used to modify the interface of polymer and nanofillers.

Radiation crosslinked fluorocarbon elastomer based conducting polymer composites chemiresistor was developed for sensitive, selective and reversible detection acetone vapour. Different network densities were obtained by irradiating with high energy gamma radiation. Irradiation using high energy radiation was found to improve sensing characteristics due to crosslink and alteration in filler-polymer interactions and diffusion kinetics of acetone vapour. It was found that the sensing response had a strong correlation with the fluorocarbon elastomer and acetone interaction parameter. Radiation crosslinked NR/CNT nanocomposite based chemiresistor can be useful in designing reversible chemiresistive sensor for the real-time detection of Isoprene. Surface functionality of CNT played a crucial role to destabilize the natural rubber latex by breaking the lipid layer and thus helping the coagulation process to form NR/CNT composites. Zeta potential measurement of NR particles and CNTs help to understand the underlying mechanism behind the coagulation method. Detection limit and sensitivity of the chmiresistors were found to be 50 ppm and 8.8 ppm^{-1} respectively. In case of PVB/CNT nanocomposites, that extremely low percolation threshold of CNTs in PVB matrix was observed and also found that the electron transport was mainly due to the tunnelling effect. The crosslinked PVB/CNT based CPC gives sensitive, selective and rapid sensing response towards ethanol vapour at room temperature. Various interactions of analytes and polymer have a strong correlation on chemo-electrical behaviour of chemiresistors and that in turn tune the selectivity of matrix.

It was found that use of NCB and CNT nanohybrid and PDMS based CPCs chemiresistors are useful for detection of BTEX vapour. Uses of CNTs not only increase electrical conductivity but also lower the temperature dependence of resistivity is reduced. Detection range of VOCs was found to increase with CNT loading. A distinct pattern of analyte can be resolved by using an array of four chemiresistors with different CNT content with the help of principle component analysis.

CNT functionality has a distinct effect on the chemiresistivity of PDMS/CNT composites. With the increase in radiation dose the chemiresistivity increased, suggesting the possibility of interfacial grafts and immobilization of PDMS segments on to CNT-COOH surface. The better interfacial interactions between the COOH functionalized CNT and PDMS translated in radiation induced modifications of PDMS/CNT-COOH interface, which eventually lead to a marked enhancement in the sensitivity of the chemiresistor.

6.2 Future study and Recommendations

A more extensive study will be done to increase sensitivity and detection limit towards different VOC mixtures. New methodologies such as increase the surface area of sensor elements by introducing interdigitated electrodes or by using porous sensors may be adopted to enhance the interaction of analyte vapours and sensors. Furthermore, new nanomaterials such as graphene and graphene oxide which has large surface area may also be used to enhance interacting site with alayte molecules that in turn enhance the sensitivity of matrix. Efforts can also make to use porous polymer matrix, which will increase the diffusion of analyte molecule inside chemiresistor efficiently and thus will increase sensitivity. Moreover grafting of intrinsic conducting polymers like polyaniline, polypyrrole, polythiophene onto nonconducting and flexible substrate can be done in order to get an all-polymer conducting matrix which can be used for standalone flexible chemiresistor. Further investigation required to explore the possibility of increasing the interaction between polymer and filler by covalent fucntionalization of carbon nanomaterials with various oligomeric, polymeric or inorganic molecules. Finally, real time monitoring of human breath and field detection of complex mixtures of VOCs will be extracted by constructing an e-nose composed of several CPC based chemiresistive sensor array.

References

[1] M. Odlyha, G.M. Foster, N.S. Cohen, C. Sitwell, L. Bullock, Microclimate monitoring of indoor environments using piezoelectric quartz crystal humidity sensors, Journal of Environmental Monitoring 2(2) (2000) 127-131.
[2] E.J. Bardana, Indoor pollution and its impact on respiratory health, Annals of Allergy, Asthma & Immunology 87(6) (2001) 33-40.
[3] M. Belloc-Santaliestra, R. van der Haar, E. Molinero-Ruiz, Occupational Exposure Assessment of Highway Toll Station Workers to Vehicle Engine Exhaust, Journal of occupational and environmental hygiene 12(1) (2015) 51-61.
[4] M. Girschikofsky, M. Rosenberger, S. Belle, M. Brutschy, S.R. Waldvogel, R. Hellmann, Optical planar Bragg grating sensor for real-time detection of benzene, toluene and xylene in solvent vapour, Sensors and Actuators B: Chemical 171 (2012) 338-342.
[5] E. Durmusoglu, F. Taspinar, A. Karademir, Health risk assessment of BTEX emissions in the landfill environment, Journal of hazardous materials 176(1-3) (2010) 870-877.
[6] A.P. Jones, Indoor air quality and health, Atmospheric environment 33(28) (1999) 4535-4564.
[7] W.H. Organization, WHO guidelines for indoor air quality: selected pollutants, (2010).
[8] H. Guo, S. Lee, L. Chan, W. Li, Risk assessment of exposure to volatile organic compounds in different indoor environments, Environmental Research 94(1) (2004) 57-66.
[9] O. Safety, H. Administration, Occupational exposure to benzene, Fed Reg 52(176) (1987) 34460-34578.
[10] H. Sakurai, G. Endo, Y. Endo, T. Hanaoka, J. Kagawa, M. Kasuya, T. Kawai, R. Kishi, A. Koizumi, Y. Kusaka, Recommendation of occupational exposure limits (2000-2001), Journal of Occupational Health 42(4) (2000) 213-228.
[11] Z. He, G. Li, J. Chen, Y. Huang, T. An, C. Zhang, Pollution characteristics and health risk assessment of volatile organic compounds emitted from different plastic solid waste recycling workshops, Environment international 77 (2015) 85-94.
[12] C.-T. Chang, B.-Y. Chen, Toxicity assessment of volatile organic compounds and polycyclic aromatic hydrocarbons in motorcycle exhaust, Journal of hazardous materials 153(3) (2008) 1262-1269.
[13] T.D.C. Minh, D.R. Blake, P.R. Galassetti, The clinical potential of exhaled breath analysis for diabetes mellitus, Diabetes Research and Clinical Practice 97(2) (2012) 195-205.
[14] J. Pereira, P. Porto-Figueira, C. Cavaco, K. Taunk, S. Rapole, R. Dhakne, H. Nagarajaram, J. Câmara, Breath Analysis as a Potential and Non-Invasive Frontier in Disease Diagnosis: An Overview, Metabolites 5(1) (2015) 3.
[15] R.F. Machado, Identifying Chronic Obstructive Pulmonary Disease and Asthma by Exhaled Breath Analysis, American Journal of Respiratory and Critical Care Medicine 180(11) (2009) 1038-1039.
[16] L. Pauling, A.B. Robinson, R. Teranishi, P. Cary, Quantitative Analysis of Urine Vapor and Breath by Gas-Liquid Partition Chromatography, Proceedings of the National Academy of Sciences 68(10) (1971) 2374-2376.
[17] B. Buszewski, M. Kęsy, T. Ligor, A. Amann, Human exhaled air analytics: biomarkers of diseases, Biomedical chromatography 21(6) (2007) 553-566.
[18] M.K. Nakhleh, H. Amal, R. Jeries, Y.Y. Broza, M. Aboud, A. Gharra, H. Ivgi, S. Khatib, S. Badarneh, L. Har-Shai, Diagnosis and classification of 17 diseases from 1404 subjects via pattern analysis of exhaled molecules, ACS nano 11(1) (2016) 112-125.

[19] G. Konvalina, H. Haick, Sensors for Breath Testing: From Nanomaterials to Comprehensive Disease Detection, Accounts of Chemical Research 47(1) (2014) 66-76.
[20] Y. Zhou, Y. Jiang, G. Xie, X. Du, H. Tai, Gas sensors based on multiple-walled carbon nanotubes-polyethylene oxide films for toluene vapor detection, Sensors and Actuators B: Chemical 191 (2014) 24-30.
[21] B. Adhikari, S. Majumdar, Polymers in sensor applications, Progress in polymer science 29(7) (2004) 699-766.
[22] J.W. Grate, S.N. Kaganove, D.A. Nelson, Polymers for chemical sensors using hydrosilylation chemistry, Pacific Northwest National Lab., Richland, WA (US), 2001.
[23] L. Wallace, Environmental exposure to benzene: an update, Environmental health perspectives 104(Suppl 6) (1996) 1129.
[24] D.E. Bergsagel, O. Wong, P.L. Bergsagel, R. Alexanian, K. Anderson, R.A. Kyle, G.K. Raabe, Benzene and multiple myeloma: Appraisal of the scientific evidence, Blood 94(4) (1999) 1174-1182.
[25] A. Mirzaei, S. Leonardi, G. Neri, Detection of hazardous volatile organic compounds (VOCs) by metal oxide nanostructures-based gas sensors: A review, Ceramics International 42(14) (2016) 15119-15141.
[26] K.R. Ritesh, A. Suganya, H.V. Dileepkumar, Y. Rajashekar, T. Shivanandappa, A single acute hepatotoxic dose of CCl4 causes oxidative stress in the rat brain, Toxicology Reports 2 (2015) 891-895.
[27] A. Songur, O.A. Ozen, M. Sarsilmaz, The toxic effects of formaldehyde on the nervous system, Reviews of environmental contamination and toxicology, Springer2010, pp. 105-118.
[28] Y.Y. Broza, L. Zuri, H. Haick, Combined volatolomics for monitoring of human body chemistry, Scientific reports 4 (2014) 4611.
[29] G. Peng, M. Hakim, Y.Y. Broza, S. Billan, R. Abdah-Bortnyak, A. Kuten, U. Tisch, H. Haick, Detection of lung, breast, colorectal, and prostate cancers from exhaled breath using a single array of nanosensors, British journal of cancer 103(4) (2010) 542.
[30] M. Hakim, Y.Y. Broza, O. Barash, N. Peled, M. Phillips, A. Amann, H. Haick, Volatile organic compounds of lung cancer and possible biochemical pathways, Chemical reviews 112(11) (2012) 5949-5966.
[31] P. Nuciforo, N. Radosevic-Robin, T. Ng, M. Scaltriti, Quantification of HER family receptors in breast cancer, Breast cancer research 17(1) (2015) 53.
[32] G. Peng, E. Trock, H. Haick, Detecting simulated patterns of lung cancer biomarkers by random network of single-walled carbon nanotubes coated with nonpolymeric organic materials, Nano letters 8(11) (2008) 3631-3635.
[33] K. Wlodzimirow, A. Abu-Hanna, M. Schultz, M. Maas, L. Bos, P. Sterk, H. Knobel, R. Soers, R.A. Chamuleau, Exhaled breath analysis with electronic nose technology for detection of acute liver failure in rats, Biosensors and Bioelectronics 53 (2014) 129-134.
[34] L. Narasimhan, W. Goodman, C.K.N. Patel, Correlation of breath ammonia with blood urea nitrogen and creatinine during hemodialysis, Proceedings of the National Academy of Sciences 98(8) (2001) 4617-4621.
[35] S.-J. Choi, B.-H. Jang, S.-J. Lee, B.K. Min, A. Rothschild, I.-D. Kim, Selective detection of acetone and hydrogen sulfide for the diagnosis of diabetes and halitosis using SnO2 nanofibers functionalized with reduced graphene oxide nanosheets, ACS applied materials & interfaces 6(4) (2014) 2588-2597.
[36] J.P.M. Finberg, M. Schwartz, R. Jeries, S. Badarny, M.K. Nakhleh, E. Abu Daoud, Y. Ayubkhanov, M. Aboud-Hawa, Y.Y. Broza, H. Haick, Sensor Array for Detection of Early Stage Parkinson's Disease before Medication, ACS Chemical Neuroscience (2018).

[37] C.F. Kneepkens, G. Lepage, C.C. Roy, The potential of the hydrocarbon breath test as a measure of lipid peroxidation, Free Radical Biology and Medicine 17(2) (1994) 127-160.
[38] M. Phillips, K. Gleeson, J.M.B. Hughes, J. Greenberg, R.N. Cataneo, L. Baker, W.P. McVay, Volatile organic compounds in breath as markers of lung cancer: a cross-sectional study, The Lancet 353(9168) (1999) 1930-1933.
[39] M. Phillips, R.N. Cataneo, B.A. Ditkoff, P. Fisher, J. Greenberg, R. Gunawardena, C.S. Kwon, F. Rahbari-Oskoui, C. Wong, Volatile markers of breast cancer in the breath, The breast journal 9(3) (2003) 184-191.
[40] B. Agnieszka, T. Ettje, S. Agnieszka, W.D. Jan, J.C.M. Edwin, A.M.D. Jackie, W. Cisca, Z. Alexandra, J.v.S. Frederik, Profile of volatile organic compounds in exhaled breath changes as a result of gluten-free diet, Journal of Breath Research 7(3) (2013) 037104.
[41] I. Ueta, Y. Saito, M. Hosoe, M. Okamoto, H. Ohkita, S. Shirai, H. Tamura, K. Jinno, Breath acetone analysis with miniaturized sample preparation device: In-needle preconcentration and subsequent determination by gas chromatography–mass spectroscopy, Journal of Chromatography B 877(24) (2009) 2551-2556.
[42] A. Allouch, S. Le Calvé, C.A. Serra, Portable, miniature, fast and high sensitive real-time analyzers: BTEX detection, Sensors and Actuators B: Chemical 182 (2013) 446-452.
[43] T. Zhang, S. Mubeen, N.V. Myung, M.A. Deshusses, Recent progress in carbon nanotube-based gas sensors, Nanotechnology 19(33) (2008) 332001.
[44] S.-W. Chiu, K.-T. Tang, Towards a chemiresistive sensor-integrated electronic nose: A review, Sensors 13(10) (2013) 14214-14247.
[45] M. Fleischer, E. Simon, E. Rumpel, H. Ulmer, M. Harbeck, M. Wandel, C. Fietzek, U. Weimar, H. Meixner, Detection of volatile compounds correlated to human diseases through breath analysis with chemical sensors, Sensors and Actuators B: Chemical 83(1-3) (2002) 245-249.
[46] P.R. Galassetti, B. Novak, D. Nemet, C. Rose-Gottron, D.M. Cooper, S. Meinardi, R. Newcomb, F. Zaldivar, D.R. Blake, Breath ethanol and acetone as indicators of serum glucose levels: an initial report, Diabetes technology & therapeutics 7(1) (2005) 115-123.
[47] W. Li, Y. Liu, Y. Liu, S. Cheng, Y. Duan, Exhaled isopropanol: new potential biomarker in diabetic breathomics and its metabolic correlations with acetone, RSC Advances 7(28) (2017) 17480-17488.
[48] G. Zhang, X. Guo, S. Wang, X. Wang, Y. Zhou, H. Xu, New graphene fiber coating for volatile organic compounds analysis, Journal of Chromatography B 969 (2014) 128-131.
[49] X. Chen, F. Xu, Y. Wang, Y. Pan, D. Lu, P. Wang, K. Ying, E. Chen, W. Zhang, A study of the volatile organic compounds exhaled by lung cancer cells in vitro for breath diagnosis, Cancer: Interdisciplinary International Journal of the American Cancer Society 110(4) (2007) 835-844.
[50] M. Moretti, M. Phillips, A. Abouzeid, R.N. Cataneo, J. Greenberg, Increased breath markers of oxidative stress in normal pregnancy and in preeclampsia, American journal of obstetrics and gynecology 190(5) (2004) 1184-1190.
[51] S. Meinardi, K.-B. Jin, B. Barletta, D.R. Blake, N.D. Vaziri, Exhaled breath and fecal volatile organic biomarkers of chronic kidney disease, Biochimica et Biophysica Acta (BBA) - General Subjects 1830(3) (2013) 2531-2537.
[52] Y. Chen, Y. Zhang, F. Pan, J. Liu, K. Wang, C. Zhang, S. Cheng, L. Lu, W. Zhang, Z. Zhang, Breath analysis based on surface-enhanced Raman scattering sensors distinguishes early and advanced gastric cancer patients from healthy persons, ACS nano 10(9) (2016) 8169-8179.
[53] F.J. Santos, M.T. Galceran, The application of gas chromatography to environmental analysis, TrAC Trends in Analytical Chemistry 21(9) (2002) 672-685.

[54] D. Helmig, Air analysis by gas chromatography, Journal of chromatography A 843(1-2) (1999) 129-146.
[55] F. Santos, M. Galceran, Modern developments in gas chromatography–mass spectrometry-based environmental analysis, Journal of Chromatography A 1000(1-2) (2003) 125-151.
[56] C. Jin, Chemometric Methods for the Determination of Volatile Organic Compounds with Microsensor Arrays, (2008).
[57] Y.I. Yashin, A.Y. Yashin, Current Trends in Gas Chromatography Methods and Instrumentation: A Scientometric Study, Journal of Analytical Chemistry 56(3) (2001) 200-213.
[58] A.K. Wanekaya, M. Uematsu, M. Breimer, O.A. Sadik, Multicomponent analysis of alcohol vapors using integrated gas chromatography with sensor arrays, Sensors and Actuators B: Chemical 110(1) (2005) 41-48.
[59] J. Gębicki, A. Kloskowski, Electrochemical Sensor for Measurement of Volatile Organic Compounds Employing Square Wave Perturbation Voltage, 17(4) (2010) 637.
[60] M. Mori, Y. Sadaoka, Potentiometric VOC detection at sub-ppm levels based on YSZ electrolyte and platinum electrode covered with gold, Sensors and Actuators B: Chemical 146(1) (2010) 46-52.
[61] T. Nagai, S. Tamura, N. Imanaka, Solid electrolyte type ammonia gas sensor based on trivalent aluminum ion conducting solids, Sensors and Actuators B: Chemical 147(2) (2010) 735-740.
[62] J.W. Grate, M.H. Abraham, Solubility interactions and the design of chemically selective sorbent coatings for chemical sensors and arrays, Sensors and Actuators B: Chemical 3(2) (1991) 85-111.
[63] J. Grate, GC Frye in Sensors Update, Vol. 2, Wiley-VCH, Weinheim, 1996.
[64] D. Lange, C. Hagleitner, A. Hierlemann, O. Brand, H. Baltes, Complementary metal oxide semiconductor cantilever arrays on a single chip: mass-sensitive detection of volatile organic compounds, Analytical Chemistry 74(13) (2002) 3084-3095.
[65] M. Maute, S. Raible, F. Prins, D. Kern, H. Ulmer, U. Weimar, W. Göpel, Detection of volatile organic compounds (VOCs) with polymer-coated cantilevers, Sensors and Actuators B: Chemical 58(1-3) (1999) 505-511.
[66] P. Chu, G. Rhoderick, D. Van Vlack, S. Wetzel, W. Lafferty, F. Guenther, A quantitative infrared spectral database of hazardous air pollutants, Fresenius' journal of analytical chemistry 360(3-4) (1998) 426-429.
[67] S. Johnson, N.-H. Pham, V. Novick, V. Maroni, Application of surface-enhanced infrared absorption spectroscopy as a sensor for volatile organic compounds, Applied spectroscopy 51(9) (1997) 1423-1426.
[68] N. Kerness, A. Koll, A. Schaufelbuhl, C. Hagleitner, A. Hierlemann, O. Brand, H. Baltes, N-well based CMOS calorimetric chemical sensors, Micro Electro Mechanical Systems, 2000. MEMS 2000. The Thirteenth Annual International Conference on, IEEE, 2000, pp. 96-101.
[69] P. Bataillard, E. Steffgen, S. Haemmerli, A. Manz, H. Widmer, An integrated silicon thermopile as biosensor for the thermal monitoring of glucose, urea and penicillin, Biosensors and Bioelectronics 8(2) (1993) 89-98.
[70] J.F. Feller, J. Lu, K. Zhang, B. Kumar, M. Castro, N. Gatt, H.J. Choi, Novel architecture of carbon nanotube decorated poly(methyl methacrylate) microbead vapour sensors assembled by spray layer by layer, Journal of Materials Chemistry 21(12) (2011) 4142-4149.

[71] Z.C. Kennedy, J.F. Christ, K.A. Evans, B.W. Arey, L.E. Sweet, M.G. Warner, R.L. Erikson, C.A. Barrett, 3D-printed poly(vinylidene fluoride)/carbon nanotube composites as a tunable, low-cost chemical vapour sensing platform, Nanoscale 9(17) (2017) 5458-5466.
[72] A. Thamri, H. Baccar, C. Struzzi, C. Bittencourt, A. Abdelghani, E. Llobet, MHDA-functionalized multiwall carbon nanotubes for detecting non-aromatic VOCs, Scientific reports 6 (2016) 35130.
[73] N. Barsan, U. Weimar, 7.3. 3 Fundamentals of Metal Oxide Gas Sensors, Proceedings IMCS 2012 (2012) 618-621.
[74] T. Hibbard, K. Crowley, A.J. Killard, Direct measurement of ammonia in simulated human breath using an inkjet-printed polyaniline nanoparticle sensor, Analytica chimica acta 779 (2013) 56-63.
[75] T. Inoue, K. Ohtsuka, Y. Yoshida, Y. Matsuura, Y. Kajiyama, Metal oxide semiconductor NO2 sensor, Sensors and Actuators B: Chemical 25(1) (1995) 388-391.
[76] N.B. Tanvir, E. Laubender, O. Yurchenko, G. Urban, Room Temperature CO Sensing with Metal Oxide Nanoparticles Using work Function Readout, Procedia Engineering 168 (2016) 284-288.
[77] T. Alizadeh, L.H. Soltani, Graphene/poly(methyl methacrylate) chemiresistor sensor for formaldehyde odor sensing, Journal of Hazardous Materials 248-249 (2013) 401-406.
[78] M. Castro, J. Lu, S. Bruzaud, B. Kumar, J.-F. Feller, Carbon nanotubes/poly(ε-caprolactone) composite vapour sensors, Carbon 47(8) (2009) 1930-1942.
[79] J. Luo, S. Ma, F. Li, X. Li, W. Li, L. Cheng, Y. Mao, D. Gz, The mesoscopic structure of flower-like ZnO nanorods for acetone detection, Materials Letters 121 (2014) 137-140.
[80] A. Berna, Metal oxide sensors for electronic noses and their application to food analysis, Sensors 10(4) (2010) 3882-3910.
[81] V. Vaishanv, P. Patel, N. Patel, Indium tin oxide thin-film sensor for detection of volatile organic compounds (VOCs), Materials and manufacturing processes 21(3) (2006) 257-261.
[82] S. Shao, B. Liu, F. Jiang, H. Wu, R. Koehn, Reversible P-N transition sensing behavior obtained by applying GQDs/Pt decorated SnO2 thin films at room temperature, RSC Advances 6(100) (2016) 98317-98324.
[83] H. Bai, G. Shi, Gas Sensors Based on Conducting Polymers, Sensors (Basel, Switzerland) 7(3) (2007) 267-307.
[84] C. Nylander, M. Armgarth, I. Lundström, An ammonia detector based on a conducting polymer, Anal. Chem. Symp. Ser, 1983, pp. 203-207.
[85] A.G. MacDiarmid, "Synthetic metals": A novel role for organic polymers (Nobel lecture), Angewandte Chemie International Edition 40(14) (2001) 2581-2590.
[86] D. Nicolas-Debarnot, F. Poncin-Epaillard, Polyaniline as a new sensitive layer for gas sensors, Analytica Chimica Acta 475(1-2) (2003) 1-15.
[87] K. Potje-Kamloth, Chemical gas sensors based on organic semiconductor polypyrrole, Critical reviews in analytical chemistry 32(2) (2002) 121-140.
[88] R.D. McCullough, The chemistry of conducting polythiophenes, Advanced Materials 10(2) (1998) 93-116.
[89] D.W. Hatchett, M. Josowicz, Composites of Intrinsically Conducting Polymers as Sensing Nanomaterials, Chemical Reviews 108(2) (2008) 746-769.
[90] K. Hosono, I. Matsubara, N. Murayama, W. Shin, N. Izu, The sensitivity of 4-ethylbenzenesulfonic acid-doped plasma polymerized polypyrrole films to volatile organic compounds, Thin Solid Films 484(1-2) (2005) 396-399.

[91] T.S. Natarajan, S.B. Eshwaran, K.W. Stöckelhuber, S. Wießner, P. Pötschke, G. Heinrich, A. Das, Strong Strain Sensing Performance of Natural Rubber Nanocomposites, ACS Applied Materials & Interfaces 9(5) (2017) 4860-4872.
[92] Z. Qiang, S. Yihu, W. Gang, S. Xubing, Relationship between the positive temperature coefficient of resistivity and dynamic rheological behavior for carbon black-filled high-density polyethylene, Journal of Polymer Science Part B: Polymer Physics 41(9) (2003) 983-992.
[93] K. Ke, P. Pötschke, N. Wiegand, B. Krause, B. Voit, Tuning the network structure in poly (vinylidene fluoride)/carbon nanotube nanocomposites using carbon black: toward improvements of conductivity and piezoresistive sensitivity, ACS applied materials & interfaces 8(22) (2016) 14190-14199.
[94] S. Chatterjee, M. Castro, J.-F. Feller, An e-nose made of carbon nanotube based quantum resistive sensors for the detection of eighteen polar/nonpolar VOC biomarkers of lung cancer, Journal of Materials Chemistry B 1(36) (2013) 4563-4575.
[95] A. Kumar, M.R. Maschmann, S.L. Hodson, J. Baur, T.S. Fisher, Carbon nanotube arrays decorated with multi-layer graphene-nanopetals enhance mechanical strength and durability, Carbon 84 (2015) 236-245.
[96] B. Kumar, M. Castro, J.-F. Feller, Tailoring the chemo-resistive response of self-assembled polysaccharide-CNT sensors by chain conformation at tunnel junctions, Carbon 50(10) (2012) 3627-3634.
[97] B. Kumar, J.-F. Feller, M. Castro, J. Lu, Conductive bio-Polymer nano-Composites (CPC): Chitosan-carbon nanotube transducers assembled via spray layer-by-layer for volatile organic compound sensing, Talanta 81(3) (2010) 908-915.
[98] L. Han, A.L. Andrady, D.S. Ensor, Chemical sensing using electrospun polymer/carbon nanotube composite nanofibers with printed-on electrodes, Sensors and Actuators B: Chemical 186 (2013) 52-55.
[99] R. Kessick, G. Tepper, Electrospun polymer composite fiber arrays for the detection and identification of volatile organic compounds, Sensors and Actuators B: Chemical 117(1) (2006) 205-210.
[100] B.J. Doleman, R.D. Sanner, E.J. Severin, R.H. Grubbs, N.S. Lewis, Use of Compatible Polymer Blends To Fabricate Arrays of Carbon Black−Polymer Composite Vapor Detectors, Analytical Chemistry 70(13) (1998) 2560-2564.
[101] B. Zhang, R.W. Fu, M.Q. Zhang, X.M. Dong, P.L. Lan, J.S. Qiu, Preparation and characterization of gas-sensitive composites from multi-walled carbon nanotubes/polystyrene, Sensors and Actuators B: Chemical 109(2) (2005) 323-328.
[102] Y. Yoon, K. Lee, S. Kwon, S. Seo, H. Yoo, S. Kim, Y. Shin, Y. Park, D. Kim, J.-Y. Choi, Vertical alignments of graphene sheets spatially and densely piled for fast ion diffusion in compact supercapacitors, Acs Nano 8(5) (2014) 4580-4590.
[103] D. Jariwala, V.K. Sangwan, L.J. Lauhon, T.J. Marks, M.C. Hersam, Carbon nanomaterials for electronics, optoelectronics, photovoltaics, and sensing, Chemical Society Reviews 42(7) (2013) 2824-2860.
[104] O.C. Compton, B. Jain, D.A. Dikin, A. Abouimrane, K. Amine, S.T. Nguyen, Chemically active reduced graphene oxide with tunable C/O ratios, ACS nano 5(6) (2011) 4380-4391.
[105] A. Yaya, B. Agyei-Tuffour, D. Dodoo-Arhin, E. Nyankson, E. Annan, D. Konadu, E. Sinayobye, E. Baryeh, C. Ewels, Layered nanomaterials-a review, Glob J Eng Des Technol 1(2) (2012) 32-41.
[106] D. Kun, Z. Yi-Chuan, T. Jian-Hua, J. Xu, L. Zhong-Ming, Anomalous attenuation and structural origin of positive temperature coefficient (PTC) effect in a carbon black

(CB)/poly(ethylene terephthalate) (PET)/polyethylene (PE) electrically conductive microfibrillar polymer composite with a preferential CB distribution, Journal of Applied Polymer Science 125(S1) (2012) E561-E570.
[107] C. Jianguo, W. Li, H. Jia, Y. Haojie, A novel polycaprolactone-grafted-carbon black nanocomposite-based sensor for detecting solvent vapors, Journal of Applied Polymer Science 121(6) (2011) 3277-3282.
[108] J. Leng, W. Huang, X. Lan, Y. Liu, S. Du, Significantly reducing electrical resistivity by forming conductive Ni chains in a polyurethane shape-memory polymer/carbon-black composite, Applied Physics Letters 92(20) (2008) 204101.
[109] H. Elhaes, A. Fakhry, M. Ibrahim, Carbon nano materials as gas sensors, Materials Today: Proceedings 3(6) (2016) 2483-2492.
[110] F. Yavari, N. Koratkar, Graphene-based chemical sensors, The journal of physical chemistry letters 3(13) (2012) 1746-1753.
[111] S.-C. Ha, Y.S. Kim, Y. Yang, Y.J. Kim, S.-M. Cho, H. Yang, Y.T. Kim, Integrated and microheater embedded gas sensor array based on the polymer composites dispensed in micromachined wells, Sensors and Actuators B: Chemical 105(2) (2005) 549-555.
[112] M.C. Lonergan, E.J. Severin, B.J. Doleman, S.A. Beaber, R.H. Grubbs, N.S. Lewis, Array-based vapor sensing using chemically sensitive, carbon black− polymer resistors, Chemistry of Materials 8(9) (1996) 2298-2312.
[113] B.J. Doleman, M.C. Lonergan, E.J. Severin, T.P. Vaid, N.S. Lewis, Quantitative study of the resolving power of arrays of carbon black− polymer composites in various vapor-sensing tasks, Analytical Chemistry 70(19) (1998) 4177-4190.
[114] P. Talik, M. Zabkowska-Wacławek, W. Wacławek, Sensing properties of the CB-PCV composites for chlorinated hydrocarbon vapours, Journal of materials science 27(24) (1992) 6807-6810.
[115] S. Iijima, Helical microtubules of graphitic carbon, nature 354(6348) (1991) 56.
[116] P.G. Collins, K. Bradley, M. Ishigami, d.A. Zettl, Extreme oxygen sensitivity of electronic properties of carbon nanotubes, science 287(5459) (2000) 1801-1804.
[117] J. Kong, N.R. Franklin, C. Zhou, M.G. Chapline, S. Peng, K. Cho, H. Dai, Nanotube molecular wires as chemical sensors, science 287(5453) (2000) 622-625.
[118] A. Goldoni, L. Petaccia, S. Lizzit, R. Larciprete, Sensing gases with carbon nanotubes: a review of the actual situation, Journal of physics. Condensed matter : an Institute of Physics journal 22(1) (2010) 013001.
[119] Z. Ting, M. Syed, V.M. Nosang, A.D. Marc, Recent progress in carbon nanotube-based gas sensors, Nanotechnology 19(33) (2008) 332001.
[120] M. Meyyappan, Carbon Nanotube-Based Chemical Sensors, Small 12(16) (2016) 2118-29.
[121] D.R. Kauffman, A. Star, Carbon nanotube gas and vapor sensors, Angewandte Chemie (International ed. in English) 47(35) (2008) 6550-70.
[122] S.J. Tans, A.R. Verschueren, C. Dekker, Room-temperature transistor based on a single carbon nanotube, Nature 393(6680) (1998) 49.
[123] X. Ma, X. Zhang, Y. Li, G. Li, M. Wang, H. Chen, Y. Mi, Preparation of Nano-Structured Polyaniline Composite Film via “Carbon Nanotubes Seeding” Approach and its Gas-Response Studies, Macromolecular Materials and Engineering 291(1) (2006) 75-82.
[124] J. Li, Y. Lu, Q. Ye, M. Cinke, J. Han, M. Meyyappan, Carbon Nanotube Sensors for Gas and Organic Vapor Detection, Nano Letters 3(7) (2003) 929-933.

[125] J. Novak, E. Snow, E. Houser, D. Park, J. Stepnowski, R. McGill, Nerve agent detection using networks of single-walled carbon nanotubes, Applied physics letters 83(19) (2003) 4026-4028.
[126] P.J.W. Hands, P.J. Laughlin, D. Bloor, Metal–polymer composite sensors for volatile organic compounds: Part 1. Flow-through chemi-resistors, Sensors and Actuators B: Chemical 162(1) (2012) 400-408.
[127] B. Kumar, M. Castro, J.F. Feller, Poly(lactic acid)–multi-wall carbon nanotube conductive biopolymer nanocomposite vapour sensors, Sensors and Actuators B: Chemical 161(1) (2012) 621-628.
[128] K. Cattanach, R.D. Kulkarni, M. Kozlov, S.K. Manohar, Flexible carbon nanotube sensors for nerve agent simulants, Nanotechnology 17(16) (2006) 4123.
[129] C. Wei, L. Dai, A. Roy, T.B. Tolle, Multifunctional chemical vapor sensors of aligned carbon nanotube and polymer composites, Journal of the American Chemical Society 128(5) (2006) 1412-1413.
[130] M. Yucel, O. Akin, M. Cayoren, I. Akduman, A. Palaniappan, B. Liedberg, G. Hizal, F. Inci, U.H. Yildiz, Hand-Held Volatilome Analyzer Based on Elastically Deformable Nanofibers, Analytical Chemistry 90(8) (2018) 5122-5129.
[131] P.-C. Ma, M.-Y. Liu, H. Zhang, S.-Q. Wang, R. Wang, K. Wang, Y.-K. Wong, B.-Z. Tang, S.-H. Hong, K.-W. Paik, J.-K. Kim, Enhanced Electrical Conductivity of Nanocomposites Containing Hybrid Fillers of Carbon Nanotubes and Carbon Black, ACS Applied Materials & Interfaces 1(5) (2009) 1090-1096.
[132] Y. Li, P. Pötschke, J. Pionteck, B. Voit, Electrical and vapor sensing behaviors of polycarbonate composites containing hybrid carbon fillers, European Polymer Journal 108 (2018) 461-471.
[133] A. Kaniyoor, S. Ramaprabhu, Hybrid carbon nanostructured ensembles as chemiresistive hydrogen gas sensors, Carbon 49(1) (2011) 227-236.
[134] F. Rigoni, G. Drera, S. Pagliara, A. Goldoni, L. Sangaletti, High sensitivity, moisture selective, ammonia gas sensors based on single-walled carbon nanotubes functionalized with indium tin oxide nanoparticles, Carbon 80 (2014) 356-363.
[135] K. Dubey, Y. Bhardwaj, C. Chaudhari, V. Kumar, N. Goel, S. Sabharwal, Radiation processed ethylene vinyl acetate-multiple walled carbon nanotube nano-composites: effect of MWNT addition on the gel content and crosslinking density, Lett 3 (2009) 492-500.
[136] J.B. Chang, V. Subramanian, E-NOSES SNIFF SUCCESS, IEEE SPECTRUM 45(3) (2008) 48-53.
[137] D.J. Hill, C.M. Preston, D.J. Salisbury, A.K. Whittaker, Molecular weight changes and scission and crosslinking in poly (dimethyl siloxane) on gamma radiolysis, Radiation physics and chemistry 62(1) (2001) 11-17.
[138] I. Manas-Zloczower, A. Nir, Z. Tadmor, Dispersive mixing in internal mixers—a theoretical model based on agglomerate rupture, Rubber Chemistry and Technology 55(5) (1982) 1250-1285.
[139] H. Fricke, E.J. Hart, The Oxidation of Fe++ to Fe+++ by the Irradiation with X-Rays of Solutions of Ferrous Sulfate in Sulfuric Acid, The Journal of Chemical Physics 3(1) (1935) 60-61.
[140] A.J. Swallow, Radiation chemistry. An introduction, (1973).
[141] A. Franck, T.I. Germany, Viscoelasticity and dynamic mechanical testing, TA Instruments, New Castle, DE, USA AN004.
[142] D. Briggs, Handbook of X-Ray and Ultraviolet Photoelectron Spectroscopy, Heyden & Son Ltd, London, UK (1977).

[143] D.K. Owens, R. Wendt, Estimation of the surface free energy of polymers, Journal of applied polymer science 13(8) (1969) 1741-1747.

[144] J. Goldstein, D. Newberry, P. Echlin, D. Joy, A. Romig Jr, C. Lyman, C. Fion, E. Lifshin, Scanning Electron Microscopy and X-ray Microanalysis: A Textbook for Biologists. Materials Scientists, and Geologists. Ed. 2, pp. 1-820, New York: Plenum Publishing Corp, 1992.

[145] L. Reimer, Scanning electron microscopy: physics of image formation and microanalysis, Springer2013.

[146] F. Kremer, A. Schönhals, Broadband Dielectric Spectroscopy, Springer Science & Business Media2012.

[147] Dielectric Spectroscopy in Analysis of Polymers, Encyclopedia of Analytical Chemistry.

[148] M. von Smoluchowski, M. von Smoluchowski, Bull. Int. Acad. Sci. Cracovie Ser. A 8, 182 (1903), Bull. Int. Acad. Sci. Cracovie Ser. A 8 (1903) 182.

[149] I. Jolliffe, Principal component analysis, International encyclopedia of statistical science, Springer2011, pp. 1094-1096.

[150] P.C. Jurs, G. Bakken, H. McClelland, Computational methods for the analysis of chemical sensor array data from volatile analytes, Chemical Reviews 100(7) (2000) 2649-2678.

[151] A. Daneshkhah, S. Shrestha, M. Agarwal, K. Varahramyan, Poly (vinylidene fluoride-hexafluoropropylene) composite sensors for volatile organic compounds detection in breath, Sensors and Actuators B: Chemical 221 (2015) 635-643.

[152] J. Jia, D. Shi, X. Feng, G. Chen, Electromechanical properties of armchair graphene nanoribbons under local torsion, Carbon 76 (2014) 54-63.

[153] C. Yan, J. Wang, W. Kang, M. Cui, X. Wang, C.Y. Foo, K.J. Chee, P.S. Lee, Highly stretchable piezoresistive graphene–nanocellulose nanopaper for strain sensors, Advanced materials 26(13) (2014) 2022-2027.

[154] A. Eatemadi, H. Daraee, H. Karimkhanloo, M. Kouhi, N. Zarghami, A. Akbarzadeh, M. Abasi, Y. Hanifehpour, S.W. Joo, Carbon nanotubes: properties, synthesis, purification, and medical applications, Nanoscale Research Letters 9(1) (2014) 393.

[155] A. Raunika, S.A. Raj, K. Jayakrishna, M.T.H. Sultan, Carbon nanotube: A review on its mechanical properties and application in aerospace industry, IOP Conference Series: Materials Science and Engineering 270(1) (2017) 012027.

[156] M. Endo, S. Iijima, M.S. Dresselhaus, Carbon nanotubes, Elsevier2013.

[157] F. Doljack, PolySwitch PTC Devices-A New Low-Resistance Conductive Polymer-Based PTC Device for Overcurrent Protection, IEEE Transactions on Components, Hybrids, and Manufacturing Technology 4(4) (1981) 372-378.

[158] B.C. Sisk, N.S. Lewis, Vapor Sensing Using Polymer/Carbon Black Composites in the Percolative Conduction Regime, Langmuir 22(18) (2006) 7928-7935.

[159] K. Jiang, T. Fei, F. Jiang, G. Wang, T. Zhang, A dew sensor based on modified carbon black and polyvinyl alcohol composites, Sensors and Actuators B: Chemical 192 (2014) 658-663.

[160] K. Arshak, E. Moore, L. Cavanagh, J. Harris, B. McConigly, C. Cunniffe, G. Lyons, S. Clifford, Determination of the electrical behaviour of surfactant treated polymer/carbon black composite gas sensors, Composites Part A: Applied Science and Manufacturing 36(4) (2005) 487-491.

[161] D.L. Johnsen, Z. Zhang, H. Emamipour, Z. Yan, M.J. Rood, Effect of isobutane adsorption on the electrical resistivity of activated carbon fiber cloth with select physical and chemical properties, Carbon 76 (2014) 435-445.

[162] J. Lu, J.F. Feller, B. Kumar, M. Castro, Y.S. Kim, Y.T. Park, J.C. Grunlan, Chemo-sensitivity of latex-based films containing segregated networks of carbon nanotubes, Sensors and Actuators B: Chemical 155(1) (2011) 28-36.
[163] S. Kittipong, S.J. M., M.M. M., K.S. Yeol, R.G. C., S.T. M., H.P. T., Spray-Layer-by-Layer Carbon Nanotube/Electrospun Fiber Electrodes for Flexible Chemiresistive Sensor Applications, Advanced Functional Materials 24(4) (2014) 492-502.
[164] H. Deng, L. Lin, M. Ji, S. Zhang, M. Yang, Q. Fu, Progress on the morphological control of conductive network in conductive polymer composites and the use as electroactive multifunctional materials, Progress in Polymer Science 39(4) (2014) 627-655.
[165] H. Parant, G. Muller, T. Le Mercier, J.M. Tarascon, P. Poulin, A. Colin, Flowing suspensions of carbon black with high electronic conductivity for flow applications: Comparison between carbons black and exhibition of specific aggregation of carbon particles, Carbon 119 (2017) 10-20.
[166] M. Fayfman, F.J. Pasquel, G.E. Umpierrez, Management of Hyperglycemic Crises: Diabetic Ketoacidosis and Hyperglycemic Hyperosmolar State, Medical Clinics of North America 101(3) (2017) 587-606.
[167] S.A. Hamed, Brain injury with diabetes mellitus: evidence, mechanisms and treatment implications, Expert Review of Clinical Pharmacology 10(4) (2017) 409-428.
[168] T. Satoh, K. Omae, H. Nakashima, T. Takebayashi, H. Matsumura, T. Kawai, M. Nakaza, H. Sakurai, Relationship between acetone exposure concentration and health effects in acetate fiber plant workers, International Archives of Occupational and Environmental Health 68(3) (1996) 147-153.
[169] A. Güntner, N.A. Sievi, S.J. Theodore, T. Gulich, M. Kohler, S.E. Pratsinis, Noninvasive body fat burn monitoring from exhaled acetone with Si-doped WO3-sensing nanoparticles, Analytical Chemistry 89(19) (2017) 10578-10584.
[170] F. Liu, C. Ma, X. Hao, C. Yang, H. Zhu, X. Liang, P. Sun, F. Liu, X. Chuai, G. Lu, Highly sensitive gas sensor based on stabilized zirconia and CdMoO4 sensing electrode for detection of acetone, Sensors and Actuators B: Chemical 248 (2017) 9-18.
[171] N. Sinha, R. Mukhopadhyay, B. Raj, Mechanical behavior of fluoroelastomer considering long term ageing, Nuclear Engineering and Design 254 (2013) 89-96.
[172] S. Ebnesajjad, Introduction to fluoropolymers: materials, technology and applications, William Andrew2013.
[173] S.-Y. Fu, X.-Q. Feng, B. Lauke, Y.-W. Mai, Effects of particle size, particle/matrix interface adhesion and particle loading on mechanical properties of particulate–polymer composites, Composites Part B: Engineering 39(6) (2008) 933-961.
[174] S. Majji, K. Dubey, R. Mondal, Y. Bhardwaj, S. Acharya, Development of Electron Beam Cross-Linked PDMS/PTFEM Composites with Low Coefficient of Friction and High Elastic Modulus, Polymer-Plastics Technology and Engineering 53(5) (2014) 435-441.
[175] H. Yang, H. Wang, Z. Hou, P. Wang, B. Li, J. Li, J. Hu, Fabrication and application of high quality poly (dimethylsiloxane) stamps by gamma ray irradiation, Journal of Materials Chemistry 21(12) (2011) 4279-4285.
[176] F. Lux, Models proposed to explain the electrical conductivity of mixtures made of conductive and insulating materials, Journal of Materials Science 28(2) (1993) 285-301.
[177] E. Garboczi, K. Snyder, J. Douglas, M. Thorpe, Geometrical percolation threshold of overlapping ellipsoids, Physical review E 52(1) (1995) 819.
[178] M. Safdari, M. Al-Haik, Electrical conductivity of synergistically hybridized nanocomposites based on graphite nanoplatelets and carbon nanotubes, Nanotechnology 23(40) (2012).

[179] P. Pötschke, S.M. Dudkin, I. Alig, Dielectric spectroscopy on melt processed polycarbonate—multiwalled carbon nanotube composites, Polymer 44(17) (2003) 5023-5030.
[180] R. Patra, S. Suin, D. Mandal, B.B. Khatua, Sequential mixing as effective method in the reduction of percolation threshold of multiwall carbon nanotube in poly(methyl methacrylate)/high-density poly(ethylene)/MWCNT nanocomposites, Journal of Applied Polymer Science 131(10) (2014).
[181] H. Stoyanov, D. Mc Carthy, M. Kollosche, G. Kofod, Dielectric properties and electric breakdown strength of a subpercolative composite of carbon black in thermoplastic copolymer, Applied Physics Letters 94(23) (2009).
[182] X. Zhao, J. Zhao, J.P. Cao, D. Wang, G.H. Hu, F. Chen, Z.M. Dang, Effect of the selective localization of carbon nanotubes in polystyrene/poly(vinylidene fluoride) blends on their dielectric, thermal, and mechanical properties, Materials and Design 56 (2014) 807-815.
[183] D.P. Almond, C.R. Bowen, D.A.S. Rees, Composite dielectrics and conductors: Simulation, characterization and design, Journal of Physics D: Applied Physics 39(7) (2006) 1295-1304.
[184] X.S. Yi, J.F. Zhang, Q. Zheng, Y. Pan, Influence of irradiation conditions on the electrical behavior of polyethylene–carbon black conductive composites, Journal of applied polymer science 77(3) (2000) 494-499.
[185] M.-K. Seo, K.-Y. Rhee, S.-J. Park, Influence of electro-beam irradiation on PTC/NTC behaviors of carbon blacks/HDPE conducting polymer composites, Current Applied Physics 11(3) (2011) 428-433.
[186] M. Hindermann-Bischoff, F. Ehrburger-Dolle, Electrical conductivity of carbon black–polyethylene composites: Experimental evidence of the change of cluster connectivity in the PTC effect, Carbon 39(3) (2001) 375-382.
[187] S.C. George, S. Thomas, Transport phenomena through polymeric systems, Progress in Polymer Science 26(6) (2001) 985-1017.
[188] A. Randová, L. Bartovská, Chapter 4 - Fundamentals and Measurement Techniques for Solvent Transport in Polymers A2 - Thomas, Sabu, in: R. Wilson, A.K. S, S.C. George (Eds.), Transport Properties of Polymeric Membranes, Elsevier2018, pp. 51-70.
[189] D.K. Abhinav, B.Y. K., C.C. V., S. Sunil, LDPE/EVA/PCR/MWNT nanocomposites: Radiation crosslinking and physicomechanical characteristics, Polymer Composites 32(5) (2011) 737-746.
[190] D.K. A., B.Y. K., C.C. V., G.N. K., S. S., R. K., C.S. K., Radiation effects on styrene–butadiene–ethylene–propylene diene monomer-multiple walled carbon nanotube nanocomposites: vulcanization and characterization, Polymers for Advanced Technologies 22(12) (2011) 1888-1897.
[191] J.H. Petropoulos, M. Sanopoulou, K.G. Papadokostaki, Physically insightful modeling of non-Fickian kinetic regimes encountered in fundamental studies of isothermal sorption of swelling agents in polymeric media, European Polymer Journal 47(11) (2011) 2053-2062.
[192] P. McLoughlin, K. Flavin, P. Kirwan, B. Murphy, K. Murphy, Modelling of Fickian diffusion to enhance polymer-modified sensor performance, Sensors and Actuators B: Chemical 107(1) (2005) 170-177.
[193] T. Kaiser, Highly crosslinked polymers, Progress in Polymer Science 14(3) (1989) 373-450.
[194] S.-M. Li, L.-X. Zhang, M.-Y. Zhu, G.-J. Ji, L.-X. Zhao, J. Yin, L.-J. Bie, Acetone sensing of ZnO nanosheets synthesized using room-temperature precipitation, Sensors and Actuators B: Chemical 249(Supplement C) (2017) 611-623.

[195] S. Liang, J. Li, F. Wang, J. Qin, X. Lai, X. Jiang, Highly sensitive acetone gas sensor based on ultrafine α-Fe2O3 nanoparticles, Sensors and Actuators B: Chemical 238(Supplement C) (2017) 923-927.
[196] X. Hao, B. Wang, C. Ma, F. Liu, X. Yang, T. Liu, X. Liang, C. Yang, H. Zhu, G. Lu, Mixed potential type sensor based on stabilized zirconia and Co1-xZnx Fe2O4 sensing electrode for detection of acetone, Sensors and Actuators B: Chemical 255(Part 2) (2018) 1173-1181.
[197] S.T. Navale, Z.B. Yang, C. Liu, P.J. Cao, V.B. Patil, N.S. Ramgir, R.S. Mane, F.J. Stadler, Enhanced acetone sensing properties of titanium dioxide nanoparticles with a sub-ppm detection limit, Sensors and Actuators B: Chemical 255(Part 2) (2018) 1701-1710.
[198] X. Kou, N. Xie, F. Chen, T. Wang, L. Guo, C. Wang, Q. Wang, J. Ma, Y. Sun, H. Zhang, G. Lu, Superior acetone gas sensor based on electrospun SnO2 nanofibers by Rh doping, Sensors and Actuators B: Chemical 256(Supplement C) (2018) 861-869.
[199] X.-Z. Song, L. Qiao, K.-M. Sun, Z. Tan, W. Ma, X.-L. Kang, F.-F. Sun, T. Huang, X.-F. Wang, Triple-shelled ZnO/ZnFe2O4 heterojunctional hollow microspheres derived from Prussian Blue analogue as high-performance acetone sensors, Sensors and Actuators B: Chemical 256(Supplement C) (2018) 374-382.
[200] X. Li, D. Lu, C. Shao, G. Lu, X. Li, Y. Liu, Hollow CuFe2O4/α-Fe2O3 composite with ultrathin porous shell for acetone detection at ppb levels, Sensors and Actuators B: Chemical 258(Supplement C) (2018) 436-446.
[201] E. Baysak, S. Yuvayapan, A. Aydogan, G. Hizal, Calix[4]pyrrole-decorated carbon nanotubes on paper for sensing acetone vapor, Sensors and Actuators B: Chemical 258 (2018) 484-491.
[202] B. Wang, Q. Yu, S. Zhang, T. Wang, P. Sun, X. Chuai, G. Lu, Gas sensing with yolk-shell LaFeO3 microspheres prepared by facile hydrothermal synthesis, Sensors and Actuators B: Chemical 258 (2018) 1215-1222.
[203] A. Thamri, H. Baccar, C. Struzzi, C. Bittencourt, A. Abdelghani, E. Llobet, MHDA-functionalized multiwall carbon nanotubes for detecting non-aromatic VOCs, Scientific Reports 6 (2016).
[204] W. Miekisch, J.K. Schubert, G.F. Noeldge-Schomburg, Diagnostic potential of breath analysis—focus on volatile organic compounds, Clinica chimica acta 347(1-2) (2004) 25-39.
[205] E.S. Deneris, R.A. Stein, J.F. Mead, Invitro biosynthesis of isoprene from mevalonate utilizing a rat liver cytosolic fraction, Biochemical and Biophysical Research Communications 123(2) (1984) 691-696.
[206] R.A. Stein, J.F. Mead, Small hydrocarbons formed by the peroxidation of squalene, Chemistry and Physics of Lipids 46(2) (1988) 117-120.
[207] A. Bajtarevic, C. Ager, M. Pienz, M. Klieber, K. Schwarz, M. Ligor, T. Ligor, W. Filipiak, H. Denz, M. Fiegl, W. Hilbe, W. Weiss, P. Lukas, H. Jamnig, M. Hackl, A. Haidenberger, B. Buszewski, W. Miekisch, J. Schubert, A. Amann, Noninvasive detection of lung cancer by analysis of exhaled breath, BMC Cancer 9(1) (2009) 348.
[208] S.J. Davies, P. Španěl, D. Smith, Breath analysis of ammonia, volatile organic compounds and deuterated water vapor in chronic kidney disease and during dialysis, Bioanalysis 6(6) (2014) 843-857.
[209] N. Alkhouri, T. Singh, E. Alsabbagh, J. Guirguis, T. Chami, I. Hanouneh, D. Grove, R. Lopez, R. Dweik, Isoprene in the exhaled breath is a novel biomarker for advanced fibrosis in patients with chronic liver disease: A pilot study, Clinical and translational gastroenterology 6(9) (2015) e112.
[210] T.H. Risby, S.S. Sehnert, Clinical application of breath biomarkers of oxidative stress status, Free Radical Biology and Medicine 27(11) (1999) 1182-1192.

[211] C.V. Chaudhari, Y.K. Bhardwaj, N.D. Patil, K.A. Dubey, V. Kumar, S. Sabharwal, Radiation-induced vulcanisation of natural rubber latex in presence of styrene-butadiene rubber latex, Radiation Physics and Chemistry 72(5) (2005) 613-618.
[212] T.-M. Wu, E.-C. Chen, Preparation and characterization of conductive carbon nanotube–polystyrene nanocomposites using latex technology, Composites Science and Technology 68(10) (2008) 2254-2259.
[213] S. Barrau, P. Demont, A. Peigney, C. Laurent, C. Lacabanne, DC and AC conductivity of carbon nanotubes− polyepoxy composites, Macromolecules 36(14) (2003) 5187-5194.
[214] T. Jose, G. Moni, S. Salini, A.J. Raju, J.J. George, S.C. George, Multifunctional multi-walled carbon nanotube reinforced natural rubber nanocomposites, Industrial Crops and Products 105 (2017) 63-73.
[215] R.A. Kalgaonkar, J.P. Jog, Copolyester nanocomposites based on carbon nanotubes: reinforcement effect of carbon nanotubes on viscoelastic and dielectric properties of nanocomposites, Polymer International 57(1) (2008) 114-123.
[216] Z. Oommen, G. Groeninckx, S. Thomas, Dynamic mechanical and thermal properties of physically compatibilized natural rubber/poly(methyl methacrylate) blends by the addition of natural rubber-graft- poly(methyl methacrylate), Journal of Polymer Science Part B: Polymer Physics 38(4) (2000) 525-536.
[217] J.-F. Feller, M. Castro, B. Kumar, Volatile organic compound (VOC) sensors made of polymer-carbon nanofiller films hierarchically assembled by spray LbL, (2012).
[218] B. de Lacy Costello, R. Ewen, H. Gunson, N.M. Ratcliffe, P.T. Spencer-Phillips, The development of a sensor system for the early detection of soft rot in stored potato tubers, Measurement Science and Technology 11(12) (2000) 1685.
[219] J.-J. Ho, Y.K. Fang, K.H. Wu, W.T. Hsieh, C.H. Chen, G.S. Chen, M.S. Ju, J.-J. Lin, S.B. Hwang, High sensitivity ethanol gas sensor integrated with a solid-state heater and thermal isolation improvement structure for legal drink-drive limit detecting, Sensors and Actuators B: Chemical 50(3) (1998) 227-233.
[220] T.-J. Hsueh, C.-L. Hsu, S.-J. Chang, I.-C. Chen, Laterally grown ZnO nanowire ethanol gas sensors, Sensors and Actuators B: Chemical 126(2) (2007) 473-477.
[221] W. Chen, K. Stewart, J. Carroll, R. Mansour, E. Abdel-Rahman, A. Penlidis, Novel gaseous phase ethanol sensor implemented with underloaded RF resonator for sensor-embedded passive chipless rfids, Solid-State Sensors, Actuators and Microsystems (TRANSDUCERS & EUROSENSORS XXVII), 2013 Transducers & Eurosensors XXVII: The 17th International Conference on, IEEE, 2013, pp. 2059-2062.
[222] J.A. Ragazzo-Sanchez, P. Chalier, C. Ghommidh, Coupling gas chromatography and electronic nose for dehydration and desalcoholization of alcoholized beverages: Application to off-flavour detection in wine, Sensors and Actuators B: Chemical 106(1) (2005) 253-257.
[223] C.M. Hussain, C. Saridara, S. Mitra, Self-Assembly of Carbon Nanotubes via Ethanol Chemical Vapor Deposition for the Synthesis of Gas Chromatography Columns, Analytical Chemistry 82(12) (2010) 5184-5188.
[224] A.A. Athawale, M.V. Kulkarni, Polyaniline and its substituted derivatives as sensor for aliphatic alcohols, Sensors and Actuators B: Chemical 67(1-2) (2000) 173-177.
[225] C. De Melo, B. Neto, E. De Lima, L. De Lira, J. De Souza, Use of conducting polypyrrole blends as gas sensors, Sensors and Actuators B: Chemical 109(2) (2005) 348-354.
[226] K. Stewart, N.M. McManus, E. Abdel-Rahman, A. Penlidis, Doped polyaniline for the detection of formaldehyde, Journal of Macromolecular Science, Part A 49(1) (2012) 1-6.

[227] P. Kar, N.C. Pradhan, B. Adhikari, Application of sulfuric acid doped poly (m-aminophenol) as aliphatic alcohol vapor sensor material, Sensors and Actuators B: Chemical 140(2) (2009) 525-531.
[228] M. Sônego, L.C. Costa, J.D. Ambrósio, Polyvinyl butyral chemically modified with a silane agent in the molten state, Polymer Engineering & Science 56(9) (2016) 971-979.
[229] P. Rajat, S. Supratim, M. Dipankar, K.B. B., Sequential mixing as effective method in the reduction of percolation threshold of multiwall carbon nanotube in poly(methyl methacrylate)/high-density poly(ethylene)/MWCNT nanocomposites, Journal of Applied Polymer Science 131(10) (2014).
[230] B.E. Kilbride, J.N. Coleman, J. Fraysse, P. Fournet, M. Cadek, A. Drury, S. Hutzler, S. Roth, W.J. Blau, Experimental observation of scaling laws for alternating current and direct current conductivity in polymer-carbon nanotube composite thin films, Journal of Applied Physics 92(7) (2002) 4024-4030.
[231] A. Linares, J.C. Canalda, M.E. Cagiao, M.C. García-Gutiérrez, A. Nogales, I. Martín-Gullón, J. Vera, T.A. Ezquerra, Broad-Band Electrical Conductivity of High Density Polyethylene Nanocomposites with Carbon Nanoadditives: Multiwall Carbon Nanotubes and Carbon Nanofibers, Macromolecules 41(19) (2008) 7090-7097.
[232] P. Sheng, E. Sichel, J.I. Gittleman, Fluctuation-induced tunneling conduction in carbon-polyvinylchloride composites, Physical Review Letters 40(18) (1978) 1197.
[233] R.K. Mondal, K.A. Dubey, J. Kumar, Jagannath, Y.K. Bhardwaj, J.S. Melo, L. Varshney, Carbon Nanotube Functionalization and Radiation Induced Enhancements in the Sensitivity of Standalone Chemiresistors for Sensing Volatile Organic Compounds, ACS Applied Nano Materials (2018).
[234] G. Hu, C. Zhao, S. Zhang, M. Yang, Z. Wang, Low percolation thresholds of electrical conductivity and rheology in poly (ethylene terephthalate) through the networks of multi-walled carbon nanotubes, Polymer 47(1) (2006) 480-488.
[235] P. Pötschke, T.D. Fornes, D.R. Paul, Rheological behavior of multiwalled carbon nanotube/polycarbonate composites, Polymer 43(11) (2002) 3247-3255.
[236] C. Penu, G.H. Hu, A. Fernandez, P. Marchal, L. Choplin, Rheological and electrical percolation thresholds of carbon nanotube/polymer nanocomposites, Polymer Engineering & Science 52(10) (2012) 2173-2181.
[237] F. Paraguay D, M. Miki-Yoshida, J. Morales, J. Solis, W. Estrada L, Influence of Al, In, Cu, Fe and Sn dopants on the response of thin film ZnO gas sensor to ethanol vapour, Thin Solid Films 373(1) (2000) 137-140.
[238] R. Mondal, J. Kumar, K. Dubey, Y. Bhardwaj, J. Melo, L. Varshney, Network density tailored standalone-flexible fluorocarbon elastomer/nanocarbon black chemiresistors for 2-propanone field detection, Sensors and Actuators B: Chemical 265 (2018) 193-203.
[239] J.R. Li, J.R. Xu, M.Q. Zhang, M.Z. Rong, Carbon black/polystyrene composites as candidates for gas sensing materials, Carbon 41(12) (2003) 2353-2360.
[240] H. Iwata, T. Nakanoya, H. Morohashi, J. Chen, T. Yamauchi, N. Tsubokawa, Novel gas and contamination sensor materials from polyamide-block-poly(ethylene oxide)-grafted carbon black, Sensors and Actuators B: Chemical 113(2) (2006) 875-882.
[241] D. Lubasova, L. Martinova, Controlled morphology of porous polyvinyl butyral nanofibers, Journal of Nanomaterials 2011 (2011).
[242] A. Bouvree, J.-F. Feller, M. Castro, Y. Grohens, M. Rinaudo, Conductive polymer nano-biocomposites (CPC): chitosan-carbon nanoparticle a good candidate to design polar vapour sensors, Sensors and Actuators B: Chemical 138(1) (2009) 138-147.

[243] R. Moolla, C.J. Curtis, J. Knight, Assessment of occupational exposure to BTEX compounds at a bus diesel-refueling bay: A case study in Johannesburg, South Africa, Science of The Total Environment 537 (2015) 51-57.
[244] M. Dehghani, M. Fazlzadeh, A. Sorooshian, H.R. Tabatabaee, M. Miri, A.N. Baghani, M. Delikhoon, A.H. Mahvi, M. Rashidi, Characteristics and health effects of BTEX in a hot spot for urban pollution, Ecotoxicology and Environmental Safety 155 (2018) 133-143.
[245] A. Masih, A.S. Lall, A. Taneja, R. Singhvi, Inhalation exposure and related health risks of BTEX in ambient air at different microenvironments of a terai zone in north India, Atmospheric Environment 147 (2016) 55-66.
[246] T.T.N. Lan, N.T.T. Binh, Daily roadside BTEX concentrations in East Asia measured by the Lanwatsu, Radiello and Ultra I SKS passive samplers, Science of The Total Environment 441 (2012) 248-257.
[247] F. Bender, R.E. Mohler, A.J. Ricco, F. Josse, Analysis of binary mixtures of aqueous aromatic hydrocarbons with low-phase-noise shear-horizontal surface acoustic wave sensors using multielectrode transducer designs, Analytical chemistry 86(22) (2014) 11464-11471.
[248] H. Zhang, J. Ma, D. Chen, J. Zhou, S. Zhang, W. Shi, P. Cheng, Microporous heterometal-organic framework as a sensor for BTEX with high selectivity, Journal of Materials Chemistry A 2(48) (2014) 20450-20453.
[249] R.R. Noble, L. Stalker, S.A. Wakelin, B. Pejcic, M.I. Leybourne, A.L. Hortle, K. Michael, Biological monitoring for carbon capture and storage–A review and potential future developments, International Journal of Greenhouse Gas Control 10 (2012) 520-535.
[250] R. Nasreddine, V. Person, C.A. Serra, S. Le Calvé, Development of a novel portable miniaturized GC for near real-time low level detection of BTEX, Sensors and Actuators B: Chemical 224 (2016) 159-169.
[251] R. Nasreddine, V. Person, C.A. Serra, C. Schoemaecker, S. Le Calvé, Portable novel micro-device for BTEX real-time monitoring: Assessment during a field campaign in a low consumption energy junior high school classroom, Atmospheric Environment 126 (2016) 211-217.
[252] L.I.B. Silva, T.A.P. Rocha-Santos, A.C. Duarte, Remote optical fibre microsensor for monitoring BTEX in confined industrial atmospheres, Talanta 78(2) (2009) 548-552.
[253] K. Zhou, C. Gu, Z. Zhang, L. Xing, X. Li, C. Fu, A novel BTEX gas sensor utilizing cataluminescence on nanosized Bi4MnO8, Digital Manufacturing and Automation (ICDMA), 2011 Second International Conference on, IEEE, 2011, pp. 81-84.
[254] K.E. Prasad, B. Das, U. Maitra, U. Ramamurty, C. Rao, Extraordinary synergy in the mechanical properties of polymer matrix composites reinforced with 2 nanocarbons, Proceedings of the National Academy of Sciences 106(32) (2009) 13186-13189.
[255] S. Sinha, K. Dubey, V. Grover, P. Sastry, Y. Bhardwaj, L. Panicker, A. Tyagi, P. Mahanwar, V. Bambole, Selective interfacial localization in conducting polycaprolactam/ethylene vinyl acetate/carbon black composites, Polymer Composites 34(6) (2013) 912-919.
[256] K. Dubey, S. Majji, S. Sinha, Y. Bhardwaj, S. Acharya, C. Chaudhari, L. Varshney, Synergetic effects of radiolytically degraded PTFE microparticles and organoclay in PTFE-reinforced ethylene vinyl acetate composites, Materials Chemistry and Physics 143(1) (2013) 149-154.
[257] X. Niu, S. Peng, L. Liu, W. Wen, P. Sheng, Characterizing and patterning of PDMS-based conducting composites, Advanced Materials 19(18) (2007) 2682-2686.
[258] S. Gong, W. Schwalb, Y. Wang, Y. Chen, Y. Tang, J. Si, B. Shirinzadeh, W. Cheng, A wearable and highly sensitive pressure sensor with ultrathin gold nanowires, Nature Communications 5 (2014) 3132.

[259] C. Pang, G.-Y. Lee, T.-i. Kim, S.M. Kim, H.N. Kim, S.-H. Ahn, K.-Y. Suh, A flexible and highly sensitive strain-gauge sensor using reversible interlocking of nanofibres, Nature materials 11(9) (2012) 795.
[260] C. Karuwan, A. Wisitsoraat, T. Maturos, D. Phokharatkul, A. Sappat, K. Jaruwongrungsee, T. Lomas, A. Tuantranont, Flow injection based microfluidic device with carbon nanotube electrode for rapid salbutamol detection, Talanta 79(4) (2009) 995-1000.
[261] K. Juwan, L. Joohyung, K. Tae Hyun, P. June, S. Maeng-Je, H. Seunghun, Large-scale assembly of carbon nanotube-based flexible circuits for DNA sensors, Nanotechnology 19(13) (2008) 135305.
[262] A. Esteves, J. Brokken-Zijp, J. Laven, H. Huinink, N. Reuvers, M. Van, Influence of cross-linker concentration on the cross-linking of PDMS and the network structures formed, Polymer 50(16) (2009) 3955-3966.
[263] M. Meléndez-Zamudio, A. Villegas, J. González-Calderón, R. Meléndrez, M. Meléndez-Lira, J. Cervantes, Study of a Polydimethylsiloxane (PDMS) Elastomer Generated by γ Irradiation: Correlation Between Properties (Thermal and Mechanical) and Structure (Crosslink Density Value), Journal of Inorganic and Organometallic Polymers and Materials 27(3) (2017) 622-632.
[264] H. Stoyanov, D.M. Carthy, M. Kollosche, G. Kofod, Dielectric properties and electric breakdown strength of a subpercolative composite of carbon black in thermoplastic copolymer, Applied Physics Letters 94(23) (2009) 232905.
[265] D.P. Almond, C. Bowen, D. Rees, Composite dielectrics and conductors: simulation, characterization and design, Journal of Physics D: Applied Physics 39(7) (2006) 1295.
[266] N.K. Kang, T.S. Jun, D.-D. La, J.H. Oh, Y.W. Cho, Y.S. Kim, Evaluation of the limit-of-detection capability of carbon black-polymer composite sensors for volatile breath biomarkers, Sensors and Actuators B: Chemical 147(1) (2010) 55-60.
[267] S.G. Chen, X.L. Hu, J. Hu, M.Q. Zhang, M.Z. Rong, Q. Zheng, Relationships between organic vapor adsorption behaviors and gas sensitivity of carbon black filled waterborne polyurethane composites, Sensors and Actuators B: Chemical 119(1) (2006) 110-117.
[268] P.-G. Su, S.-C. Huang, Electrical and humidity sensing properties of carbon nanotubes-SiO2-poly (2-acrylamido-2-methylpropane sulfonate) composite material, Sensors and Actuators B: Chemical 113(1) (2006) 142-149.
[269] A. Sujith, C. Radhakrishnan, G. Unnikrishnan, S. Thomas, Mass transfer characteristics of natural rubber/ethylene vinyl acetate blends, Journal of applied polymer science 90(10) (2003) 2691-2702.
[270] H. Lei, W.G. Pitt, L.K. McGrath, C.K. Ho, Modeling carbon black/polymer composite sensors, Sensors and Actuators B: Chemical 125(2) (2007) 396-407.
[271] Q. Fan, Z. Qin, T. Villmow, J. Pionteck, P. Pötschke, Y. Wu, B. Voit, M. Zhu, Vapor sensing properties of thermoplastic polyurethane multifilament covered with carbon nanotube networks, Sensors and Actuators B: Chemical 156(1) (2011) 63-70.
[272] V. Thomsen, D. Schatzlein, D. Mercuro, Limits of detection in spectroscopy, Spectroscopy 18(12) (2003) 112-114.
[273] I.T. Jolliffe, Graphical representation of data using principal components, Principal component analysis (2002) 78-110.
[274] T. Alizadeh, Chemiresistor sensors array optimization by using the method of coupled statistical techniques and its application as an electronic nose for some organic vapors recognition, Sensors and Actuators B: Chemical 143(2) (2010) 740-749.
[275] C. Klason, J. Kubát, Anomalous behavior of electrical conductivity and thermal noise in carbon black-containing polymers at Tg and Tm, Journal of Applied Polymer Science 19(3) (1975) 831-845.

[276] R. Mondal, K. Dubey, Y. Bhardwaj, L. Panicker, L. Varshney, Acronitrile butadiene styrene/polycaprolactam/nano carbon black composites: Selective percolation, glass transition and temperature dependence of electrical conductivity, Polymer Composites 37(2) (2016) 481-487.
[277] I. Dube, D. Jiménez, G. Fedorov, A. Boyd, I. Gayduchenko, M. Paranjape, P. Barbara, Understanding the electrical response and sensing mechanism of carbon-nanotube-based gas sensors, Carbon 87 (2015) 330-337.
[278] A. Boyd, I. Dube, G. Fedorov, M. Paranjape, P. Barbara, Gas sensing mechanism of carbon nanotubes: from single tubes to high-density networks, Carbon 69 (2014) 417-423.
[279] P. Ajayan, O. Stephan, C. Colliex, D. Trauth, Aligned carbon nanotube arrays formed by cutting a polymer resin—nanotube composite, Science 265(5176) (1994) 1212-1214.
[280] J.-M. Thomassin, X. Lou, C. Pagnoulle, A. Saib, L. Bednarz, I. Huynen, R. Jeroˆme, C. Detrembleur, Multiwalled carbon nanotube/poly (ε-caprolactone) nanocomposites with exceptional electromagnetic interference shielding properties, The Journal of Physical Chemistry C 111(30) (2007) 11186-11192.
[281] J. Amarasekera, Conductive plastics for electrical and electronic applications, Reinforced Plastics 49(8) (2005) 38-41.
[282] B. Zhang, R. Fu, M. Zhang, X. Dong, L. Wang, C.U. Pittman, Gas sensitive vapor grown carbon nanofiber/polystyrene sensors, Materials Research Bulletin 41(3) (2006) 553-562.
[283] R.J. Chen, Y. Zhang, D. Wang, H. Dai, Noncovalent Sidewall Functionalization of Single-Walled Carbon Nanotubes for Protein Immobilization, Journal of the American Chemical Society 123(16) (2001) 3838-3839.
[284] P.G. Collins, A. Zettl, H. Bando, A. Thess, R.E. Smalley, Nanotube Nanodevice, Science 278(5335) (1997) 100-102.
[285] Z. Spitalsky, D. Tasis, K. Papagelis, C. Galiotis, Carbon nanotube–polymer composites: chemistry, processing, mechanical and electrical properties, Progress in polymer science 35(3) (2010) 357-401.
[286] C.S. Boland, U. Khan, G. Ryan, S. Barwich, R. Charifou, A. Harvey, C. Backes, Z. Li, M.S. Ferreira, M.E. Möbius, Sensitive electromechanical sensors using viscoelastic graphene-polymer nanocomposites, Science 354(6317) (2016) 1257-1260.
[287] A.K. Kota, B.H. Cipriano, M.K. Duesterberg, A.L. Gershon, D. Powell, S.R. Raghavan, H.A. Bruck, Electrical and Rheological Percolation in Polystyrene/MWCNT Nanocomposites, Macromolecules 40(20) (2007) 7400-7406.
[288] R.K. Mondal, K.A. Dubey, Y.K. Bhardwaj, L. Varshney, Novel hybrid nanocarbons/poly(dimethylsiloxane) composites based chemiresistors for real time detection of hazardous aromatic hydrocarbons, Carbon 100 (2016) 42-51.
[289] S. Nag, A. Sachan, M. Castro, V. Choudhary, J.F. Feller, Spray layer-by-layer assembly of POSS functionalized CNT quantum chemo-resistive sensors with tuneable selectivity and ppm resolution to VOC biomarkers, Sensors and Actuators B: Chemical 222 (2016) 362-373.
[290] P. Liu, Modifications of carbon nanotubes with polymers, European Polymer Journal 41(11) (2005) 2693-2703.
[291] I. Szleifer, R. Yerushalmi-Rozen, Polymers and carbon nanotubes—dimensionality, interactions and nanotechnology, Polymer 46(19) (2005) 7803-7818.
[292] C.V. Chaudhari, K.A. Dubey, Y.K. Bhardwaj, S. Sabharwal, Radiation Processed Styrene-Butadiene Rubber/Ethylene-Propylene Diene Rubber/Multiple-Walled Carbon Nanotubes Nanocomposites: Effect of MWNT Addition on Solvent Permeability Behavior, Journal of Macromolecular Science, Part B 51(5) (2012) 839-859.

[293] K. Dubey, Y. Bhardwaj, C. Chaudhari, N. Goel, S. Sabharwal, K. Rajkumar, S. Chakraborty, Radiation effects on styrene–butadiene–ethylene–propylene diene monomer-multiple walled carbon nanotube nanocomposites: vulcanization and characterization, Polymers for Advanced Technologies 22(12) (2011) 1888-1897.
[294] Q. Guo, Q. Xue, J. Sun, M. Dong, F. Xia, Z. Zhang, Gigantic enhancement in the dielectric properties of polymer-based composites using core/shell MWCNT/amorphous carbon nanohybrids, Nanoscale 7(8) (2015) 3660-3667.
[295] K. Goswami, A.E. Daugaard, A.L. Skov, Dielectric properties of ultraviolet cured poly (dimethyl siloxane) sub-percolative composites containing percolative amounts of multi-walled carbon nanotubes, RSC Advances 5(17) (2015) 12792-12799.
[296] J. Zhang, M. Mine, D. Zhu, M. Matsuo, Electrical and dielectric behaviors and their origins in the three-dimensional polyvinyl alcohol/MWCNT composites with low percolation threshold, Carbon 47(5) (2009) 1311-1320.
[297] P.G. Whitten, H.R. Brown, Polymer entanglement density and its influence on interfacial friction, Physical Review E 76(2) (2007) 026101.
[298] I.N. Haugan, M.J. Maher, A.B. Chang, T.-P. Lin, R.H. Grubbs, M.A. Hillmyer, F.S. Bates, Consequences of Grafting Density on the Linear Viscoelastic Behavior of Graft Polymers, ACS Macro Letters 7(5) (2018) 525-530.
[299] B.J. Anderson, C.F. Zukoski, Rheology and microstructure of entangled polymer nanocomposite melts, Macromolecules 42(21) (2009) 8370-8384.
[300] K. Stockelhuber, A. Svistkov, A. Pelevin, G. Heinrich, Impact of filler surface modification on large scale mechanics of styrene butadiene/silica rubber composites, Macromolecules 44(11) (2011) 4366-4381.
[301] F. Wu, S. Zhang, Z. Chen, B. Zhang, W. Yang, Z. Liu, M. Yang, Interfacial relaxation mechanisms in polymer nanocomposites through the rheological study on polymer/grafted nanoparticles, Polymer 90 (2016) 264-275.
[302] F. Helaly, W. Darwich, M.A. El-Ghaffar, Effect of some polyaromatic amines on the properties of NR and SBR vulcanizates, Polymer Degradation and Stability 64(2) (1999) 251-257.
[303] A. Nazran, D. Griller, Hydrogen abstraction from amines: formation of aminyl vs.. alpha.-aminoalkyl radicals, Journal of the American Chemical Society 105(7) (1983) 1970-1971.
[304] M. Salamone, I. Giammarioli, M. Bietti, Tuning hydrogen atom abstraction from the aliphatic C–H bonds of basic substrates by protonation. Control over selectivity by C–H deactivation, Chemical Science 4(8) (2013) 3255-3262.
[305] M. Mooney, A theory of large elastic deformation, Journal of applied physics 11(9) (1940) 582-592.
[306] H. Koerner, W. Liu, M. Alexander, P. Mirau, H. Dowty, R.A. Vaia, Deformation–morphology correlations in electrically conductive carbon nanotube—thermoplastic polyurethane nanocomposites, Polymer 46(12) (2005) 4405-4420.
[307] S. Schlögl, M.-L. Trutschel, W. Chassé, G. Riess, K. Saalwächter, Entanglement effects in elastomers: Macroscopic vs microscopic properties, Macromolecules 47(9) (2014) 2759-2773.
[308] S.C. Roh, E.Y. Choi, Y.S. Choi, C. Kim, Characterization of the surface energies of functionalized multi-walled carbon nanotubes and their interfacial adhesion energies with various polymers, Polymer 55(6) (2014) 1527-1536.
[309] V. Khoshkava, M. Kamal, Effect of surface energy on dispersion and mechanical properties of polymer/nanocrystalline cellulose nanocomposites, Biomacromolecules 14(9) (2013) 3155-3163.

[310] K.S. Khare, F. Khabaz, R. Khare, Effect of carbon nanotube functionalization on mechanical and thermal properties of cross-linked epoxy–carbon nanotube nanocomposites: role of strengthening the interfacial interactions, ACS applied materials & interfaces 6(9) (2014) 6098-6110.

[311] M. Nour, K. Berean, S. Balendhran, J.Z. Ou, J. Du Plessis, C. McSweeney, M. Bhaskaran, S. Sriram, K. Kalantar-zadeh, CNT/PDMS composite membranes for H2 and CH4 gas separation, International Journal of Hydrogen Energy 38(25) (2013) 10494-10501.

[312] K.A. Wepasnick, B.A. Smith, J.L. Bitter, D.H. Fairbrother, Chemical and structural characterization of carbon nanotube surfaces, Analytical and bioanalytical chemistry 396(3) (2010) 1003-1014.

[313] C. Cao, M. Ge, J. Huang, S. Li, S. Deng, S. Zhang, Z. Chen, K. Zhang, S.S. Al-Deyab, Y. Lai, Robust fluorine-free superhydrophobic PDMS–ormosil@ fabrics for highly effective self-cleaning and efficient oil–water separation, Journal of Materials Chemistry A 4(31) (2016) 12179-12187.

[314] W. Zhang, H. Zhang, J. Xiao, Z. Zhao, M. Yu, Z. Li, Carbon nanotube catalysts for oxidative desulfurization of a model diesel fuel using molecular oxygen, Green Chemistry 16(1) (2014) 211-220.

[315] M. Weimer, Highly crosslinked polymer dielectric films for improved capacitor performance, Google Patents, 2017.

[316] S. Xu, O. Rezvanian, K. Peters, M. Zikry, The viability and limitations of percolation theory in modeling the electrical behavior of carbon nanotube–polymer composites, Nanotechnology 24(15) (2013) 155706.

[317] J. Jancar, J. Douglas, F.W. Starr, S. Kumar, P. Cassagnau, A. Lesser, S.S. Sternstein, M. Buehler, Current issues in research on structure–property relationships in polymer nanocomposites, Polymer 51(15) (2010) 3321-3343.

Appendix

A1. Composition of FCE/NCB nanocomposites

Wt % of FCE	Wt % of NCB	Volume fraction of NCB (ϕ)	Sample designation
90	10	0.1	VT10
85	15	0.19101	VT15
80	20	0.23944	VT20
75	25	0.28814	VT25
70	30	0.33711	VT30
65	35	0.38636	VT35
60	40	0.4111	VT40

A2. Composition of NRL/CNT nanocomposites

Volume of NRL solution (ml)	Dry rubber contained	Weight of CNT	Wt % of CNT	Volume fraction of CNT (ϕ)
25	15	0.15	1	0.005
25	15	0.375	2.5	0.014
25	15	0.75	5	0.029
25	15	1.5	10	0.06
25	15	2.25	15	0.093

A3. Composition of PVB/CNT nanocomposites

Wt % of PVB	Wt % of CNT	Volume fraction of CNT (ϕ)
99	1	0.0067
97.5	2.5	0.017
95	5	0.034
92.5	7.5	0.0514
90	10	0.07
85	15	0.1

A4. Composition of PDMS/NCB/CNT hybrid nanocomposites

Sample designation	Wt % of PDMS	Wt% of NCB	Wt % of CNT
M0	70	30	0
M1	69	30	1
M2	68	30	2
M3	67	30	3

A5. Composition of PDMS/ CNT and PDMS/ functionalized CNT nanocomposites

Wt % of PDMS	Wt % of CNT and functionalized CNT	Volume fraction of CNT and functionalized CNT (ϕ)
99	1	0.004
97.5	2.5	0.009
95	5	0.02
92.5	7.5	0.03
90	10	0.04
85	15	0.06